CRANFIELD UNIVERSITY

SCHOOL OF ENGINEERING

CENTRE OF PROPULSION

PhD

Thesis

KONSTANTINOS KARAMOLEGKOS

Ducted Tail Rotor Perfomance Prediction Using CFD

Supervisor : Dr V.Pachidis

Completion date : 12^{th} May 2014

All rights reserved, no part of this publication may be reproduced without the written permission of the copyright owner

Abstract

Aviation industry has a crucial impact on society on the grounds that it offers wider social and economic benefits. The demand of transportation is increasing and it is expected that the worldwide fleet of aircraft and rotorcraft will increase accordingly. This growth will introduce an increased environmental impact which can be controlled with the introduction and the implementation of new and greener technologies which can provide both a reduced carbon footprint and increased efficiency. Therefore, the simulation of new designs with tools that can capture the flow physics accurately is crucial, on the grounds that an accurate simulation could provide novel designs and new ways in order to design from scratch new vehicles as well as providing a better appreciation of the physics that are involved. This work has a central aim to propose a methodology which combines CFD simulations and the method of performance mapping. It focuses on the application of a ducted tail rotor which can offer significant performance benefits compared to a conventional tail rotor. The developed methodology was tested against the results of an in-house rotorcraft comprehensive code and provided a reasonable qualitative correlation. In principle, this methodology can work for all helicopter flight phases such as hover, climb, cruise, descend but due to the complexity of the investigations, together with the lack of experimental data that can be used to refine the CFD model, only the hover and forward flight were considered. Although CFD studies of a ducted tail rotor currently exist in the literature (though scarce), this work can be considered, to the best knowledge of the author as a first attempt in investigating the performance of the configuration, from low to high forward flight speed, by combining CFD and performance mapping.

Keywords: Ducted tail rotor, Conventional tail rotor, Edgewise flow, CFD, Performance Mapping

Acknowledgements

First of all, I would like to thank Professor Pilidis who gave me the opportunity to pursue PhD studies at the Centre of Propulsion at Cranfield University. My wholehearted gratitude goes to my supervisor Dr Vassilios Pachidis who gave me guidance and advice all these years. I will really miss working together on the Clean Sky project.

I would like also to thank my colleague Dr Ioannis Goulos for providing me an executable of his code. I would also like to thank Dr Joao Texeira, for his friendship and for our fruitful discussions about CFD and its validation. In addition, I would also like to thank two former academic staff of Cranfield, Dr Vladimir Titarev and Dr Evgeniy Shapiro who introduced me to the discipline of CFD. I will always thank them for that.

I would also like to thank the secretary staff, Gill Hargreaves and Nicola Datt who were always willing to offer a helping hand and always with a smile on their faces. Many thanks also to my friend and colleague Christos. Finally, I would like to thank my family for their support and love and especially my Mother just for everything.

Contents

List of Figures

List of Tables

Nomenclature

A	Rotor disc area, 19
A_e	Diffuser exit plane area, 19
α	angle of attack, 36
b	Fin span, 91
β_{1c_T}	Cyclic flapping angle, 82
β_{1s_T}	Lateral flapping angle, 82
c	Airfoil chord, 42
$C_{l,max}$	Maximum lift coefficient, 55
C_p	Pressure coefficient, 59
C_P	Power coefficient, 47
c_r	Chord length at the root, 91
C_{Treq}	Required thrust coefficient, 83
c_t	Chord length at the tip, 91
C_T	Thrust coefficient, 47
C_T/σ	Blade loading coefficient, 61
δ	Relative pressure, 69
δ_o	Density at ISA conditions, 68
δ_{tip}	Blade tip clearance, 25
$\frac{dC_l}{d\alpha}$	Lift slope, 74
g	Acceleration of gravity, 69
h	Altitude, 66
h_T	Height of the tail rotor hub from the fuselage reference point, 82
ISA_{dev}	ISA deviation, 74
L_d	Diffuser length, 25
l_{ref}	Reference length for the computational domain, 158
l_T	Distance between the tail rotor hub from the fuselage reference point, 82
λ	Temperatute lapse rate, 69
M_∞	Freestream Mach number, 74
$\mathbf{U}$	Vector of tangential velocity, 108
$\mathbf{V_r}$	Vector of relative velocity, 108
$\mathbf{V}$	Vector of absolute velocity, 108
$\mathcal{R}$	Ideal gas constant, 69
μ	advance ratio, 28
N_b	Number of blades, 42
Ω	Angular Velocity of the Rotor, 28
Ω_{main}	Main rotor's rotational speed, 197

Ω_T Angular velocity of the tail rotor, 80

p Atmospheric pressure, 69

P Power, 32

p_{atm} Atmospheric pressure, 218

p_∞ Freestream static pressure, 121

P_i Induced power, 20

p_o Atmospheric pressure at ISA conditions, 68

ϕ Induced angle of attack, 74

Q Torque of main rotor, 79

Q_T Torque of tail rotor, 80

r Non-dimensional radial position, 43

R Blade Radius, 28

r Non-dimensional distance used for the shroud surface pressure distributions in hover, 116

r_∞ radius of the wake, 153

r_{lip} Inlet lip radius, 25

R_M Main rotor's radius, 197

R_T Tail rotor's radius, 197

ρ Density, 20

σ Blade solidity, 42

σ Relative density, 69

σ_d Diffuser expansion ratio, 19

T Thrust force, 17

T Temperature, 68

T' ISA Temperature offset, 71

T_o Temperature at ISA conditions, 68

T_{req} Required thrust, 83

T_{rotor} Rotor thrust, 17

T_{shroud} Shroud thrust, 17

T_{total} Total thrust of the rotor-shroud system, 17

T_T Tail Rotor Thrust, 79

τ_w Wall shear stress, 102

Θ Relative temperature, 69

θ Blade pitch angle, 75

$\theta(r)$ Hyperbolic pitch angle, 43

$\theta_{0.75R}$ Blade collective angle at 75% of the blade radius, 134

θ_0 Blade collective, 66

θ_d Diffuser angle, 25

θ_{tip} Blade collective angle at the blade tip, 43

U Local relative wind, 75

u_* Friction velocity at the wall, 102

U_P Out-of-plane velocity normal to rotor disk plane, 75

U_T In-plane velocity parallel to rotor disk plane, 75

υ_∞ freestream velocity, 28

υ_i Induced velocity of the rotor, 18

v_{tip} blade tip speed, 34

v Kinematic viscosity of the fluid, 102

w Far wake velocity, 18

x_{cg} Center of gravity location, 82

x_T Distance between main rotor and tail rotor shaft, 79

y Distance to the nearest wall used by turbulence models, 102

y^+ y plus value, 102

Abbreviations

BEMT	Blade Element Momentum Theory
BERP	British Experimental Rotor Program
BEVT	Blade Element Vortex Theory
BVI	Blade Vortex Interaction
CFD	Computational Fluid Dynamics
DBM	Discrete Blade Models
EHOC	European Helicopter Operators Committee
FEA	Finite Element Analysis
FM	Figure of Merit
FOD	Foreign Object Damage
HECTOR	HEliCopTer Omni-disciplinary Research platform
ISA	International Standard Atmosphere
ISA	International Standard Atmosphere
MAV	Micro Aerial Vehicle

MRF	Multiple Reference Frame
MSM	Momentum Source Method
MTOW	Maximum Take-Off Weight
NOTAR	No TAil Rotor
PL	Power Loading
PUMA	Parallel Unstructured Maritime Aerodynamics
RANS	Reynolds-Averaged Navier Stokes simulations
SAR	Search And Rescue
SIMPLE	Semi-Implicit Method for Pressure Linked Equations
SST	Shear Stress Transport
TURNS	Transonic Unsteady Rotor Navier-Stokes
UAV	Unmanned Aerial Vehicle
V/STOL	Vertical and Short Take-Off and Landing

Chapter 1

Introduction

1.1 Motivation and Background

In the following sections a brief overview of the various helicopter antitorque devices as applied to large scale helicopters is given. The ducted tail rotor configuration is thoroughly described as well as a historic reference is given to the very first applications of a ducted rotor for helicopter configurations. Subsequently, the aims and objectives of the current work are provided.

1.1.1 Helicopter Antitorque Devices

The idea of rotorcraft and the strive for achievement of vertical flight has been always, since the early beginning of the 20th century, a fertile area of rigorous aerodynamic research. The helicopter or the rotorcraft emerged in the first thirty years of the 20th century [1] and has shown its diversity and more importantly the difficulty of its aerodynamic design to achieve sustained flight with comparison to the fixed-wing aircraft. Every rotorcraft configuration has a main rotor which produces the necessary thrust and propulsive force for hover and forward flight. The torque which is created by the main rotor will

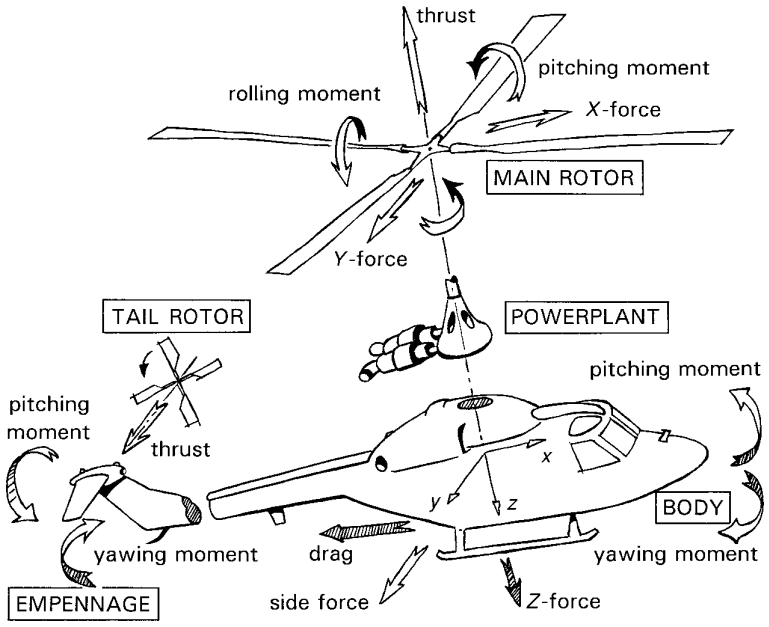

Figure 1.1: The main components of a conventional helicopter configuration [3]

tend to rotate the rotorcraft's fuselage to a direction opposite to the main rotor's rotation. Hence, a means of an antitorque mechanism must be present in order to counteract this torque. According to Yihua et al, [1] in the very first rotorcraft designs, antitorque functionality was performed with the aid of several rotors. Coaxial and Tandem rotors were the first rotorcraft designs, which were limited by the technology of the day. The form of the modern helicopter can be traced back to the Russian aerodynamicist Boris Yuriev and his initial design [2] which had a main rotor and a tail rotor. The majority of today's helicopters adhere to this layout. The forces which are applied over a conventional helicopter are illustrated in Fig 1.1

The tail rotor is a necessary component for every helicopter because it compensates the torque of the main rotor along with providing authority in the yaw axis. The thrust that the tail rotor produces acts on a longitudinal arm about the main rotor shaft. In terms of power requirements, the tail rotor will

typically consume 5-10% of the available power and this figure can be up to 20% at extreme regions of the flight envelope[2]. However, the tail rotor itself is considered as a handicap [4] because it requires the transfer of power over a long distance from the engine. This introduces additional mechanical components, such as the intermediate gearbox due to the fact that the tail rotor's blades have a smaller length. Therefore, it will have a higher RPM number than the main rotor.

The tail rotor operates in a challenging flow regime, it is subjected to the main rotor's wake and it is also affected by the shedding of the main rotor tip vortices and of the fuselage. These complex aerodynamic phenomena, which are illustrated in Fig 1.2, introduce blade stresses and can cause instabilities which can deteriorate the performance of the tail rotor and the helicopter in general. In addition, conventional configurations have their own limitations such as the forward speed limit which is caused due to the potential presence of shock waves in the advancing blade and the stall of the retreating blade at high collectives.

In terms of operational safety the conventional tail rotor configuration also has certain disadvantages. More specifically the conventional tail rotor is prone to (FOD) damage such as gravel, pebbles, stones, trees, bushes etc, the consecutive impact with these elements will be destructive. It has also been reported [5] that ground personnel have been struck by the tail rotor during start-up and stopping operations or whilst loading with the rotors running. Finally, during flight if an incident occurs which will affect the tail rotor transmission or the tail rotor itself e.g. loss of a blade, then autorotational landing must be performed by the pilot with all the accompanying dangers that this manoeuvre involves.

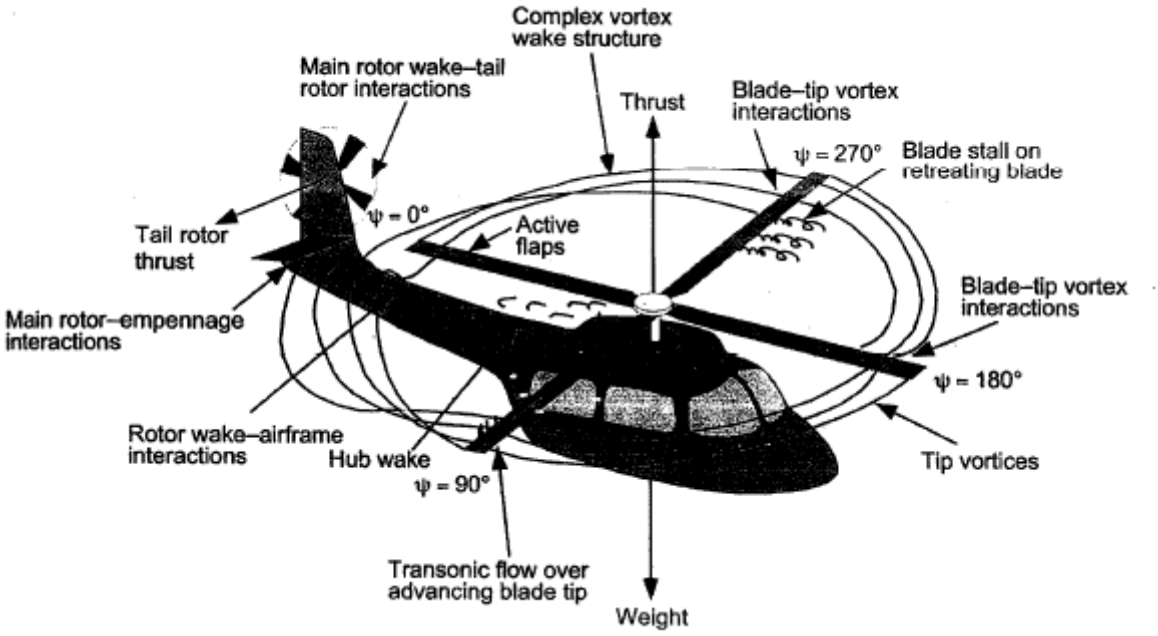

Figure 1.2: Schematic showing a typical flow structure of a helicopter and its aerodynamic phenomena [2]

1.1.2 Ducted Tail Rotor

By taking into account the aforementioned concerning the conventional tail rotor's operational safety both in ground and in flight, a need for a safer alternative configuration has always been present. An alternative configuration which can offer advanced safety features on the ground and during flight is the ducted (shrouded[1]) tail rotor. The first helicopter which has been developed with such an antitorque device was the SA. 341 Gazelle (Fig 1.3) [4], a shrouded antitorque tail rotor which is generally known by the term Fenestron (derived from the Latin word fenestra which means window). The Fenestron was introduced at the end of the 1960's as a second experimental model of the SA. 340 by Sud Aviation which later merged to Aerospatiale (SA. 341 Gazelle) and consequently to Eurocopter.

[1]The words ducted and shrouded will be both used interchangeably.

Nonetheless, the concept of shrouding the rotor for helicopter antitorque purposes has been deployed by other helicopter manufacturers as well, such as the Russian KAMOV (Ka-60 Kasatka) and the American Boeing-Sikorsky (RAH 66 Comanche, S-67 Blackhawk) and Bell (Bell 222). The ducted tail rotor concept has been proven quite successful and it has been used for light and medium size helicopters. One of the main reasons for the implementation of this concept was the associated increased safety features of actually shrouding the rotor and protecting it from external "aggressions" [4, 5]. In particular, as the blades are shrouded by the duct, this reduces the possibility of ground staff accidents as well as the destruction of the machine by FOD . For example, during take off or landing a small stone could not possibly hit the rotor due to the fact that the stone would have to make a turn of 90^{o} degrees. In addition, a ducted tail rotor provides improved performance efficiency due to the augmented lift from the duct[2].

Figure 1.3: SA. 341 Gazelle [4]

[2]The detailed shroud aerodynamics will be presented in a later chapter. The main performance benefits of a ducted tail rotor are encountered in forward flight

What is more, in terms of acoustics a ducted tail rotor exhibits a lower noise level in the plane of blade rotation due to the masking effect of the shroud. Mouille[4] mentions that since the application of this concept to helicopters there has not been recorded any accident involving tail rotor blade contact with personnel. On the other hand, the rate of helicopters crashed due to failed or impacted conventional tail rotors is 0.15 per 10,000 hours of flight [4].

Thus, a ducted tail rotor can offer enhanced safety, reduced noise and performance benefits which will be explained in detail later. A typical ducted tail rotor consists of multiple heterogeneous components such as the rotating blades, the shroud or duct and the vertical fin. The blades of a ducted tail rotor have shortened chords in order to effectively decrease the axial length of the duct. Thus, for the purpose of achieving a required total area of the rotor blades, which is determined by the horsepower absorbing capacity of the tail rotor [1], the number of the blades must increase.

The majority of the existing ducted tail rotor configurations utilize 8 to 13 blades. The rotational speed of such a configuration can reach typically 2,500 RPM to 5,000 RPM. The rotating blades are mounted on the hub and they incorporate a blade pitch hinge which is used for applying changes in the collective angle of attack.

The blade pitch hinge is provided with bearings which are self-lubricating and for the Gazelle SA. 341 the blade material used was aluminum alloy. The tail rotor is supported by a small gearbox which encloses a bevel gear system which transmits the drive from the main gearbox, the arrangemet of the SA. 341 Gazelle is illustrated in Fig 1.4.

A ducted tail rotor does not require the use of a flap hinge (in contrast to a conventional tail rotor where a flap hinge is always present) and the blades are considered rigid. More precisely, it has been found by measurement of loads in flight that at a forward speed of 140 knots without sideslip, the blade stresses do not exceed 1450 psi. These stresses are considered so low that there is a possible elimination of fatigue tests on the blades during series production [4].

It has also been reported that due to the short length of the blades in a ducted tail rotor, the stress level in the blades remain very low. Consequently, due to the flap hinge's absence in the case of a ducted tail rotor, rotor instabilities are not present as in the case of the conventional tail rotor, which further simplifies the aerodynamic analysis. In the case of a ducted tail rotor the fan and the shroud are crucial for its performance and its aerodynamic behaviour. Nevertheless, these are not the only components which contribute to its superiority over a conventional design in terms of flight performance.

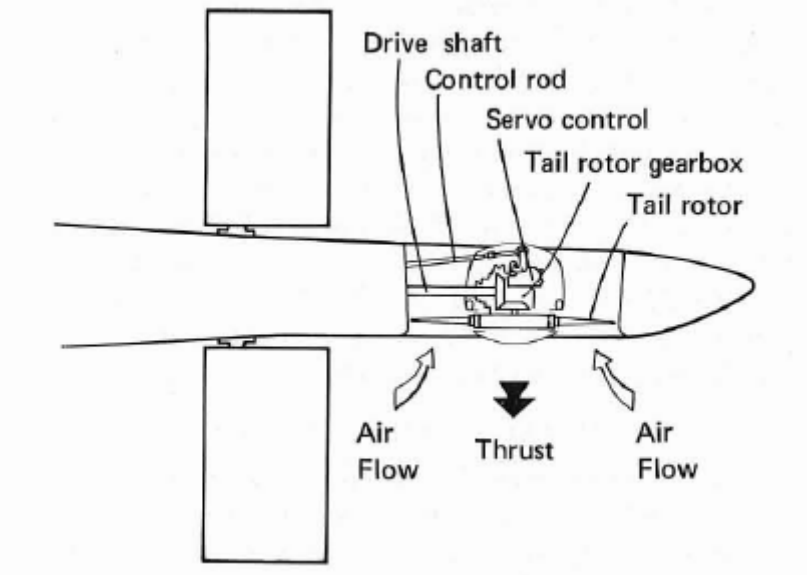

Figure 1.4: Fenestron configuration of SA.341 Gazelle [4]

In ducted tail rotors the fin also plays an important role. For helicopters with conventional tail rotors, the fin is generally a part of the empennage and it is mainly constructed to enhance stability about the yaw axis as well as providing a small thrust component (for antitorque purposes) and it is also referred as a vertical stabilizer. However, the fin in ducted tail rotors apart from providing stability about the yaw axis it is also used to off-load the fan during forward flight.

The fin is an aerodynamic surface (see Fig 1.5), a wing which normally has a cambered airfoil and it has an incidence with respect to the rotorcraft's centerline. Thus, as the helicopter forward speed is increasing the fin will operate as a wing, suction forces will be developed in the upper part of the fin (the part which is directed towards the antitorque thrust direction) and over-pressure forces on the pressure side of the fin. It is clear that as the tail incidence of the fin increases its thrust magnitude will eventually increase, a typical fan off-loading in forward flight for a ducted tail rotor is illustrated in Fig 1.6.

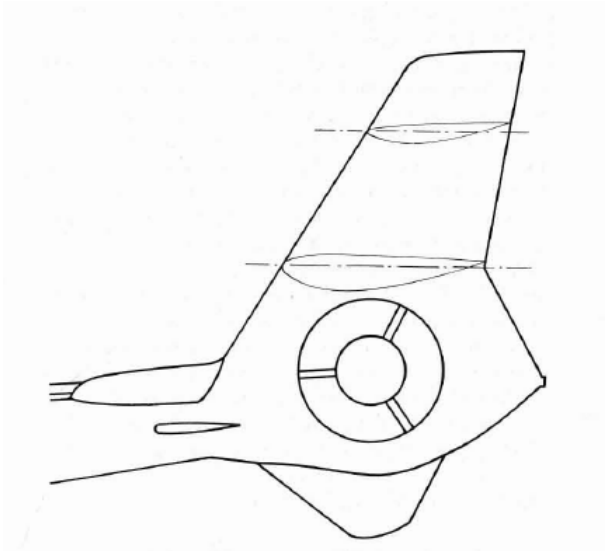

Figure 1.5: Fin arrangement of SA. 341 Gazelle [4]

The build up of these forces on the fin will create a total thrust which will eventually off-load the fan at normal cruise conditions e.g the RAH–66 Comanche ducted tail rotor at 150 knots will operate with a fan collective of approximately 0^{o} which is a very small collective angle [6] . In addition, by inspecting Fig 1.6 it can be seen that as the vertical fin force increases the device thrust or the fan thrust decreases which means reduced collectives and reduced power consumption of the fan.

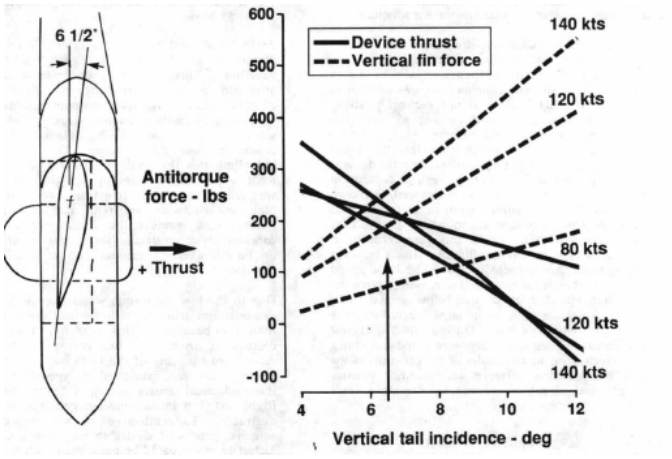

Figure 1.6: Fan unloading in forward flight H76 FANTAIL [7]

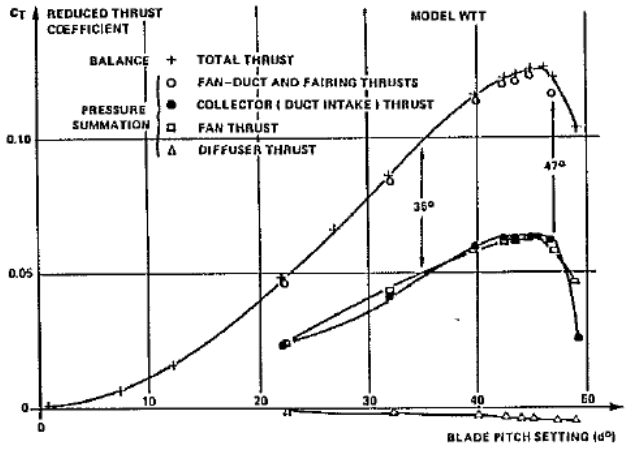

Figure 1.7: Thrust sharing between fan and duct and dependence on collective angle [5]

1.2 Aims and Objectives

In rotorcraft aerodynamics in order to estimate the upper level performance of the rotorcraft, a rotorcraft comprehensive code is utilized. Such a code will provide an aerodynamic analysis of a rotorcraft configuration based on first principles methods. Froude's momentum theory which is based on the application of Newton's 2nd Law to an infinitesimal disk (actuator disk) was the first attempt of rotorcraft aerodynamicists to estimate the performance of a helicopter[3].

momentum theory is a 1-D analysis and does not include geometrical parameters such as the blade twist, the planform distribution and the shape of the airfoils creating the need for a more advanced theoretical tool such as the Blade Element Momentum (BEMT) Theory which is considered as the basis of most modern analyses of helicopter rotor aerodynamics [2]. BEMT and momentum theory (which are going to be described later with more detail) do not take into account the viscosity of the fluid as well as compressibility effects although corrections can be made in order to include these effects.

These methods have been proven more than adequate to provide an upper level estimate of the developed forces and moments on the rotor disk but they have a significant disadvantage, they are empirical methods. By the term empirical it is acknowledged that these methods need empirical correlations, in the form of look-up tables in order to work. Such tables can be lift, drag and moment coefficients for different angles of attack, Reynolds and Mach numbers hence proving them as a posteriori methods in the sense that they are dependent on previous empirical results in order to provide a meaningful result.

[3]Froude's momentum theory can also be applied to propellers, ducted fans and generally rotors.

In addition, these methods can not give a three dimensional description of the complex flow-field that is encountered on a rotor as well as neglecting important and fundamental fluid flow effects such as the turbulence of the flow-field. Thus, it is of paramount importance to perform wind tunnel experiments and flight test campaigns in order to derive such correlations in order for these methods to have the necessary input [8].

In the case of a ducted tail rotor the flow regime is extremely complex due to the fact that it is not stationary and there is significant cross flow as well as flow parallel to the duct axis. Hence, it can be acknowledged that separation phenomena (viscous flow) will dominate its performance.

The utilization of test rigs, wind tunnels and flight campaigns formed the basis of the development and optimisation of ducted fan configurations. However, this procedure is quite expensive and nowadays it is only used for the ultimate verification of a new design [8]. It is clear that Computational Fluid Dynamics (CFD) tools, in the context of Reynolds-Averaged Navier Stokes simulations (RANS) , are appropriate for such an aerodynamic analysis and performance prediction. This is due to the reduced cost compared with experimental tools as well as on the grounds of acquiring a complete three dimensional description of the flow-field with an acceptable accuracy.

The main objective of this work is the construction of a generic ducted tail rotor model with discrete blades [4] in CFD and the analysis of its performance in hover and forward flight . The overall objectives and approach can be summarized in the following :

[4]The term discrete blades conveys the fact that the full geometry of the blades has been used in order to represent the rotor

1. To design, develop and validate a CFD model of a generic ducted tail rotor by using publicly available information

2. To develop a methodology based on performance mapping in order to use the derived power/thust (polar) curves for calculating the power requirements for a given thrust. The performance maps will be deployed in order to derive the ducted tail rotor performance subject to the main rotor's antitorque requirements provided by an in-house rotorcraft comprehensive code. Thus, these maps can be used in order to estimate the performance at specified flight conditions where a comparison with a conventional tail rotor model can be also performed.

The aforementioned objectives reflect a high level approach of simulating a generic ducted tail rotor in order to derive accurate results which are based on RANS simulations. The simulations will also utilize an accurate representation of the three dimensional geometry which can give a further insight into the aerodynamics and performance of a ducted tail rotor.

1.3 Organisation of the thesis

A brief overview of the ducted tail rotor configuration has been given together with the aims and objectives of the current work. Chapter 2 introduces the reader to the ducted fan aerodynamics and the performed literature review on ducted rotor configurations. Ducted fan aerodynamics are presented in terms of the two investigated flight regimes i.e. hover and forward flight. After this, the literature review sections provides information about the performance of ducted propellers especially in terms of the shroud performance and its dependency on certain geometric parameters. Also, the helicopter antitorque applications are presented together with the applicable analytical methods, for performance prediction, and the state of the art CFD simulations.

Chapter 3 presents the proposed methodology and serves a two-fold goal: firstly, to present the methodology and the assumptions with regards to the construction of the performance maps. Secondly, to present the numerical approach of the CFD simulations together with presenting a validation case in hover. Chapter 4 describes the results in hover in the form of power polar curves and the variation of thrust and power coefficients with respect to the blade collective angle [5]. Subsequently, Chapter 5 provides the results in forward flight together with the associated analysis again in the form of power polar curves. In addition, the results of the performance subroutine are qualitatively compared with an available power consumption distribution, with respect to increasing forward flight speed, of a real ducted tail rotor configuration. Chapter 6 concludes the current research work and provides possible areas of further future research.

[5]The term blade collective angle refers to the geometric, pitch blade angle. This change is collective in the sense that all the blades have the same change in their geometric angle of attack [2]

Chapter 2

Literature Review

2.1 Ducted Fan Aerodynamics

This chapter gives a succint overview of the ducted fan aerodynamics and the geometric parameters which dominate its performance. In addition, previous work done is reported which spans from ducted fan applications in ducted propellers to helicopter configurations. Finally, the available performance prediction methods are briefly presented as well as the current state of the art of CFD simulations in ducted tail rotors.

2.1.1 Hover

From the preceding discussion, it can be acknowledged that a helicopter antitorque device is a vital component for achieving sustained flight as well as flight safety. Conventional tail rotors have been used by numerous helicopter manufacturers for a plethora of their helicopters. However, the safety drawbacks of this design gave birth to other configurations such as the ducted tail rotor configuration and NOTAR (NO TAil Rotor).

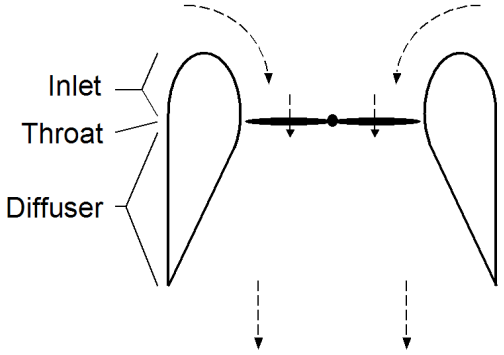

Figure 2.1: Cross-section of a ducted rotor in hover illustrating the inlet and diffuser sections [9]

In this work, a ducted tail rotor configuration was used due to the performance benefits that it can offer in forward flight.In addition, due to the fact that the blades are rigid, there is no need for a coupled CFD-FEA analysis which further simplifies the aerodynamic analysis. A ducted tail rotor or generally a ducted fan can be considered as a turbomachine which operates as a compressor i.e. it imparts energy to the surrounding fluid and provides the required antitorque force. The shrouded rotor in its basic form involves a cylindrical shroud which surrounds the rotor and resembles an annular airfoil wing which has a camber and a finite thickness which can vary along its length. The shroud consists of a leading edge part where the freestream flow enters and a tapered trailing edge which form the inlet and outlet (diffuser) sections respectively (Fig 2.1). The ducted rotor is a relatively simple configuration which has been extensively investigated for almost over half a century and has resulted in significant gains in aerodynamic performance in terms of thrust and power consumption compared to the open rotor. The concept of the ducted rotor has been applied in various designs as a means of propulsive force, from ducted propellers to ducted fans in V/STOL aircraft, UAVs and ducted tail rotors in helicopters (Fig 2.2).

(a) Boeing-Sikorsky RAH-66 Comanche

(b) Eurocopter Fenestron AS 365N Dauphin

(c) Bell X22-A

(d) Vanguard omniplane

(e) Sikorsky Cypher I

(f) Sikorsky MARINER Cypher II

Figure 2.2: Applications of ducted rotors

A typical shroud profile as shown in Fig 2.1 will be cambered inwards in order for the flow to be accelerated towards the rotor. The performance benefit of this acceleration consists of a gain of shroud thrust due to the acceleration of the flow at the inlet section i.e. the differential pressure distribution along[1] the shroud as in the case of a wing where the pressure distribution is the dominant source of lift[2]. The shroud thrust is caused by the turning of the flow, from the inlet lip through the rotor.

In addition, in forward flight the shroud also acts as an annular wing and also provides lift with less than half the induced drag of a planar wing of the same aspect ratio [9]. By inspecting Fig 2.1, it is easily understood that the thrust of the shroud and the rotor or generally the total thrust is generated also by the ability of the diffuser to restrain the natural contraction of the rotor wake (decreased wake velocity).

For a ducted rotor in hover the total thrust is the sum of the rotor thrust and the shroud thrust, $T_{total} = T_{rotor} + T_{shroud}$. The thrust forces in helicopter aerodynamics are written in a similar way as the lift force the fixed wing case. Thus, the thrust force T is given by the expression:

$$T = \frac{1}{2}\rho A(\Omega R)^2 C_T \tag{2.1}$$

where ρ is the density of the fluid, A is the reference area which is the rotor disc area, Ω is the angular velocity of the rotor, R is the blade radius and C_T is the thrust coefficient [3]. The natural wake contraction of a helicopter in hover, assuming 1-D, quasi-steady, incompressible and inviscid flow, is shown

[1]Suction forces build up at the inlet lip and over-pressure forces at the bottom surface of the shroud

[2]Although pressure forces are the dominant source of lift, the aerodynamic force could not exist without the shear stress distribution i.e. viscous forces

[3]In ducted fan aerodynamics individual thrust components such as the shroud thrust component and the rotor thrust component can be expressed using the relation 2.1

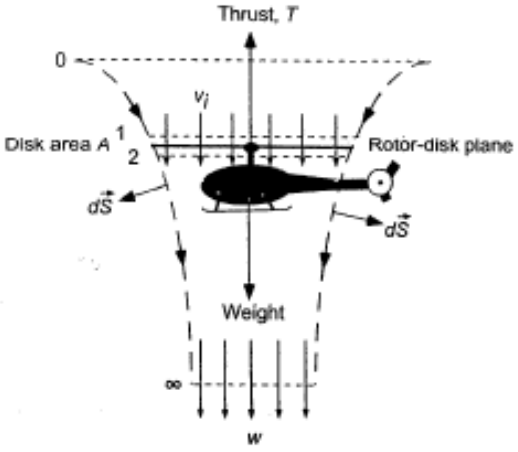

Figure 2.3: Wake contraction over a conventional helicopter [2]

in Fig 2.3 where υ_i is the ideal induced velocity of the rotor. The corresponding control volume illustrates that the flow contracts and has a value of w which is the velocity at the far wake plane (the vena contracta) denoted by ∞.

As the flow contracts, the velocity increases beneath the rotor plane and by applying classical momentum theory as well as the fundamental conservation laws of fluid mechanics, the predicted value of the far wake velocity is twice the value of the induced velocity at the rotor plane [2]. Thus, by mass conservation a decrease in the area of the control volume is present in order to accomodate the excess velocity.

The contraction ratio of the flow or slipstream in the far wake is proven to be 0.5 which means that the area of the section at the far wake is half of that at the rotor plane. This induced velocity rise represents the induced increase in the kinetic energy of the fluid caused by the rotor and it also corresponds to the minimum possible (ideal) power required in order to generate a given amount of thrust. It is apparent that this velocity increase will reflect an induced power expenditure, the ideal induced power is given by:

$$P_i = T_{rotor}\upsilon_i \tag{2.2}$$

From the preceding discussion it can be shown that if this velocity decreases then the required power will decrease accordingly. This is what is achieved in the case of a ducted rotor. The diffuser section in a ducted rotor will either maintain the same area of the slipstream or it will increase it forcing the undesirable excess velocity to reduce hence reducing the induced power requirements. The corresponding streamtubes for an open and a ducted rotor are shown in Fig 2.4. However, this reduction can only be achieved as long as the flow is attached at the diffuser. By increasing the diffuser angle the flow will encounter strong adverse pressure gradients and will separate causing a loss in thrust.

momentum theory can be also used in the case of a ducted rotor in hover for a first order prediction of its performance. However, there is one difference in its implementation where instead of using an actuator disk for representing the rotor, the assumption which is made is that the slipstream flow at the exit plane of the diffuser is without swirl [2] and has expanded back to ambient atmospheric pressure. This is an ideal situation in hover and it does not generally hold for every flight regime. Nonetheless, momentum theory can be used to identify key parameters that will affect the performance of a ducted rotor such as the diffuser expansion ratio σ_d which is equal to the ratio of the diffuser plane area A_e to the rotor disk area A :

$$\sigma_d = \frac{A_e}{A} \tag{2.3}$$

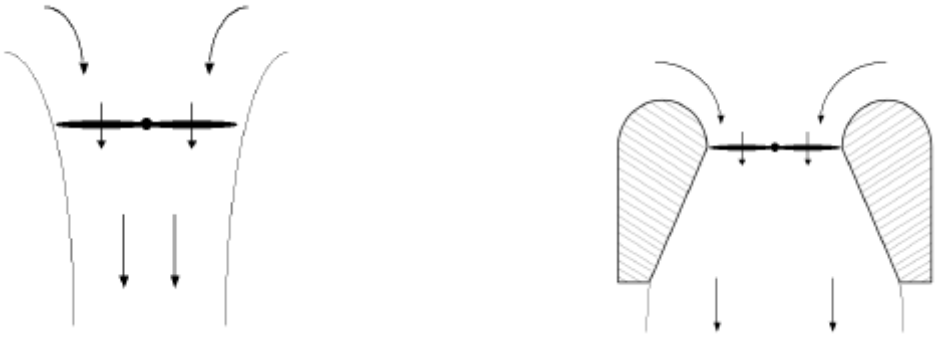

(a) Open rotor (b) Ducted rotor

Figure 2.4: Slipstream flow comparison of open and ducted rotor [9]

The expansion ratio clearly depends on the diffuser angle of the shroud. momentum theory also gives the following relations, which are derived in Appendix A:

$$v_i = \sqrt{\frac{\sigma_d T_{total}}{\rho A}} \tag{2.4}$$

$$P_i = \frac{T_{total}^{3/2}}{\sqrt{4\sigma_d \rho A}} \tag{2.5}$$

$$\frac{T_{rotor}}{T_{total}} = \frac{w}{2v_i} = \frac{A}{2A_e} = \frac{1}{2\sigma_d} \tag{2.6}$$

$$\frac{T_{shroud}}{T_{total}} = 1 - \frac{1}{2\sigma_d} \tag{2.7}$$

These relations can be used in order to give an illustration of the benefit of shrouding the rotor, in the case of an open rotor $T_{rotor} = T_{total}$. When the expansion ratio increases (shrouding the rotor) the total thrust will be much greater than the thrust acting on the rotor alone. The turning of the

flow over the inlet lip radius will create suction forces which are the principal reason for the additional inlet thrust (shroud thrust). The inner surface of the diffuser will also experience suction forces hence producing a negative thrust [9]. However, the diffuser negative thrust is not large enough and the inlet thrust is dominant. From the above relations, it is clear that momentum theory can be used to estimate the performance of the ducted rotor by changing certain fundamental parameters. If it were for an open rotor and a shrouded one to be compared with identical rotor disk areas and same ideal power then with increasing expansion ratio the total thurst produced by the shrouded rotor would have increased continuously relative to the open rotor thrust. It can be seen from Eqs (2.4-2.7) that the induced velocity of the rotor and mass flow will increase with increasing expansion ratio but the thrust produced by the rotor will decrease. The total thrust will increase due to the increased shroud's thrust contribution albeit the decrease in rotor thrust. It can be stated that the rotor is off-loaded by the shroud with increasing expansion ratio hence reducing the induced power requirements. For example, for an expansion ratio of 1 which corresponds to a straight sided cylindrical diffuser a ducted rotor can produce theoretically 26% more thrust than an open rotor [9] of the same size with the same power consumption or 29% less power consumption with the same thrust. In theory, by increasing the expansion ratio the performance improvements can be infinite. Nonetheless, this does not occur in reality due to phenomena which relate to viscosity such as flow separation and frictional losses which are not taken into account by using momentum theory. When the diffuser expansion ratio increases the wake velocity reduces but at some point due to the strong adverse pressure gradients the flow can not remain attached to the diffuser and it separates [7, 9]. Hence, this is an example where momentum theory shall be used with care and it illustrates the need for empirical correlations or

for a CFD analysis. Viscous flow phenomena can deteriorate the performance of the shrouded rotor by changing other geometric parameters as well. Thus, for example if the inlet lip radius is small then the turning of the flow will be increased. This will subsequently increase the inlet suction forces [10] until some point with enough small lip radius where the flow will separate. This will lead to an ingestion of distorted flow through the rotor which will deteriorate its performance. Therefore a solution to this problem would be a careful selection of inlet lip radius which is great enough in order to keep the flow attached as possible. For the edgewise flow encountered in helicopter antitorque devices which is perpendicular to the rotor axis it is clear from the preceding discussion that one can either optimize the performance of the shrouded rotor for specific segments of the flight i.e. either optimizing for hover or forward flight but not for both. For example, a small inlet lip radius can be very beneficial for hover flight where the flow outside the rotor is considered quiescent but in very high forward speeds that could lead to premature separation with all its associated drawbacks. Flow separation in the case of the diffuser can be delayed if the diffuser length is increased but it comes with a weight and drag penalty. Thus, in the case of the shrouded rotor configuration there is a plethora of parameters that can dictate its performance across the flight envelope not to mention the specific details of airfoil profiles of the blades as well as the effect of blade tip clearances. In a shroud design a compromise is usually made in order for the shroud to generally exhibit good performance across the mission profile of the rotorcraft. From the aforementioned, it can be acknowledged that for a successful aerodynamic design and analysis of a shrouded rotor, sufficiently accurate prediction tools must be used. This is for the purposes of deriving an understanding of its performance across the flight envelope which will typically include hover and forward flight.

2.1.2 Forward Flight

In forward flight the behavior of the shrouded rotor is different from that in hover. The flow has an angle of 90 degrees with respect to the rotor axis. As the forward speed increases the turning of the flow increases and this change of direction is much more abrupt at the windward (forward) side of the shroud than that at the leeward (aft) side. This translates to a difference in pressure distribution and a difference in the shroud thrust (it can be said that the windward side operates at a higher angle of attack than the aft side). Therefore, this effect will cause a pitch moment[4] which is a significant control problem in the case of ducted fans (UAV) but not that important (in terms of control) in the case of a helicopter due to the presence of the fin (a rudder input from the fin can counteract this moment).

Nonetheless, this non-uniformity of the flow-field proves momentum theory as inadequate to capture this phenomenon. Figure 2.5 illustrates a comparison of the flow-fields and pressure distributions in hover and edgewise flow (the freestream velocity vector has an angle of attack $\alpha = 90^{\circ}$ relative to the rotor axis). An axisymmetric shroud will experience a uniform pressure distribution in hover as the flow is induced through the rotor by all directions.

As the velocity increases the turning of the flow is greater at the windward side than the leeward side and hence creating a difference in the pressure distribution. The flow which is presented to the rotor is also different than in hover and there is a longitudinal variation in the rotor inflow. The ducted tail rotor can offer significant performance benefits but its design requires a compromise of several parameters e.g. expansion ratio and inlet lip radius.

[4]For the case of a helicopter ducted tail rotor this will be a yaw moment.

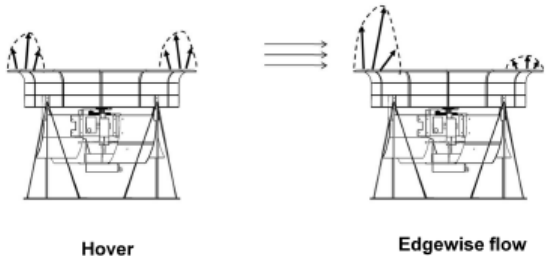

Figure 2.5: Comparison of the flow-fields and pressure distributions in hover and edgewise flow for a ducted fan (UAV)[10]

Hence, the performance of the ducted tail rotor depends solely on the geometry of the configuration like the shape of the shroud, the profiles of the rotor blades,the Reynolds and Mach number of the flow. These effects cannot be analyzed by applying momentum theory. Therefore more sophisticated models must be used like CFD as well as experiments in order to have a proper design. [11, 9].

2.2 Previous research in ducted fan configurations

The careful choice of such geometric parameters (Figure 2.6) as the shroud inlet lip radius, the length of the diffuser, the blade tip gap, the expansion ratio as well as the aerodynamic profile of the rotor is a crucial step towards the design of a shrouder rotor configuration. The aerodynamic behavior of a ducted fan is dictated by these parameters and their proper selection is by no means a simple task to perform.

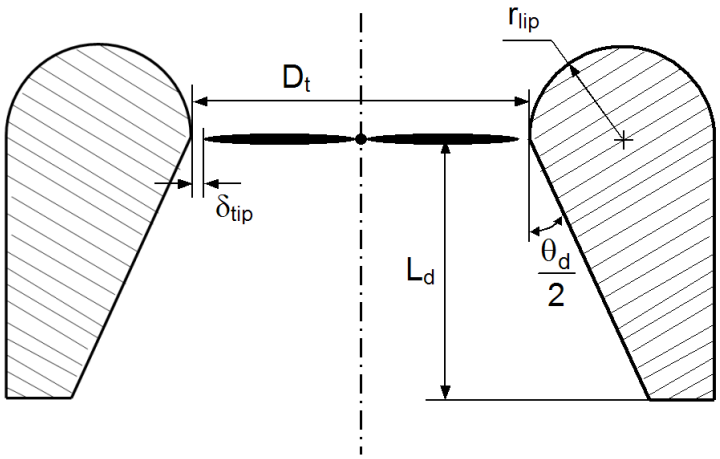

Figure 2.6: Shroud parameters which affect the performance: diffuser angle θ_d, diffuser length L_d , inlet lip radius r_{lip} and blade tip clearance δ_{tip} [9].

Sacks and Burnell [12] performed a study which concerned the state of the art (at that time) in ducted propellers and compiled a preliminary list which in terms of important parameters includes the following:

- Duct variables

    1. chord/diameter ratio
    2. profile thickness/chord ratio
    3. profile camber
    4. leading edge radius
    5. chord line orientation relative to axis
    6. profile trailing edge angle
    7. position of maximum thickness

- Propeller/Rotor variables

    1. solidity

2. overall pitch setting
3. pitch distribution (twist)
4. blade profile
5. chord distribution (taper)

- Overall variables

1. propeller location within shroud
2. ratio of hub diameter to propeller diameter
3. clearance between blade tips and duct surface
4. centerbody shape (nose shape, tail shape)
5. centerbody location relative to shroud

In the following sections a succinct literature review is presented in order to highlight the significance of the corresponding shroud and rotor parameters in terms of aerodynamic performance. The literature review consists of previous experimental work, analytical models as well as state of the art CFD studies provided publicly from helicopter manufacturers and various researchers. Therefore, the aim of the following sections is to indicate and justify the rationale behind the selection of the geometric parameters of the generic geometry [5] which will be used for the aerodynamic analysis.

[5] Due to the fact that a full 3D geometry can not be provided by a helicopter manufacturer, the selection of the geometric parameters is justified based on previous and similar work done on helicopter antitorque configurations.

2.2.1 Ducted Propellers

A first implementation of the concept of ducting a propeller in order to improve its propulsive efficiency is attributed to Ludwig Kort [13] and dates back to 1933. Kort's application concerned a ship propeller where different nozzle-shaped geometries were attached to the ship's hull. This early work failed to provide a meaningful performance improvement due to the fact that "none of the geometries were uniting the proper shape of the nozzle with the proper relation between the propeller, its revolutions, the areas at the narrowest cross section and at the mouth of the nozzle and the form, speed and resistance of the ship".

Another research work concerning shrouding rotors was done by Luigi Stipa from Italy. Stipa [14, 15] examined the integration effects of a propeller with a hollow aircraft where its fuselage was shaped like a Venturi tube. Stipa also performed wind tunnel experiments for two airplane propellers and he used three different shroud shapes. The shroud length was about three times the diameter of the propeller and the inner profile was like a venturi tube and the outer like a wing. The propellers were located exactly at the inlet of the shroud and not at the point of the venturi throat.

The expansion ratio in this configuration was 1 due to the fact that the diameter at the inlet and exit planes was the same. The more profound changes that were deployed regarded the effect of decreasing the thickness of the shroud which eventually altered (increased) the throat diameter and moved the actual throat location downstream of the shroud. These shrouded propellers exhibited increased thrusts and power loadings compared to the open propellers.

Generally, the efficiency was better by ducting the propeller and the thinner profiles had lower profile drag, higher thrust and efficiency. Research in shrouded rotors and in particular work which concerned the shroud shape was done by Kruger [16] and the objective of his work was to increase the performance of airplane propellers. According to the author, the increase in inflow due to the shroud and due to the fact that during cruise the inflow is uniform, more efficient performance was obtained for the propeller.

Kruger also investigated the effect on performance of the shroud airfoil profiles. The diameter of the propeller was kept constant with a value of approximately 9.5 inches. The investigated geometric parameters were the thickness, camber and the chord of the shroud and the expansion ratios tested were from 0.75 to 1.7 as both contracting ($\sigma_d < 1$) and expanding ($\sigma_d > 1$) diffusers were examined.

The deployed tests involved a parametric analysis of different blade collectives and the effect of the advance ratio which is defined as:

$$\mu = \frac{v_\infty}{\Omega R} \tag{2.8}$$

where v_∞ is the freestream velocity. The advance ratios examined were up to 1.4. The results have shown that the sharper lips do not exhibit good performance in static or near static (very small advance ratio) conditions due to flow separation which reduced the shroud thrust. At higher advance ratios thinner profiles had less drag hence increased shroud thrust. By increasing the advance ratio the propeller thrust decreased faster in the case of thinner shrouds. Kruger also investigated the potential performance benefits by introducing a nose split ring (Figure 2.9) at the leading edge of the thinner shrouds.

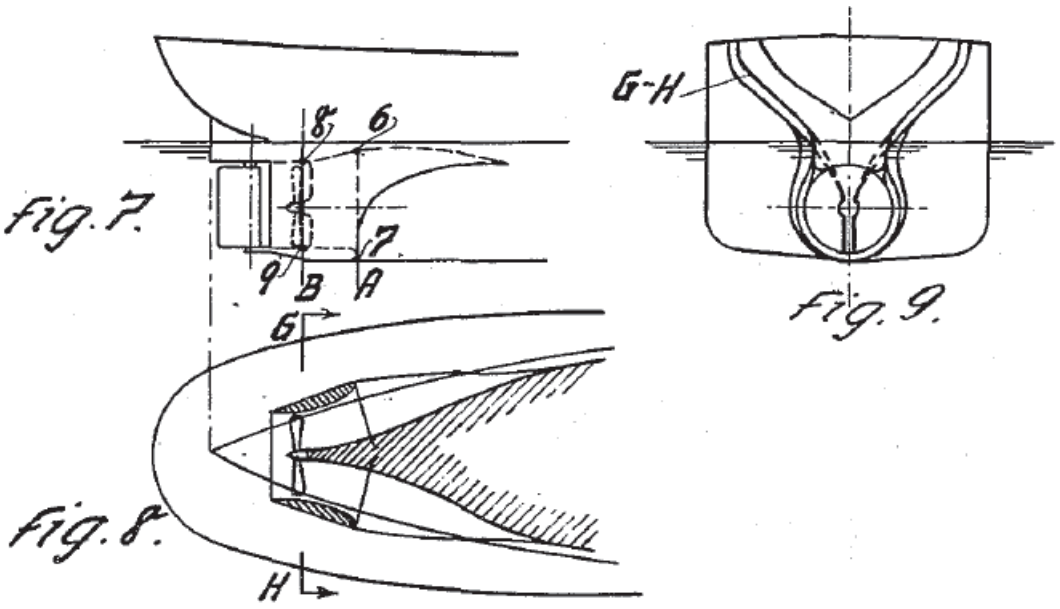

(a) Kort's patent for ship propellers [13]

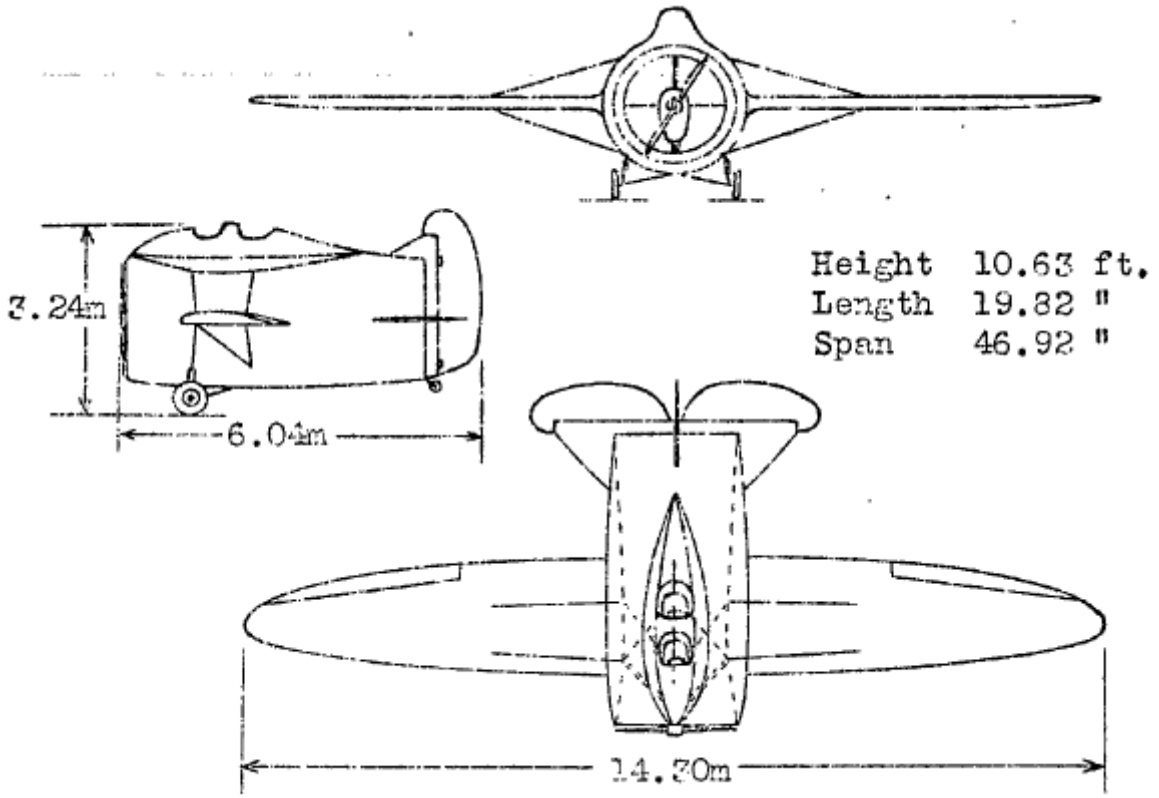

(b) Venturi fuselage monoplane of Stipa [15]

Figure 2.7: First applications of the concept of shrouded rotors

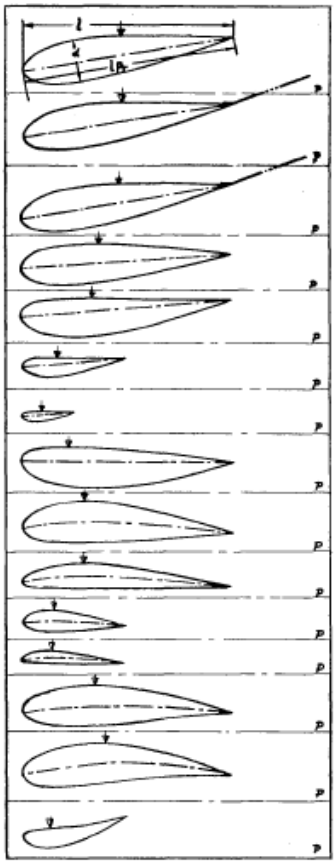

(a) Tested shapes

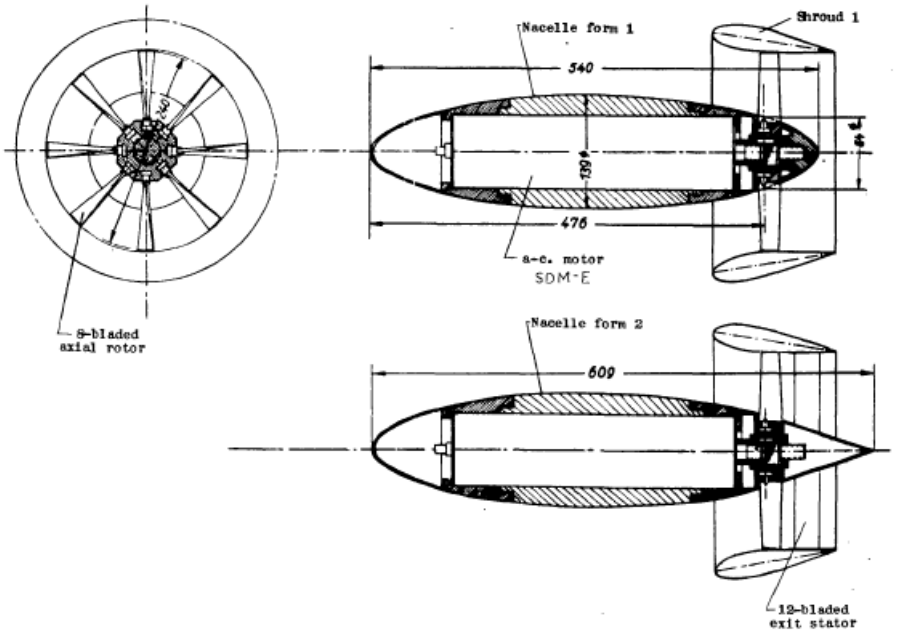

(b) Geometric configuration of the investigated shrouded propeller

Figure 2.8: Kruger's shrouded propeller geometry schematics [16]

Performance did improve in static conditions and in low advance ratios yielding static thrust coefficients which were two times higher than those obtained by an open propeller. The total thrust was greater in the configuration with the split ring but the power expenditure (power coefficient) was the same for ring and non-ring configurations.

It was also reported that stall occured more sharply by increasing collective as compared to the open propeller as well as deterioration in performance for advance ratios above 0.3. Finally, Kruger investigated the effect of introducing stator vanes after the rotor which further increased rotor thrust whereas the power coefficient was the same.

As expected the introduction of the stators offered a recovery in the pressure losses through diffusion (conversion of increased rotational kinetic energy to static pressure) hence increasing the thrust coefficient and the Figure of Merit (FM) of the propeller.

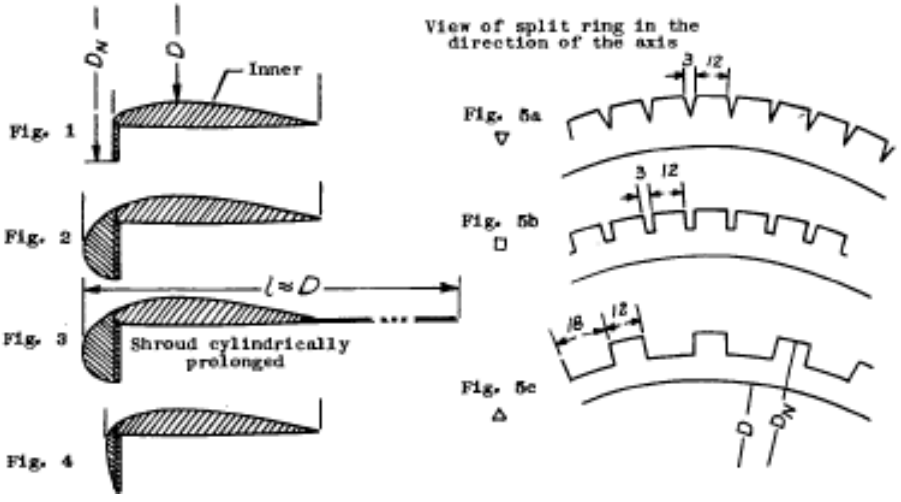

Figure 2.9: Improvement in thust by using a split ring [16]

The figure of merit or the static thrust factor of merit [17] is a non-dimensional number which expresses the ratio of the ideal amount of power required by the rotor in order to generate a specific amount of thrust over the value of the actual amount of required power:

$$FM = \frac{P_i}{P} \tag{2.9}$$

The maximum possible value of FM for an open rotor is 1.0 and this will imply an ideal rotor with no losses. However, in the case of ducted rotors the FM could be greater than 1.0, according to Beveridge [17], due to the fact that greater static thrust can be obtained with the shroud [16]. Beveridge mentions that the maximum FM of a ducted rotor/propeller is 2.0 assuming no viscous losses. Thus, FM is an important parameter in the general field of helicopter aerodynamics and it directly gives an idea about the efficiency of the rotor/propeller.

In Kruger's experiments the maximum FM was 0.7 which is considered a small value for a ducted propeller and is due "to the natural drag of the shroud". It was shown by smoke flow visualisation that the expansion ratio only depends on the geometry of the body, which means that the slipstream was not changed with varying loading. Also, a very large expansion ratio with the value of 1.7 had severe pressure losses and it was completely inefficient.

Kruger concluded that it will be of no use to increase the expansion ratio more than the value 1.0. A concise study of the effect of different diffuser angles and lengths has been provided by Platt [18]. Platt considered three different shroud shapes as shown in Fig 2.10 with σ_d spanned from 1.1 to 1.3 (two shrouds with an expansion ratio of 1.3) and three different diffuser angles (7^{o}, 14.4^{o} and 22.4^{o}).

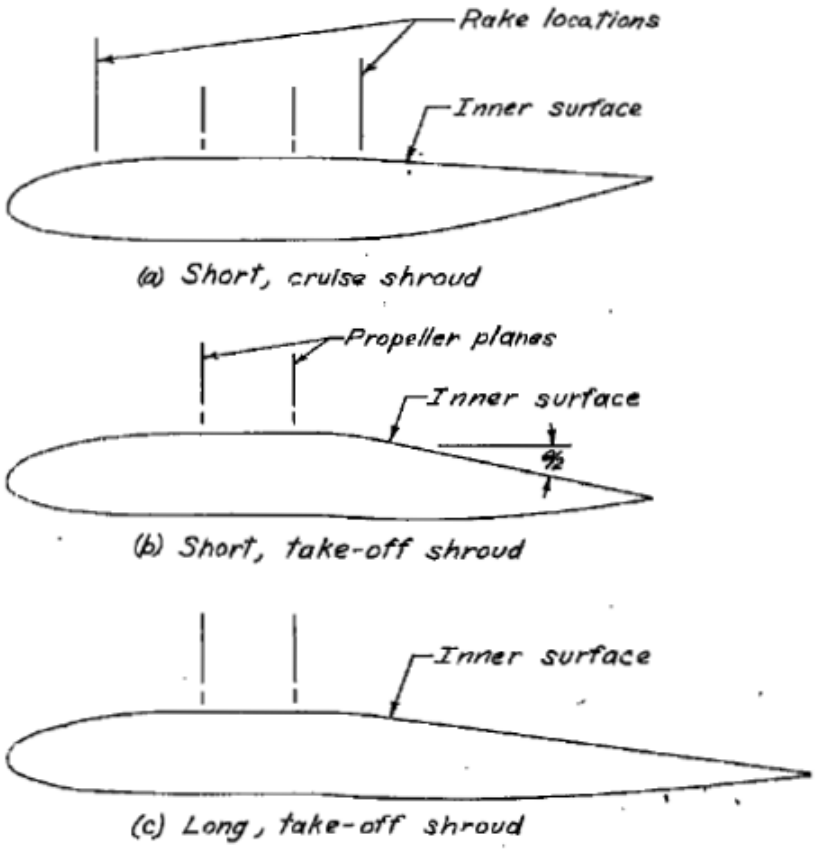

Figure 2.10: Shroud shapes used by Platt [18]

The model shrouded propeller had a diameter of 48 inches with a blade tip clearance of 1/16 inch. The first shroud with σ_d 1.1 and diffuser angle of 7^{o} was termed as a short cruise shroud whereas the other two shrouds were considered as short and long take-off shrouds. The main conclusion of Platt's work was the fact that with a fixed expansion ratio, the longest shroud (smallest diffuser angle) resulted in a higher power loading at the same power coefficient where power loading (PL) is the ratio of the produced thrust (T) and the consumed power (P) to produce the specific amount of thrust:

$$PL = \frac{T}{P} \tag{2.10}$$

PL is a dimensional quantity which is another measure of rotor efficiency and it is widely used in helicopter aerodynamics. This quantity can be rendered non-dimensional by multiplying it with the blade tip speed υ_{tip} giving $C_T/C_P = \upsilon_{tip} \times T/P$. C_T/C_P decreased, in Platt's experiments, with decreasing diffuser angle and keeping the diffuser length constant. By further increasing σ_d the power coefficient decreased at a given blade angle and this effect was greatest at the highest collective but even at this collective the reduction was only about 10%.

Finally, it has been mentioned that in the tested collective range (35° to 45° with increments of 5°) for the same consumed power the shrouded rotor produced twice the amount of static thrust compared to the open propeller. The open propeller stalled at these high angles whereas the shrouded propeller did not experience any stall. From the discussion so far, it can be stated that the shrouded rotor's performance is dictated by the following parameters: the expansion ratio and diffuser (or expansion) angle, the inlet lip radius and the blade tip clearance [12].

The previous work performed by various researchers has shed light to the effect of the first three parameters. The fourth parameter i.e. the blade tip clearance is considered as one of the most crucial parameters in ducted fan aerodynamics. It is well known from aerodynamics that a wingtip vortex is formed at the edge of a wing due to the convection of vorticity and the difference of the pressure distribution on the upper and low surface of the wing [19]. Wingtip vortices represent an induced drag and deteriorate the performance of the wing or the propeller/rotor. In the case of helicopters, the convected vortices of the leading blade can interact with the vortices shedded from the blade that follows causing the Blade Vortex Interaction (BVI).

Thus, a blade tip vortex represents in the general case of a rotating blade a loss of thrust. The obvious benefit of shrouding the rotor originates on the grounds that the presence of the shroud impedes the formation of strong tip vortices and improves performance. It is apparent that if the blade tip clearance was zero then the flow regime could be considered as 2D. However, in the real world this cannot happen and a blade tip clearance is always present.

The blade tip clearance practically consists of the gap between the shroud and the tip of the rotor. Due to the operation of the fan which is to increase the pressure below the rotor, the adverse pressure gradient will cause certain leakage flow to appear which is unavoidable. However, the smaller the gap the better the performance, in terms of thrust production, of the rotor. The performance improvements of shrouding the rotor are greater than those predicted by momentum theory which assumes ideal conditions [9, 20]. At the same thrust coefficient the greater induced velocities at the rotor, cause the blades to operate at a smaller effective angle of attack. This is the reason why shrouded rotors do not stall at high blade collectives in contrast to the open rotors. A minimum blade tip clearance is imposed by the possibility of the blades to strike the shroud.

In the RAH-66 Comanche FANTAIL helicopter the gap is almost closed by using an abradable material or a brush [9] mimicking the technology of seals which is applied in gas turbines . Hubbard [21] tested the effect of different blade tip clearances (0.2% to 4.4% of the rotor diameter) and he concluded that an increase in blade tip clearance could result in an 84% reduction in total thrust and an approximate 15% reduction in power. The majority of the total thrust loss was due to shroud thrust loss and it was found that the incoming flow separated at the leading edge of the shroud but it reattached when the speed increased.

2.2.2 Helicopter Antitorque Applications

The above discussion shed light to the complex aerodynamics that are encountered in a ducted rotor or a ducted propeller configuration. It has been shown that the performance of a ducted rotor is dictated by numerous geometric parameters and the proper aerodynamic design of such a configuration is not a trivial task. The majority of the presented applications accounted for the implementation of a ducted rotor as a means of enhancing thrust for fixed-wing aircraft. It can be acknowledged that by using a ducted rotor, significant benefits in performance can be achieved in terms of thrust production and power consumption. In fixed-wing applications, the oncoming flow, in forward flight, to the rotor and the shroud has an angle of attack (with respect to the rotor axis) $\alpha = 0^{\circ}$ and the flow can be regarded as axial flow[6].

In helicopters due to the antitorque role of the ducted rotor and the shroud, the flow is always perpendicular to the rotor axis ($\alpha = 90^{\circ}$) in forward flight (in hover however the flow is axially encountered by the rotor). The edgewise flow which represents that the windward and leeward side will experience a different oncoming flow will cause an assymetric pressure distribution (see Fig 2.5).

With increasing forward speed the suction pressure that is created at the windward side will increase as well [10] and at the leeward side there will be a negligible change. This assymetrical distribution of forces will give rise to a yawing moment about the tail rotor's center of gravity. In addition, the component of this suction pressure force which is parallel to the oncoming flow will result in drag.

[6]For a fixed wing during normal cruise conditions the oncoming flow is always axial except for the climb and descent flight phases

All these effects and generally the complex integrated performance of the rotor and the shroud depend on the selection of the geometric parameters that have been discussed so far. Thus, the use of CFD can be proven beneficial in terms of providing the integrated performance of the rotor and the shroud as well as a detailed flow description. Although the concept of shrouding the rotor in the case of the helicopter plays a different role than in the fixed-wing applications, the performance of the tail rotor will be subject to the (same) interdependence of these parameters as well as the freestream conditions.

Typically, the shrouded rotor has only been used throughout the years on small and medium helicopters (single engine light, twin engine light and twin engine medium). For the case of larger helicopters, the size and the weight of the shroud as well as the fin prohibit its successful and viable application. In addition, safety considerations become less important due to the fact that a conventional tail rotor is mounted at the top of a pylon [4, 2].

The majority of a typical helicopter's flight envelope will consist of hover and forward flight segments hence a careful selection of the inlet lip radius, expansion ratio and duct length is of paramount importance in order to achieve a compromise between forward flight (edgewise flow) and hover (axial flow) performance. Clark [22] published a work in which the development of the fan-in-fin antitorque system for the S-67 Blackhawk Boeing-Sikorsky helicopter was presented.

In his work an ideal duct design was proposed that will ideally produce, as close as possible, a uniform flow distribution while maintaining fully attached flow in all phases of flight. The duct had an inlet lip radius of one-tenth of the rotor diameter which provided a good balance between the inlet flow distortion caused by smaller radii and the risk of flow separation on the leading edge of the duct with larger radii. The "deep duct" that he used, as shown

in Fig 2.11 , was needed in order to allow the flow to return to a uniform distribution before reaching the fan proving that this "relaxation" of the flow is a "principal requirement of the inlet of a ducted fan device". The requirement of uniform flow is less crucial in hover or low speed flight due to the fact the flow distribution is almost uniform, but it is crucial in high speed/ low thrust conditions [22].

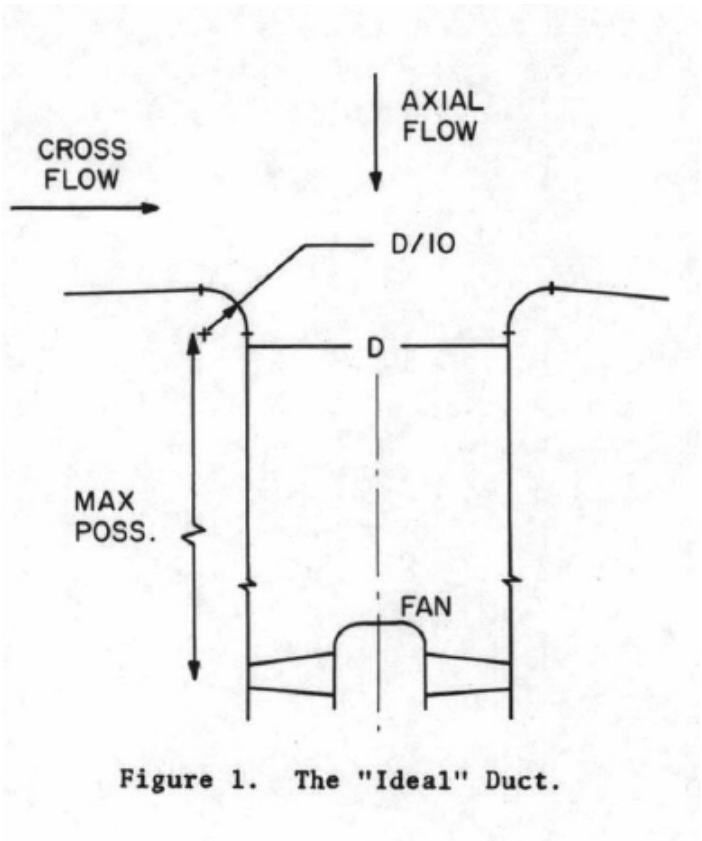

(a) Cross-section of the "Ideal" duct

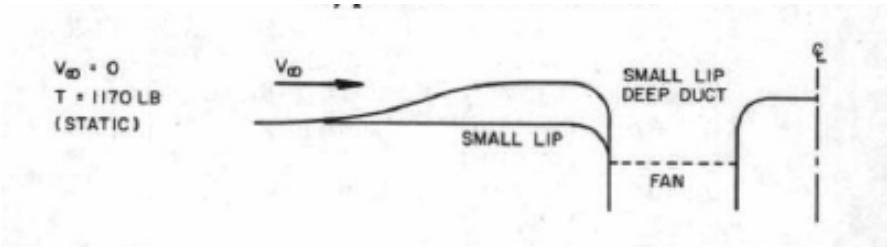

(b) Deep duct illustration

Figure 2.11: "Ideal duct" S-67 Boeing Sikorsky [22]

Nevertheless, the maximum position between the inlet lip and the position of the fan was not explicitly reported and it was also reported that the design behaved well for hover and sideward flight, but the performance in high speed forward flight was somewhat less than ideal. An important assumption from Clark's work is that despite the differences which exist between ducted rotors for antitorque applications and ducted rotors which are used in fixed-wing aircraft, a large amount of the experimental database which exists for fixed-wing aircraft is directly applicable to the case of helicopters.

Finally, it was mentioned that because of the higher disc loading ($DL = T/A$) of the fan more power was required in hover compared to the power of a conventional tail rotor. Research work pertaining to the effect of the inlet lip radius on the performance of the ducted rotor has also been undertaken by Keys et al [23] during the development of the FANTAIL for the Boeing/Sikorsky Comanche Light Helicopter.

Wind tunnel tests have showed that by decreasing the inlet lip radius from 6.5% to 0.9% of the rotor diameter flow separation would occur from the inlet surface which degraded the performance as well as reduced the FM by 7%. In order to achieve maximum hover performance, a value of 7.5% was chosen which compromised the forward flight performance. They also reported that a "sharp diffuser exit radius" was required for best hover performance. One constraint of the applicability of the ducted rotor concept to helicopter tail rotors is the fact that the length of the shroud will be limited by the width of the tailboom. Fairchild et al [24] provided a significant experimental database where they tested shroud lengths which span from 20% to 60% of the rotor diameter and diffuser angles from 0° to 20°.

By increasing the shroud length, the contribution of the shroud to the total thrust T_{shroud}/T_{total} and the total thrust was found to increase , from the shortest to the longest, approximately from 36% to 53% respectively. At fixed shroud length, the increase in the diffuser angle T_{shroud}/T_{total} increased as expected but the shroud thrust fraction increased slightly at the case of longest shroud (60% of the rotor diameter). This was due to "premature flow separation at the diffuser" and the low disk loading. In addition, the authors have investigated the effect of the blade collective angle on thrust performance .

At 10° collective angle there was no difference between the ducted rotor thrust and the open rotor thrust. By increasing the collective the total thrust increased as well as the shroud thrust fraction. It was reported that the effect of increasing the collective angle was greater than the effect of increasing the shroud length. As it was seen before and also reported in their work the shrouded rotor stall angle was greater than the stalling angle of the open rotor.

According to Fairchild et al. the shrouded rotors did not stall up to the maximum test angle of 30°. Generally, by increasing the diffuser angle, the maximum thrust will increase up until the point where flow separation will occur at the diffuser. Therefore the choice of the proper diffuser angle, for a given shroud shape and antitorque requirements, must be done carefully in order to avoid flow separation at the diffuser exit. Aerospatiale [5] indicated that a maximum of 10° should be chosen in order to counteract flow instabilities caused by the interaction with the main rotor wake. However, these instabilities have not been encountered when the isolated model was tested.

In the case of the helicopter, due to the limitations on the width imposed by the tailboom, the diffuser expansion ratio of a helicopter has a typical value of 1.0 to 1.1. Aerospatiale fenestron helicopters (Dauphin) utilized an expansion ratio of 1.0 and a diffuser angle of 8°. The FANTAIL Comanche helicopter had an expansion ratio of 1.0 where a diffuser angle of 5° was used. This value led to a total thrust (in hover) augmentation values (T_{total}/T_{rotor}) of 1.8 to almost 2.0 which is considered as the "theoretical maximum" [7].

This theoretical maximum value ([7]$T_{total}/T_{rotor} = 2$) assumes an ideal fan in hover where the thrust created by the inlet lip suction forces is equal to the rotor thrust. It has been reported in a study concerning the handling qualities of the H-76 FANTAIL demonstrator [7] that during hover and sideward flight the augmentation factor's real value was very close to the ideal. Wind tunnel experiments performed by TsAGI [25] in Moscow for the KAMOV Ka-60 Kasatka helicopter confirmed also a, close to ideal, total thrust augmentation factor of 1.82.

In order to close the discussion concerning the geometric parameters, that dictate the performance of the ducted rotor, a brief outline will be given about the rotor parameters and their performance effect. As far as the blade collective is concerned, it was shown that the rotor thrust will increase with increasing blade collective. In addition, ducted rotors tend to exhibit higher operating angles than the open rotors and will stall at a higher angle. Vuillet [5] has reported that slightly after the post-stall angle, the suction forces on the shroud are sustained due to the existence of high tangential (swirl) velocities (the axial component of the velocity reduces when the blade is stalled).

[7]Assuming an expansion ratio of $\sigma_d = 1$ see Equation 2.6

Pereira [9] has reported that by tapering the rotor blade, there would be a slight performance degradation (6% reduced thrust reduction) compared with a squared untapered rotor. Tapering the rotor blade, effectively reduces the blade loading coeffcient (at the tip of the blade) C_{Trotor}/σ where C_{Trotor} is the rotor thrust coefficient and σ is the blade solidity[8] which is defined as the total planform area of all blades over the rotor disk area:

$$\sigma = \frac{N_b c R}{\pi R^2} = \frac{N_b c}{\pi R} \tag{2.11}$$

The ducted rotor performance will be also strongly depended on the selection of the rotor airfoils. Traditionally in Aerospatiale Fenestron helicopters, the OA2 (Onera/Aerospatiale) family of airfoils were used as the main rotor blade profiles [26]. These airfoils have been used since the 1970's and exhibit higher lift to drag ratios compared to the NACA 0012 airfoil (see Fig 2.12). For the Fenestron tail rotor, the most advanced airfoil profiles are of the OAF family, which have been proven to provide optimum performance over a wide flight operating envelope.

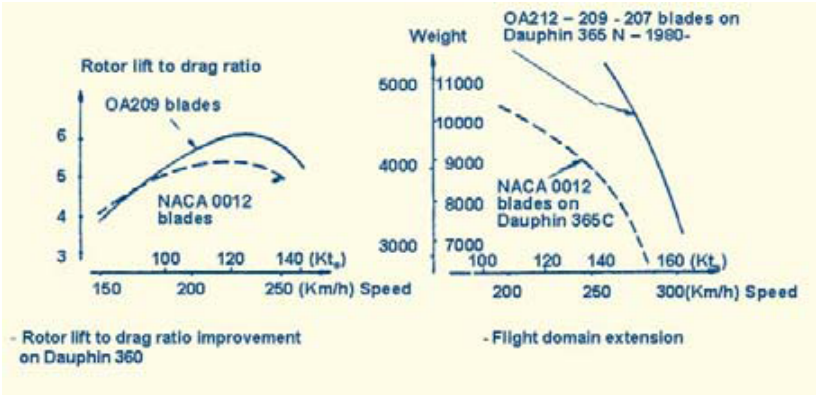

Figure 2.12: Flight test results on Dauphin 365C airfoils (main rotor) [26]

[8]Solidity is a very important parameter, generally, of helicopter aerodynamics and it expresses the power absorbing capacity of the rotor.

Finally, a rotor parameter which has an effect on performance is the blade twist. The majority of the helicopter blades, both on main and tail rotors, are twisted in order to decrease the pitch angle towards the blade tip where the local velocities are higher in magnitude. This means that by adding blade twist, the inflow distribution is kept as uniform as possible. In theory [2], a non-linear "ideal twist" will introduce a uniform inflow across the rotor disk. The ideal hyperbolic form of pitch angle is given by:

$$\theta(r) = \frac{\theta_{tip}}{r} \tag{2.12}$$

where θ_{tip} is the blade collective at the blade tip.

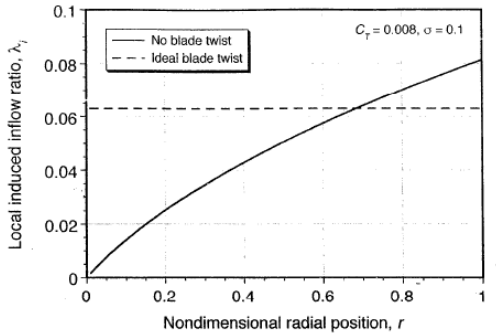

(a) Induced inflow ratio distribution comparison of ideal and no blade twist

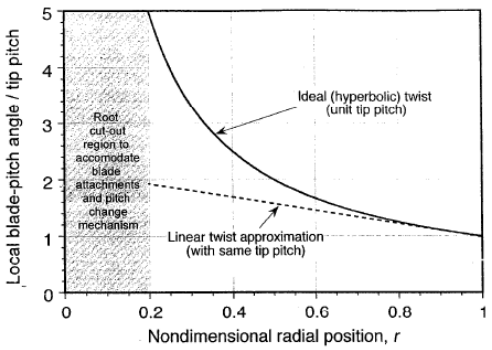

(b) Radial distribution of ideal and linear blade twist

Figure 2.13: Ideal Blade Twist [2]

The hyperbolic twist distribution cannot exist in reality as $r \to 0$ but due to the fact that the blade pitch variation is not important from the hub up until the root cutout location. A linear twist distribution, as shown in Fig 2.13a, is considered close to the ideal case [2] over the root cutout location. Root cut-out is a blade parameter, usually denoted as a percentage of the blade radius, which expresses the distance between the centerbody and the beginning of the actual rotor blade. For example, a root cut-out of 40% means that the blade profile starts from 0.4R hence the effective blade radius is actually 0.6R[9].

In helicopters equipped with ducted tail rotor typical values of blade twist fall within the range of $-7°$ to $-12.5°$. The early Gazelle Fenestron used $-12.5°$ blade twist which was later reduced to $-7°$ due to adverse interactions with the main rotor wake which deteriorated yaw authority [4, 5]. Generally, highly twisted blades are not desirable in helicopter applications because this, according to Leishman, can lead "to less efficient lift and propulsion generation from the advancing side of the disk at high advance ratios". However, there are considerable performance benefits, in hover and low speed forward flight, associated with some blade twist.

[9]In the general literature of helicopter aerodynamics, the blade radius R will be measured from the center body

2.3 Performance Prediction Methods

2.3.1 Analytical Methods

For predicting the upper level performance of the ducted tail rotor, analytical methods and tools such as momentum theory, BEMT, Blade Element Vortex Theory (BEVT) and potential flow methods have been used extensively in the past. In terms of theory and modelling requirements, a ducted rotor can be regarded as a ring airfoil with certain camber and thickness in which there exists a pressure discontinuity i.e. the rotor itself.

All these methods assume an ideal, inviscid incompressible fluid e.g. the method of singularities consider a potential vortex ring where the superposition of a number of singularities will produce an arbitrary distribution of circulation strength. In these methods, the Kutta condition is satisfied at the diffuser exit (duct trailing edge), and the slipstream is considered to fully expand to ambient conditions at this location. One of the oldest published work concerning the modelling of a ducted rotor is the work done by Kuchemann and Weber [27] .

They developed potential flow methods based on the method of singularities and they considered 2D annular airfoils along with their vortex ring distributions assuming a uniform inflow over the rotor. Krieber and Mendenhall [28] put forward a theoretical study of a ducted propeller at angle of attack so as to predict thrust ratios, normal force, drag and pitching moment. These studies were extended in order to include duct pressure distributions and boundary layer characteristics.

The rotor was modelled as an actuator disk and the duct was represented as a thick, cambered ring airfoil. Considerably good agreement was reported with available experimental data but there were some discrepancies due to the "high non-uniform blade loading". Mendenhall and Spangler [29] have developed, as an immediate result of previous work, a computer program which was able to determine the performance of a ducted rotor in axial flight at a specified angle of attack. Their method consisted of a potential flow solver where the flow was uniform, inviscid and incompressible. This program was able to deduce the thrust, drag and pitching moment coefficients and it is mainly based on the work done previously by Kriber and Mendenhall [28].

Fairchild et al [24] implemented a therotical analysis which was based on McCormick's [30] method of replacing the whole duct with a vortex ring located at the duct quarter-chord and defining the circulation strength in order for the flow conditions to be satisfied at the three quarter chord. However, this method was used for the static (hover) performance of the ducted and correction factors have been utilized for the performance estimates.

In Aerospatiale [5], around late 80's, two simulation methods were used in order to predict the ducted rotor performance. The first method was a simple BEMT analysis which incorporated an actuator disk. Airfoil characteristics and local pitch angle were given in a table look-up form. This method was used for performance estimation and sizing purposes and it depended on available experimental results. The second method incorporated a more advanced theory developed by METRAFLU and it was based on a compressor calculation code. Both methods correlated well with available experimental results in hover.

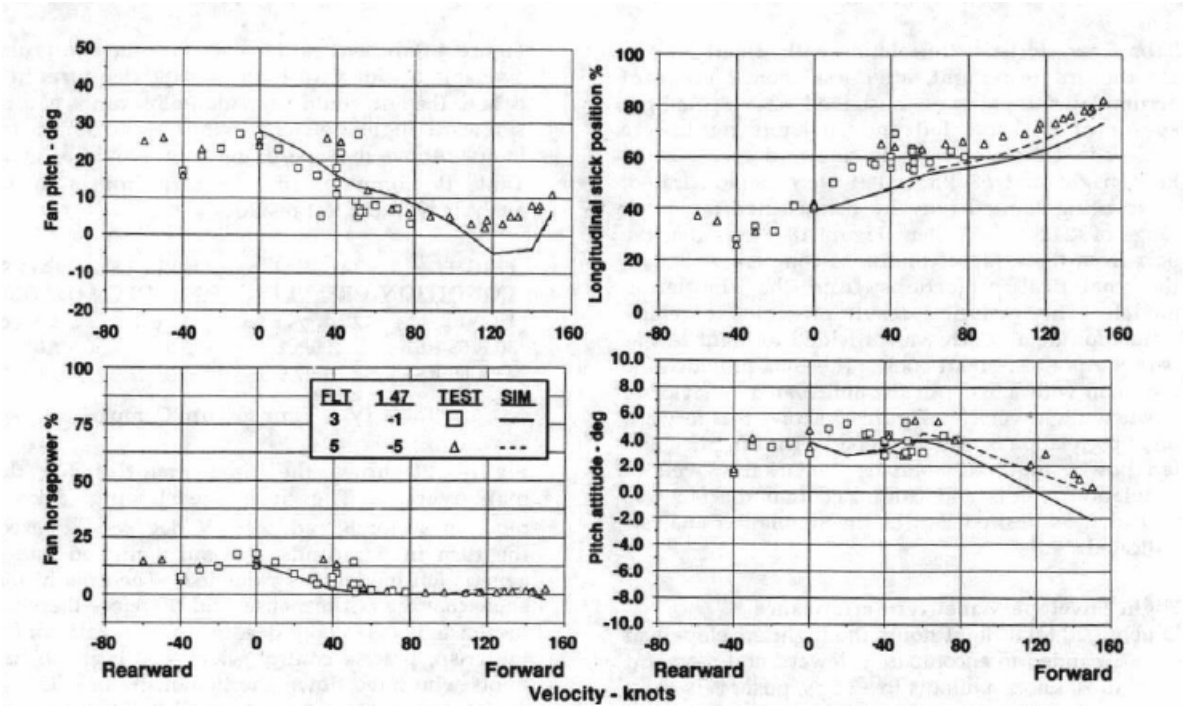

Figure 2.14: H-76 FANTAIL Fan Model Correlation with Flight Test in forward flight [7]

It was reported that METRAFLU did not capture well the shroud pressure distribution, from the inlet lip to the rotor, due to the blade tip vortices which are not taken into account due to the inviscid fluid assumption and lack of turbulence modelling. Wright et al [7] developed a fan model based on the momentum theory approach, as well as "extensive wind tunnel testing", which was used on the H-76 FANTAIL. A fixed total thrust augmentation factor of 2.0 was used in order to include the effect of the shroud thrust. This model gave good correlation at various flight regimes including hover and forward flight. However, only the fan pitch is reported (see Fig 2.14) as a function of forward speed, rotor polar curves (C_T vs C_P) and shroud pressure distributions were not presented[10].

[10]Although thrust values were not given, the first graph in Fig 2.14 depicting the relation between fan pitch and forward flight speed is useful on the grounds of construction of a performance map.

Additional studies which pertain to the applicability of BEVT for ducted rotor performance predictions, and in particular the effect of the tip clearance, have been performed by Gibson [31] . It was reported that by reducing the blade tip clearance, thrust was increased as anticipated. However, in small tip clearances (1% of the rotor diameter) the predicted thrust was decreased and this was due to the inability of the model to capture the interaction of the blade tip vortex and the shroud boundary layer. Thus, the need of a more advanced theory or tools is necessary in order to provide a realistic description of the very complex flowfield.

A more recent study and method was that of Bourtsev and Selemenev [25] which was undertaken by the Russian helicopter manufacturer KAMOV and was used in the design of the Ka-60 Kasatka helicopter which utilizes a ducted tail rotor. Their method, applicable only to axial flow, was based on the modified theory of Shaidakov, which considered momentum theory for modelling the global effect of the shroud by using a total thrust augmentation factor of 1.82, derived by experimental results. The diffuser was conical and the flow was assumed to be fully expanded at the diffuser exit.

The rotor was modelled by using the Joukovsky-Vetchinkin disk vortex theory together with "two new correction factors of influencing of a shroud". These factors were used in order to include the geometric effects of the shroud on the rotor thrust. In addition, the effect of the blade tip clearance was modelled by using a so called "Prandtl-Shaidakov" factor which is similar to the Prandtl tip loss correction applied for open rotors. The method correlated well with the available experimental results but it must be noted that the model was calibrated according to previous experimental results (total thrust augmentation factor).

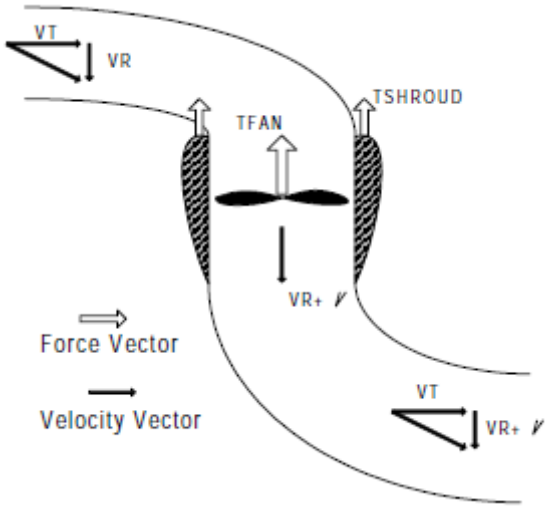

Figure 2.15: RAH-66 Comanche Forward Flight Analysis [32]

Kothmann and Ingle [32] during the development of the Boeing RAH-66 Comanche FANTAIL put forward an analysis method which was capable of predicting the unsteady thrust response of a ducted rotor in various flight regimes and was correlated with flight tests. Their method was based on the Glauert's BEMT for an open rotor with the forward flight results reducing to the axial flow results as a special case.

It was assumed that the slipstream is turned back into the direction of the freestream flow, no wake contraction and that there are not any radial or azimuthal inflow variations. This last assumption is false due to the fact that the inflow distribution will be dependent on the exact geometry (inlet lip radius). Wright et al [7] have mentioned that during forward flight "lip separation occurs for most conditions" hence BEMT is proven inadequate to capture these viscous separation effects.

To conclude, it can be stated that the majority of the work presented concerns applications of BEMT and BEVT to the axial flow regime (hover and sideward flight) and this has been acknowledged by other researchers as well [12] . According to Sacks and Burnell et al [12] there were a small amount of researchers who attempted theoretical studies in non-axial flow i.e. translating flight. One of the main assumptions used in the case of non-axial flow, is that the "wake forms a cylindrical extension of the shroud in the direction of the duct axis", which limits the analysis to forward speeds which are small compared with the wake velocity. It must be noted that, in forward flight the analysis models as presented before, were calibrated (in the form of empirical factors) by available experimental results.

Thus, more advanced tools are needed in order to capture such effects as the inlet lip separation, the interaction of the blade tip vortices with the shroud as well as the drag and pitching moment coefficients. The inherent assumptions of these methods such as inviscid, incompressible and irrotational flow prove them as inadequate to address the modelling requirements of the ducted rotor, especially in forward flight. CFD methods although expensive can provide a detailed description of the complex flowfield around a ducted rotor and can represent the full three dimensional effects such as the blade tip vortices.

2.3.2 Computational Fluid Dynamics Methods

The flow regimes which are encountered in rotorcraft aerodynamics are quite complex. The rotation of the blades causes non-linearities [33].. In addition, the dominant flow structures such as the blade tip vortices, are three dimensional and can only be regarded as unsteady especially in the advancing side of the main rotor. The blades of the rotor shed vortices which can cause aerodynamic interactions between the rotating and non-rotating parts. This rich variation of challenging aerodynamic problems which appear in rotorcraft aerodynamics, make attractive the application of CFD in order to tackle these problems.

In addition, from an experimental and modelling point of view, it is considered extremely difficult to study the fluid flow of a rotating component, especially when other stationary components are present [34]. Thus, CFD can offer a cheap and practical alternative to wind tunnel experiments but this does not imply that experiments should be abandoned in favor of CFD. An excellent historical overview about the applicability of CFD methods to rotocraft aerodynamics is provided by McCroskey [33], Caradonna and Tung [35] and Conlisk [34].

The first applications of CFD in rotorcraft aerodynamics concerned the implementation of Euler and Navier-Stokes codes in investigating the aerodynamic performance of 2D static (hover) airfoil characteristics. McCroskey [33] has used the NASA-Ames code ARC2D which solves the Reynolds Averaged, thin-layer Navier-Stokes together with the Baldwin-Lomax eddy viscosity turbulence model. A wide range of Reynolds and Mach numbers has been tested in various collectives.

A classic problem in CFD methods for rotorcraft applications is the prediction of the flowfield of an isolated rotor blade in hover. The prediction of this flow regime, due to its simplicity in comparison with the forward flight, is often used as a benchmark simulation for validating CFD codes and the seminal experimental work of Caradonna and Tung [35] is used.

The flowfield in hover is periodic and the near field prediction of vortical structures and consecutively the blade loads is straightforward. Far field predictions as well as blade vortex interaction studies are extremely challenging due to the fact that the numerical schemes tend to smear the vortex due to their numerical dissipation.

However CFD capture adequately the near field formation of the tip vortex and the blade airloads [36]. Srinivasan et al [36] have applied the Navier-Stokes CFD code TURNS (Transonic Unsteady Rotor Navier-Stokes) in order to calculate the realistic helicopter rotor configurations of the UH-60 and BERP (British Experimental Rotor Program) for lifting hover configurations as well as assessing the importance of planform effects on the blade airloads.

They have reported that the CFD code has captured quite accurately, the near field vortical wake and its trajectory without the need of a prescribed wake model. The induced flow in the rotor plane as well as the calculated pressure distribution agreed well with experimental data. Finally, they stressed the fact that the Navier-Stokes method enhances "the tip flow simulation which involves resolving the three dimensional separated flow and concentrated tip vortex" as well as " the accurate simulation of strong viscous-inviscid interaction involving shock-induced separation at high blade tip speeds".

In general, it can be acknowledged that CFD methods have played an important and versatile role towards a better understanding of the challenging and complicated aerodynamic problems. CFD methods as applied to the ducted rotor have been done by various researchers and the applications involve coupled CFD-momentum analysis to the more computationally intensive Discrete Blade Models (DBM). Rajagopalan and Keys [37] have applied a coupled CFD Momentum Source Method (MSM) for investigating the flow-field and performance of the RAH-66 FANTAIL in hover and sideward flight.

Their results were used in the detailed design of the FANTAIL structure, blades and transmission cooling. Their method was based on a finite difference Navier-Stokes code which solves the steady incompressible, viscous laminar Navier-Stokes equations in an axisymmetric body (see Fig 2.16). The flow solver utilized non-body-fitted grids.

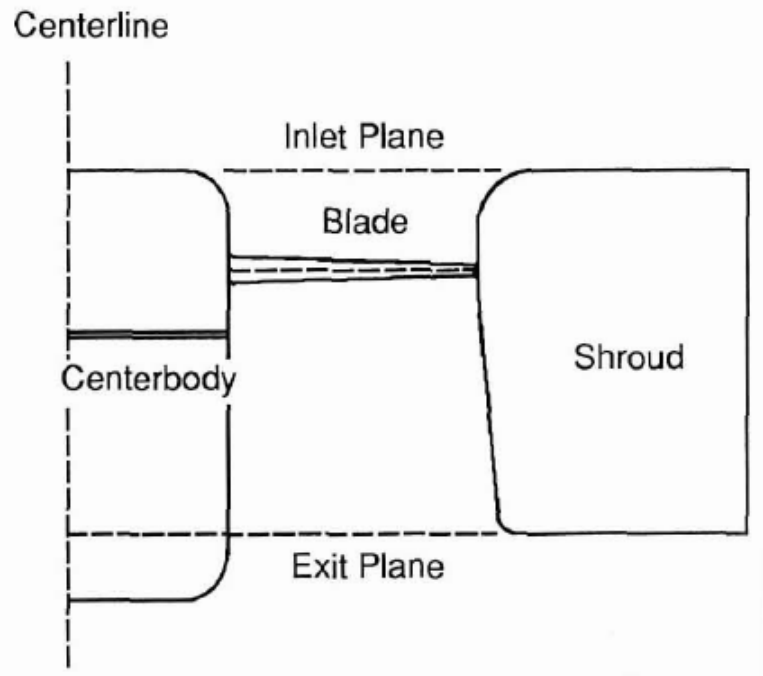

Figure 2.16: Radial Cross Section of the axisymmetric Body used in FANTAIL [37]

In their analysis, the presence of the blades has been represented as momentum source terms which required two dimensional airfoil lift coefficient and drag coefficient as a function of Mach number. The duct geometry including the hub has been modeled by Navier-Stokes simulations. Thus, the whole domain is simulated with the Navier-Stokes except from the fan which is considered as an actuator disk. It must be noted that the deployed geometry was axisymmetric due to the hover and sideward flight regime where a uniform and periodic flow is expected at the rotor plane.

This assumption facilitated the simulations in terms of grid generation and computation time. The axisymmetric geometry assumption is commonly used in hover CFD calculations [8, 38, 11, 39], however in forward flight the realistic geometry which varies azimuthally shall be used. An illustration of the deployed computational domain and the flowfield in hover is illustrated in Fig 2.17. Finally, their analysis showed good correlation, for all the test cases, with experimental results, however they reported a more realistic approach like the DBM should be used.

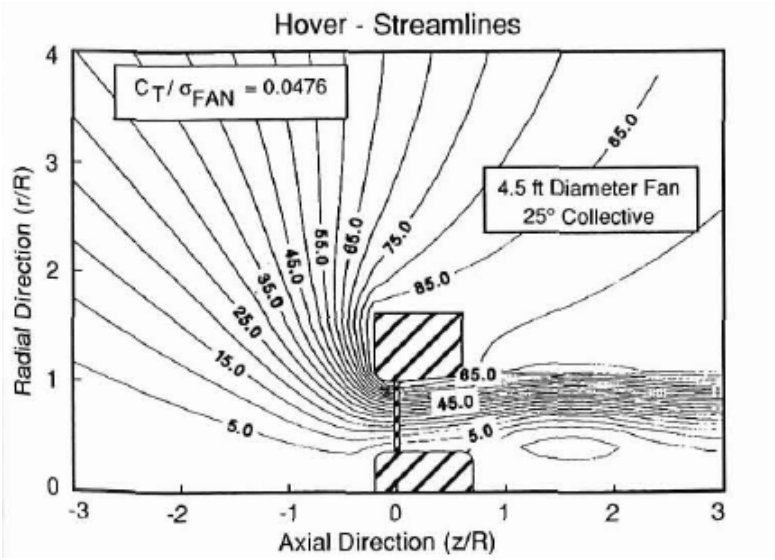

Figure 2.17: flow-field in hover and computational domain, FANTAIL [37]

Nygaard et al [40] have introduced an improved MSM method which was implemented in the OVERFLOW-D Navier-Stokes code and used in order to simulate the hover and sideward flight regimes of the FANTAIL . Their method was similar with the previous work made by Rajagopalan et al [37] in terms of the calculation of the blade airloads. However, their revised model included a model for the forces in the tip region and the axial distribution of the source terms which gave a more realistic representation of the induced flowfield on the rotor plane. OVERFLOW-D utilized body-fitted structured overset (Chimera) grids.

Their method compared well with experimental data for a collective pitch angle of 38°measured at 75% of the blade's radius. The authors have also made a comparison between their MSM method against DBM data and they reported that the correlation between angle of attack and lift coefficient is good except at the blade root and tip. At the tip, the angle of attack becomes very large and the lift coefficient's value surpass the peak value of the $C_{l,max}$ in the two-dimensional airfoil table. This analysis demonstrated the sensitivity of the shroud thrust prediction to the accurate modelling of the effect of the blade tip clearance. This is due to the fact the flow at this region is three-dimensional and "the applicability of the 2D airfoil tables becomes questionable".

An MSM-BEMT method coupled with the CFD solver PUMA 2 (Parallel Unstructured Maritime Aerodynamics) has been used by Alpman et al [6] for the steady-state inviscid simulation of the FANTAIL, together with its original fuselage, in hover, sideward and forward flight. The authors reported acceptable correlation with available experimental results (validation was performed only for the axial-flow cases) and the observed discrepancies were due to the geometric differences, the use of an inviscid solver and the fact that more "representative blade lift curves were not used".

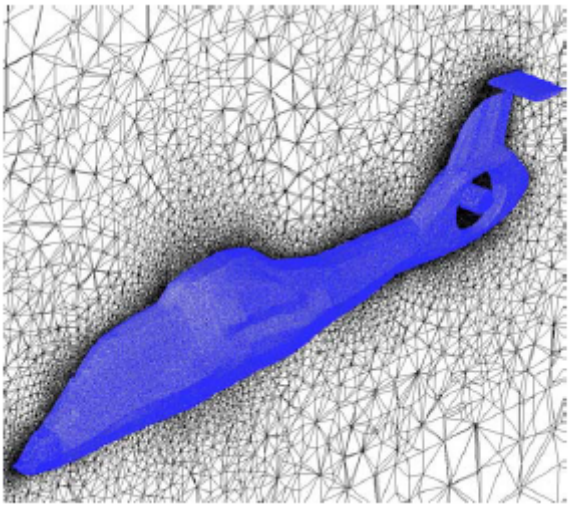

Figure 2.18: Computational mesh of RAH-66 Comanche FANTAIL [6]

An illustration of the deployed unstructured grid is shown in Fig 2.18. The importance of the three-dimensional flow at the blade tip region was demonstrated by Ruzicka et al [11] where the authors have used a DBM method in order to investigate the flowfield in hover of the FANTAIL. The authors performed steady RANS simulations by using OVERFLOW-D and they considered an overset grid methodolgy for the grid generation.

For the simulation of the hover flow regime, due to the periodicity of the flow, a "frozen rotor" approach was used by the authors. This is based on the fact that the flowfield is steady when viewed from a blade-fixed frame of reference. Thus, rotational source terms are applied to the Navier-Stokes equations in order to transform the unsteady problem to steady hence saving computational time. It was also reported that the axi-symmetry of the deployed inlet lip and the shroud is a key requirement for the existence of a steady-state solution. In the steady CFD simulations the rotor and an axisymmetric shroud have been simulated using a quadrant of the model due to the periodicity of the flow regime.

Furthermore, the attachment of the blade root to the hub has not been simulated and a boundary condition that ensures no flow within this space has been used. In addition, an inviscid wall boundary condition was deployed for the hub since the flow-field was not "expected to be sensitive in conditions in that region" [11]. The CFD results showed that the thrust of the rotor was overpredicted but the overall thrust-power curve showed good agreement. In addition, the shroud thrust was underpredicted and the shroud pressures were noticeably above experiment. The reason for this , as the authors state [11], is probably the computational error involved in the simulation and the use of an axisymmetric body.

Actually, the geometry that was used was a simplification of the actual geometry and the experimental determination of the shroud force is approximate. Finally, it was acknowledged that a complete understanding of the differences between experiment and computations is a goal of future studies. The results of the shroud force and rotor force as well as the pressure contours within the inner part of the duct are shown below.

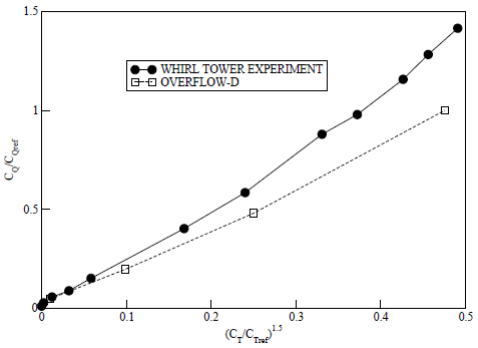

(a) FANTAIL rotor thrust power comparison in hover

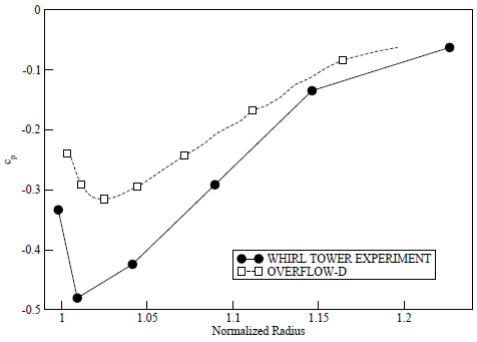

(b) OVERFLOW-D and experimental FANTAIL pressures on shroud lip: hover, 38°

Figure 2.19: OVERFLOW-D FANTAIL Results [11]

D'Alascio et al [8] have applied CFD tools in order to investigate the performance of the EC135 helicopter in hover flight conditions. The authors have stressed the importance of using CFD tools not only on the grounds of a better three-dimensional description of the flowfield and deeper understanding of it but also because RANS simulations are less expensive than wind tunnel experiments and flight test campaigns. The authors have assessed the accuracy of two CFD solvers which are used in EUROCOPTER i.e. FLOWer developed by DLR [41] and elsA developed by ONERA [42] as well as the commercial solver EURANUS developed by NUMECA.

Three approaches have been used where in the first one the complete components of the helicopter were simulated namely the tailboom including horizontal stabilisers, shroud, fin, bumper, the rotors and stators, the hub and the drive shaft fairing. This approach has been chosen due to the deep level of description and because it can be used both for hover and forward flight along with the fact that it can provide an "exhaustive" thrust decomposition over the geometry components. FLOWer is a 3D Navier-Stokes solver which utilizes a rotating frame of reference (frozen rotor) and the discretization is done by a 2nd order central difference scheme. The grid generation was done by using an overset multi-block grid.

The difference between an overset grid and a classical structured grid is that in overset grids, individual components such as the blades and the shroud do not need to be connected in a pointwise manner like in the body-fitted structured grids. This introduces flexibility in the analysis where parametric studies are needed e.g. changing collectives. The Chimera grids as shown in Fig 2.20 overlap between themselves and interpolation is done on the boundaries in order to transfer the fluxes between the grid cells.

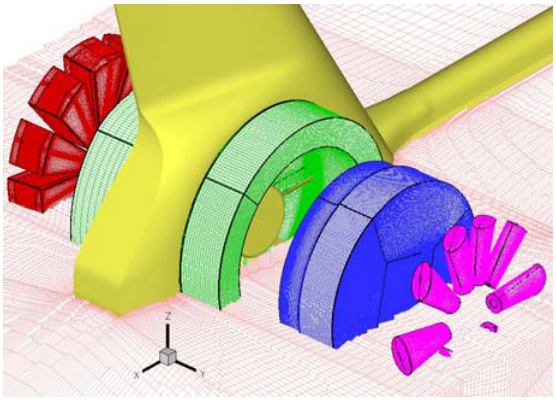

Figure 2.20: View of the Chimera grid of the EC135 tail [8]

The authors in the first approach performed both unsteady and steady simulations (three simulation points with stators and one without stators). It was reported that due to the extremely high computational time, the unsteady approach is not suitable for optimization studies and the assessment of results could be done by using "simpler and faster approaches". A section of the Fenestron duct depicting the qualitative instantaneous C_P distribution as well as the comparison of time-averaged and instantaneous[11] C_p distributions is shown in Fig 2.21

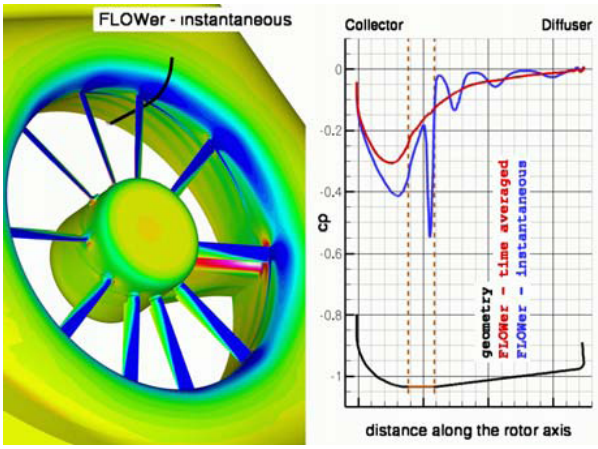

Figure 2.21: Instantaneous pressure coefficient distribution FLOWer, EC135 Fenestron [8]

[11]The oscillations which are depicted in the instantaneous C_P distribution denote the convection of the blade tip vortices.

The second approach utilized only one tenth of the Fenestron including the rotor without the stators, the shroud (axisymmetric) and the hub on the grounds that the flowfield in hover is periodic and the use of periodic conditions is applicable. The rotor mesh and the rotor hub were assigned a rotating frame of reference where the surrounding fluid rotates with the operating angular velocity whereas the blades are fixed.

In addition, in the real configuration the blade distribution is assymetrical in order "to spread the acoustic energy in a broader frequency band hence reducing its human perception". However, rig tests have shown that an asymmetrical distribution has minimal influence in the performance and a symmetrical distribution has been used instead in order to facilitate the grid generation process. The elsA code, a 3D Navier-Stokes code that encompasses the Wilcox's k-ω turbulence model coupled with the Zheng limiter, was used for this case.

The third approach followed by the Technical University of Munich was similar to the second approach but in this approach the stators have been included again. The EURANUS solver was used which solves the Favre-averaged Navier-Stokes and an interface was used between the stator and the rotor which is treated by the mixing plane approach. The authors for this case, applied the Spalart-Allmaras turbulence model. On balance, the numerical results from all approaches compared well with the available experimental data which were mainly global thrust and torque measurements. The derived polar curve (C_P vs C_T)[12] for all three approaches is illustrated in Fig 2.22.

[12]The power and thrust coefficients have been divided by the solidity of the rotor. This representation is common in helicopter aerodynamics and it removes the effect of solidity when two rotors with different solidities are compared.

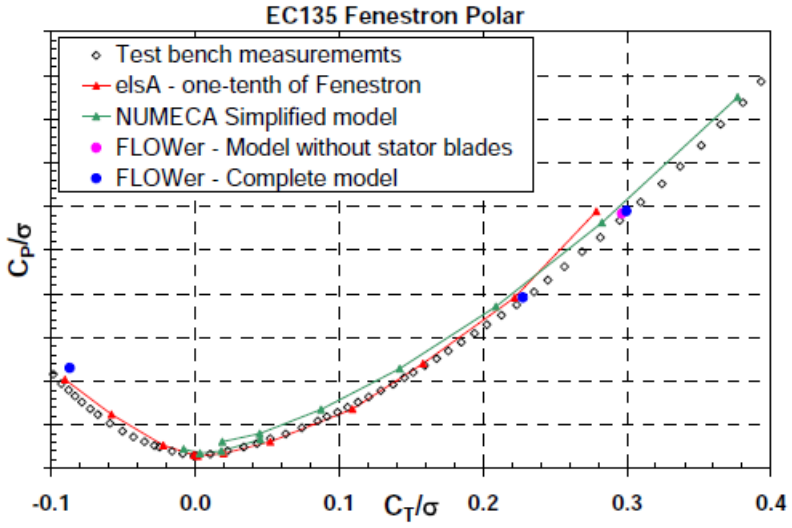

Figure 2.22: EC135 Fenestron power curve [8]

By inspecting Fig 2.22 it is obvious that all three approaches produce similar results except for the high thrust region of the graph where the complete model shows a better agreement. An additional conclusion that can be drawn is that the presence of stators did not have an effect on the polar curve even at the maximum computed angle ($C_T/\sigma = 0.3$).

Additional CFD applications of isolated[13] ducted tail rotors in hover were done by Lee et al [38] and Mouterde et al [39] . Lee et al used an inviscid unstructured solver with periodic boundary conditions. In order to validate his method he used the same tail rotor as in the Ka-60 KAMOV Kasatka helicopter. It was reported that the rotor thrust was overpredicted by 8% and no reference was made to the shroud thrust (agreement with experimental data). Mouterde et al have validated the elsA and FLOWer codes for two hover cases. The first one was simplified axisymmetric geometric model of the Dauphin SA365N3 Fenestron and the second was the complete model of the EC135.

[13]The word isolated conveys that only the axisymmetric duct and hub, rotor and/or stators are considered.

Good agreement with experimental results, in terms of the polar curve, was reported for both cases. Gardarein et al [43] applied the elsA code in order to investigate the performance of the Dauphin Fenestron and this work was the only one, to the best knowledge of the author, where a DBM model was applied in forward flight (simulation point at 150 knots) in order to assess the acoustics of the configuration. The authors did not validate their results with experimental data as these were not available. However, they mentioned that in forward flight there was a "heterogeneity of the inflow at the Fenestron inlet, combined with areas of flow separation of significant extension".

2.4 Chapter Summary

The preceding discussion presented the main objectives and ideas of the literature review, which consitute the backbone of the methodology and results section. Firstly, an introduction has been given about the ducted fan concept as an alternative configuration for either enhancing thrust (fixed-wing applications) or for providing an antitorque force (helicopters). It has been shown that a ducted tail rotor is benefited by the presence of the shroud. More precisely, the shrouding of the rotor can provide additional thrust and performance benefits which cannot be obtained by an open rotor. In the case of helicopters the shrouding of the rotor can offer enhanced safety features, noise attenuation and improved performance in forward flight due to the off-loading of the rotor by the fin. Also, the extensive literature review served in the identification of important, interdependent geometric parameters (expansion ratio, diffuser angle, blade tip clearance and inlet lip radius) which dictate the performance of the ducted fan. In addition, the previous work of other researchers shaped the selection (and justification) of these parameters in the design of the generic

geometry which will be presented in the next chapter. The previous work done was divided in two major sections which consisted of the applications of the ducted fan concept in fixed-wing aircraft and rotorcraft. Researchers in the field of ducted fan aerodynamics have stressed the importance and the crucial effect of geometric parameters selection on the performance. It has been acknowledged that it is impossible to select geometric parameters which will optimise both hover and forward flight. However, the literature review has shown specific guidelines, in terms of their selections, which will be followed and applied in Chapter 3.

Moreover, the available analytical methods as well as current state of the art CFD simulation work has been presented. The analytical methods can provide an upper level estimate of the performance. However, these methods do bear specific limitations such as the assumption of inviscid flow. Researchers from the CFD school of thought showed the benefits as well as the limitations of CFD analysis in the modelling of ducted tail rotors. Finally, one of the main contributions of the literature review, was the identification of the so called thrust augmentation factors. These factors will be used as a means of verifying the results which could not be properly validated due to the lack of well established experimental data.

Chapter 3

Methodology

3.1 Overview

In the following sections the methodology of this work is presented. Firstly, a reference is given in the simplifying assumptions about the construction of the performance maps with regards to their dependency of the thrust and power coefficients on the Reynolds and Mach number. Consequently, the generic ducted tail rotor geometry is presented along with its specific geometric characteristics and the reasoning behind its design. An available validation case for the CFD simulations in hover is provided for a similar ducted tail rotor configuration. In addition, the followed methodology with regards to the CFD modelling is given in detail.

3.1.1 Simplifying Assumptions & International Standard Atmosphere (ISA)

The main aim of developing a ducted tail rotor model is to estimate the performance requirements of the ducted tail rotor at specified flight conditions. These performance requirements, which are dictated by the main rotor, are namely in terms of required power for a given thrust. In this work, a CFD model of a ducted tail rotor is developed which can be used for hover as well as forward flight.

Performance prediction tools must always take into consideration, the fact that a helicopter will always fly a specified mission which will include hover, climb, cruise and descend segments. Thus, ideally a performance prediction tool should be able to provide the power requirements at any flight condition (forward speed, ambient conditions, altitude). Nonetheless, CFD tools can only provide solutions at discrete simulation points which means that, normally the simulations will be performed at specified flight and ambient conditions.

Hence, one of the main aims of this research work is to provide a set of performance maps which can be used potentially in a complete helicopter mission analysis. The performance maps must be able to relate two main parameters which are the tail rotor power and the corresponding amount of thrust. It must be noted that due to the antitorque purpose of a tail rotor (either conventional or ducted) its thrust and subsequently its consumed power will be always subject to the main rotor's requirements.

The required thrust is also dependent on the collective angle of the rotor and on the forward speed which means that the CFD model must be constructed in different collectives (which corresponds to a set of different computational grids). In hover, the performance map will satisfy the function: $C_P = f(C_T)$

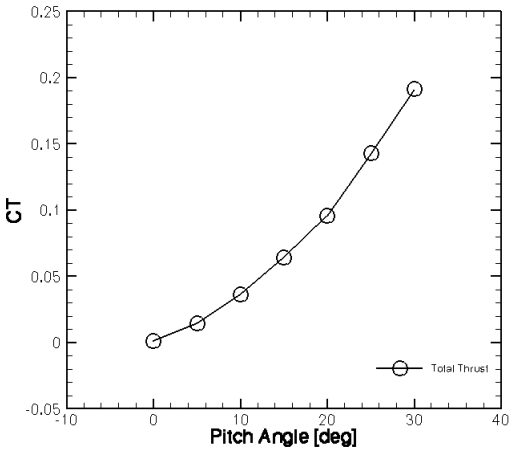

Figure 3.1: Ducted tail rotor thrust versus collective polar curve in hover

where $C_T = f(\theta_0, h)$ where θ_0 is the collective angle of the blades and h is the altitude (which will reflect different ambient conditions such as the atmospheric pressure, density and temperature). In an experiment, a rotor polar power curve ($C_P = f(C_T)$) is derived in the same manner as described above. The rotor will be tested at different collectives and the collectives which are not tested will be found by interpolation. A representative polar curve for a ducted tail rotor which shows the variation of the coefficient of thrust as a function of the blade collective angle ($0° - 30°$ with increments of $5°$) is shown in Fig 3.1[1]. Then for the tested collectives, the shaft torque is measured as well which will provide the power polar curve, where a representative curve is illustrated in Fig 3.2. By inspecting Figures 3.1-3.2, it can be seen that the relationship between the plotted variables is close to quadratic or cubic which means that polynomial fits can be applied in order to represent these curves. In general purpose rotating machinery, the rotor is also tested at different RPM as well in order for the relationship of RPM, thrust and power to be derived.

[1]Figure 3.1 shows the polar curve at hover of the generic ducted tail rotor which will be presented in the section 3.2

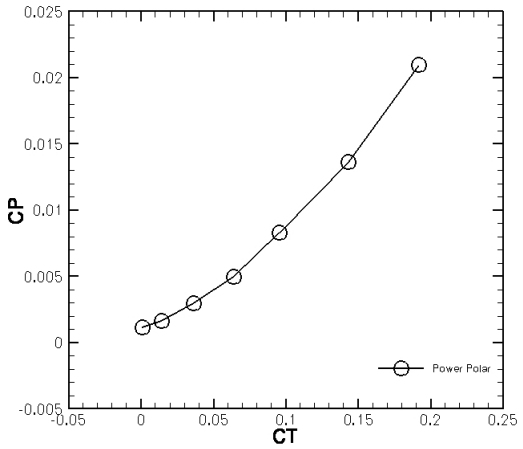

Figure 3.2: Ducted tail rotor power versus thrust polar curve in hover

However, this is not a requirement for helicopter rotors, which are mainly operated at fixed RPM [44]. Vikram [20] has performed a study concerning the effect of RPM on the thrust and power coefficients. In his experiments, Vikram investigated different airfoils that can be used for a ducted Micro Aerial Vehicle (MAV) rotor.

Vikram [20] showed that at Reynolds numbers between 30,000-100,000 the power and thrust coefficients remained almost constant at high RPM's (above 2000) which indicated that Reynolds number effects are not present, as illustrated in Figure 3.3. This conclusion is very important because it can be used as an assumption for the aforementioned performance maps.

Since the thrust and power coefficients remain the same for such an extreme case where the Reynolds number is relatively low (where the flow is dominated by viscous effects hence more prone to viscous separation), it will be safe to consider that the power and thrust coefficients are independent of changes in Reynolds number.

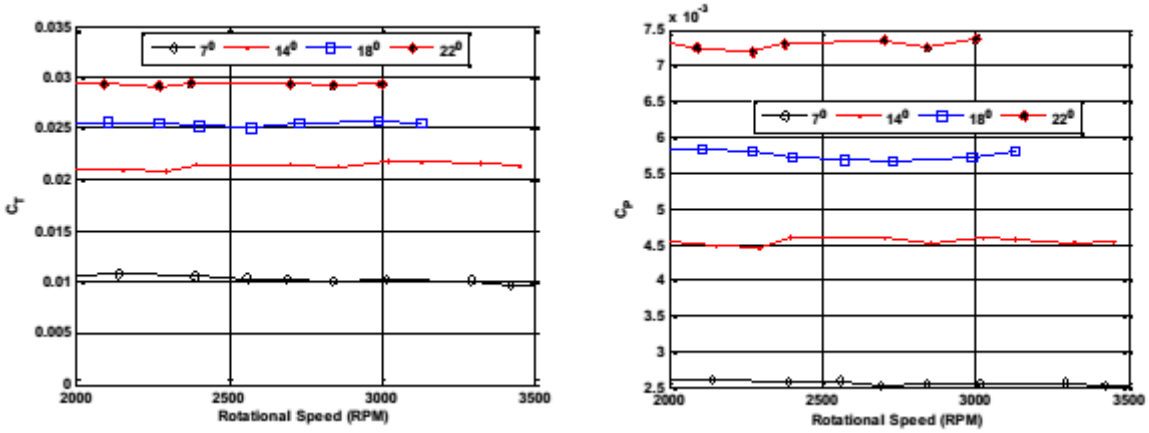

(a) Thrust coefficient vs RPM

(b) Power coefficient vs RPM

Figure 3.3: Variation of thrust and power coefficients for a two bladed rectangular rotor [20]

In the case of a ducted helicopter tail rotor where the rotational velocity is held fixed at the majority of the flight envelope (347-365 RPM operating range for a Eurocopter AS365 N3 Dauphin [44]), variations in Reynolds number can be attributed only to the ambient conditions. However, these changes will be significantly smaller compared to a change caused by varying the rotational velocity. Thus, a fundamental assumption pertaining to the derivation of the performance maps is that the power and thrust coefficients remain approximately constant at all altitudes (up to 10,000 ft) and at different International Standard Atmosphere (ISA) level conditions.

Generally, performance calculations are performed in ISA conditions considering the sea level conditions which are used as a point of reference. Therefore, all measurements at different altitudes in hot or cold days are normalised with respect to this reference point. Temperature variation with altitude, at the layers of troposphere, can be linearly expressed by using the following expression:

$$T = T_o - \lambda h \tag{3.1}$$

where T_o (the subscipt o will denote standard conditions) is the standard sea level temperature (288.15 K), λ is the temperature lapse rate which is equal to 6.5 K/km (or 0.0065 K/m) and h is the altitude in meters. By considering the ideal gas low and rearranging:

$$\frac{p}{\rho T} = \frac{p_o}{\rho_o T_o} = \mathcal{R} \tag{3.2}$$

where p is the atmospheric pressure and R is the gas constant (equal to 287J/kg K). Equation 3.2 can be written as:

$$\frac{p}{p_o} = \frac{\rho}{\rho_o}\frac{T}{T_o} \tag{3.3}$$

The above ratios of pressure, density and temperature represent relative values and usually are expressed by:

$$\delta = \sigma\Theta \tag{3.4}$$

where δ is the relative pressure , σ is the relative density and Θ is the relative temperature. In order to find the pressure/altitude and density altitude relationships the hydrostatic equation can be applied:

$$\frac{\partial p}{\partial h} = -\rho g \tag{3.5}$$

Combining Eq 3.1 and 3.5 the relationship becomes:

$$\frac{\partial p}{\partial T} = -\frac{\rho g}{\lambda} = -\frac{pg}{\lambda \mathcal{R} T} \tag{3.6}$$

Rearranging Eq 3.6 and integrating yields:

$$\ln\left(\frac{p}{p_o}\right) = \frac{g}{\lambda\mathcal{R}}\ln\left(\frac{T}{T_o}\right) \tag{3.7}$$

and

$$\delta = \frac{p}{p_o} = \left(\frac{T}{T_o}\right)^{g/\lambda\mathcal{R}} \tag{3.8}$$

which is the pressure/altitude correlation and by inserting Eq 3.1 it becomes:

$$\delta = \left(1 - \frac{\lambda}{T_o}h\right)^{g/\lambda\mathcal{R}} \tag{3.9}$$

By combining Eqs 3.9 and 3.4 the density/altitude correlation is

$$\sigma = \frac{\left(1 - \frac{\lambda}{T_o}h\right)^{g/\lambda\mathcal{R}}}{1 - \frac{\lambda}{T_o}h} \tag{3.10}$$

The variation of the relative density with altitude up to 10 km is illustrated in Fig 3.4. Equations 3.9 and 3.10 are approximation functions and can relate any measured values with the reference values.

The thrust and power coefficients of a rotor are given by the equations:

$$C_T = \frac{T}{\frac{1}{2}\rho\Omega R^2 A} \tag{3.11}$$

$$C_P = \frac{P}{\frac{1}{2}\rho\Omega R^3 A} \tag{3.12}$$

The density in Eq 3.11 can be written as $\rho = \rho_o\sigma$ in order for its variation due to altitude (at ISA conditions) to be taken into account. The ISA conditions for the various atmospheric parameters such as pressure and temperature are useful in terms of performance comparison at different altitudes. However,

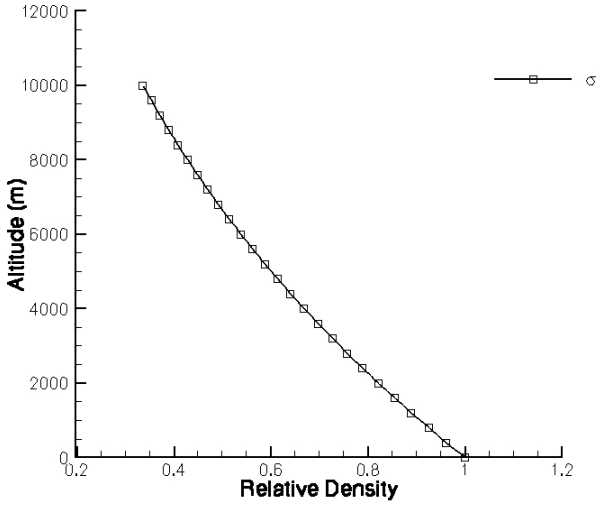

Figure 3.4: Variation of relative density with altitude, ISA conditions

when the temperature will deviate from the reference ISA value e.g a "hot" day with an ISA deviation of +10 these conditions are characterized as non-ISA. Hence, a temperature offset is present which can represented as:

$$T' = T_o + \Delta T \tag{3.13}$$

where ΔT is the ISA deviation. By using a similar analysis as above due to the fact that lapse rate of temperature remains the same as well as the pressure variation with altitude (pressure altitude and not geometric altitude), the relative density can be written as:

$$\sigma = \frac{\left(1 - \frac{\lambda}{T_o} h\right)^{g/\lambda\mathcal{R}}}{\left(1 - \frac{\lambda}{T_o} h + \frac{\Delta T}{T_0}\right)} \tag{3.14}$$

The variation of density with respect to the altitude, at non-ISA conditions, is shown in Fig 3.5

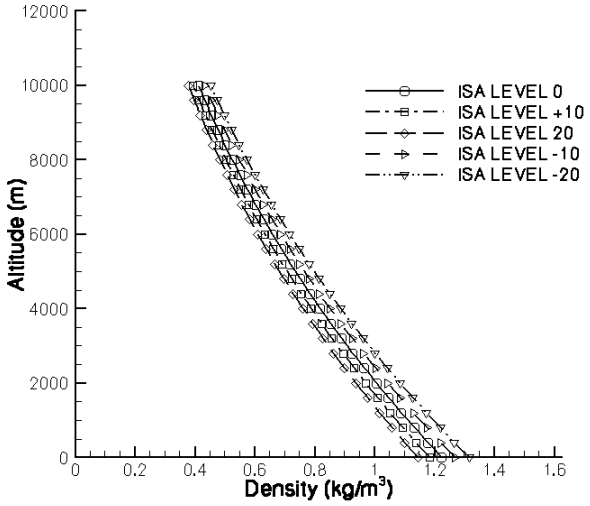

Figure 3.5: Variation of density with altitude, non-ISA conditions

3.1.2 Assumption Regarding Reynolds and Mach Number Effects

The discussion above stressed on the importance of the assumption regarding the independency of the power and thrust coefficients on the Reynolds number. This assumption discards the necessity of performing simulations at different altitudes or at different non-ISA conditions which means that only one reference calculation (at ISA 0 ft altitude) needs to be performed. The rotational speed of a helicopter remains approximately constant during its flight and changes in the Reynolds number due to varying ambient conditions can be assumed as low.

As far as the Mach number effects are concerned and particularly compressibility effects, no corrections are applied to the power and thrust coefficients due to the fact that the ideal gas law will be used in the CFD simulations.

However, there is a slight change of the sound speed with altitude which will subsequently have an effect on the Mach number itself. According to the European Helicopter Operators Committee (EHOC) , a Search And Rescue (SAR) helicopter will typically fly at an altitude of 3,000 ft at normal cruising conditions.

In hover and high speed forward flight, compressibility effects (i.e. the variation of density) will be present mainly over the rotor, where at the blade tip the speed is about 200 m/s. By allocating the blade tip speed value (211 m/s for AS365 N3 Eurocopter Dauphin [44]) as the freestream velocity value in the Mach number definition and considering ISA conditions, the expected variations due to altitude and ISA deviations are shown in Tables 3.1 and 3.2 respectively. By inspecting Tables 3.1 and 3.2 it can be shown for all the possible combinations such as fixed ISA deviation and varying altitude or fixed ISA deviation, the absolute value of the greatest difference is less than 4%.

/	ISA 0	ISA +20	ISA -20
M_∞ 0 ft	0.6200	0.5996	0.6427
M_∞ 3000 ft	0.6265	0.6054	0.65
% Change	1.05	0.97	1.13

Table 3.1: Mach number percentage differences with respect to different altitudes

/	Altitude 0 ft	Altitude 3000 ft
ISA 0	0.6200	0.6265
ISA +20	0.5996	0.6054
ISA -20	0.6427	0.6500
% Change $ISA_{0,+20}$	-3.29	-3.36
% Change $ISA_{0,-20}$	3.66	3.75

Table 3.2: Mach number percentage differences with respect to different ISA deviations

Thus, it can be assumed that varied altitude and/or ISA deviations ($-20 \leq ISA_{dev} \leq 20$) do not have a gross effect on the Mach number. It must be also noted that compressibility effects are more important at high subsonic-transonic or supersonic flows and mainly when shock waves are present. In the operating flight envelope of a ducted helicopter tail rotor, shock waves can not appear due to the shielding effect of the shroud. To be more specific, even at high forward flight speed e.g 140 knots the flow will be presented almost axially[2] to the rotor (parallel to the rotor axis), whereas in the case of a conventional rotor the flow is presented perpendicularly. Thus, shock wave formation in a ducted helicopter tail rotor is almost impossible to be achieved, unless the RPM will rise significantly enough in order to allow transonic blade tip speeds. Another argument in support of the assumption that has been made, with regards to the independency of the thrust and power coefficients to the Reynolds and Mach number effects, at a specific range of altitudes (0-10,000 ft), is the shrouding effect of the rotor. The shrouded rotor even in high blade collectives (35°-45°) does not experience any stall [16] in contrast to the open rotor. This is due to the greater induced velocity (greater induced angle of attack ϕ , see Fig 3.6), in the case of ducted rotor, and are partly caused due to the acceleration of the flow over the inlet lip of the shroud. Thus, greater induced velocities imply that the rotor is operating at a smaller effective angle of attack α which subsequently prevents aerodynamic stall at high blade collectives (at those collectives where an open rotor would have stalled). In addition, it is a well known fact which has also been observed in numerous experiments [19] that the lift slope ($\frac{dC_l}{d\alpha}$) of an airfoil will be independent to Reynolds number variations at the linear portion of the polar curve.

[2]Pure axial flow is only present in hover and at sideward flow such as gusts of wind either from the right (starboard) or left side (port) of the ducted tail rotor configuration.

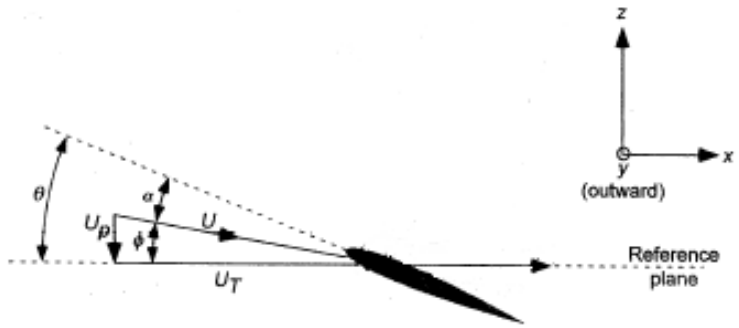

Figure 3.6: Effective aerodynamic angle of attack $\alpha = \theta - \phi$ where θ is the blade pitch angle. U is the local relative wind and U_P and U_T are the induced and tangential (rotational) velocity of the rotor respectively.

This is due to the fact that the flow over the airfoil (or wing) will be attached to the body and it will not be separated at relatively small angles of attack. As the angle of attack increases, the lift coefficient reaches its $C_{l\,(max)}$ value. Then, the flow will separate and the airfoil will be stalled and owing to the fact that flow separation is dependent on the viscosity of the fluid, it will be subject to the variations of the Reynolds number of the flow. By inspecting Fig 3.7, which shows the lift coefficient polar curve of a NACA 0012[3], it can be seen that at the linear portion of the curve the lift slope is the same for all three different Reynolds numbers. However, at the portion of the curve where the airfoil has stalled it can be seen that there is a small difference at the lift coefficients. To be more specific, a decrease in the Reynolds number will cause a decrease in the maximum ($C_{l\,(max)}$) and post stall lift coefficient values. These three values of Reynolds number reflect three different operational altitudes, as shown in Table 3.3, and clearly illustrate that the effect of altitude (at the specified range) on the $C_{l\,(max)}$ can be considered negligible.

[3]For the generation of the plot in Fig 3.7, Javafoil has been used. Javafoil uses a panel method in order to derive aerodynamic data such lift, drag and moment coefficients for a given airfoil profile.

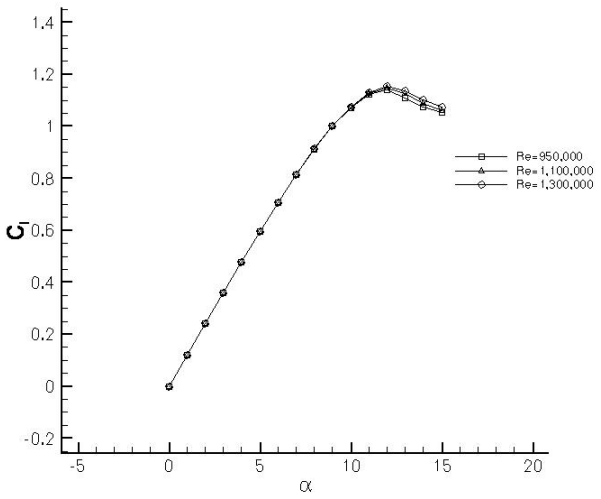

Figure 3.7: NACA 0012 $C_l - \alpha$ polar curve at three different Reynolds number

Re	950,000 (~10,000 ft)	1,100,000 (~5,500 ft)	1,300,000 (~0 ft)
$C_{l\,(max)}$	1.139	1.147	1.156

Table 3.3: $C_{l\,(max)}$ variations with respect to different Reynolds number at ISA conditions. NACA 0012 at $\alpha = 12°$

The percentage reduction in $C_{l\,(max)}$ between 0 ft and 10,000 ft is of the order of - 1.5%. The three different Reynolds number were computed by assuming a blade tip speed of 211 m/s and a characteristic length scale of 0.094 m (the airfoil chord) which were both held fixed. The variations in the computed Reynolds numbers are only due to the ambient conditions namely the different density at different altitudes[4]. Drag and moment coefficients also bear similarity to the lift coefficient's variation with respect to the Reynolds and Mach number [19].

Finally, the key arguments in support of this assumption regarding Reynolds and Mach number effects, at the specified altitude range (0-10,000 ft), are the following:

[4]Dynamic viscosity variation can be considered negligible in this range of altitudes

1. Lift coefficients and subsequently thrust coefficients are constant and independent of Reynolds number effects at the linear portion of the polar curve i.e. at small angles of attack

2. At high angles of attack, $C_{l\,(max)}$ variation due to Reynolds number variations can be considered negligible at an altitude range of 0-10,000 ft

3. Reynolds number variation is only due to different ambient conditions only (RPM of the rotor is held fixed)

4. Mach number effects, i.e. the increase of C_l with M_∞ , are only due to different ambient conditions only (RPM of the rotor is held fixed). Compressibility effects (density changes) are taken into account by the CFD solver by using the ideal gas law

5. Shrouded rotors in comparison to open rotors display a delay in stall due to the higher induced velocities on the rotor

It must be acknowledged that the aforementioned assumptions are applied only for the sake of saving computation time. Thus, for the purposes of the current work, which has the main aim to present this new methodology, rather than offering extremely accurate results, these assumptions can be considred valid. In order to derive, more accurate results more simulation points would be needed. It must be noted that all aerodynamic coefficients are dependent on Reynolds and Mach numbers. However, as it was shown in the previous discussion, at the specified altitude range (0-10,000ft) and ISA deviation range (-20 to +20) these variations are small and will not have a significant effect on the results. In addition, due to the fact that a typical operational flight altitude of a helicopter is about 3,000-5,000 ft [45], the discrepancies in the results will be even smaller.

3.2 Generic Ducted Tail Rotor Model

The previous section elaborated on the main simplifying assumptions with regard to the derivation of the performance maps and the dependency of the main coefficients to altitude and non-ISA conditions effects. This section will cover the specific details with regards to the structure of the ducted tail rotor subsystem and the performance maps. The outputs of the CFD model will be presented as well as the method of translating this information to the in-house rotorcraft comprehensive code.

3.2.1 Ducted Tail Rotor Subsystem

It is common in rotorcraft aerodynamics, for the purposes of performance prediction, to model the components of a rotorcraft configuration i.e. the main rotor, fuselage, empennage and the tail rotor, as isolated components. Thus, by evaluating the performance of each sub-component the overall behavior of the helicopter can be estimated. However, the flow-field of a rotorcarft will give rise to strong aerodynamic interactions such as the main rotor's wake interaction with the airframe (fuselage and empennage) and the tail rotor. These interactions will influence the performance of these components and in certain circumstances, their effect can be detrimental to the overall performance of the helicopter [2].

In the present work, the isolated ducted tail rotor will only be considered without the interactions of the fuselage, empennage and the main rotor. A detailed 3D numerical simulation of the complete helicopter configuration requires enormous computational resources, in order to have an adequate fidelity in the predictions. In addition, due to the fact that the flow regime over a helicopter is considered vortex-dominated, the turbulence of the rotor wake and

subsequently its modelling is extremely difficult. Turbulence modelling in helicopter aerodynamics presents a challenge even to the most advanced CFD tools which are available today [2]. Interaction phenomena over a helicopter is a topic of continuous research especially with regards to the construction of numerical methods (high-order methods) which would demonstrate less numerical dissipation[5]. Nonetheless, in the case of a ducted tail rotor these interactions and particularly the interaction caused by the main rotor wake does not influence the performance of the ducted tail rotor, in such a high degree as in the case of the conventional open rotor, due to the shielding effect of the shroud [4, 5]. Therefore, on the grounds of saving computational time, simplicity of the analysis as well as due to the characteristic flowfield over a ducted tail rotor, the modelling of aerodynamic interactions can be discarded. However, due to the fact that the fin will also be part of the CFD model the fin/ducted tail rotor blockage effect will be included as part of the analysis. As it was discussed before the sole operation of the tail rotor in every helicopter is to provide the required antitorque force as imposed by the main rotor as well as providing authority in the yaw axis. The tail rotor thrust required by the main rotor will be:

$$T_T = \frac{Q}{x_T} \tag{3.15}$$

where Q is the main rotor's torque and x_T is the distance of the main rotor shaft to the tail rotor shaft. This expression does not imply any off-loading caused by the shroud and/or the fin. The power required by the tail rotor will typically vary between 3 and 5% [2]. However, in certain extreme circumstances of the flight envelope, such as the autorotation or strong sidewinds and due to

[5]The main problem lies in the fact that current low order numerical methods (2nd or even 3rd order) will dissipate the vortex e.g. when modelling the Blade Vortex Interaction (BVI) which proves them inadequate to accurately model such strong interaction phenomena.

interference effects the tail rotor power consumption could be as much as 30% of the main rotor power [3]. The tail rotor power is given by the expression:

$$P = Q_T \Omega_T \tag{3.16}$$

where Q_T is the tail rotor torque and Ω_T is the angular velocity of the tail rotor. It is common in rotorcraft aerodynamics to refer the tail rotor forces and moments to the aircraft center of gravity. A typical tail rotor subsystem (for an open rotor) is illustrated in Fig 3.8. An assumption that can be made, due to the fact that the thrust of a tail rotor is relatively small with comparison to the main rotor thrust (approximately 2220 and 4440 N for a Lynx class helicopter [3]), is that the X and Z components of the force[6] (as referred to the rotorcraft's center of gravity x_{cg}) are relatively small and can be ignored [3]. For a conventional open tail rotor the tail rotor forces and moments, according to Padfield [3], are approximately given by the expressions

$$X_T \approx T_T \beta_{1c_T} \tag{3.17}$$

$$Y_T = T_T \tag{3.18}$$

$$Z_T \approx -T_T \beta_{1s_T} \tag{3.19}$$

$$L_T \approx h_T Y_T \tag{3.20}$$

[6]The forces and moments which are act on an aerodynamic body are generally listed with the following coordinates for forces (X, Y, Z) and for moments (L, M, N) (see Fig 3.9).

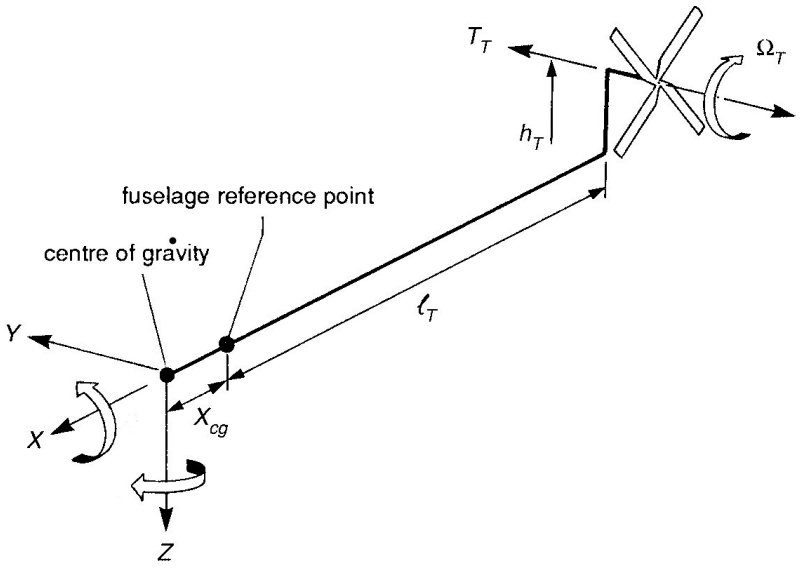

Figure 3.8: Tail rotor subsystem [3]

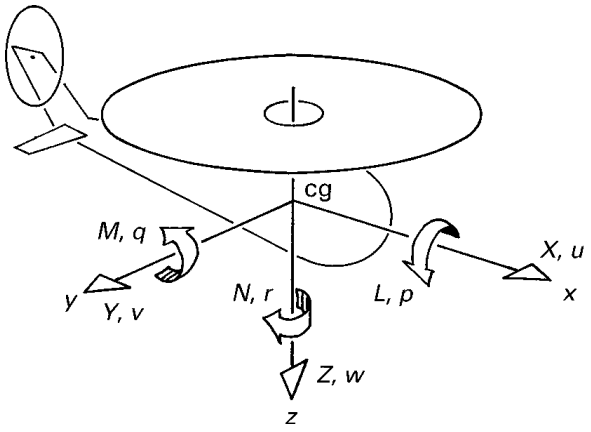

Figure 3.9: Orthogonal axes system for helicopter flight dynamics

$$M_T \approx (l_T + x_{cg})Z_T - Q_T \tag{3.21}$$

$$N_T = -(l_T + x_{cg})Y_T \tag{3.22}$$

where β_{1c_T} is the cyclic flapping angle, β_{1s_T} is the lateral flapping angle[7], h_T is the height of the tail rotor hub above the fuselage reference point and l_T is the distance between the tail rotor hub and the fuselage reference point (as depicted in Fig 3.8). It is common to assign the location of the main rotor's shaft (the axes's origin as depicted in Fig 3.9), as the location of the x_{cg} of a rotorcraft configuration. Therefore, the sum $l_T + x_{cg}$ will be considered as the distance (moment arm) of the main rotor shaft to the tail rotor shaft ($l_T + x_{cg} \equiv x_T$). In the case of the ducted tail rotor the blades are rigid hence the flapping angles are zero. Thus, equations 3.17 and 3.19 can be discarded for the present analysis[8].

3.2.2 Performance Maps Subroutine

For the purposes of reading the main rotor's antitorque requirements and utilizing the CFD derived ducted tail rotor performance maps, a small program has been in written in FORTRAN. The main steps of this program are the following:

- Identification of the flight regime which can be hover or forward flight. This is specified by the given advance ratio μ. For hover $\mu = 0$ and for forward flight $\mu > 0$

[7]Both these angles are zero in the case of a ducted tail rotor due to the fact that the blades are not allowed to flap

[8]By neglecting the X and Z components of the applied forces on the tail rotor and that the blades are rigid, the equations describing the forces and moments referred to the helicopter's center of gravity will be: $Y_T = T_T$, $L_T \approx h_T Y_T$, $M_T \approx -Q_T$, $N_T = -(x_T)Y_T$

- The altitude of the rotorcraft configuration as well as the thrust required from the main rotor are given as inputs to the program. Then the required[9] thrust coefficient C_{Treq} will be computed by using equation 3.11 and replacing T with the required thrust T_{req}. In addition, the altitude and possible ISA deviations will be taken into account by correcting the density in the thrust equation by using $\rho = \rho_o \sigma$.

- For the hover case, as soon as the required thrust coefficient is defined and corrected for the given altitude and ISA deviation, a table look-up process will be launched which will search the required C_{Treq} and the power coefficient C_P for the given required thrust. Quadratic interpolation is used in order to search the required C_{Treq} value between increments of the blade collective angle θ_0.

- For the forward flight case, the forward flight velocity of the helicopter is given as an input and the above step is performed at the specified forward flight velocity (advance ratio).

- The final output of the program is the power coefficient for the given C_{Treq} at the specified flight and ambient conditions.

Thus, by using equations 3.18 and 3.20-3.22 the required forces and moments as referred to the rotorcraft center of gravity can be computed. However, it must be noted that this final step will not have an effect on the performance maps derivation.

[9]The subscript "req" denotes the required thrust

3.3 Generic Ducted Tail Rotor Geometry

In order for this analysis to be as realistic as possible, a real helicopter configuration has been used in order to design the generic ducted tail rotor geometry. The Eurocopter AS365 N3 Dauphin, as depicted in Fig 3.10, has been used as a reference configuration in order to construct the generic ducted tail rotor CFD model. The term *generic* is used due to the fact that it is impossible to know all the exact rotor/shroud information especially with regards to the shroud profile thickness distribution.

However, the selection of important geometric parameters such as the shroud inlet lip radius, the radius of the rotor blades, airfoil profiles, and the diffuser angle has been based on existing public information (as presented in the literature review). This rotorcraft configuration has been chosed on the grounds that information about the blade tip speed as well as airfoil profiles is publicly available [45]. This helicopter is considered as a medium size/class helicopter (similar to the Lynx class) with a Maximum Take Off Weight (MTOW) of 4,300 kg and the expected antitorque thrust (in hover) can be around 4000-4500 N.

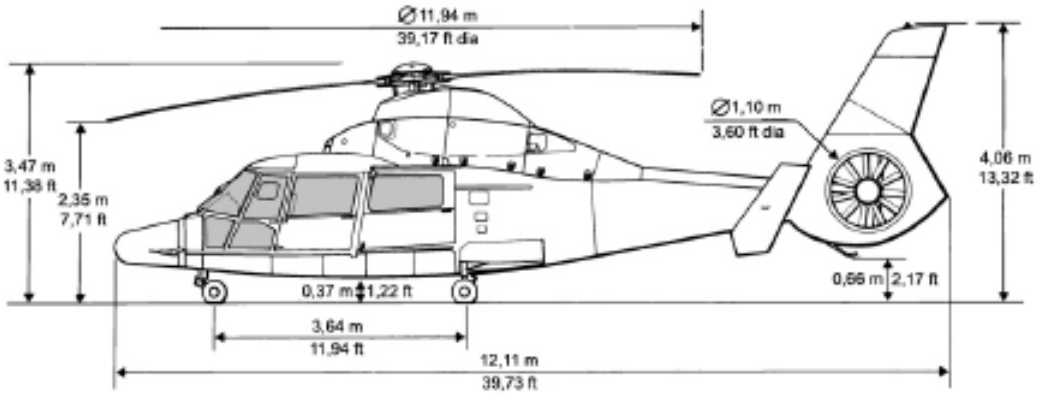

Figure 3.10: Eurocopter Dauphin AS365 N3 specs [44]

3.3.1 Shroud Design

3.3.1.1 Inlet Lip Radius

As it has been described earlier in the literature review, the ducted tail rotor configuration performance is dictated by a subset of geometric parameters. The inlet lip radius was chosen to be 10% of the rotor diameter (0.2R, where R is the rotor radius). This considerably high inlet lip radius can offer better hover performance and provide a more uniform flow distribution and will not encourage flow separation. This value of 10% has been also selected, after a survey of experimental data, in the S-67 ducted tail rotor [22] for the same reasons as explained above.

3.3.1.2 Diffuser Length

The diffuser length that was deployed in the design was 35% of the rotor diameter in order for the configuration to demonstrate an acceptable efficiency in hover [21]. Ducted tail rotor configurations with longer diffuser will exhibit better efficiency at the same C_P and this is due to the fact that shroud thrust will tend to increase with diffuser length [21]. However, a longer diffuser length will increase the weight and the profile drag of the configuration. This value has been also used in the KAMOV-60 ducted tail rotor configuration [25, 38].

3.3.1.3 Diffuser Angle & Expansion Ratio

As far as the diffuser angle is concerned, a value of 8° was selected and it was the same value as the one used in KAMOV-60 [25, 38] and Aerospatiale Fenestron helicopters. It was shown before that by increasing the diffuser angle the shroud thrust increases up to a point where the flow will separate from the diffuser trailing edge. Thus, this value has been chosen on the grounds of

avoiding premature flow separation from the diffuser wall which will degrade the performance of the configuration.

Finally, the resulted expansion ratio of the deployed geometry is 1.12 which is a typical value for helicopter ducted tail rotor configurations.

θ_d	r_{lip}	L_d	σ_d
8°	0.2R	0.7R	1.12

Table 3.4: Deployed shroud parameters

Although higher expansion ratios will improve the static performance, the actual width of the shroud is also dependent on weight considerations hence this value can be considered adequate. The geometric parameters of the shroud are tabulated in Table 3.4.

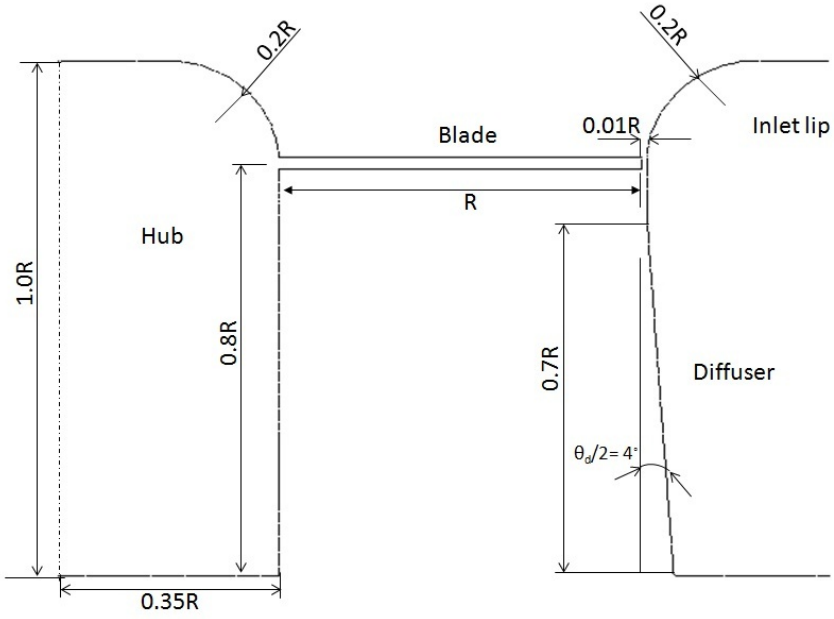

Figure 3.11: Cross-section of the shroud and hub at mid azimuth of the generic ducted tail rotor

3.3.2 Rotor Design

3.3.2.1 Rotor Main Characteristics

The rotor was designed as realistically as possible by using information and data which are publicly available. The deployed rotor diameter is 1.1m which gives a blade radius of 0.55m. It must be mentioned here that the actual value of radius includes the blade root cut-out section hence the origin location is the center of the hub (or the center of the rotation axis). This is a common assumption in helicopter ducted tail rotor configurations, however the actual effective blade portion will be less than R. The selected blade root cut-section was 35% R, this value is a typical length of helicopter ducted tail rotor configurations [25, 38]. In addition, the length of the blade tip clearance was chosen as 1%R which is also a typical value for such configurations [38].

3.3.2.2 Airfoil Profiles

The airfoil profile that was used in order to represent the rotor is the OAF 128 (see Fig 3.12) which has been used widely in Aerospatiale Fenestron helicopters [5]. As it was shown before, there is a spanwise variation of the airfoil profile in order to increase the blade loading (especially towards the tip). However, this information concerning the specific airfoil profile variations at the spanwise locations is not available. Thus, for the sake of simplicity a constant (spanwise) airfoil profile was used. The family of OAF profiles has been widely used in ducted tail rotor configurations (Aerospatiale Dauphin) and can provide optimum performance over a vast range of operating conditions [46]. The last three digits of the OAF profile indicate the maximum thickness which is 12.8% (at 23.2% chord). The maximum camber is 2% and lies at the 46.9% chord location.

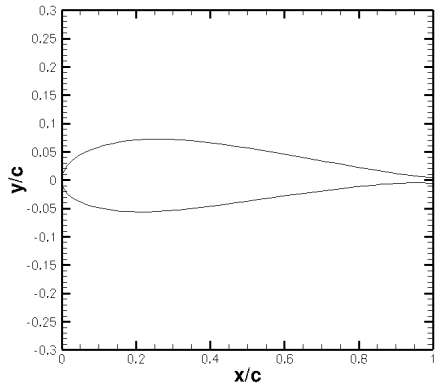

Figure 3.12: OAF 128 Airfoil Profile

The blade planform that was used was without any taper in order to avoid performance degradation (effective reduction of the blade loading coefficient) as described in the literature review section. As far as the blade spacing is concerned, a uniform spacing has been chosen. Although an uneven blade spacing is implemented in modern helicopter ducted tail rotor configurations, for noise propagation and reduction reasons, the overall performance of the configuration (in terms of thrust and power) does not change significantly [8, 43]. Thus, a uniform blade spacing was used for simplicity of the geometry generation.

3.3.2.3 Blade Twist

The blade twist of the rotor was linearly varied from the root to the tip and the value of 10° was selected (as applied also to the Eurocopter AS365 N3 Dauphin [44]). This variation means that e.g if the blade pitch angle is $\theta_{0.75R}$ then the pitch angle at the blade tip will be $\theta_{0.75R} - 10°$. A blade twist is necessary in order to keep an as uniform flow distribution as possible over the rotor.

3.3.2.4 Rotor Solidity

The deployed rotor solidity has been selected according to available technical data of the Eurocopter AS365N3 Dauphin [44] which report a chord length of 0.094m and a total blade number of 10. Thus, by using equation 2.11 the solidity of the rotor, according to the given information regarding the blades, is 0.544 which lies in the range of typical values for a ducted helicopter tail rotor (0.5-0.6) [45].

3.3.2.5 Rotor RPM and Direction of Rotation

The blade tip speed of this ducted tail rotor configuration is 211 m/s ($M_\infty = 0.62$) which gives a fan rotational speed of 3,663 RPM. The rotation direction of the tail rotor is top-aft which is the preferred direction for the tail rotor in order to minimize any adverse interaction with the main rotor wake [47].

According to Johnson [47] , this is due to the fact that the effectiveness of the tail rotor reduces if it rotates in the same direction as the swirl in the flow-field. The top-aft rotation is also preferred for noise reduction purposes as well [47]. All the rotor design and operation parameters are summarized in Table 3.5

Parameter	Value	Parameter	Value
Rotor diameter D	1.1 m	Blade Twist	$-10°$
Blade chord c	0.094 m	Root cut-out	0.35%R
Number of Blades N_b	10	Fan Rotation Direction	top aft
Rotor Solidity σ	0.544	Tail rotor moment arm x_T	9 m
Rotor rotational speed	3,663 RPM	Airfoil section	OAF218

Table 3.5: Rotor Design & Operation Parameters

3.3.3 Fin & Tailboom Design

The fin and the tailboom's design is part of the empennage design. In this analysis the horizontal stabilizers are excluded in order to save computational time. In a CFD model the detailed representation of the viscous horizontal stabilizer wall would create a need for a larger grid hence computational resources. However, the horizontal stabilizer does not have a profound effect on the local aerodynamic performance of the ducted tail rotor. The tailboom is only included in order to help the flow to actually reach the inlet of the fan as smoothly as possible. The length of the tailboom was chosen to be 2 metres. If the tailboom was not included and there was only the shroud/fin and the rotor then the body would have behaved as a bluff body. The fin structure is actually a wing which has a certain incidence with respect to the rotorcraft's geometric centerline, as depicted in Fig 3.13, in order to provide the necessary antitorque thrust during forward flight and off-load the rotor.

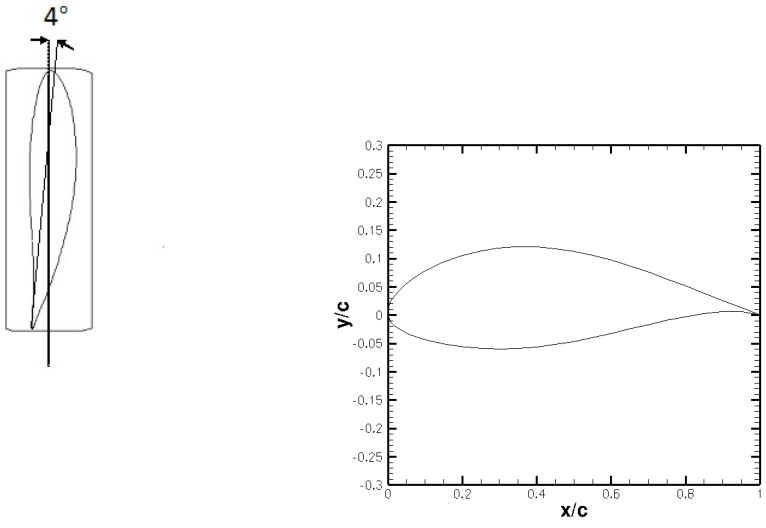

(a) Fin incident with respect to the rotorcraft's centerline

(b) NACA 63(3)618 airfoil profile

Figure 3.13: Fin geometric design

The range of incidence angles which is typically deployed is about $4° \sim 6°$ [46][7], the value of $4°$ has been chosen for this generic ducted tail rotor configuration. The airfoil profile of the fin is the NACA 63(3)618 (see Fig 3.13) which has a maximum thickness of 18% at 34.7% chord location. This airfoil is cambered at 3.3% at 50% chord location in order to increase the maximum lift coefficient of the fin. Camber helps the fin to unload the ducted tail rotor and high-speed cruise.

The exact details of the span of the fin as well as its aspect ratio are not available, thus the length of the span and the chord at the root have been approximated by using the specs (see Fig 3.10) as included in the technical data of the Eurocopter AS365N3 Dauphin [44]. Thus, the span of the fin[10] b is 1.6 m and the chord at the root of the fin c_r is 1.386 m and by using a taper ratio[11] of 0.6 the chord at the tip c_t is 0.832. The sweep back angle, as measured at the leading edge of the fin with respect to the Z axis is $32°$, and this value is typical for helicopter tail fins [48]. The design variables of the deployed fin are summarized in Table 3.6 below.

Paramenter	Value
Area S	1.774 m^2
Span b	1.6 m
Root chord c_r	1.386 m
Tip chord c_t	0.832 m
Sweep angle Λ_{LE}	$32°$
Incidence	$4°$
Aspect Ratio AR	1.443
Airfoil	NACA 63(3)318

Table 3.6: Fin design parameters

[10] A typical range of fin (vertical stabilizers) span is in the range of 4-7 ft for small and medium weight helicopters [48]

[11] The recommended range of taper ratio values for conventional wings is 0.3-0.6 according to Raymer [49]

3.4 Validation Case, KAMOV Ka-60 in Hover

One of the main problems and strict requirements for every CFD simulation is the validation of the numerical simulation (usually) with well established experimental results. Validation is often referred as "*solving the right equations*" in the CFD literature [50] and its main aim is to show whether the numerical simulation bears any relation to the physical problem of interest. Strict validation of this generic geometry, as described in the previous sections, cannot be done due to the fact that detailed experimental results are not available. To be more specific, flight test results should be available which at least can provide the polar curves of the ducted tail rotor in hover and forward flight.

In addition, due to the fact that this study will also concentrate on the parametric performance of the rotor (e.g power coefficients versus the advance ratio), its validation with the exact geometry at the exact boundary conditions is impossible. However, an understanding about the physical behavior of the configuration can be derived by examining the trends of similar configurations[12].The only experimental results, to the best knowledge of the author, which are publicly available and provide sufficient information in order for a CFD simulation to be validated are the TsAGI [25] results for the KAMOV Ka-60. Therefore, a CFD simulation (with discrete blades) was performed in order to validate the proposed approach in a quantitative manner, at least in hover where results are available. For the forward flight cases the results were examined towards their relation to the expected physical behavior by examining the trends of the derived curves.

[12]The Fenestron EC 135 polar curve as depicted in Fig 2.22 although it clearly shows the trend of the curve and the values of the blade coefficient, it does not give any information with regards to the absolute value of the consumed power.

3.4.1 Experimental Setup and Geometry

The validation of the model in the present calculation has been done by using the results taken at TsAGI [25] for a ducted tail rotor which is installed on the Ka-60 helicopter. A full configuration of this medium sized helicopter can be seen in Fig 3.14, the rotor has 11 equally spaced blades with a rectangular planform shape (constant airfoil chord) and a linear twist of $-12°$ from root to tip where the negative angle means that if the blade angle at the root is e.g $40°$ the angle of the blade at the tip will be $28°$. The size of the blade tip clearance is 1% of the rotor radius. The geometrical characteristics of the rotor and the shroud are tabulated in Table 3.7.

In this simulation since the exact geometry of the shroud, like the azimuthally varying shroud radial thickness, is not given the same geometry as in [38] was used and can be seen in Fig 3.15. This shroud geometry is of a "doughnut" shape with a relevant low shroud length of 0.35D. The geometry of the current simulation was consisted of the rotor, the hub and the shroud only. The blade collective that was used is $40°$ (at 35% blade radius).

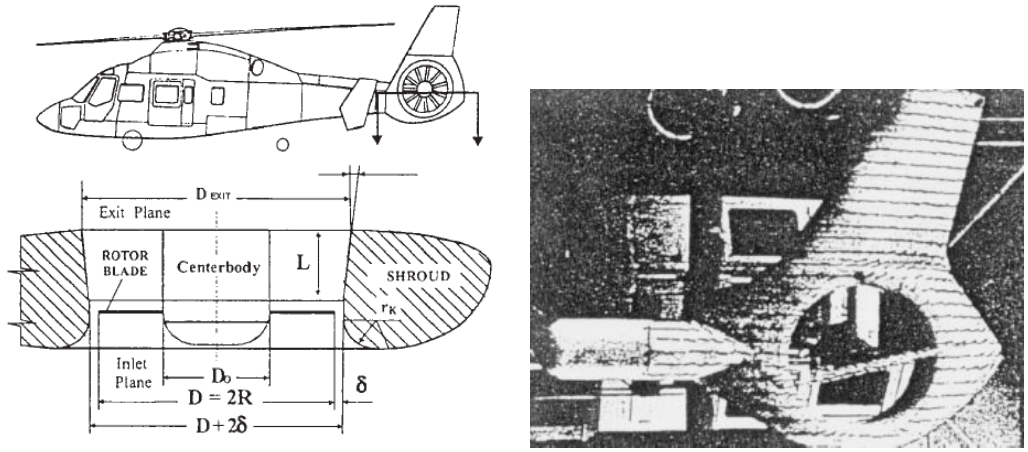

(a) Mid-azimuth section of the KAMOV Ka-60 (b) Complete configuration including a portion of the tailaboom

Figure 3.14: KAMOV Ka-60 helicopter and the shroud's cross section [25]

Parameters	Value
N_b	11
σ	0.4951
Twist angle	$-12°$
Blade tip speed	74.6 m/s ($M_{tip} = 0.22$)
Blade tip clearance	0.01R
r_{lip}	0.2R
L_d	0.7R
θ_d	8°
Blade root cut-out	0.35R
Airfoil	NACA23012

Table 3.7: Geometric dimensions of the KAMOV Ka-60 ducted tail rotor [25]

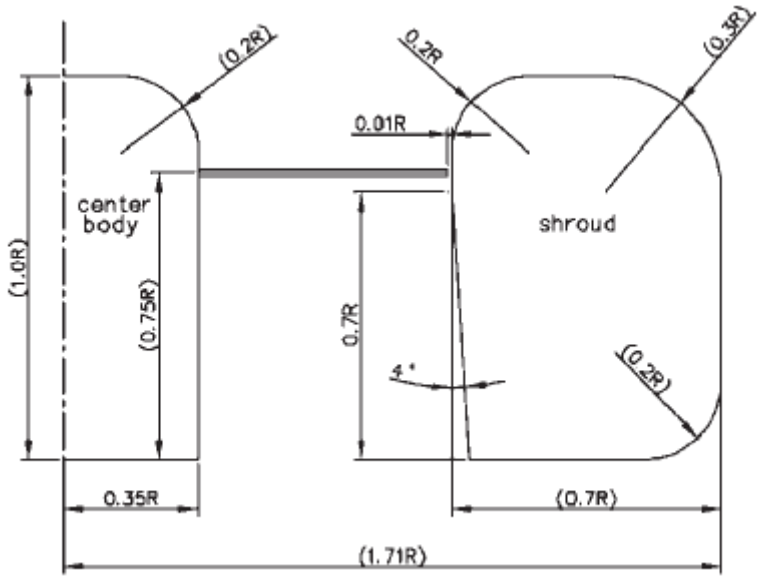

Figure 3.15: Simplified configuration of the shrouded rotor used in [38]

3.4.2 Grid Generation

The grid generation process is by all means the most laborous and time consuming part of every CFD simulation especially if it involves a complex geometry. A common difficulty which is always present when simulating complex geometries is that a single, continuous multi-block structured grid is not sufficient to represent the flow features. In addition, it is extremely difficult to obtain a single structured mesh which will be connected in a pointwise manner. This point to point connection which is required in structured grids will create extraneous cells at regions where high grid density is not necessary.

An example is that in hovering rotor CFD simulations, it is difficult to represent the blade surface mesh and off body features such as tip vortices and the region of the shroud and blade tip gap. Therefore, in such cases unstructured grids can be deployed in order to facilitate the construction of such complex geometries. However, for the purposes of validating this case a hybrid grid was deployed. A hybrid mesh/grid is a grid where the boundary layer resolution of a viscous wall is constructed by extruding structured hexahedral cells (or prismatic/polyhedral cells) and by using tetrahedral cells (unstructured) for these regions which are away from the boundary layer region.

This approach combines the benefits of a structured grid at the boundary layer which is required, in order to resolve the abrupt, normal to the wall velocity gradients and the versatility of an unstructured grid. Thus, in this geometry the surface mesh of the blades was consisted of structured quadrilateral cells whereas on the surface mesh of the shroud, diffuser and the hub, triangular cells will be used. The boundary layer of the blades was resolved by using hexahedral cells whereas at the other bodies (shroud, diffuser, inlet lip) polyhedral cells is used for the boundary layer resolution. The computational grids were made with the commercial software Pointwise.

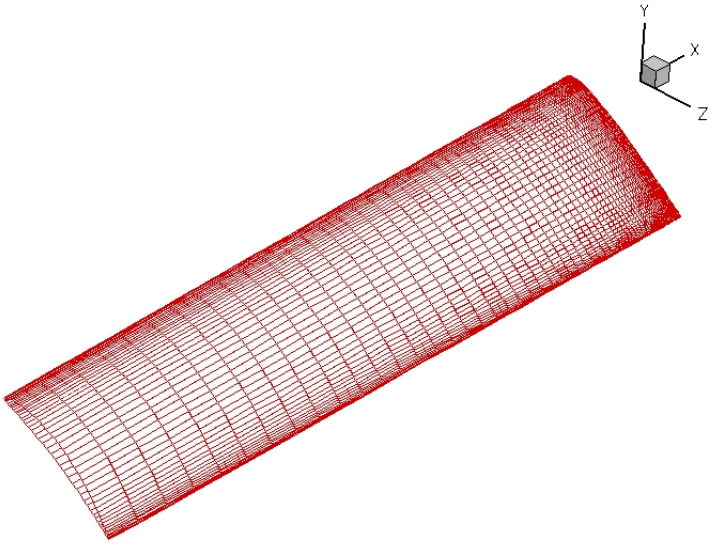

(a) Blade stacking

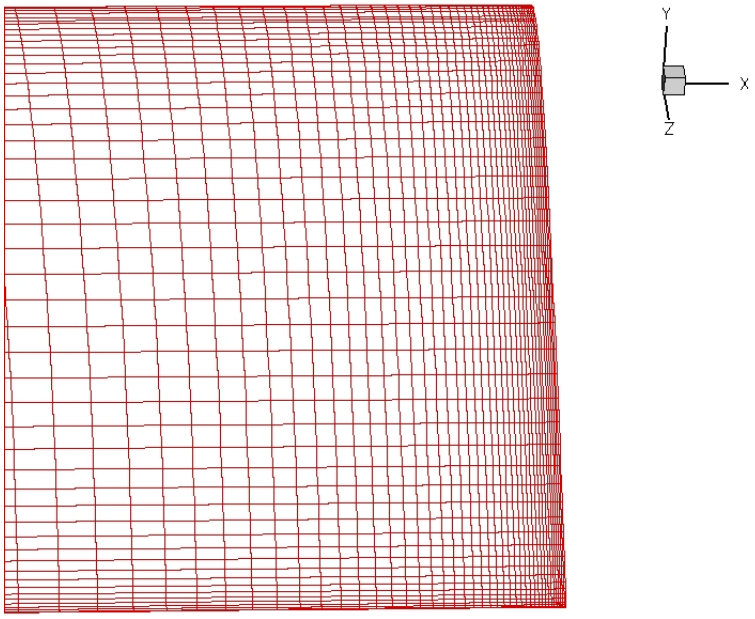

(b) Blade tip region

Figure 3.16: Blade surface mesh and stacking

The blade surface mesh is depicted in Fig 3.16 and this is the grid spacing that was used for the medium mesh, a detailed grid convergence study will be described later. By inspecting Fig 3.16 it can be observed that the stretching of the mesh is performed towards the blade tip. This is due to the fact that the blade loading itself increases towards the tip hence the grid cells must be clustered towards this area in order to yield an accurate distribution of the pressure and viscous forces which are acting on the blade. It must be noted that although grid cells can be clustered towards the hub as well, in this simulation the boundary layer of the hub is not resolved and the hub is considered as an inviscid wall. The justification of this boundary condition is that at the hub region there is not any significant thrust production and for the sake of computational time and resources as well as grid generation effort, the boundary layer is not resolved at this region. This approach/assumption has been also followed by other researchers as well [11]. Extreme caution has been taken in order to resolve the blade tip vortex, which requires the concentration of numerous cells towards the tip. Approximately 70% of the cells, at the spanwise direction, are clustered above the $r/R = 0.6$ location where r/R denotes the non-dimensional distance of the blade at the spanwise direction (at $r/R = 1$ is the location of the blade tip). The boundary layer mesh as depicted in Fig 3.17 has been created by hyperbolic extrusion with at least 30 inflation layers (for the medium mesh) in order to resolve the boundary layer and reach a y^+ value of 1 which is a requirement of the applied turbulence model ($k - \omega$ SST). The first cell's distance from the wall was of the order of 10^{-5}. The clustering has been towards the leading edge and the trailing edge in order to resolve the stagnation point and the wake of the blade respectively.[13]

[13]Actually by clustering towards the trailing edge the wake is not resolved but the grid stretching needs to be smooth in order to capture the separation of the flow from the trailing edge towards the wake region.

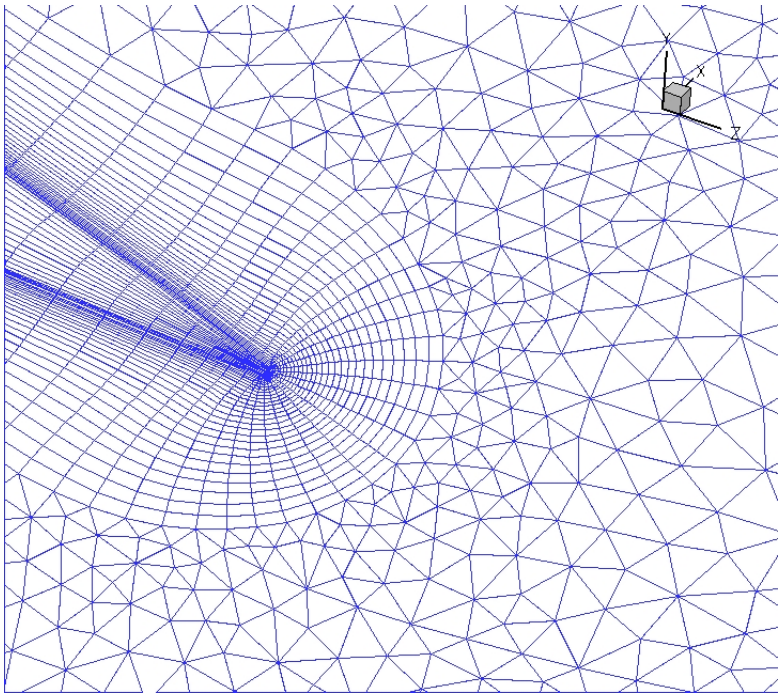

(a) Trailing edge mesh

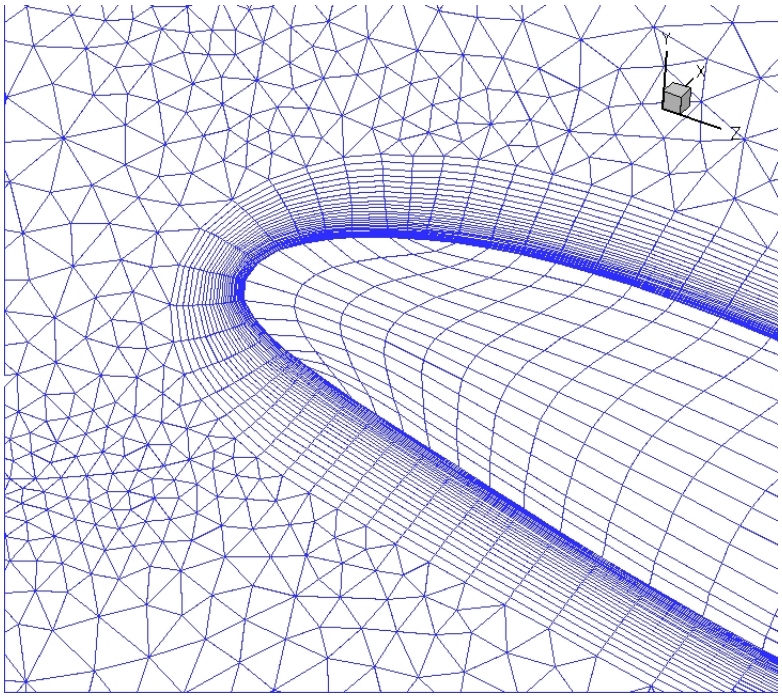

(b) Leading edge mesh

Figure 3.17: Boundary layer mesh of a single blade and its projection to the shroud wall (medium mesh)

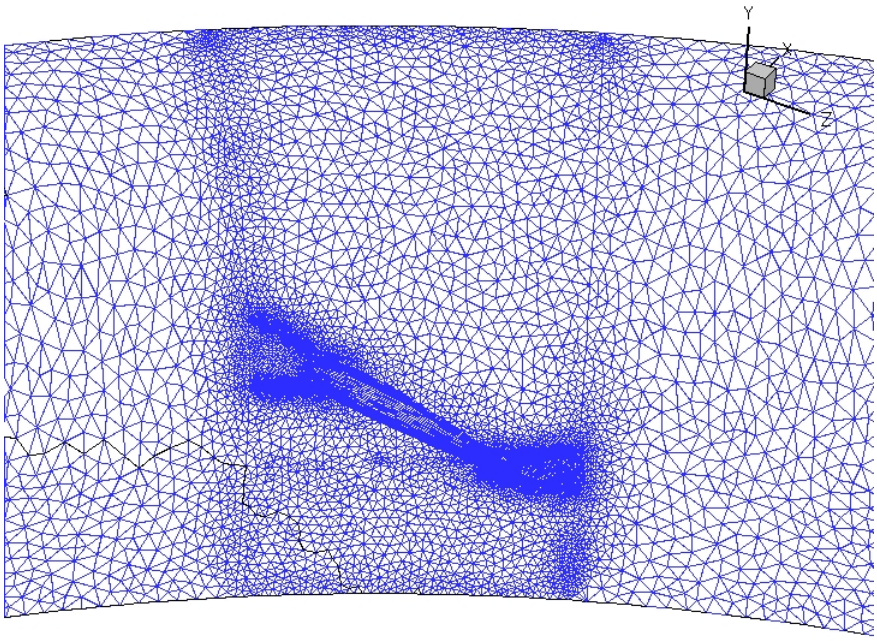

Figure 3.18: Duct inlet mesh and projection of the blade (medium mesh)

Fig 3.17 also shows that quadrilateral cells were used in order to define the geometry (the projection) of the airfoil. This is due to the fact that at the blade tip edge quadrilateral cells are used in order to construct a structured grid at the blade tip region. This denotes a significant drawback (high jump between the cells see Fig 3.17(b) of structured and hybrid grids for such specific applications. It must be mentioned that an alternative are the overset (Chimera) grids which do not display this problem [10]. However, the C_p distribution, on the shroud, at the inlet and blade region did not manifest any significant deviation from the expected trends (which will be discussed later). The duct inlet and blade tip region surface meshes, on the shroud, are shown in Fig 3.18.

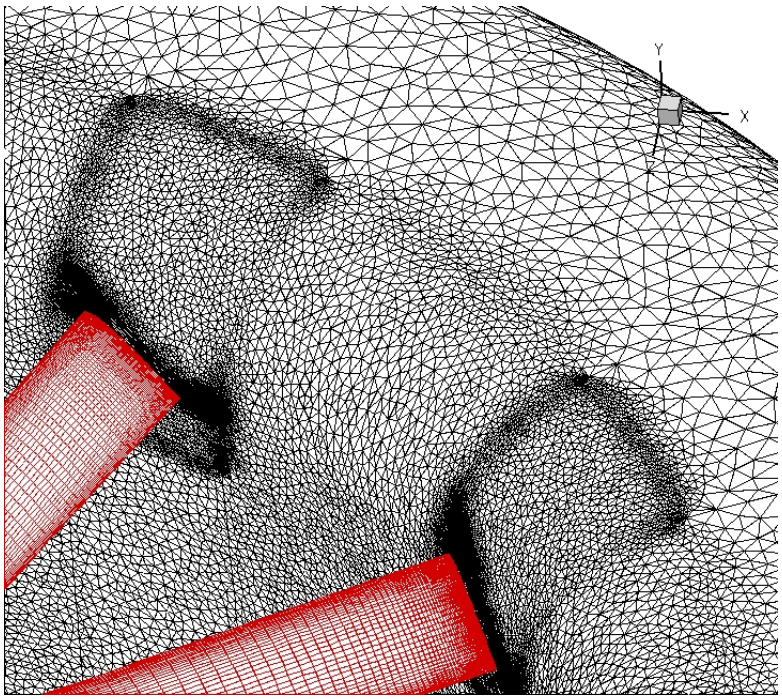

Figure 3.19: Shroud mesh (medium mesh)

It must be noted that the clustering of the cells has been performed mainly towards the blade region in order to capture the increase in pressure (from the inlet region, where suction forces are present, to the diffuser end where over-pressure forces are dominant). However, the grid is also clustered towards the inlet lip in order to better describe the curvature of the body as depicted in Fig 3.19. A 2D cross-section of the duct inlet and diffuser mesh is illustrated in Fig 3.20 where the boundary layer mesh and the propagation of the cells towards the inner region is clearly shown. This region is extremely important due to the fact that at this region, an accurate resolution of the boundary layer will provide an accurate prediction of the suction forces which develop over this surface. The boundary layer mesh of the shroud for the medium mesh was consisted of 20 inflation layers and the first cell's distance from the wall was of the order of 10^{-5}. In addition, the boundary layer mesh of the blades was consisted of 30 inflation layers and the same first cell distance was deployed.

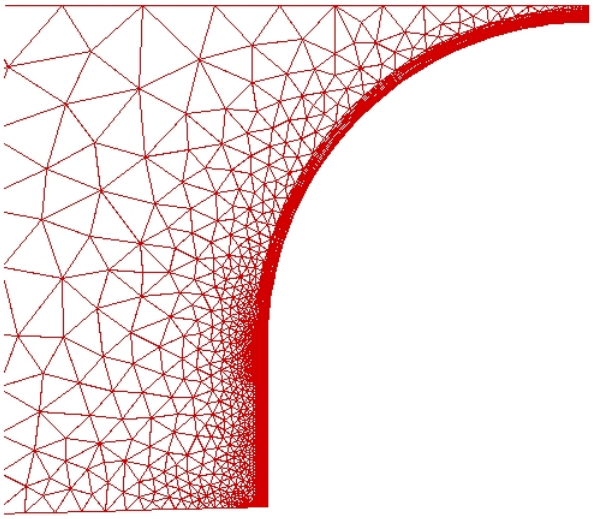

(a) Boundary layer and far-field mesh of the 2D section

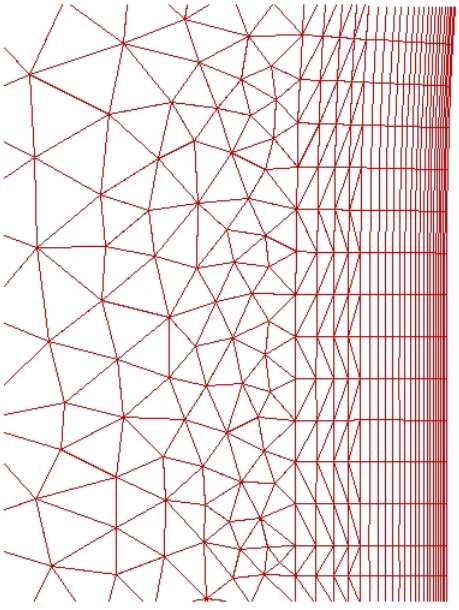

(b) Inflation layers of the boundary layer mesh

Figure 3.20: 2D section of the shroud mesh (inlet lip)

By inspecting Fig 3.20(b) it can be seen that the polyhedral cells of the boundary layer are isotropically extruded from the surface. Immediately after these cells, there are 4 layers of anisotropic cells which are diagonalized structured cells. This was done in order to have a better resolution and a smoother transition to the off boundary layer region. It is rather important to stress the fact, that due to the specific topology of the geometry, namely the very small distance between the blade tip and the shroud wall an assumption has been made with regards to the creation of the shroud boundary layer. The boundary layer of the shroud at the inlet lip and diffuser sections will not be subject to such high gradients as the boundary layer of the blades (due to the rotational velocity of the blades). Therefore, the first cell's distance is not required to be in the order of 10^{-5}. This conclusion can be verified by recalling the definition of the y^+ which is given by the expression:

$$y^+ = \frac{u_* y}{v} \tag{3.23}$$

where y is the distance to the nearest wall, v is the kinematic viscosity of the fluid and u_* is the friction velocity at the wall. u_* is given by the expression

$$u_* = \sqrt{\frac{\tau_w}{\rho}} \tag{3.24}$$

where τ_w is the wall shear stress. Thus, the boundary layer of the shroud does not need as much inflation layers as the blade and clearly the distance of the first cell from the wall can be larger (in order to reach a value of $y^+ = 1$). However, if it were not for the two boundary layers (blades and shroud wall) to be constructed with the same distance from the wall and the same cell growth rate, they would have overlapped each other.

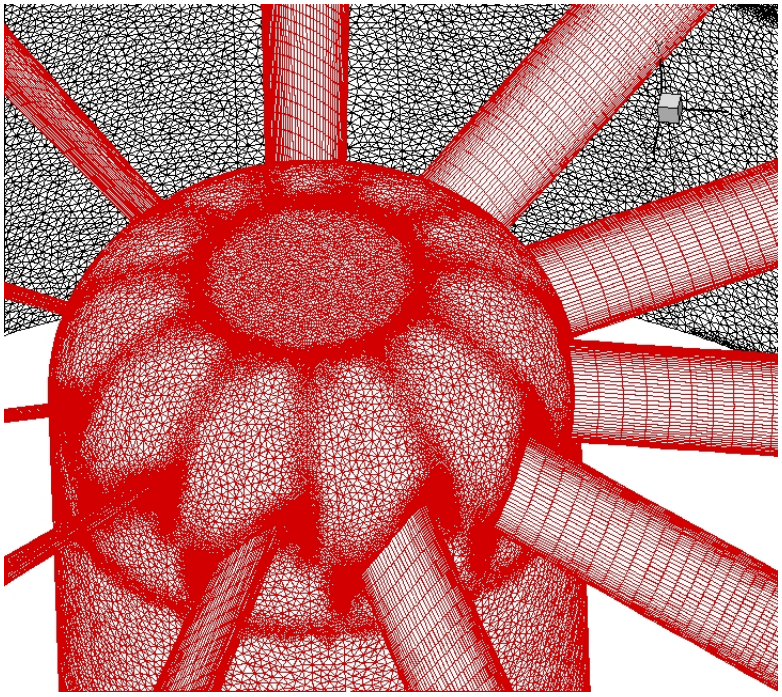

(a)

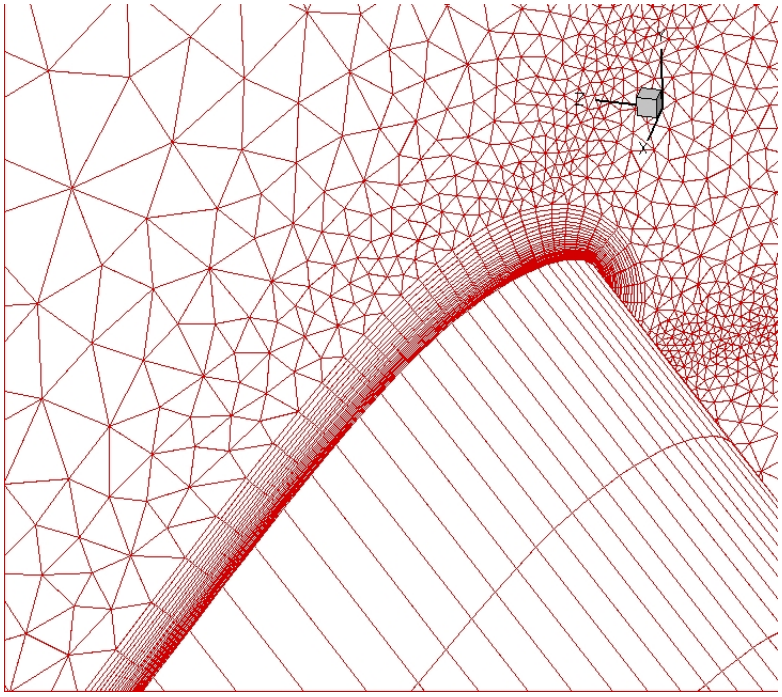

(b)

Figure 3.21: Hub mesh (medium mesh)

Clearly, a multi-block hybrid grid does not allow the individual grids to overlap between each other, hence both boundary layers have been created with the same growth rate and distance from the wall (first cell's distance). Fig 3.21 illustrates the surface mesh of the rotor hub along with its connection with the blades. In real helicopters the blade root connection does not have an aerodynamic surface. However, for the sake of simplicity in the grid generation process the blade root connection was designed by projecting the blade's airfoil profile to the hub surface. By inspecting Fig 3.21 it can be seen that there are fewer blade cells clustered towards the hub. This is due to the inviscid wall boundary condition which was applied for the hub wall. However, caution was taken whilst constructing the mesh in order to avoid highly skewed cells at this region. The complete geometry that was used in the numerical simulation is illustrated in Fig 3.22. It must be mentioned that the stators are not included in the current geometry on the grounds of saving computational time and resources as well as effort for the grid generation process.

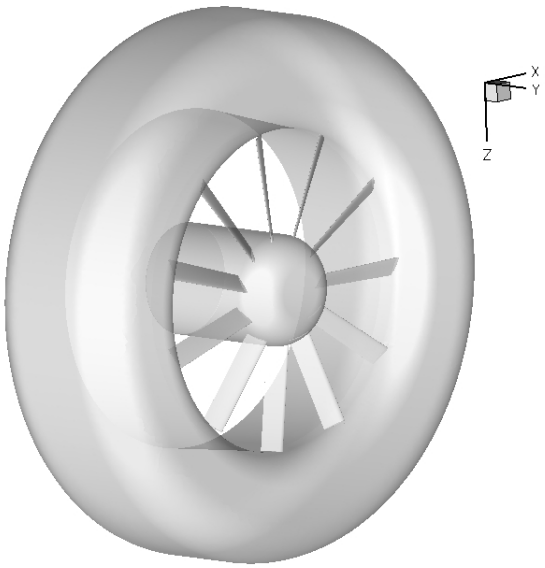

Figure 3.22: KAMOV Ka-60 isolated ducted tail rotor geometry

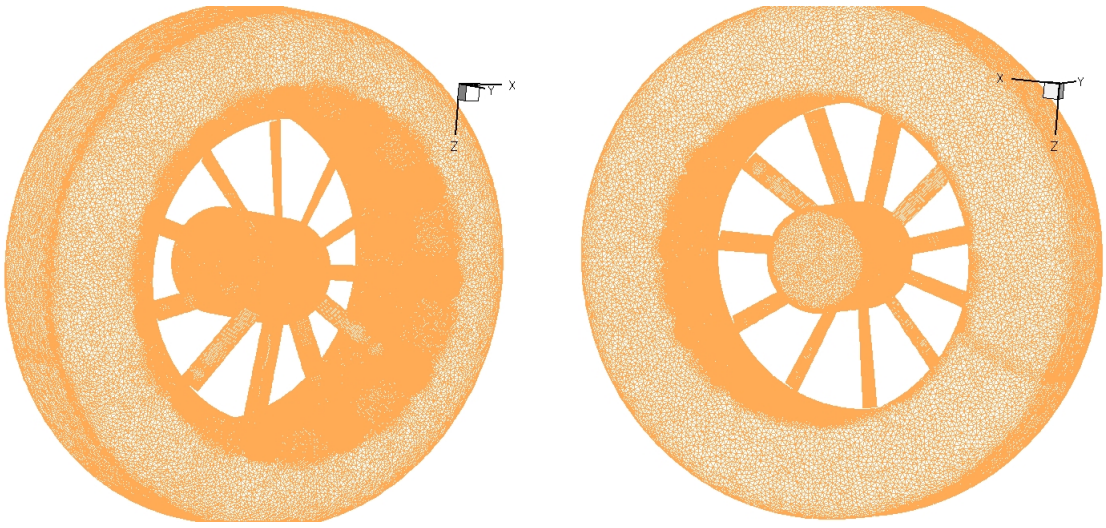

(a) Starboard view (b) Port view

Figure 3.23: Surface mesh of the KAMOV-60 ducted tail rotor geometry (medium mesh)

Although stators are beneficial for such configurations due to the pressure recovery that they can offer. However, it was shown in a study from a helicopter manufacturer[8], that the inclusion of the stators in a CFD model did not alter significantly the polar curve of the configuration (see Fig 2.24). The surface mesh of the complete ducted tail rotor geometry is shown in Fig 3.23.

3.4.3 Numerical Simulation

The commercial CFD solver ANSYS FLUENT was used in order to perform the numerical simulation of this validation case. The specific details of the numerical methods as integrated in the solver will not be discussed here and the interested reader can find more information in FLUENT's user guide [51]. However, the deployed numerical schemes as well as the turbulence modelling will be briefly discussed, on the grounds of justifying their applicability in modelling rotors in hover, and more specifically in the particular ducted tail rotor geometry.

3.4.3.1 Boundary Conditions

The prescription of boundary conditions in the hovering rotor flowfield is crucial in order to derive meaningful results. The flow away from the rotor is quiescent[36], which practically means that the rotor-duct system falls within a "computational box" where zero flow conditions are present in the boundaries. As it is stated by other researchers [36, 8, 39, 37] this is exactly the flow regime that is mimicked in hover test chambers. Thus, the boundary conditions that have been used for this simulation were pressure inlets for the top and sides of the domain and a pressure outlet for the bottom side where the flow will exit the domain. The computational domain which is normally deployed in CFD simulations of hovering rotors is a cylindrical domain. The deployed computational domain along with the surface mesh of the boundaries is illustrated in Fig 3.24. Both the bases of the domain have the same diameter which was chosen to be 12D where D is the diameter of the rotor[14] .

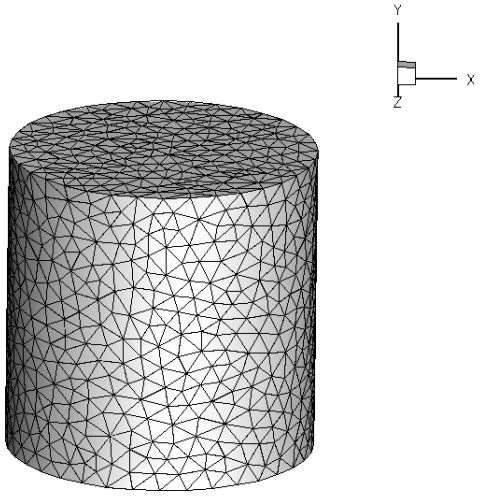

Figure 3.24: Cylindrical domain used for the CFD simulation

[14]For hover a lot of researchers have used at least 10 times the rotor diameter as the extend of the domain [36]

The origin of the axes lies in the center of the hub (at the exit of the diffuser plane) and the total height of the domain was 24D. The deployed relatively long distances of the boundaries of the domain from the walls of the geometry were allocated in order to allow the rotor's downwash to fully expand and to avoid any recirculation of the flow back to the boundaries. Traditionally, in rotor hover simulations the specification of the boundaries are performed by taking into account the quiescent flow which is outside the computational box. Some researchers [36, 11] have applied a three dimensional sink whose strength is a function of thrust of the rotor and is located at the axis of rotation of the rotor. In the current validation case, in order to ensure that flow will enter into the computational domain and exit at the outlet, hence satisfying the conservation laws, non-zero flow boundary conditions are applied.

To be more specific, a stagnation pressure value has been assigned to the pressure inlets in order to ensure that there will be a flow of 1m/s normal to these boundaries. At the pressure outlet, which is located at the bottom of the computational domain, static pressure was assigned which was equal to the atmospheric pressure (101325 Pa). The stagnation pressure at the pressure inlets was calculated using Bernoulli's equation for an incompressible flow. The blades and the shroud have been assigned with a viscous wall boundary condition where the no-slip condition applies i.e. the flow will have zero velocity (normal and tangential components of the velocity) relative to the boundary, whereas the hub has been assigned as an inviscid wall with slip conditions. As discussed before, in this region the blade does not contribute to the rotor thrust production hence a boundary layer resolution of this region was not required.

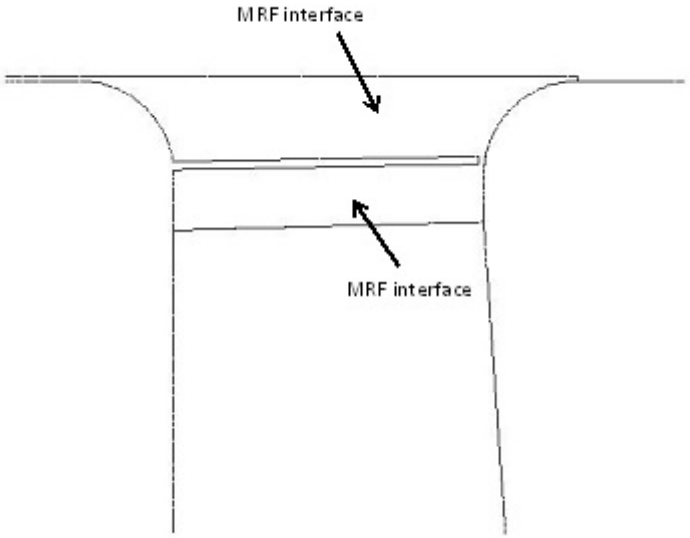

Figure 3.25: MRF interfaces

For simulating this flow in order to take into account the rotation of the blades a "frozen rotor" approach has been used. In FLUENT this approach is called Multiple Reference Frame (MRF) . In this approach a problem which is unsteady in the stationary (inertial) frame becomes steady with respect to the moving frame. This is achieved by transforming the equations of fluid motion to the rotating frame. The fluid velocities are transformed from the stationary frame to the rotating frame using the following equation:

$$\mathbf{V_r} = \mathbf{V} - \mathbf{U} \tag{3.25}$$

where $\mathbf{V_r}$ is the vector of the relative velocity, $\mathbf{V}$ is the absolute velocity vector (the velocity as viewed from an observer on the stationary frame), and $\mathbf{U}$ is the tangential velocity of vector or whirl of the rotating frame. The MRF approach does not imply that there is a relative motion between the moving/rotating bodies and the stationary bodies, hence the grid remains fixed.

What is simulated effectively is a snapshot of the flow or the instantaneous flow-field. Usually, in MRF simulations the computational domain is divided in two (or even more) sub-domains and the rotating parts are enclosed by the rotating reference frame. However, this does not imply that there is no possibility to place a stationary body within the rotating reference frame. A requirement of the MRF is that the interfaces which separate the moving region from the adjacent stationary regions must be oriented in such a way such that the component of the frame velocity normal to the boundary to be zero. This means that the interfaces must be surfaces of revolution about the axis of rotation of the rotating reference frame [51].

Thus, the region which encloses the blades as well as the rotor hub was defined as a rotating reference frame with a steady frame angular velocity of 2398 RPM (as in the experiment). The MRF approach does not accomodate accelerating frames e.g unsteady angular velocity. Fig 3.25 illustrates the interfaces of the rotating reference frame region. It must be mentioned here that the rotating reference frame region reaches up to the entrance of the inlet lip. This could seem as counter-intuitive due to the fact that the flow does not rotate at this region due to the fact that the cone of the hub lies in the same height as the entrance of the inlet lip[15]. The portion of the shroud wall inside the rotating region has a zero absolute velocity with respect to the stationary (absolute) frame. The blades and the portion of the hub which rotates have a zero velocity relative to the rotating frame i.e. they move with the rotational velocity of the frame

[15]The C_p distributions over the inlet lip (which will be shown later) do not show any abnormality in the region. This design has been done on the grounds of avoiding an irregular interface shape between the rotating and stationary regions.

The other walls which lie in the stationary frame have a zero absolute velocity i.e. the walls do not move in the absolute (stationary) frame but they move with the velocity of the fluid with respect to the rotating reference frame. The boundary between the two different frames has been made conformal which means that the grid node locations are identical at the boundaries where the two reference frames meet. This alleviated the need of defining explicit interfaces and an interior zone boundary condition was deployed.

The flow at the interfaces of the two different zones is not expected to be non-uniform e.g. if the stator blades were accounted then a mixing plane procedure should take place in order to exhange the information (fluxes) at the interfaces between the stationary and rotating zones. This was one of the reasons also why stators are not included in the simulation. Finally, as far as the interface treatment is concerned the absolute velocity formulation was used where the governing equations in each sub-domain are written with respect to the adjacent reference frame [51]. However, the velocities are stored in the absolute frame which does not require any transformation at the interface between the different sub-domains.

The flow-field for this validation case, with the deployed angular velocity ,can be considered as incompressible and isothermal. Similar studies have been performed by various researchers [37, 11, 38]. The hover flow-field is quasi-periodic in nature which means that at every azimuth angle the flow distribution (over the rotor) is the same. Therefore, it is a usual assumption in such flow regimes to use periodic boundary conditions and instead of creating the whole geometry, only a portion of it is actually modelled. In this work, this approach was not followed on the grounds of performing a sanity check for the generic ducted tail rotor geometry which was described before. The primary aim was, due to the absence of validation data for forward flight, to use a similar case

for a different but similar geometry in order to examine whether the deployed mesh topology and solver setup could actually provide meaningful results. A similar approach has been followed by Alascio et al [8].

3.4.3.2 Numerical Solver

The numerical solver which was used for simulating this case is the Pressure-Based solver as implemented in FLUENT. This solver is suitable for both incompressible and compressible flows and utilizes an algorithm which belongs to a general class of methods called projection methods [51]. In such an algorithm the pressure field is derived from the continuity and momentum equations whereas the velocity field, which is corrected by the pressure, satisifes the continuity equation. This numerical technique is the same technique which is applied in the SIMPLE algorithm [52]. All equations are solved in a segregated way i.e. they solved sequentially one after another and the solution convergence is relatively slow [51].

A more efficient algorithm is the so called coupled solver which uses exactly the same algorithm as applied in SIMPLE with the difference that the equations are solved in a coupled manner. Thus, instead of updating each equation sequentially, a simultaneous system of momentum and pressure-based continuity equations is solved. Although this coupling procedure requires more computational resources, it increases the rate of convergence compared with segregated algorithms. For this case a steady second order interpolation scheme is deployed which reconstructs the pressure with a spatial accuracy of second order. For the momentum equations as well as for the transport equations of the turbulence model a steady second order upwind scheme is applied. The Pressure-Based solver also employs a multigrid method in order to accelerate the convergence and to reduce the simulation time which is applicable for

such large scale simulations (medium mesh approximately 18.5 million cells). Finally, in order to further accelerate the convergence of the simulations and reduce the simulation time a full multigrid initialization was deployed. This initialization method solves the Euler equations by using an explicit solver together with a multigrid approach. Thus, a better initialization of the flow-field is achieved which reduces significantly the computation time.

3.4.3.3 Turbulence Modelling

The turbulence model that was used in the simulation was Menter's [53] k-ω Shear Stress Transport (in its baseline formulation) mainly due to its applicability in flows where strong flow separation and adverse pressure gradients occur. Specifically, k-ω SST is an isotropic two equation eddy viscosity turbulence model which implements the k-ω turbulence model formulation for the boundary layer (for the viscous, buffer and logarithmic layers) and the k-ε formulation away from the wall. This is achieved by a blending function which makes this model a zonal turbulence model. The success of this model and its applicability to a wide range of incompressible and compressible flows with large separations and adverse pressure gradients lies in the fact that it is based on the beneficial elements of both k-ω and k-ε .

To be more specific, k-ω is superior over k-ε in terms of boundary layer resolution which means the boundary layer separation which causes the blade tip vortex will be better captured. k-ω is also robust and superior to other turbulence models in terms of numerical stability [53]. However, k-ω exhibits a sensitivity to the freestream values of the specific dissipation rate ω whereas k-ε does not have this problem [53] and is more appropriate for the wake region of the boundary layer. The values of the turbulent kinetic energy and the specific dissipation rate were calculated by estimating the turbulence in-

tensity and the turbulent length scale due to the fact that the values of these variables were not given in the experiment and could not be known a priori. The deployed turbulence intensity was set to 0.1% which is a common value encountered in wind tunnels [51] and the turbulent length scale was assigned a value of 0.05m which corresponds to about 6% of the blade radius. It must be mentioned here, that due to the inherent empiricism of the turbulence models, the solution could be very different if there will be small changes in the constants of the model (of the order of 5-10% [53]). Thus, for the purposes of this study the baseline configuration of k-ω SST is implemented and the main aim is to derive meaningful realistic results and not to perform a parametric study of altering the turbulence model's constants (which can either improve or deteriorate the results).

3.4.3.4 Results

Before discussing the results of this validation case, a grid convergence study will be shown in order to prove that the numerical results are grid independent which means that with further grid refinement the solution does not change. Three grids have been used, a coarse mesh with ~13.5 million cells, a medium mesh with ~18.9 million cells and the refined mesh which had a total of ~24 million cells. Due to the hybrid nature of the grid as well as the complexity of the geometry, a constant grid refinement ratio cannot be achieved by uniformly refining the grid in all three directions. Therefore, the methodology of grid convergence reporting proposed by Roache [50] will not be used in the present work. A constant grid refinement ratio of 2 e.g would require to refine every base triangle into four new triangles. However, the coarsening or refinement of the grid generation algorithm is also unstructured.

/	Coarse	Medium	Refined	Experimental
C_{Trotor}	0.1035	0.1028	0.1010	0.0893
C_{Ttotal}	0.1865	0.1863	0.1835	0.1544
C_{Trotor}/σ	0.2090	0.2077	0.2040	0.1805
C_{Ttotal}/σ	0.3767	0.3763	0.3706	0.3120

Table 3.8: Validation results

Error %	Coarse	Medium	Refined
C_{Trotor}	15.90	15.11	13.10
C_{Ttotal}	20.79	20.66	18.85
C_{Trotor}/σ	15.78	15.06	13.02
C_{Ttotal}/σ	20.73	20.60	18.79

Table 3.9: Grid refinement level errors against the experimental data [25]

Thus, the results will be compared against the available experimental results and C_p distributions will be used in order to show that the solution does not significantly differ between the different grids. The results of the three meshes, in terms of rotor and total thrust coefficients and blade loading coefficient are shown in Table 3.8. The corresponding errors of each grid refinement level with respect to the experimental results are shown in Table 3.9.

By inspecting Tables 3.8 to 3.9 it can be seen that the differences between the numerical results across the three grid refinement levels is small and the results are comparable. Thus, it can be concluded that the solution is grid independent. In terms of results reporting there is not any strict rule of which mesh level to use. For example, if the grid convergence study is performed with two grid levels [50], either the medium mesh can be used in order to save time or the refined for possibly more accurate results. However, it must be stressed that such study is not performed, in order to examine which grid provides more accurate results, but to show that with further grid refinement, the results are comparable [50, 54]. In grid convergence studies it is usual to use three grid levels [54] or even more [55]. In the current research work, two

grid levels will be used in the main body of the CFD simulations (Chapter 4 and 5) and the corresponding discussion of results will be performed by using the medium mesh in order to reduce the computational time. In the validation case, the boundary layer mesh (medium) of the blade had 113 cells in the streamwise direction, 70 cells in the spanwise direction and 30 cells in the normal direction. The blade tip clearance gap had 30 cells in the spanwise direction and the cell distribution for the rest dimensions of the gap is in accordance with the blade profile (see Figures 3.17-3.19). The total mesh size of one blade was circa 583,000 cells including the unstructured tetrahedral cells off the boundary layer region. The boundary layer meshes of the shroud inlet lip and diffuser were consisted of 149,800 and 42,600 cells respectively. The large discrepancies between the experiment and the numerical results can be attributed to the following reasons:

1. The computation of rotor thrust during an experiment is done by using a mechanical balance and the uncertainty in this measurement is not available. In addition, turbulent quantities such as the turbulent intensity of the wind tunnel is not given and even a small change of this parameter could yield different results

2. There is no information whether the pressure taps at the experiment where only positioned at the inlet lips of the duct. Ruzicka et al[11] claims that for the RAH-66 FANTAIL pressure taps "were installed throughout the model fairings, mainly on the inlet side duct lips and the vertical tail". In the present numerical simulation both the thrust produced by the inlet lip and the rest of the shroud is taken into account.

3. The geometry of the shroud is an approximation to the real geometry (uniform shroud radial thickness)

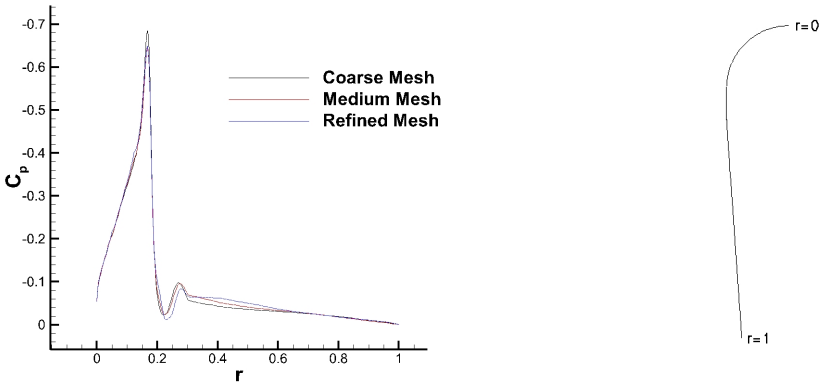

(a) C_p distributions comparison for the three different grid refinement levels

(b) Coordinate system for pressure distribution plots

Figure 3.26: Pressure distribution at mid azimuth (Z=0) over the inlet lip and diffuser of the shroud

Despite the large though justifiable discrepancies in terms of the rotor thrust, total thrust and blade loading coefficients, the derived total thrust augmentation factor was equal to 1.81 which is almost identical to the value that was derived during the experiment (1.82). This finding further suggests that although the computed quantitative values do not show a perfect agreement with the experiment, the computational model captures well this macroscopic value i.e. the distribution of forces between the rotor and the shroud which is a significant attribute of a hovering ducted tail rotor (the shroud thrust contribution is about 50% of the total thrust in hover). Fig 3.26 shows the C_p distributions based on the blade tip velocity of the three different grid refinement levels and the results are comparable. The pressure distribution along the inlet lip and diffuser is plotted due to their significance in thrust production. A coordinate system has been implemented, as shown in Fig 3.26 (b), where the non-dimensional distance r is used. The coordinate r is set to 0 at the entrance of the inlet lip and 1 at the exit plane of the diffuser.

As it was expected the suction forces ($C_p < 1$) are dominating over the inner surface of the shroud. The flow accelerates further along the inlet lip reaching a suction peak slightly upstream of the rotor, at the blade tip gap region ($r = 0.18$). The highest suction forces are due to the air leakage through the gap between the blade tip and the shroud wall as well as because of the reversal of the flow from the higher pressure region below the rotor. The flow below the rotor is stagnated and the increase in pressure can be seen along the diffuser. The flow expands almost completely to ambient atmospheric pressure ($C_p = 0$) at the diffuser exit plane ($r = 1$). The suction forces over the inlet lip of the shroud are clearly greater than those developed over the diffuser. These high suction forces are mainly responsible for the overall shroud thrust contribution. Fig 3.27 depicts the pressure coefficient distribution over the shroud inlet lip and it clearly shows that the maximum suction forces are developed at the blade tip region.

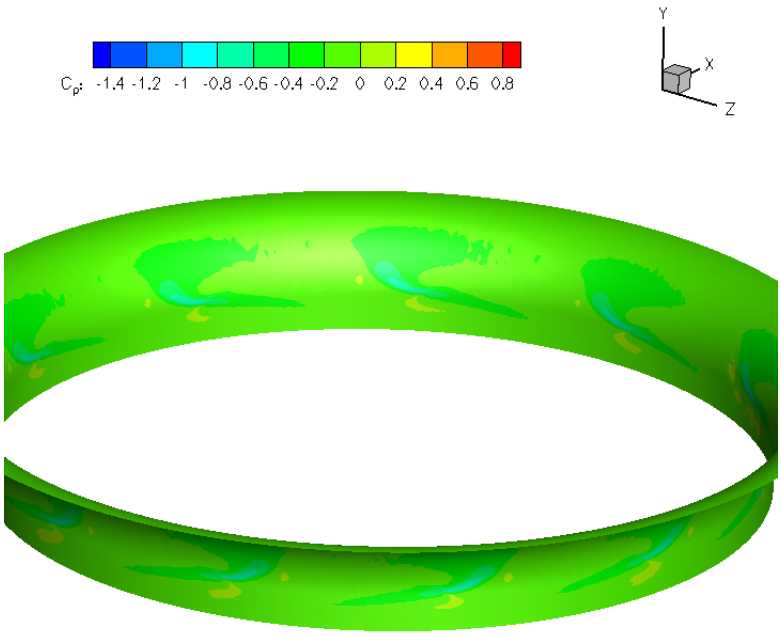

Figure 3.27: Inlet lip C_p contours

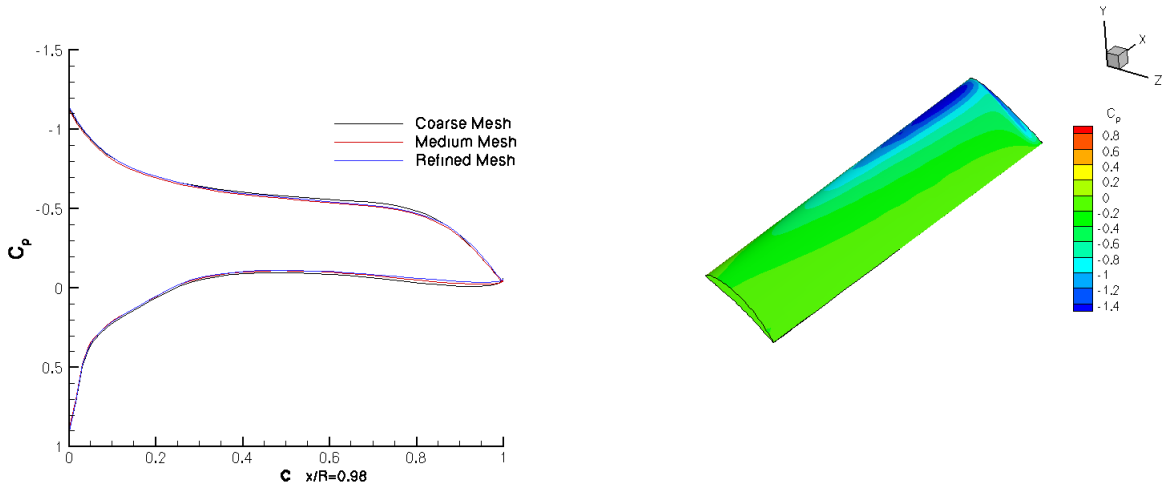

(a) Chordwise C_p distribution of a 2D section of the blade at x/R=0.98

(b) C_p contour over the blade

Figure 3.28: Blade section C_p distributions convergence and contour

The chordwise C_p distributions at x/R=0.98 for the three grid refinement levels are shown in Fig 3.28 and it can be seen that the results are comparable. The maximum suction peak is located at leading edge of the upper surface of the blade as expected and the adverse pressure gradient, moving towards the trailing edge, is clearly depicted as well.

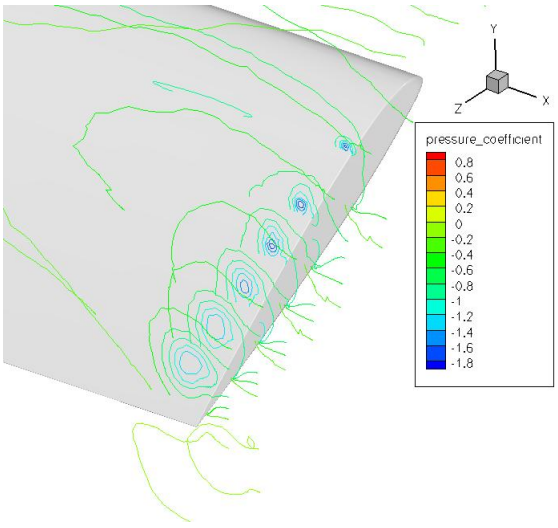

Figure 3.29: Convection of blade tip vortex

The C_p contours over the surface of blade illustrate the fact that the spanwise blade loading increases as we approach the blade tip and the maximum thrust occurs at the region of the blade tip. This is due to the fact that the presence of the shroud tends to prevent the formation of the blade tip vortex (three dimensional flow). The blade tip vortex formation is illustrated in Fig 3.29.

3.5 Chapter Summary

The main methodology of the current research work as well as a validation case for the CFD simulations have been discussed so far. Firstly, an overview has been given about the methodology and its main simplifying assumptions. The proposed methodology along with its assumptions, pertains to the development of the generic ducted tail rotor model at specified flight conditions. It has been shown that for a proper construction of performance maps, the different altitude conditions must be taken into account. This is done by deploying ISA conditions, in the form of corrected thrust and power coefficients, as well as considering non-ISA conditions.

It can be considered that the main core of the assumptions lies in the Reynolds and Mach number invariance. It was shown that for the range of altitudes where a typical helicopter operates (0-3,000ft), it is safe to consider that the thrust and power coefficients are weakly dependent on these non-dimensional numbers. With regards to the Reynolds number, the invariance is due to the fact that the tail rotor's RPM is constant at the examined flight conditions (hover and forward flight). Also, due to the fact that a shrouded rotor can accommodate higher induced velocities, compared to an open rotor, it does not experience stall even in high collectives. These conclusions have been also verified by the available literature [16, 20]. As far as the Mach number effects

and variations are concerned, they will only be due to the varying altitude (change in the local speed of sound). In addition, the shrouding of the rotor offers a shield effect to the tail rotor. Thus, transonic and/or supersonic flow is prevented within the rotor.

Following the discussion about the methodology, the generic ducted tail rotor model was presented. The performance maps subroutine as well as the structure of the performance maps was explained. In addition, it was shown that the selection of geometric parameters of both the shroud and the rotor has been performed by a consistent and thorough study of the available literature review. This was done in order to have a final geometry, as realistic as possible, for the CFD simulations. Finally, a CFD validation case was presented in order to validate, in a quantitative manner the subsequent CFD results. The validation case was deployed, in order also to provide a guideline for the construction of the computational grids, the assignment of boundary conditions and for the numerical approach which will be applied in the main body of the CFD simulations. The validation showed considerably large discrepancies of the order of 15% and 20% for the rotor and shroud thrust respectively. However, despite the large discrepancies it was shown that the thrust sharing (total thrust augmentation factor) was almost identical (0.55% error) to the experiment. This finding shows that the current approach can provide meaningful results in terms of performance trends. Also, it further supports that the exact geometric details and conditions of the experiment must be known in order to estimate the quantitative error more adequately. The hover results of the generic ducted tail rotor model will be presented in Chapter 4

Chapter 4

Hover Performance Maps

This chapter presents the performance of the generic ducted tail rotor in hover. The results and the associated analysis will be presented in terms of performance characteristics (thrust, power and efficiency) and shroud surface pressure distributions. Analysis will also be given on the effect of the blade collective on the aforementioned pressure distributions and flow-field. In every case, the data will be presented in non-dimensional form i.e. power coefficient, thrust coefficient normalized with the throat area of the shroud and the blade tip velocity. The power and thrust coefficients will be further normalized by the blade solidity yielding the blade loading coefficients[1].The pressure coefficient C_p is normalized by the blade tip velocity of the rotor and is given by:

$$C_p = \frac{p - p_\infty}{\frac{1}{2}\rho V_\infty^2} \tag{4.1}$$

[1]As discussed before the blade loading coefficient is the ratio of the rotor thrust and blade solidity. However, in ducted tail rotor aerodynamics literature the total thrust is used instead.

where the symbol ∞ denotes the freestream values. However, V_∞ in this occasion and generally in helicopter aerodynamics denotes the velocity of the blade at the tip. where the symbol ∞ denotes the freestream values.

4.1 Performance Polar Curves

In hover in order to derive the performance map which gives information about the power consumption at given thrust a total of 7 simulation points was chosen (from 0° to 30° blade collective angle with an increment of 5 degrees). This range has been assigned by using the main rotor's required thrust provided by the in-house rotorcraft comprehensive code (it will be described in Chapter 5). To be more specific, the required thrust was of the order of 4200N and the total thrust at 30° blade collective angle was 4693N. Thus, the required thrust corresponds to a value between 25° and 30°. The grid system that was used for these simulations will be presented in the next chapter, which deals with the forward flight, due to the fact that the applied grid system was the same for both hover and forward flight. The corresponding thrust polars with respect to increasing blade collective is shown in Fig 4.1. It can be seen, as expected, that both the rotor thrust and the shroud thrust increases with increasing blade collective. The blade collective at the presented plots is taken at the 75% of the blade radius which is a common assumption [2]. The rotor thrust increases with increasing blade collective due to the increased flow acceleration over the blades which creates more lift. The plots clearly demonstrate that the ducted tail rotor even at high blade collectives does not exhibit any stall. As it was discussed before this is due to the increased induced flow caused by the presence of the shroud.

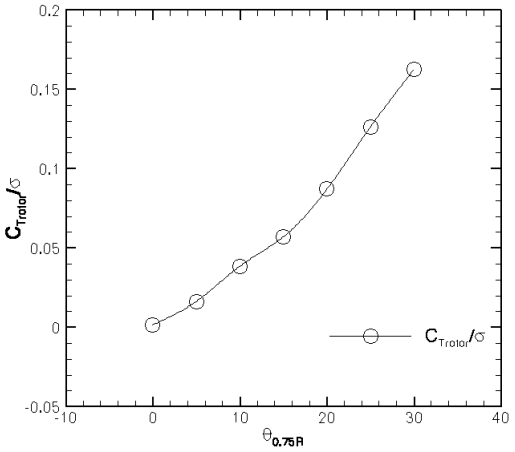

(a) Rotor thrust coefficient versus blade collective

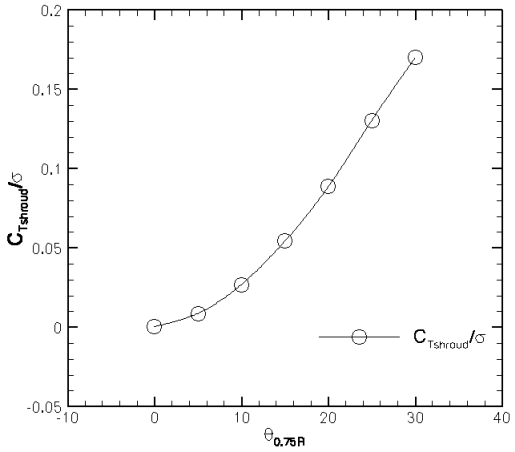

(b) Shroud thrust coefficient versus blade collective

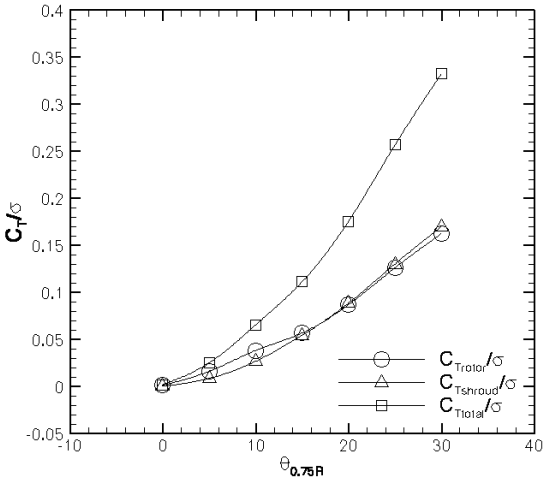

(c) Total thrust coefficient versus blade collective angle

Figure 4.1: Thrust coefficient polars with respect to the blade collective as measured at the 75%R location.

The shroud thrust increases with increasing blade collective following the same trend as the rotor thrust and this increase is due to the increased induced flow over the inlet lip of the shroud. This progressively greater induced flow, with increasing blade collective, will cause high suction pressures over the surface of the inlet lip which is the main cause of the shroud thrust.

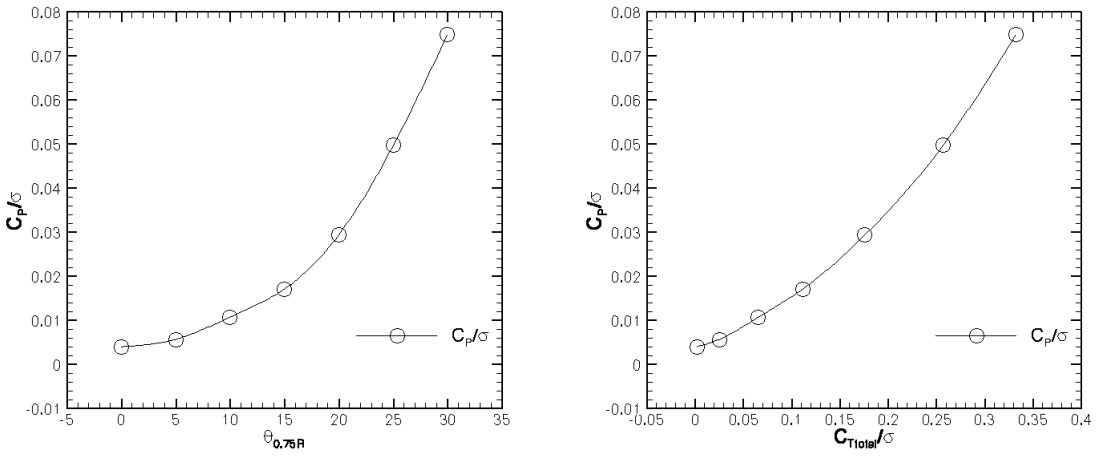

(a) Power coefficient versus blade collective (b) Power coefficient versus total thrust coefficient

Figure 4.2: Rotor power polar

This will be shown more clearly with the shroud surface pressure distributions which will be presented later. By inspecting Fig 4.1c the maximum value of C_{Ttotal}/σ is approximately 0.33 which is comparable to a similar configuration (Fig 2.24 [8]). The resulting power polar-power versus thrust coefficient - for this generic configuration is shown in Fig 4.2. This power polar curve demonstrates the behavior of the ducted tail rotor configuration in terms of power consumption at a given thrust which is of course a direct function of the blade collective. Thus, at any given thrust requirement, which lies in the boundaries of this map, the power consumption can be reconstructed by the power coefficient using Eq 3.12. It must be reiterated that for the purposes of this work there is not any need of investigating the effect of changing the RPM (as it is done for a compressor map). This is due to the fact that the rotational velocity of the blades is almost constant and display a very slight variation of a few revolutions [44] which will not have a drastic effect on performance. For all the values between the simulated points interpolation was necessary in order to capture the quadratic and cubic trends of the data. A cubic spline

interpolation was performed in order to derive the presented polars although quadratic interpolation did not display any significant difference. As it was discussed previously, due to the lack of well-established experimental data for the deployed geometry and conditions the validation of these results is by no means trivial. However, at least qualitatively the trends of the current data do bear a strong similarity with available public domain polars. Although the range of the blade loading coefficient is given in such data (see Fig 2.24) the power coefficient range is not disclosed possibly due to the confidentiality of the data. However, in pursuit of justifying the realism of the present simulations, the efficiency of the rotor could be analysed and compared with available public domain information. For a helicopter aerodynamicist or practicioner one measure of efficiency is the power loading (T/P) which shall be made as large as possible in order to have an efficient rotor. Nevertheless, this ratio is a dimensional quantity and the standard for expressing the efficiency of a rotor, or the power penalty, in hover is the figure of merit which is a measure of the static thrust efficiency [2]. As stated previously, the figure of merit (FM) is the ratio of the ideal power required to hover over the actual power required to hover and it signifies the amount of total input power which is converted into useful thrust. A value of 1 would represent an ideal rotor for the real configurations the FM is always < 1. momentum theory gives that the induced power of a rotor is equal to:

$$P_i = T v_i = \frac{T^{3/2}}{\sqrt{2\rho A}} \tag{4.2}$$

and in non-dimensional form the FM is given by:

$$FM = \frac{C_T^{3/2}}{C_P \sqrt{2}} \tag{4.3}$$

In this form the FM is only a function of the thrust and power coefficients which are also a function of the blade collective angle which means that a power polar can also provide the efficiency of the rotor at least in hover. The preceding discussion accounted for an open rotor where the wake contracts to a final cross-sectional area which is one-half of the rotor disk and the value of expansion ratio is 0.5. In the case of the ducted tail rotor the natural contraction of the wake is dictated by the diffuser's geometry and in the particular case, the expansion ratio has a value of 1.12. In this case, the ideal power is given by:

$$P_i = T\upsilon_i = \frac{T}{2\sigma_d} \times \sqrt{\frac{\sigma_d T}{\rho A}} \tag{4.4}$$

and the formulation of the FM will be:

$$FM = \left(\frac{T}{2\sigma_d} \times \sqrt{\frac{\sigma_d T}{\rho A}} \right) / P \tag{4.5}$$

where T is the total thrust of the configuration. The FM's variation with respect to the blade load coefficient and the blade collective angle is shown in Fig 4.3. The maximum FM of this configuration was 0.645 which falls within a representative range of values for such configurations (0.69 for the H-76 FANTAIL [7] and 0.71 for the AS365 N1 Dauphin [5, 4]). However, these aforementioned values were derived by using an expansion ratio of 1 and therefore the current value (0.645) cannot be directly quantitatively compared with the representative values of the manufacturers. Fig 4.3 is presented on the grounds of giving a qualitative comparison i.e. a trend in order to confirm whether the computations are realistic or not. From Eq 4.4 it can be seen that if the expansion ratio is increased, whilst holding thrust and rotor area constant, the ideal power decreases and hence the FM will consequently have a lower value.

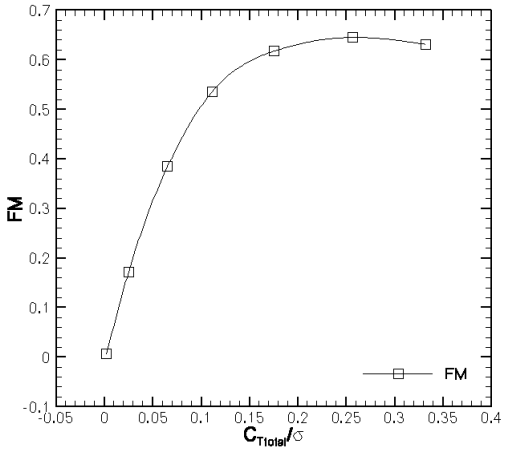

(a) FM variation with respect to the blade loading

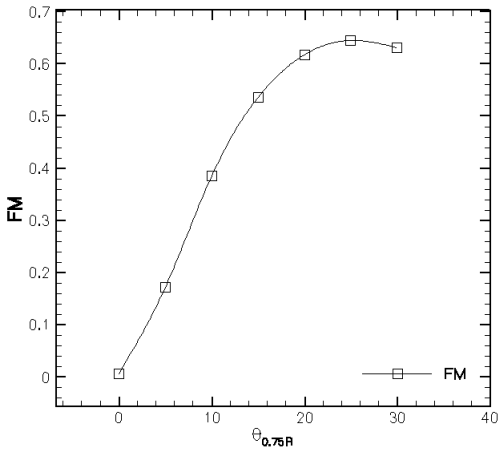

(b) FM variation with respect to the blade collective angle

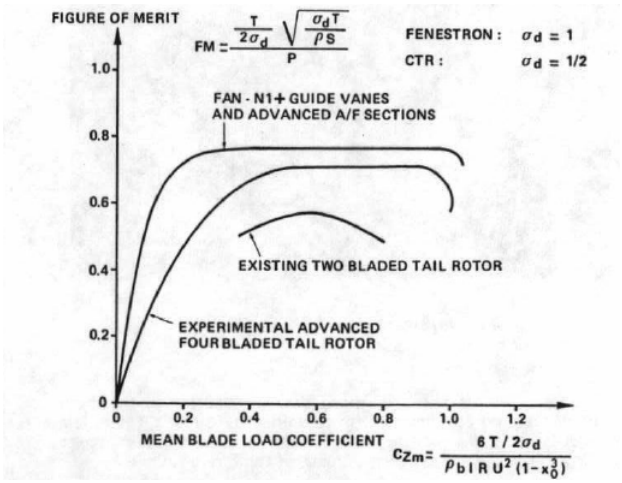

(c) FM Eurocopter Dauphin AS365 N1 [4]

Figure 4.3: Figure of Merit of the ducted tail rotor configuration and qualitative comparison public domain data

As it was explained earlier, by increasing the expansion ratio the degree of rotor unloading increases (increased shroud thrust and reduced rotor thrust). The blades will operate at lower angles of attack hence giving reduced power losses. This conclusion is drawn by the momentum theory (see Appendix A).

4.2 Shroud Surface Pressure Distributions

The results presented previously suggest that the shroud thrust contributes equally to the total thrust production and in some angles, for the given configuration, it produces more thrust than the rotor. In order to shed light in the physical mechanism of this thrust production as well as the thrust sharing between the rotor and the shroud, a detailed analysis must be given. Such an analysis is based on the actual shroud surface pressure distributions especially on the region of the inlet and the diffuser.

In addition, in pursuit of providing a means of a sanity check of the results, momentum theory will be used in order to estimate whether the computed thrust sharing between the rotor and the shroud is reasonable. With the same reasoning as it was done in the KAMOV-60 validation case the shroud surface pressure distributions have been depicted in a two dimensional form.

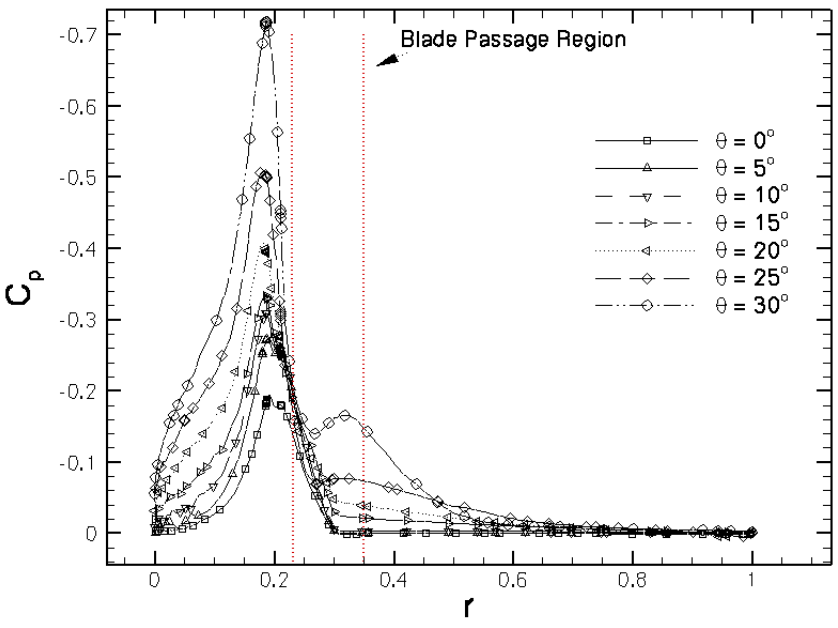

Figure 4.4: Shroud surface pressure distributions versus the blade collective angle

It must be mentioned that due to the fact that the inner region of the shroud (inlet lip and diffuser) is mainly responsible for the production of thrust, only this region is considered and presented. The shroud surface pressure distribution data are shown in Fig 4.4 which shows the effect of changing the blade collective on the pressure distribution. For each angle, the computed distributions are illustrated by using corresponding symbols which are connected through solid, dash and dash-dot lines which are joined together by using a cubic spline interpolation.

The data of the windward side are presented only due to the fact that for hover (axial flow) the pressure distribution on the leeward side does not change (symmetric) as the flow displays a degree of periodicity. The data are plotted in a coefficient form as a function of the non-dimensional distance r using the coordinate system as described in p.g 116 (Fig 3.26). The data consist of a set of 7 distinct simulation points reflecting a blade collective (at 75%R) range from 0° to 30° with an increment of 5 degrees.

It must be noted that the C_p axis has been inverted in order to show the increase in suction pressure i.e. the suction peaks (in a similar fashion as it is done for a typical airfoil pressure distribution). As it was expected, for all the blade collectives suction pressures ($C_p < 0$) are seen throughout the entire region of the inner surface of the shroud. The flow in each case returns completely to ambient atmospheric pressure at the diffuser exit plane ($r = 1$). The location of the maximum suction pressure peaks which are shown in the figure are slightly upstream of the rotor location (blade passage region. $r = 0.2$). It can also be seen that the inlet lip is dominant in terms of shroud thrust production and the suction pressures at this region are considerably higher than those at the diffuser wall.

This increase of suction pressure at the inlet lip as we approach the rotor blade tip region is mainly due to the acceleration of the flow over the inlet lip. In addition, the flow-field which results within the region between the stationary shroud and the rotor blade tip creates a complex leakage flow. The complexity of the flow-field at this region is due to the interaction of the rotor wake, the boundary layer of the shroud and the leakage flow. This leakage flow is due to the difference in pressure between the high pressure area below the rotor (pressure side) and the low pressure area (suction) above the rotor. Thus, this flow can be considered as a pressure-driven flow occuring from the pressure to the suction side.

In addition, the relative movement between the moving rotor and the stationary shroud contributes to the generation of this leakage flow [56, 57]. The tip leakage flow and the associated separation of the shroud boundary layer creates a three dimensional vortex which has turbulent characteristics. However, it must be mentioned that for the purposes of the current work and investigation the macroscopic properties of the flow (thrust, power) are considered. Details of the tip leakage flow mechanisms will not be examined as this would require the investigation of different blade tip clearances. By inspecting Fig 4.4 the profound effect of the blade collective angle on the pressure distributions can be seen.

As it was expected, by increasing the blade collective angle the suction forces that are generated in the inner region of the shroud increase. This is due to the increased induced velocity with increasing the blade collective angle which is associated with the increasing rotor thrust. It can be acknowledged that the rotor plays an important role on the shroud and the system of the rotor-shroud is strongly interdependent. In every case, the distinctive characteristic of this graph i.e. the suction peak is present for all cases and its location

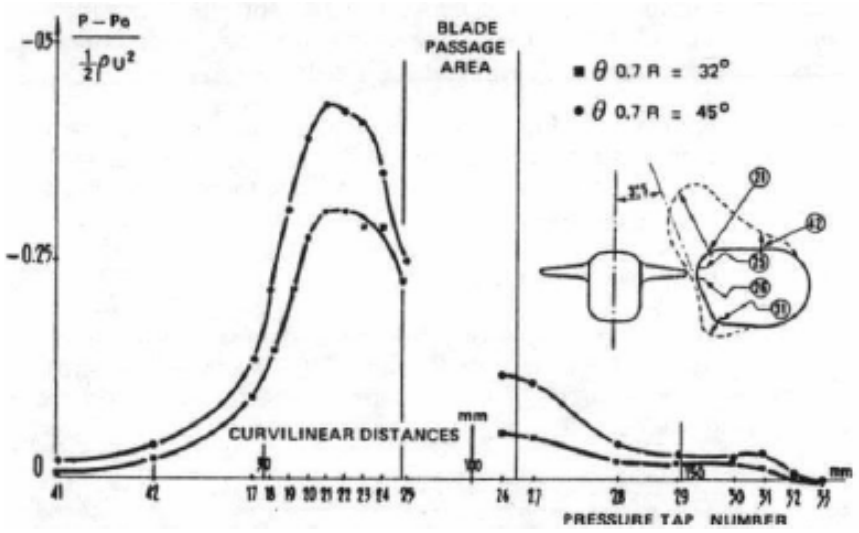

Figure 4.5: Shroud surface pressure distribution, Aerospatiale [4]

(slightly upstream of the rotor) does not change with increasing blade collective. For all angles, after the suction peak the pressure rises and the flow expands clearly to ambient atmospheric pressure. Another feature that can be derived from the pressure distributions plot is that the suction forces increase abruptly after the blade collective of 20°. This is also present at the rotor polars graphs (Fig 4.2) and denotes the scaling of the rotor and shroud thrust with the square of the induced velocity.[2]

Finally the computed surface pressure distributions compare qualitatively well with existing public domain data, as illustrated in Fig 4.5, which further increases the confidence in the results. However, it must be mentioned, that due to the absence of well established experimental results performed for the same geometry and at the same ambient conditions, there is a degree of ambiguity in the results, at least in terms of quantitative comparison i.e. the magnitude of thrust components and power requirements for the given blade collective angles.

[2]This conclusion will be shown in Appendix A in the momentum theory derivations.

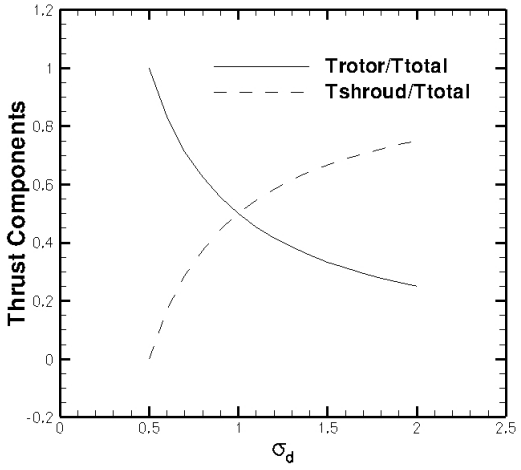

Figure 4.6: Thrust components variation with respect to the shroud expansion ratio (momentum theory results)

In order to address the issue of the non-availability of decent experimental results, an alternative way of showing that the results are reasonable is the investigation of the thrust sharing. It is apparent from the previous discussions that the thrust sharing between the rotor and the shroud is an important and unique characteristic of a ducted tail rotor configuration. From the literature review regarding the application of the ducted tail rotor to a helicopter configuration it was shown that approximately half of the total thrust is produced by the shroud.

Nevertheless, the majority of the authors, in the available ducted tail rotor literature, fail to quote the value of the expansion ratio which strongly dictates the performance of the ducted tail rotor. By applying the momentum theory relations (Eq 2.4-2.7, p.g 20) an estimation of the maximum thrust components can be derived. Fig 4.6 shows the variation of the rotor thrust component (T_{rotor}/T_{total}) and the shroud thrust component (T_{shroud}/T_{total}) with respect to increasing expansion ratio. For example a value of $T_{rotor}/T_{total} = 1$ means that 100% of the system's thrust is produced solely from the rotor and corresponds

to an expansion ratio of 0.5. With the shrouding of the rotor the expansion ratio increases and the rotor thrust component and shroud thrust component reduce and increase respectively.

For an expansion ratio of 1 which corresponds to a staight cylindrical diffuser each component takes a value of 0.5 which means that both the shroud and rotor contribute equally to the total thrust generation. By further increasing the expansion ratio, it can be seen that the shroud thrust components is greater than the rotor's. Thus, the shroud further unloads the rotor. Despite the fact that these values, computed by momentum theory, are ideal due to the inviscid and incompressible flow assumptions, they can be used as a theoretical maximum and a way of quantifying the computed thrust sharing.

In the current generic ducted tail rotor configuration that was used for the simulations the expansion ratio has a value of 1.12 and momentum heory predicts a value of 0.446 for the T_{rotor}/T_{total} and 0.554 for the T_{shroud}/T_{total}. These values correspond to the theoretical upper values for a ducted tail rotor with the deployed expansion ratio. For the thrust component this value is the theoretical minimum for the rotor's contribution since the rotor thrust component decreases with increasing expansion ratio. On the contrary, this value for the shroud thrust component corresponds to the theoretical maximum as the shroud thrust component increases with increasing expansion ratio.

Fig 4.7 illustrates the variation of the individual thrust components with respect to increasing blade collective angle and it can be acknowledged that the shroud unloads the rotor with increasing blade collective angle. For the maximum computed collective angle (30°) the values of thrust sharing components are 0.488 for the rotor and 0.512 for the shroud. The computed and theoretical values are tabulated for convenience in the table below:

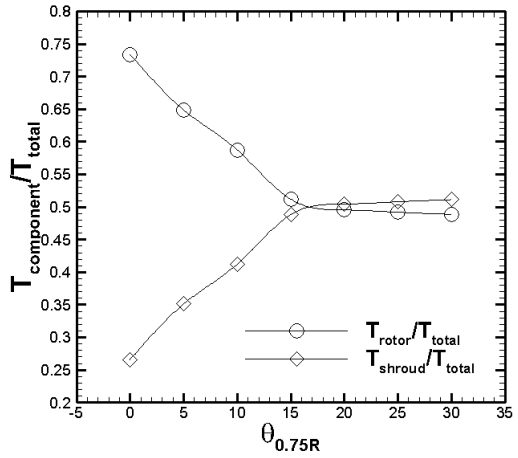

Figure 4.7: Thrust sharing between the rotor and the shroud with respect to increasing blade collective (computed results)

\	T_{rotor}/T_{total}	T_{shroud}/T_{total}	T_{total}/T_{rotor}
momentum theory	0.446	0.554	2.24
CFD simulations ($\theta_{0.75R} = 30°$)	0.488	0.512	2.05
Percentage difference	9.41%	-7.58	-8.5%

Table 4.1: Thrust components comparison between CFD predictions and momentum theory results.

The results for the maximum collective angle indicate that the thrust sharing conforms with the expected theoretical values. For the shroud thrust component a difference of -7.58% is observed meaning that the shroud produces less thrust than the theoretical maximum. This is due to the non-ideal nature of the flow where the viscosity of the fluid will introduce losses. As far as the rotor thrust component is concerned, the inverted value of T_{rotor}/T_{total} gives the total thrust augmentation factor. The ideal augmentation factor is 2.24 for an expansion ratio of 1.12 and the computed augmentation factor is 2.05 which corresponds to a percentage difference of -8.5%. These results suggest that the CFD simulations provide a reasonable estimate of the thrust sharing.

On the grounds of comparing these values to an available experimental value of a similar configuration, it is repeated that the total thrust augmentation factor for the KAMOV-60 was 1.82. The ideal theoretical value was 2.0 ($\sigma_d = 1$), which corresponds to a difference of -9%. Thus, it can be concluded that the derived results are in accordance with available experimental data, at least in terms of the total thrust sharing between the shroud and the rotor. However, by inspecting Fig 4.7 it can be seen that the thrust sharing between the individual components converge to an almost equal value from $\theta_{0.75R} \geq 15°$.

To the best knowledge of the author, there is not any reference in the available literature of the thrust sharing at low-power conditions (low blade collective angles) and instead the augmentation factors at the operating point (for hover this will correspond to increased blade collectives) are probably reported. The reason for this behavior could be that due to the low thrust produced by the rotor and the associated low induced velocities the suction forces on the inner surface of the shroud are low. It must be reminded, that the suction forces over the inner surface of the shroud are mainly produced by the turning of the accelerating flow which shares a dynamic relationship with the blade collective angle.

At small angles the induced velocities are low enough and there is little flow acceleration in order to generate an adequate amount of thrust. In order to conclude this section, it must be reiterated that for a proper validation of the CFD results, experimental data are mandatory in order to quantify the errors in terms of the thrust and power coefficients. Nonetheless, the analysis of the results has shown that there is a significant degree of confidence on the results with regards to the resulting trends of the rotor polars and the shroud surface pressure distributions.

4.3 C_p Contours

The present section gives a succinct overview of the pressure coefficient contours over the generic ducted tail rotor configuration. The pressure coefficient contour plots are presented over the surface of the inlet and the whole configuration, in an attempt to explain better the behavior of the configuration with increasing blade collective. Figures 4.8 to 4.10 illustrate the C_p distributions over the inlet lip of the shroud and the starboard view of the configuration for each computed collective.

By inspecting the C_p contours, the profound effect of the blade collecive on the pressure distributions is immediately apparent. At low collectives, small suction forces are present and the velocity gradients of the flow, at the immediate blade tip passage region, are not strong enough. This is due to the fact that the induced velocities are not high enough and the flow acceleration of the inlet lip is relatively small. By increasing the blade collective, these velocity gradients get steeper, and in a sense they reflect the vortex shedding caused by the blade tip vortices which rotate in the opposite direction of the rotor's rotation.

The increase in the blade collective, will accelerate the flow over the blade sections and will encourage the formation of the blade tip vortices. The blade tip vortices convect with a high velocity and constitute a primary cause of the low pressure area over the shroud-blade tip gap. The region of low suction forces over the shroud surface corresponds to the suction peaks which were discussed before in the shroud surface pressure-distributions section. In addition, for all blade collectives it can be seen that the flow is stagnated beneath the plane of the rotors, which is also the entrance of the diffuser.

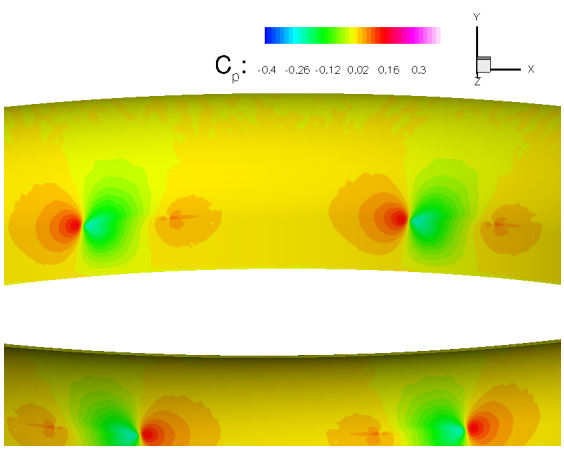

(a) Inlet lip $C_p$contours $\theta_{0.75R} = 0°$

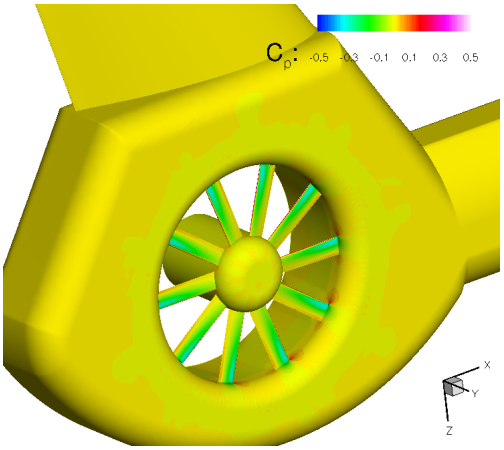

(b) Starboard surface C_p contours $\theta_{0.75R} = 0°$

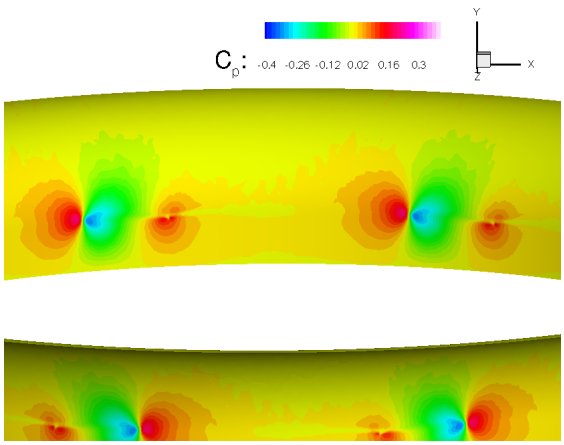

(c) Inlet lip C_p contours $\theta_{0.75R} = 5°$

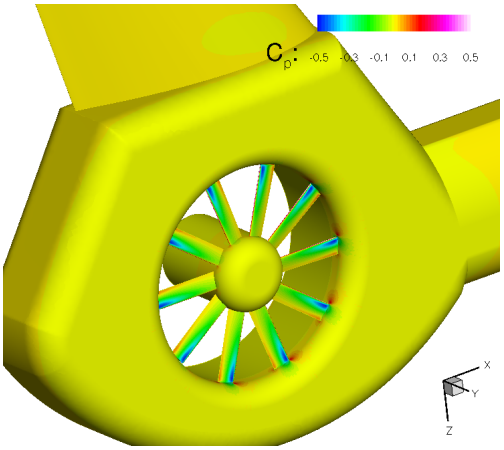

(d) Starboard surface C_p contours $\theta_{0.75R} = 5°$

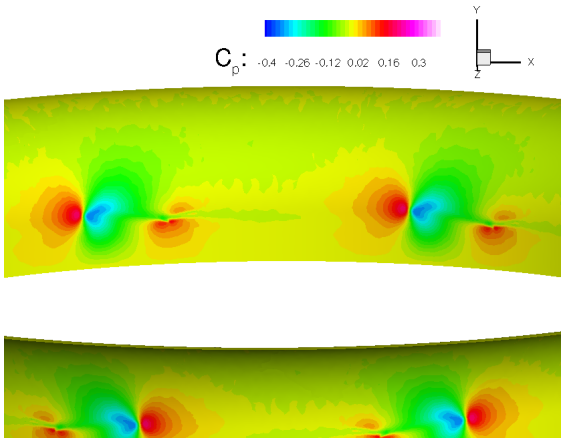

(e) Inlet lip C_p contours $\theta_{0.75R} = 10°$

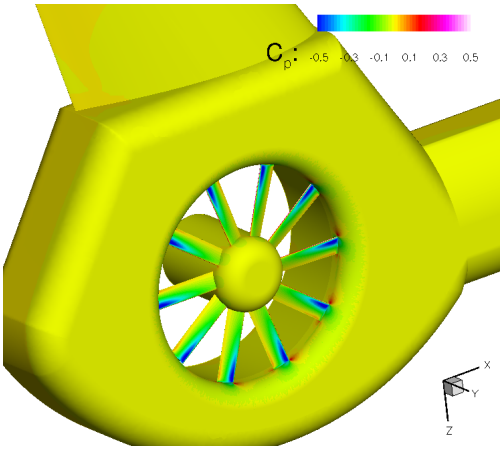

(f) Starboard surface C_p contours $\theta_{0.75R} = 5°$

Figure 4.8: Surface C_p contours for blade collective angles 0°, 5°,10°

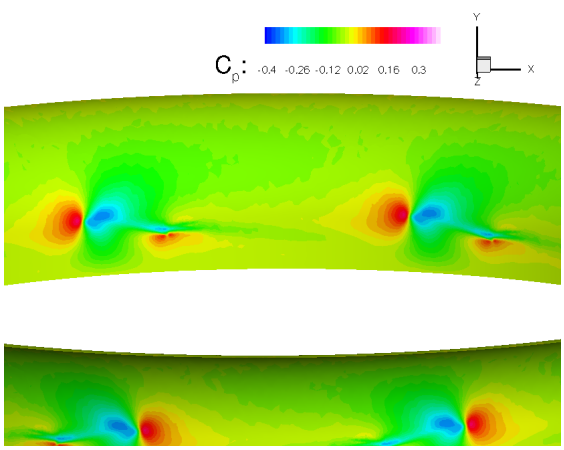

(a) Inlet lip C_p contours $\theta_{0.75R} = 15°$

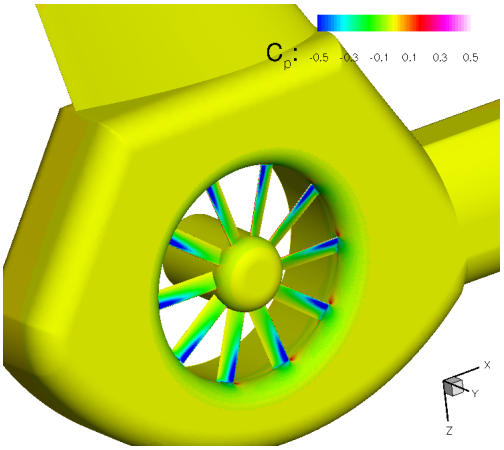

(b) Starboard surface C_p contours $\theta_{0.75R} = 15°$

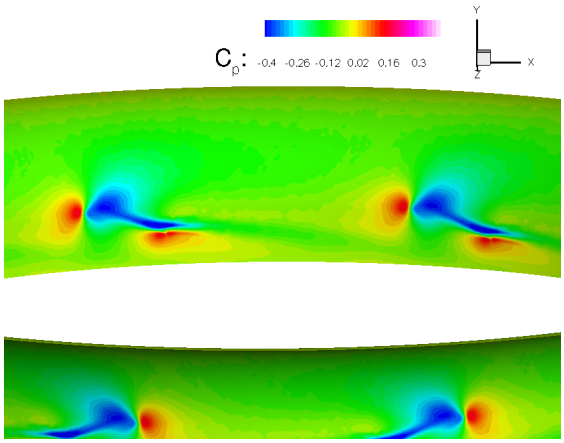

(c) Inlet lip C_p contours $\theta_{0.75R} = 20°$

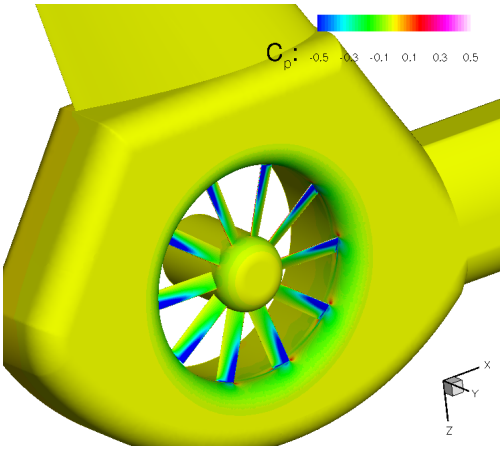

(d) Starboard surface C_p contours $\theta_{0.75R} = 20°$

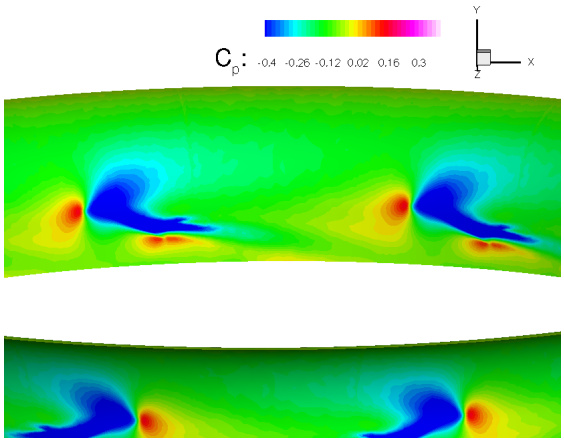

(e) Inlet lip C_p contours $\theta_{0.75R} = 25°$

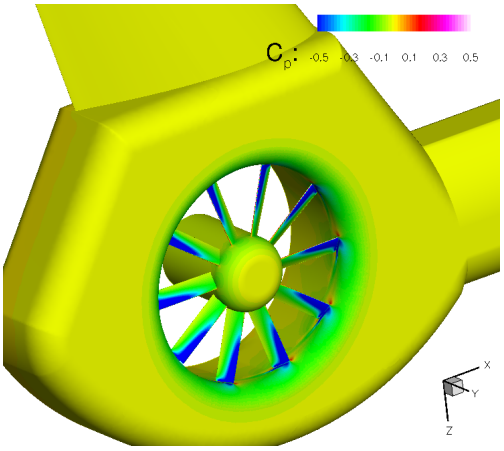

(f) Starboard surface C_p contours $\theta_{0.75R} = 25°$

Figure 4.9: Surface C_p contours for blade collective angles 15°, 20°,25°

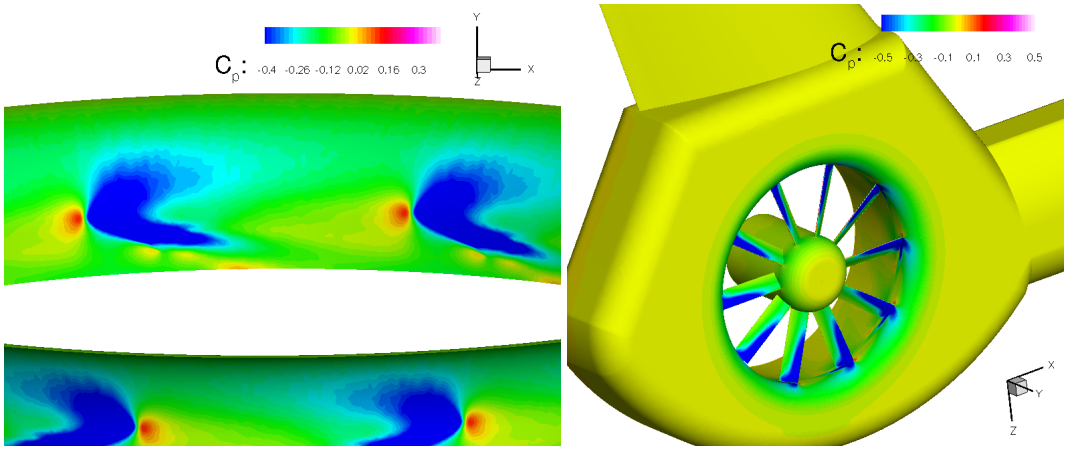

(a) Inlet lip C_p contours $\theta_{0.75R} = 30°$

(b) Starboard surface C_p contours $\theta_{0.75R} = 30°$

Figure 4.10: Surface C_p contours for blade collective angle 30°

The starboard plots indicate, as expected, that the pressure distribution is uniform over the blades due to the periodicity (quasi-periodic) of the flow which is an inherent characteristic of hovering flight. Finally, the starboard plots also suggest that the inlet lip of the shroud, and this is more apparent at the high collectives, is mainly responsible for the generation of the shroud thrust.

4.4 Flow-Field Visualisation

In order to explain further, as well as to illustrate, the complex flow regime of the hovering ducted tail rotor, a succinct overview of the flow-field will be presented. This will be done by illustrating the velocity vectors for different blade collective angles as well as the total pressure and axial velocity (induced velocity) distributions at the inlet, rotor (upstream and downstream) and diffuser plane.

4.4.1 Velocity Vector Plots

The velocity vector plots are a useful tool which can highlight the flow distribution. The purpose of this illustration is to show the effect, of increasing the blade collective angle on the flow distribution. The velocity vector plots as well as the total pressure planes were drawn for four distinct blade collective angles. The deployed blade collective angles range from 0° to 30° with an increment of 10° in order to cover both the extreme and intermediate values. This approach was followed due to the fact that it will be extraneous, in order to show the effect of the blade collective angle, to use all the simulated points. Figure 4.11 shows the deployed plane's location for deriving the velocity vector plots (mid-azimuth plane). The mid-azimuth plane is used extensively, in ducted tail rotor aerodynamics literature [11, 37, 38], in order to depict the flow distribution. Figures 4.12 and 4.13 show the overall flow distribution and the local distribution at the blade tip gap close to the shroud wall.

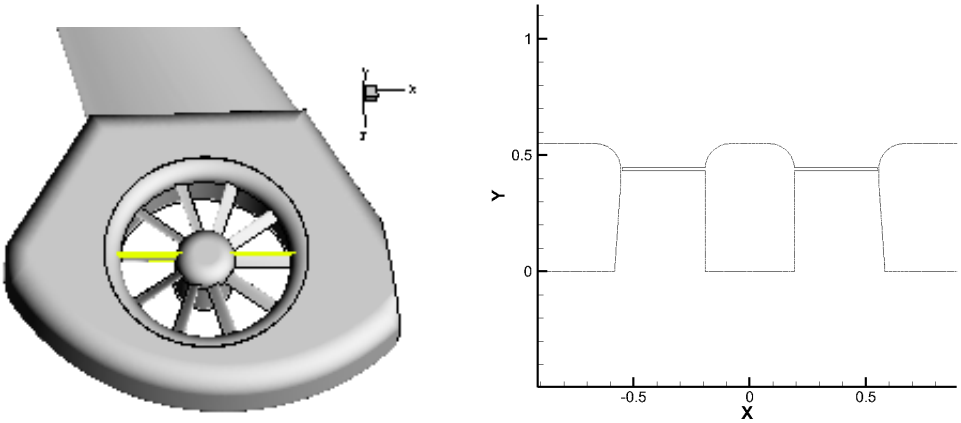

(a) Mid-azimuth plane location (b) Mid-azimuth plane 2D illustation

Figure 4.11: Planes location for the velocity vector plots

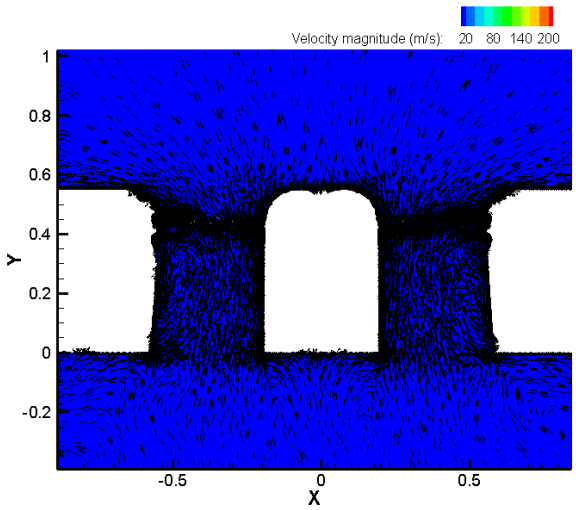

(a) Velocity vectors at mid-azimuth, $\theta_{0.75R} = 0°$

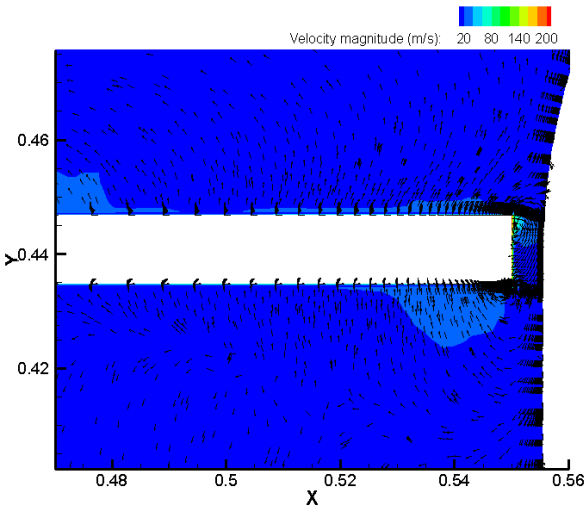

(b) Velocity vectors at blade tip region, $\theta_{0.75R} = 0°$

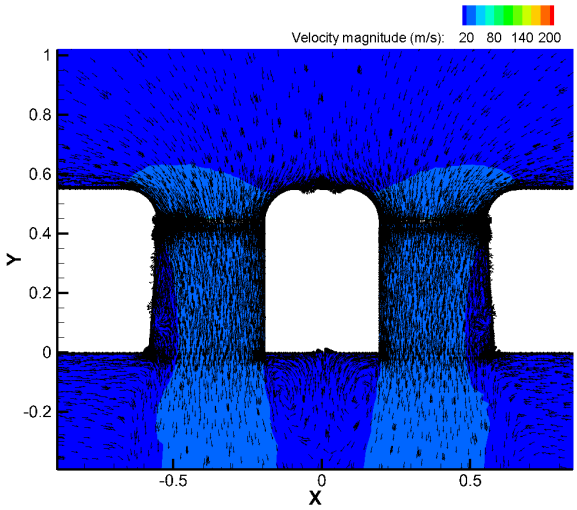

(c) Velocity vectors at mid-azimuth, $\theta_{0.75R} = 10°$

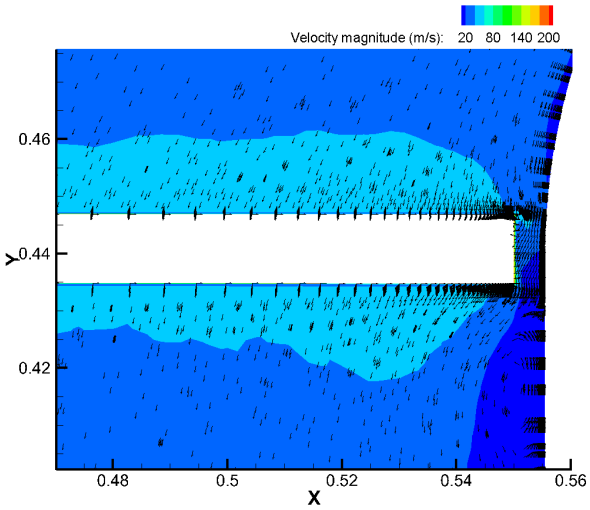

(d) Velocity vectors at blade tip region, $\theta_{0.75R} = 10°$

Figure 4.12: Vector plots for $\theta_{0.75R} = 0°$ and $\theta_{0.75R} = 10°$

A general observation that can be made, for each blade collective, is that the overall flow distribution is uniform, in terms of flow ingestion in and through the rotor, which is expected for hover. The rotor receives mass flow from all directions and does not show any significant recirculation zones.

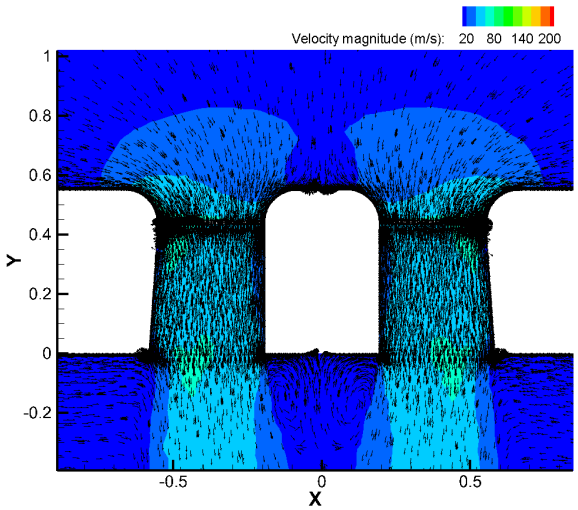

(a) Velocity vectors at mid-azimuth,$\theta_{0.75R} = 20°$

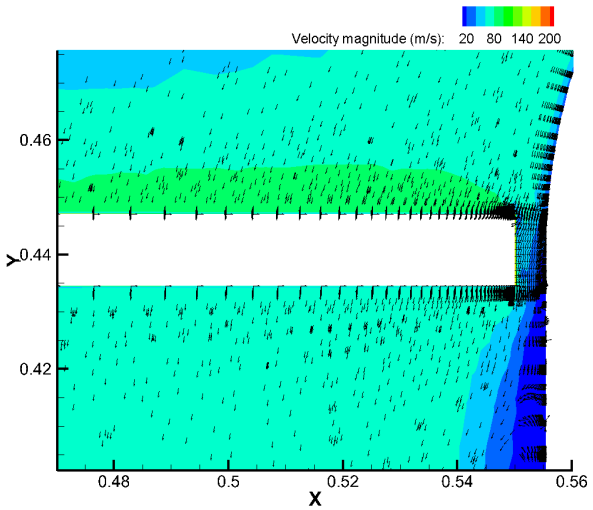

(b) Velocity vectors at blade tip region, $\theta_{0.75R} = 20°$

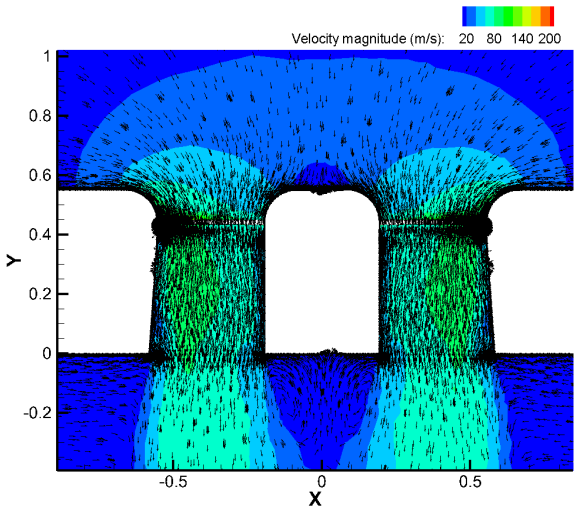

(c) Velocity vectors at mid-azimuth, $\theta_{0.75R} = 30°$

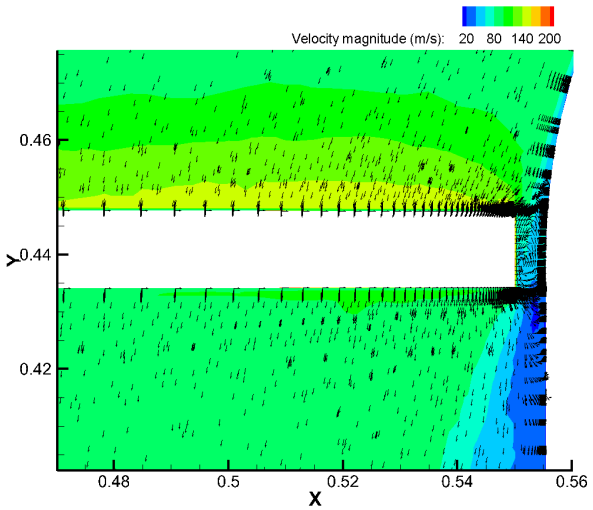

(d) Velocity vectors at blade tip region,$\theta_{0.75R} = 30°$

Figure 4.13: Vector plots for blade collective angles $\theta_{0.75R} = 20°$ and $\theta_{0.75R} = 30°$

However, separation zones start to build up at the vicinity of the rotor hub when the blade collective angle increases. This is due to the increased axial momentum which is caused by the increase of the induced velocity together with the effect of pressure build-up when the blade collective angle increases.

More precisely, the velocity vector plots indicate that the blade collective angle increase accomodates an increase in the local velocity magnitude. The rotational velocity of the ducted tail rotor is fixed therefore by increasing the blade collective angle, the induced velocity (downwash) increases which increases as well the resultant local flow velocity or relative wind (see Figure 3.6). The increase of the blade collective angle increases the thrust of the rotor which is manifested with low-pressure regions upstream of the rotor (as it was shown in the C_p distributions, Figures 4.8-4.10). As far as the shroud thrust is concerned, the increase in velocity magnitude corresponds to the low pressure regions shown in the C_p distributions over the inlet lip. At the diffuser section, the local velocity magnitude is low (close to the freestream quiescent velocity values) and corresponds to an over pressure region.

The imbalance of pressure, over the inlet lip and diffuser sections is the main cause of the shroud thrust, which is of course dependent on the blade collective angle. Finally, it can also be seen that for the case of $\theta_{0.75R} = 0°$, at the blade tip region the flow reverses indicating a negative thrust. This is due to the very low blade collective angle which corresponds to a low blade loading coefficient (see Figure 4.1a). Due to the fact that the applied blade twist is linear and negative (0° referenced at 75% of blade radius), it means that at the tip, the blade collective will be negative. Nevertheless, the total thrust produced by the blade at $\theta_{0.75R} = 0°$ is still positive. In autorotation and in manoeuvres, the ducted tail rotor can have negative values of blade collective (reverse thrust) [4, 7]. This implies that the rotor produces thrust in the opposite direction than in the case of positive blade collective angles. However, negative blade collective angles have not been tested in this project, due to the fact that autorotation, manoeuvres and generally reverse thrust conditions were not taken into consideration.

4.4.2 Total Pressure Planes

In order to describe further the flow-field within the ducted tail rotor, the total pressure distributions are shown. The regions, as illustrated in Figure 4.14, which can give a reasonable description of the flow-field are the inlet, rotor (upstream and downstream) and the diffuser. For all the derived planes the rotation of the disc is counter-clockwise. Figure 4.15 refers to the total pressure distribution for a $\theta_{0.75R} = 0°$. It is shown that for the inlet and diffuser sections, the total pressure distribution is almost the same (though the total pressure is slightly higher at the diffuser section). This is due to the expansion of the flow to atmospheric ambient conditions as well as the contraction of the rotor wake which contributes to the total pressure. It must be noted here that at the inlet section, the hub area (white circular area) seems "smaller" than the one of the diffuser and rotor planes. This is mainly due to the location used for the inlet plane, in order to fully depict the inlet lip area, which can show any potential flow separation in forward flight.

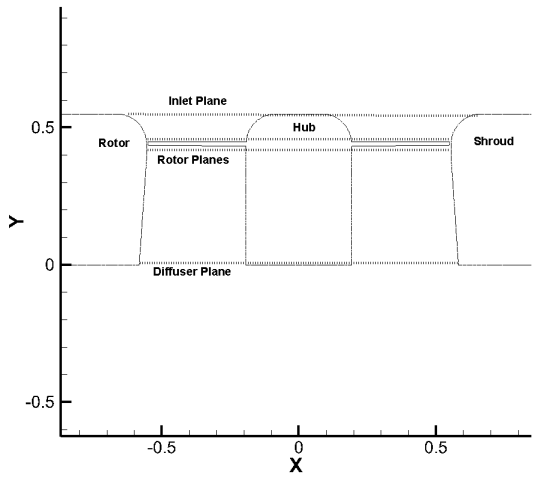

Figure 4.14: Location of planes, at the miz-azimuth section, for driving the total pressure distributions

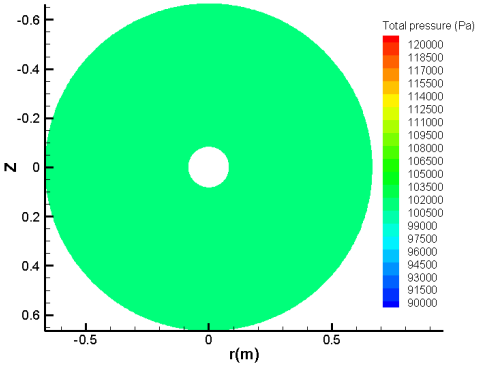

(a) Total pressure distribution over the inlet plane,$\theta_{0.75R} = 0°$

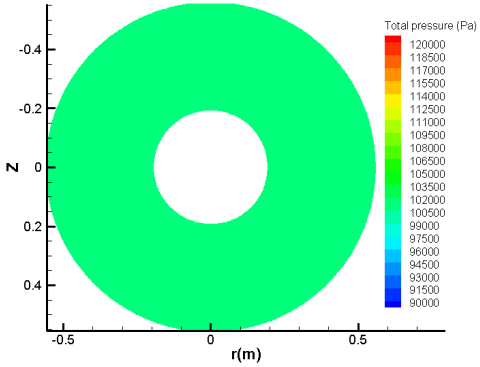

(b) Total pressure distribution over the diffuser plane, $\theta_{0.75R} = 0°$

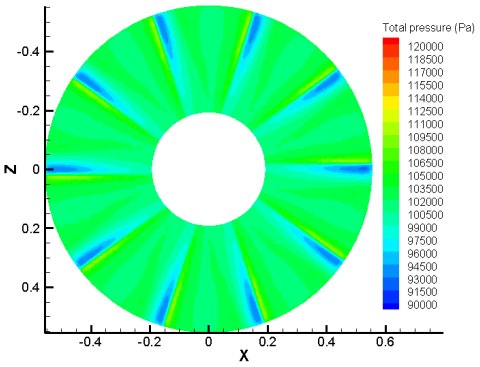

(c) Total pressure distribution over the upstream rotor plane, $\theta_{0.75R} = 0°$

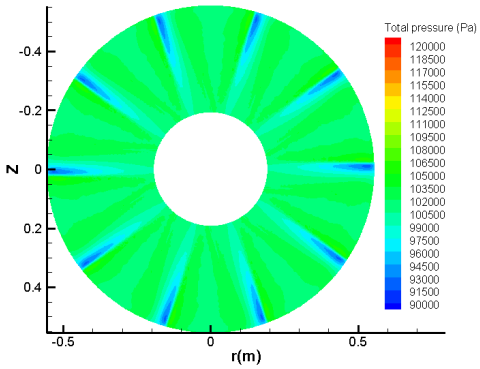

(d) Total pressure distribution over the downstream rotor plane, $\theta_{0.75R} = 0°$

Figure 4.15: Total pressure distribution, $\theta_{0.75R} = 0°$

For the regions upstream and downstream of the rotor there is not any apparent difference in the contours. However, by expressing the results along a polyline (two-dimensional plots) which crosses the mid-azimuth plane later on, it will be shown that the total pressure is slightly increased at the downstream location. This increase comes in agreement with the theory which dictates that total pressure increases through the rotor due to the fact that the rotor provides work to the surrounding fluid i.e. increasing its kinetic energy and pressure.

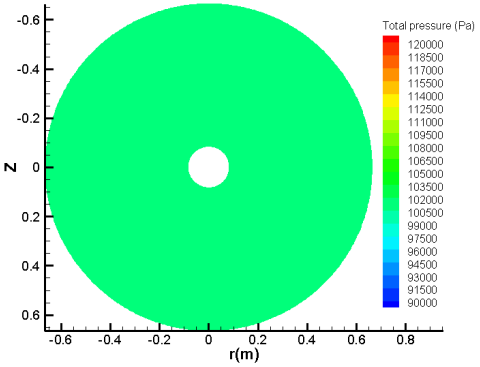

(a) Total pressure distribution over the inlet plane, $\theta_{0.75R} = 10°$

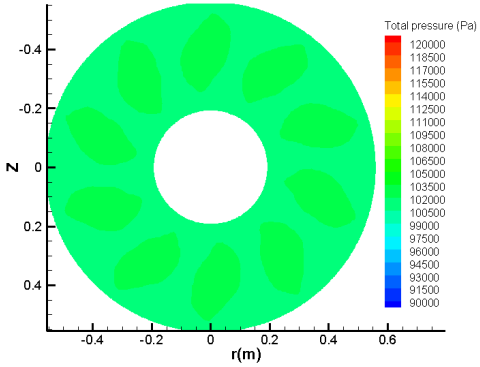

(b) Total pressure distribution over the diffuser plane, $\theta_{0.75R} = 10°$

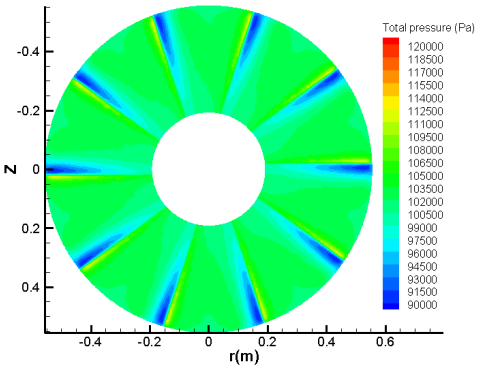

(c) Total pressure distribution over the upstream rotor plane, $\theta_{0.75R} = 10°$

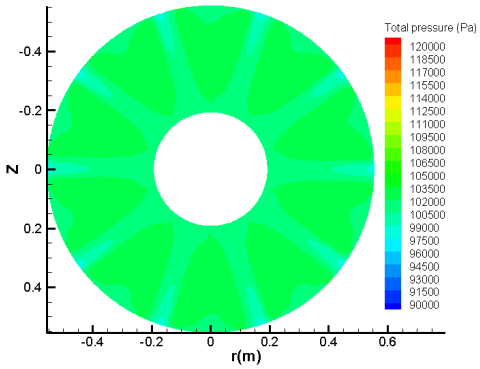

(d) Total pressure distribution over the downstream rotor plane, $\theta_{0.75R} = 10°$

Figure 4.16: Total pressure distribution, $\theta_{0.75R} = 10°$

Figure 4.16 illustrates the total pressure distributions for $\theta_{0.75R} = 10°$. Between the inlet and diffuser plane it can be seen that there are small differences (which would be highlighted better by expressing the two-dimensional distributions). The flow at the diffuser plane indicates that it has expanded to ambient values leading to an over-pressure region over the diffuser.

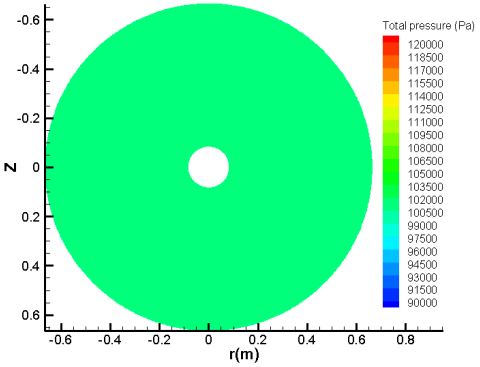

(a) Total pressure distribution over the inlet plane, $\theta_{0.75R} = 20°$

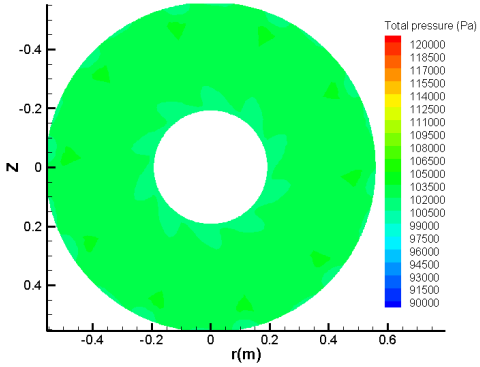

(b) Total pressure distribution over the diffuser plane, $\theta_{0.75R} = 20°$

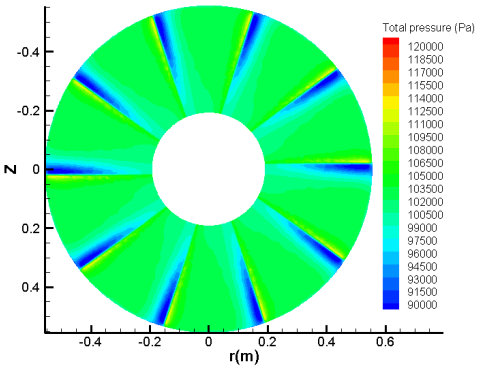

(c) Total pressure distribution over the upstream rotor plane, $\theta_{0.75R} = 20°$

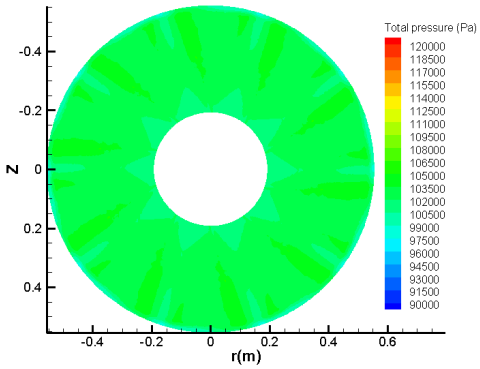

(d) Total pressure distribution over the downstream rotor plane, $\theta_{0.75R} = 20°$

Figure 4.17: Total pressure distribution, $\theta_{0.75R} = 20°$

The upstream and downstream total pressure distributions convey that the total pressure increases at the downstream region of the rotor as expected. In addition, by inspecting Figure 4.16d, it can be seen that at the blade tips the total pressure has lower values. This phenomenon expresses the losses in thrust, which inevitably occur at the blade tip regions, as well as the local high-velocities. However, these high velocities create the low pressure regions over the inlet lip which are the main contributor of the shroud thrust.

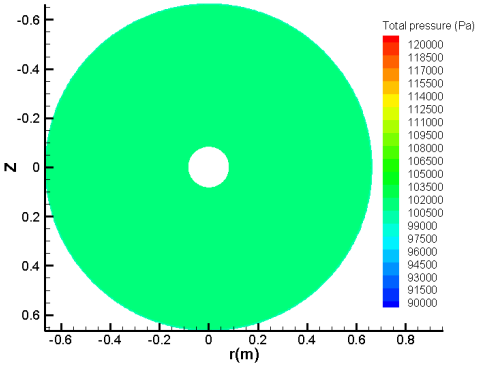

(a) Total pressure distribution over the inlet plane, $\theta_{0.75R} = 30°$

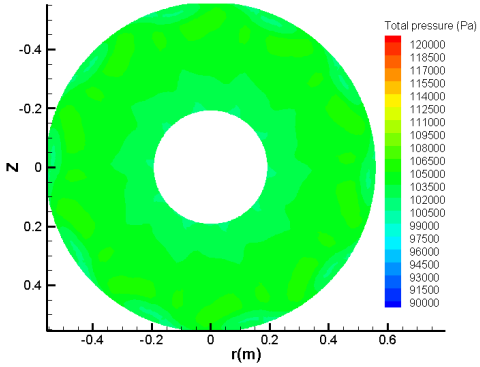

(b) Total pressure distribution over the diffuser plane, $\theta_{0.75R} = 30°$

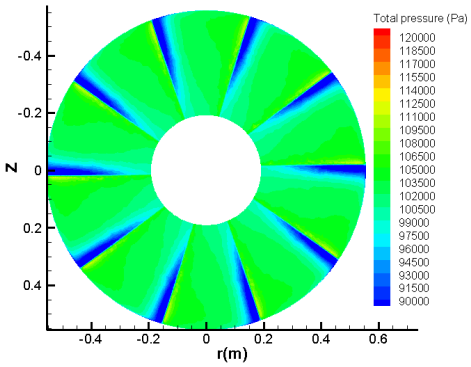

(c) Total pressure distribution over the upstream rotor plane, $\theta_{0.75R} = 30°$

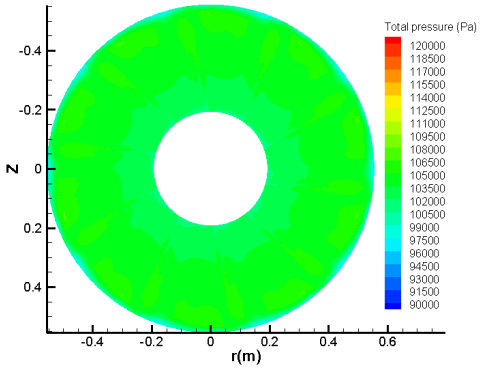

(d) Total pressure distribution over the downstream rotor plane, $\theta_{0.75R} = 30°$

Figure 4.18: Total pressure distribution, $\theta_{0.75R} = 30°$

It must be noted that the last conclusion, concerning the losses in thrust, holds for every examined blade collective angle. However, due to the low thrust value of $\theta_{0.75R} = 0°$ this conclusion can not easily be discerned at least qualitatively. Figures 4.17-4.18 show the total pressure distributions for blade collective angle of $\theta_{0.75R} = 20°$ and $\theta_{0.75R} = 30°$ respectively. It can be acknowledged, that there is a profound effect of the blade collective angle increase on the total pressure distributions. From comparing the inlet and diffuser planes, it can

be seen that the flow mainly has expanded to ambient values but low total pressure regions are present near the hub and the blade tip. The low total pressure regions near the hub are manifested by the presence of separation (two counter-rotating vortices) at the vicinity of the hub (at the plane of the diffuser) as shown in the vector plots previously (Figures 4.12-4.13). By increasing the blade collective angle the aforementioned phenomena, concerning the hub's separation regions and the high velocities at the blade tip, become more evident due to the increase of thrust.

4.4.3 Total Pressure & Axial Velocity Distributions

In the current sub-section, the total pressure and axial velocity distributions, along a polyline drawn at the mid-azimuth plane are discussed. Such a description can explain further the impact of increasing the blade collective angle on the flow within the ducted rotor. Figure 4.19 shows the total pressure distributions over the inlet, rotor and diffuser (exit of the duct) planes for the blade collective angles which were used to illustrate the total pressure planes previously. At the inlet plane, the total pressure remains constant for all the blade collective angles. This happens because the flow starts to accelerate at this point and this location represents the entrance of the duct (ambient atmospheric values). Upstream of the rotor, the total pressure decreases with increasing blade collective angle. The acceleration of the flow-field and the associated increase of the induced velocity will create suction forces upstream of the rotor. These suction forces have their greatest value at the highest blade collective angle. Immediately downstream of the rotor the total pressure magnitude increases, which illustrates the addition of energy to the flow-field from the rotor. Again, the highest total pressure magnitude appears at the highest blade collective angle.

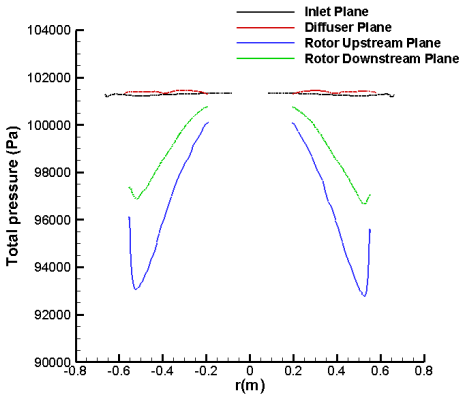

(a) Total pressure distributions over the inlet, rotor and diffuser planes at $\theta_{0.75R} = 0°$

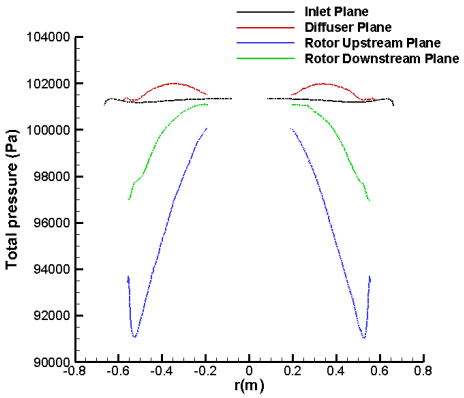

(b) Total pressure distributions over the inlet, rotor and diffuser planes at $\theta_{0.75R} = 10°$

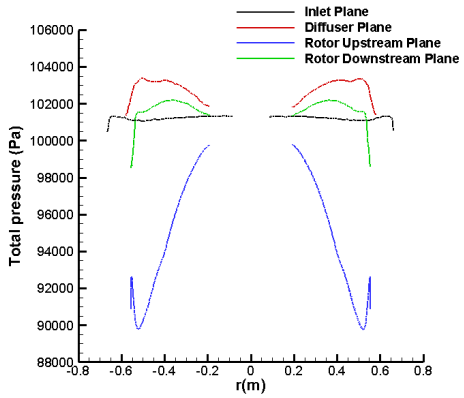

(c) Total pressure distributions over the inlet, rotor and diffuser planes at $\theta_{0.75R} = 20°$

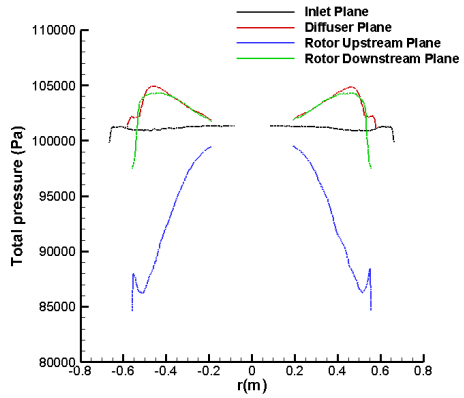

(d) Total pressure distributions over the inlet, rotor and diffuser planes at $\theta_{0.75R} = 30°$

Figure 4.19: Total pressure distributions over the inlet, rotor and diffuser planes

Finally, at the diffuser section the flow has expanded back to atmospheric ambient conditions. However, the total pressure magnitude increases due to the corresponding increase of the slipstream (axial velocity increase). For all the spanwise variations shown, it must be noted that the inlet plane and diffuser planes extend further after the location of the blade's radius (which is r(m)=0.55m and -0.55m, the blades are distributed symmetrically). It can be acknowledged that the loading increases towards the blade tip region as

expected. This is better illustrated by looking at the peaks of the downstream plane distributions for all blade collective angles. In addition, the blockage effect caused by the shroud wall and its boundary layer development [5], is shown by the decrease of the total pressure magnitude after the blade tip region. This effect is more apparent when the blade collective angle increases due to more energised flow-field which also means more induced power losses. The total pressure distributions together with the velocity vector plots and the pressure coefficient contours give an adequate description of the complex flow behavior within the duct. In addition, it can be acknowledged that there is a strong interdependence of the shroud and the rotor, on the grounds that blade collective angle changes alter the thrust of the shroud. In order to better show this strong coupling and further explain the effect of blade collective angle, the axial velocity distributions are shown. The axial velocity, in the case of the ducted tail rotor, is equal to the induced flow. Figure 4.20 shows the axial velocity distributions over the inlet, rotor and diffuser planes for a range of blade collective angles. For each plot, increasing absolute values of axial velocity are towards the negative y axis hence lower negative values represent increased axial velocity magnitude. By inspecting Figure 4.20, it can be seen that for $\theta_{0.75R} = 0^\circ$ (see Figure 4.20a), the trends of the curves at the upstream and downstream locations are different than the trends of the rest angles. This is due to the change of flow behavior at this angle. As it was stated previously, at the vicinity of the blade tip region the flow reverses due to the local negative values of pitch. The flow reversal is signified, at the upstream location, by the change of sign (around r(m)=0.45). The same trend applies for the downstream location but in a much smaller degree. However, it must be mentioned here that positive values of axial velocity (indicating flow reversal) are not present in the majority of the blade's portion.

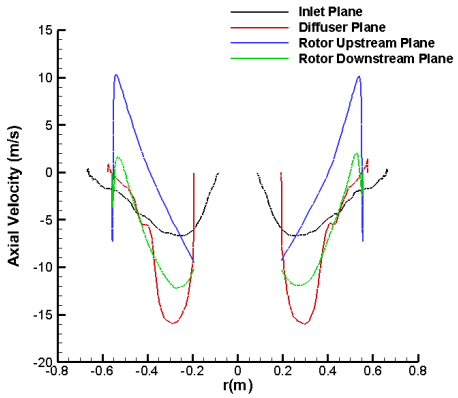

(a) Axial velocity distributions over the inlet, rotor and diffuser planes at $\theta_{0.75R} = 0°$

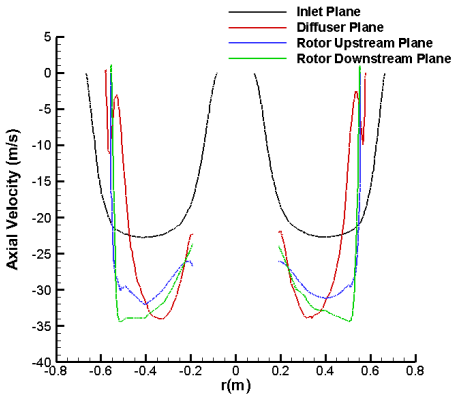

(b) Axial velocity distributions over the inlet, rotor and diffuser planes at $\theta_{0.75R} = 10°$

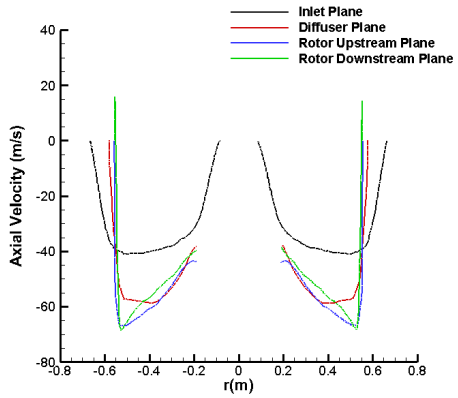

(c) Axial velocity distributions over the inlet, rotor and diffuser planes at $\theta_{0.75R} = 20°$

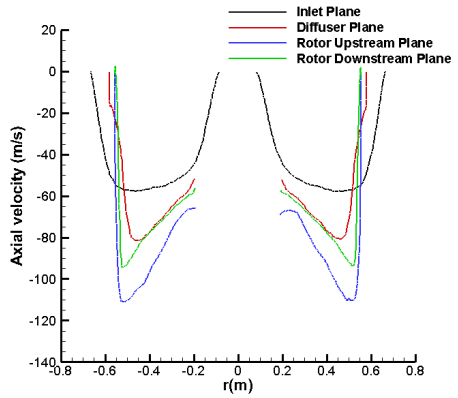

(d) Axial velocity distributions over the inlet, rotor and diffuser planes at $\theta_{0.75R} = 30°$

Figure 4.20: Axial velocity distributions over the inlet, rotor and diffuser planes

The total thrust of the blades, for $\theta_{0.75R} = 0°$, is still positive[3] though very small in value. By looking at the spanwise variation of the axial velocity, it can be said that the axial velocity approaches the value of zero at the shroud wall (for each angle shown). This is due to the blockage effect of the shroud. Figure 4.20a shows that the peak downwash location at the diffuser plane is

[3]Despite the obvious fact, that these distributions can help in describing the flow behavior, they only represent a snapshot of the flow at the particular plane. Thus, the macroscopic values of thrust give the conclusion about the the overall flow behavior.

located inboard and it represents the contraction of the wake [9]. However, this conclusion at first sight may not seem reasonable, due to the fact that the shroud is supposed to restrain the natural contraction of the wake. By inspecting all the plots of Figure 4.20 it can be seen at the diffuser plane, the peak downwash moves outboard (towards the shroud wall). In addition, it can be seen that for low blade collective angles the axial velocity is higher at the downstream location than the upstream (signifying contraction of the wake). However, as the blade collective angle increases the axial velocity will be smaller immediately downstream of the rotor than upstream of the rotor.

The aforementioned signify that the blade collective angle does have an effect on the effective expansion of the flow that can be achieved by the shroud. The degree of expansion of the wake can be estimated by applying the momentum theory. By applying equation 2.3 which gives the expansion ratio of a ducted rotor, the wake contraction ratio i.e. the ratio of the radius of the wake to the radius of the rotor can be computed:

$$\frac{r_\infty}{R} = \sqrt{\sigma_d} \tag{4.6}$$

where r_∞ is the radius of the wake.

The contraction ratio of an open rotor ($\sigma_d = 1/2$) is $1/\sqrt{2}$. For a ducted rotor the thrust sharing between the shroud and the rotor relates to the value of expansion ratio (equation 2.7). Therefore by combining equations 2.7 and 4.6 the wake contraction ratio takes the form:

$$\frac{r_\infty}{R} = \frac{1}{\sqrt{2\left(1 - \frac{T_{shroud}}{T_{total}}\right)}} \tag{4.7}$$

Therefore the wake contraction ratio can be regarded as a function of $\frac{T_{shroud}}{T_{total}}$.

$\theta_{0.75R}$	$\frac{T_{shroud}}{T_{total}}$	$\frac{r_\infty}{R}$
0°	0.266	0.825
5°	0.351	0.877
10°	0.409	0.920
15°	0.480	0.980
20°	0.504	1.004
25°	0.507	1.008
30°	0.512	1.012

Table 4.2: Wake contraction ratio as a function of the shroud-rotor thrust sharing

Values smaller than 1 signify contraction of the wake whereas values of 1 and above imply expansion of the wake. The momentum theory analysis for the thrust augmentation factors, showed that the thrust sharing is a function of the blade collective angle (see Figure 4.7). The values of the thrust sharing at hover and effective wake contraction are tabulated below:

By inspecting Table 4.2, an interesting conclusion can be made about the expansion of the wake of a ducted tail rotor. It can be seen that the wake at low blade collective angles does contract (up until blade collective angle of 20°). For higher blade collective angles ($\geq 20°$) the wake expands as it is supposed to be. The contraction of the wake in ducted tail rotor (for MAV applications) has also been reported in the literature [10]. The reason behind this phenomenon is solely the blade collective angle. When the blade collective angle increases, the flow below the rotor becomes more energized i.e. the static pressure will be higher. This high pressure field, together with the expanding area of the diffuser, will decelerate the flow hence restricting the natural tendency of the wake to contract. The ideal expansion of the wake (using the ideal shroud thrust augmentation factor of 0.554, see Table 4.1) based on momentum theory will 1.058. Therefore, there is a percentage difference of -4.34% between the computed wake contraction ratio (at the maximum blade collective angle) and

the ideal value provided by momentum theory. This can be due to the non-ideal losses associated with the viscosity of the fluid.

4.5 Chapter Summary

The hover results have been presented and compared against public domain performance trends. The hover simulations have been performed at 7 distinct simulation points in order to reflect a representative operating blade collective range. The performance polar curves indicate that the results are valid and conform to the expected trends. It was shown, that the shroud and rotor thrust increase with increasing blade collective angle as expected. This increase, for the case of the shroud, is due to the accelerated flow over the shroud inlet lip which experiences suction forces. The rotor thrust increase is due to the increased flow acceleration over the blades which creates more lift. In addition, the computed blade loading coefficient, at the greatest blade collective angle (30°), compares with the value ($C_{Ttotal}/\sigma = 0.33$) of a similar configuration. Furthermore, it was presented that the trend of the FM curve, as well as its absolute value compares well with public domain data. The resulting hover performance polar curves can be used in order to estimate the power consumption for a given/required thrust.

Finally, due to the fact that detailed experimental data were not available, an extra step towards the verification of the results was used, the thrust sharing between the shroud and the rotor. momentum theory was employed for this task in order to provide theoretical upper values. It was found that the total thrust augmentation factor has a 8.5% difference with the maximum theoretical value. This result compares well with the available data from the Kamov-60 helicopter [25] which reflected a percentage difference of 9%. In addition, the

velocity vector plots have been shown in order to give a qualitative description of the flow. The total pressure and axial velocity distributions gave information about the effect of changing the blade collective angle. It was found that the blade collective angle has a drastic effect on the effective expansion of the wake immediately downstream of the rotor. Finally, the application of the presented hover performance maps for the estimation of power consumption as well as the forward flight performance maps, will be presented in Chapter 5.

Chapter 5

Forward Flight Performance Maps

This chapter presents the performance of the generic ducted tail rotor in forward flight. In a similar fashion with the hover results, the associated analysis will be presented in terms of performance characteristics (thrust and power) at the different advance ratios and the different blade collective. In addition, the shroud surface pressure distributions will also be presented. For the forward flight case apart from investigating the effect of the blade collective over the pressure distributions, the effect of the forward flight speed will also be discussed. The non-dimensionalisation of the thrust and power coefficients is performed in the same way as for the hover case.

5.1 Grid system

5.1.1 Computational Domain and Boundary Conditions

The specific details of the geometry of the generic ducted tail rotor geometry have been presented before in section 3.3 (p.g 84) and will not be repeated here. The medium mesh that has been used for the simulations is approximately

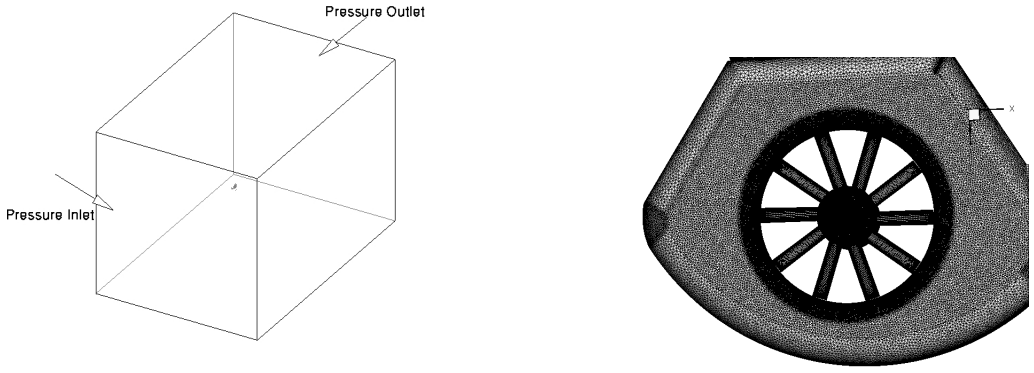

(a) Computational domain

(b) Starboard view of the computational surface grid

Figure 5.1: Computational domain and mesh

19 millions cells. For the construction of the computational grid, the same methodology has been applied as in the KAMOV-60 validation case. To be more specific the same methodology has been used in order to create a similar topology and retain a similar grid distribution. Fig 5.1 illustrates the deployed computational domain and the resulting surface grid of the configuration. The computational domain is consisted of a rectangular parallelepiped (rectangular cuboid) with a length of $100 \times l_{ref}$ and both the width and height are $80 \times l_{ref}$ where l_{ref} is the rotor diameter (1.1m). The reason for chosing a computational domain of that size is to avoid any possible numerical reflections by assuring that the flow has expanded and developed considerably well. For the forward flight case, the sides of the pressure inlet and pressure outlet are shown in the plot. The other sides can have as boundary conditions, a symmetry condition or they can be assigned as an inviscid wall.

In the present simulations, the symmetry boundary condition was used because they can also be used to model a zero-shear wall in viscous flows [51]. Thus, the remaining sides were assigned with the symmetry boundary condition. Due to the fact that the same grid system is used for the hover simulations as well,

the boundary conditions cannot be the same. The only difference is that the top side towards the negative Z axis direction will be assigned as a pressure inlet and the bottom side, towards the positive Z axis direction, was assigned as a pressure outlet. The remaining sides were assigned as pressure inlets and the velocity specification for all the pressure inlets was normal to the surface (in order for the velocity vectors to point towards the body).

5.1.2 Fin Grid

Until now the importance of the shroud-rotor system has been stressed due to the dynamic relationship of these heterogeneous components. However, in forward flight the fin plays an important role as it further contributes to the off-loading of the rotor. Thus, in order to represent the fin a high quality grid must be employed. The fin grid system is shown in Fig 5.2 and it consists of the surface grid of the fin, the boundary layer mesh and the junction with the shroud. The medium surface grid of the fin is shown in Fig 5.2a and it can be seen that the grid distribution is performed towards the fin tip as well as the root.

The boundary layer mesh is shown in Fig 5.2b and it consists of 26 inflation layers in order to adequtely represent the high velocity gradients of the viscous wall. The y^+ value was 1 and this value corresponds to a first cell's distance from the wall of the order of 0.3×10^{-5}. At the rectangular blade tip, the grid, on the surface of the fin, is clustered towards this region in order to capture the tip vortex and represent the loading of the fin which increases towards the tip. The surface of the blade tip wall at $r/R = 1$ (Fig 5.2c) is represented with an unstructured mesh on the grounds of flexibility of the mesh generation process and that there is not any adjacent wall (as in the case of the rotor blades).

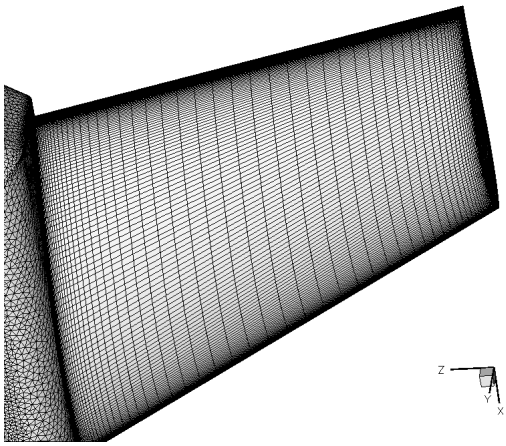

(a) Surface grid of the fin, grid distribution

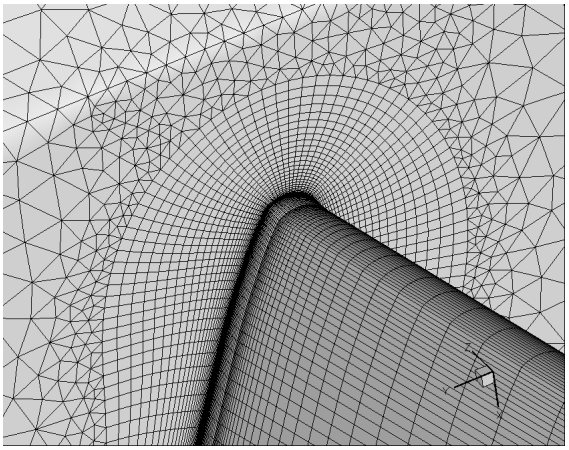

(b) Boundary layer mesh at the shroud-fin junction

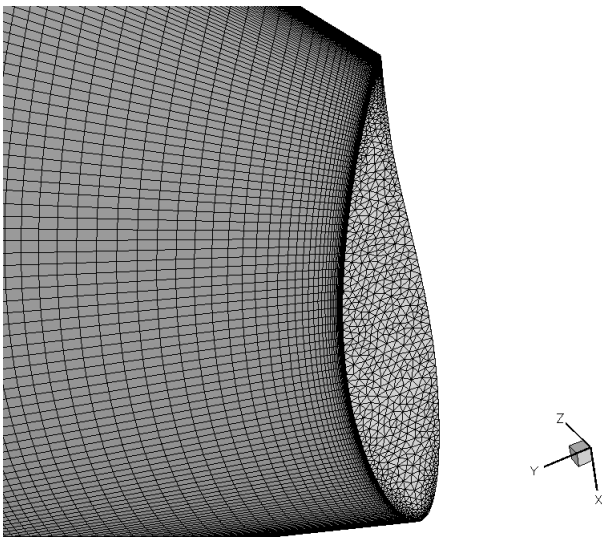

(c) Blade tip clustering

Figure 5.2: Fin grid

The tailboom surface grid is illustrated in Fig 5.3 which is assigned as a viscous wall in the CFD simulations. As it was explained before due to the fact that the tailboom does not contribute to the generation of the configuration's thrust, there is no need for significant clustering. However, the boundary layer mesh was represented with 20 inflation layers in order to keep a y^+ value approximately close to 1.

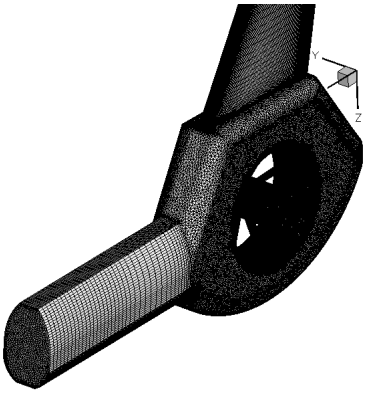

Figure 5.3: Tailboom surface grid

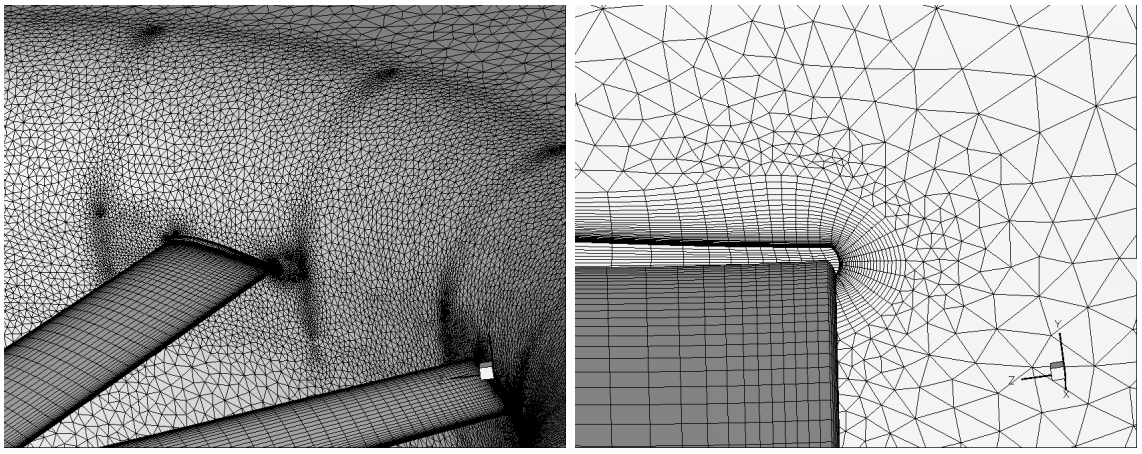

(a) Shroud inlet surface grid

(b) Boundary layer grid of the blade and blade tip passage area

Figure 5.4: Inlet lip and blade surface grids

Fig 5.4 shows a portion of the inlet surface mesh together with the boundary layer of a blade. The grids were constructed with the same methodology as applied in the validation case. The shroud's boundary layer mesh has 20 inflation layers whereas the blade's boundary layer mesh had 30 inflation layers. The first cell's distance from the wall for both the blade and the shroud was of the order of 10^{-5}.

5.1.3 Grid Independence Study

A grid independence study was performed in order to show that the solution does not change significantly with further grid refinement. However, it will be reported again that due to the hybrid topology of the mesh as well as the complexity of the geometry, a constant grid refinement ratio could not have been used. A uniform grid refinement, as proposed by Roache [50] in all three directions is difficult to be achieved in such geometries. However, the C_p distributions can illustrate the differences between the different refinement levels.

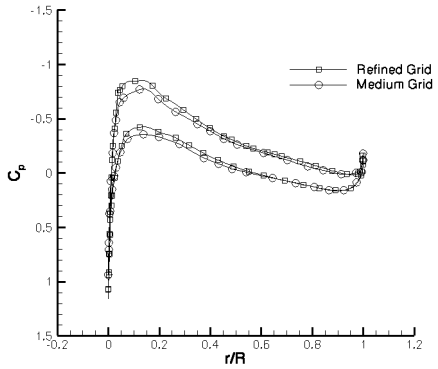

(a) Rotor blade section at 0.95%R

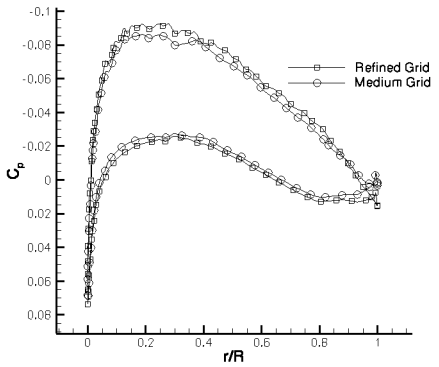

(b) Fin section at 90% of the wingspan

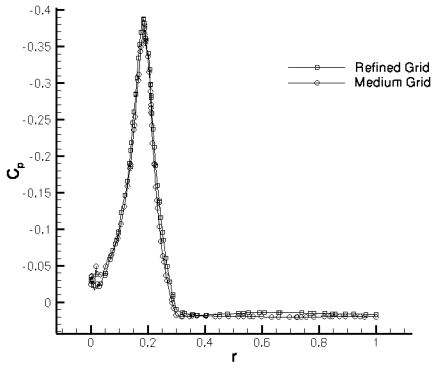

(c) Shroud section at mid-azimuth

Figure 5.5: Grid independence study C_p distributions of a rotor blade, shroud and fin

For the sake of saving time, only two grid sizes were taken into account, a medium grid with approximately 19 million cells and a refined grid of about 29.5 million cells. The C_p distributions for a rotor blade, inlet and diffuser section and the fin are shown in Fig 5.5 and suggest that the computational results are reasonably grid independent.

5.2 Performance Polar Curves

In forward flight the performance maps must give information about the power consumption at a given thrust in the same way as in hover. Clearly the additional parameter which must be taken into account is the forward flight speed and its relationship with the blade collective angle. The performance maps of the forward flight need to reflect the change of the blade collective angle which has its maximum value (30°) in hover and then reduces progressively with increasing flight speed. This reduction in the collective angle corresponds to the off-loading of the rotor from the shroud and the fin. Therefore the simulation were done both at different blade collectives and different advance ratios.

An available distribution of blade collective angle with respect to forward flight speed of the H-76 FANTAIL is provided by Wright [7] (see Fig 2.14 p.g 47). According to the aforementioned, the range of the different freestream velocity values that were used for the simulations, with respect to blade collective angle is illustrated in Table 5.1. The method of performance mapping, although it is convenient and can provide an estimate at non-simulated points, its fidelity depends on the number of available simulated data. The ideal scenario would have been to simulate as many cases as possible (with a smaller increment of blade collectives as well) in order to increase the accuracy of the map.

$\theta_{0.75R}$	V_∞
$0°$	$20-140$ knots with an increment of 20 knots
$5°$	$20-140$ knots with an increment of 20 knots
$10°$	$20-140$ knots with an increment of 20 knots
$15°$	$20-80$ knots with an increment of 20 knots
$20°$	$20-40$ knots with an increment of 20 knots
$25°$	$20-40$ knots with an increment of 20 knots

Table 5.1: Range of V_∞ at different blade collectives

However, this would require an enormous amount of computational resources. Therefore, due to the fact that the scope of this work is not to simulate a helicopter in real time flight, a higher increment (20 knots) was used. On the other hand, the calculated performance maps can provide an estimate of the power consumption at specified forward flight conditions. Before discussing the performance polar curves, it must be acknowledged that a fundamental assumption of the current CFD simulations of the forward flight regime were steady state. This was performed on the grounds of saving time and computational resources. A typical unsteady simulation for such a configuration and by employing a sliding mesh would need approximately 5 complete rotor revolutions, with a time step of $2°$ blade azimuth [8].

The performance polar curves for the different examined blade collectives are shown in Figures 5.6-5.8. Each polar curve for each angle includes the total thrust coefficient variation with increasing advance ratio as well as the power polar. The variation of advance ratio is performed using the data from Table 5.1. The individual thrust components of the rotor, shroud and the fin are divided by the solidity and each is represented by a different symbol. However, it must be stressed that there is not e.g a fin loading coefficient. As explained before, it is common to divide the total thrust with the solidity of the blade.

In the power polar curves (C_P/σ vs C_{Ttotal}/σ) the power coefficient was computed by using the rotor's torque only (as the shroud and fin do not consume any power). By inspecting Fig 5.6, which shows the performance polar curves for $\theta_{0.75R} = 0° - 5°$ it can be seen that by increasing the advance ratio all the individual thrust components increase as well. For the $\theta_{0.75R} = 0°$ rotor thrust increases almost linearly and this is due to the increase in-plane velocity at the rotor plane. An increase in the freestream velocity will increase the mass flow through the rotor which further explains the increase in thrust.

The shroud thrust increases as well following the same trend with the rotor and it can be seen that for high advance ratios the shroud thrust is greater than the rotor thrust. The increase in shroud thrust occurs due to the acceleration of the flow over the inlet lip of the shroud (as in hover). Unfortunately, in the forward flight case momentum theory cannot be used as it is done in hover in order to derive ideal thrust augmentation factors. Such factors in forward flight could be derived by combining experimental data and flight test campaigns [7]. As long as the fin's contribution to the antitorque requirements, it is apparent that the thrust of the fin is greater than the rotor's and the shroud's thrust and is increasing at a higher rate.

It can also be acknowledged that fin's thrust scales with the square of the freestream velocity. By inspecting Fig 2.14 it can be seen that during high forward flight speed ($\sim$ 140 knots) the range of collectives, for the given rotorcraft configuration, is around $0° - 5°$ which furthers suggests the significant off-loading provided by the fin. The polar curve for this collective exhibits a low change in power requirements with increasing thrust requirements. This is because of the relatively low blade collective and its associated low induced velocities.

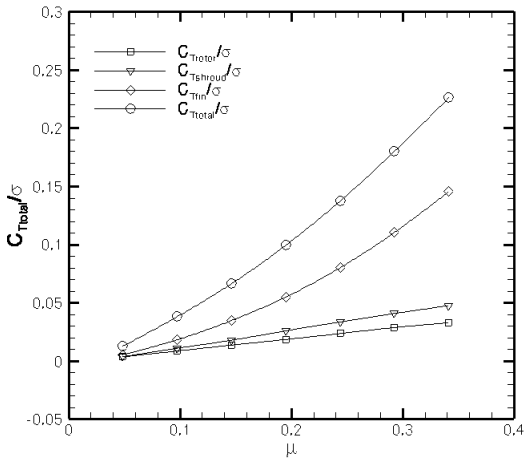

(a) Total thrust coefficient versus advance ratio, $\theta_{0.75R} = 0°$

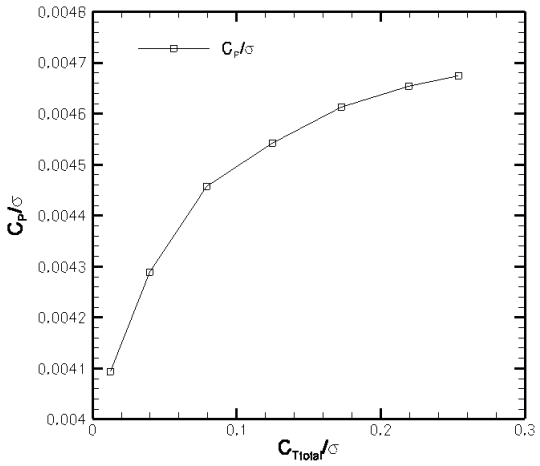

(b) Power coefficient versus total thrust coefficient, $\theta_{0.75R} = 0°$

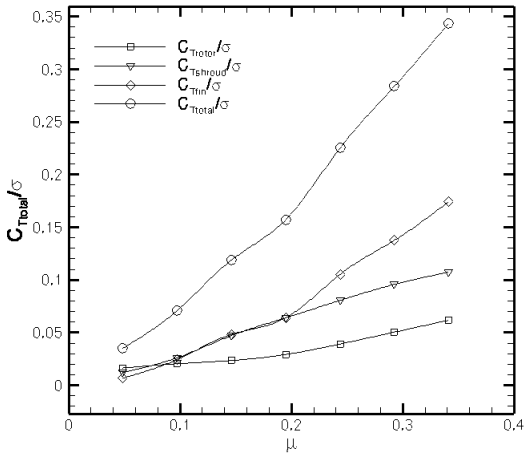

(c) Total thrust coefficient versus advance ratio, $\theta_{0.75R} = 5°$

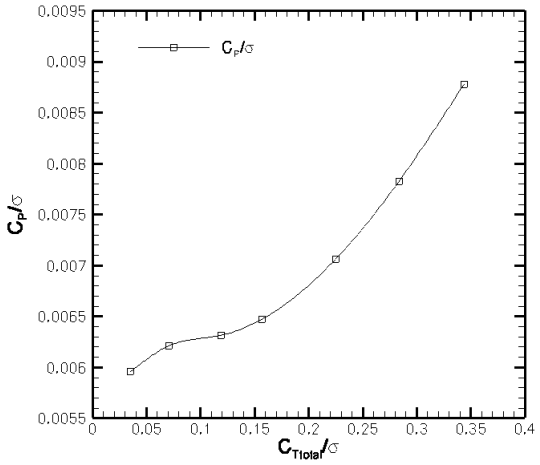

(d) Power coefficient versus total thrust coefficient, $\theta_{0.75R} = 5°$

Figure 5.6: Polar curves for $\theta_{0.75R} = 0°$, $5°$

At blade collective $\theta_{0.75R} = 5°$ similar trends occur for the each individual thrust component. The rotor thrust increases at a higher rate than the $\theta_{0.75R} = 0°$ case and this is clearly the effect of increasing the blade collective. As in the hover case, by increasing the blade collective the induced velocites over the plane of the rotor further increase together with the supply of more flow at increasing advance ratio. The shroud thrust increases accordingly due to the high suction forces which are developed over the inlet lip and the over-pressure forces that are developed below the diffuser. It can be seen that the shroud thrust increases at a higher rate than the rotor. Unfortunately, due to the lack of experimental data at the particular flight conditions, a quantification of the error, especially of the rotor-shroud thrust sharing can not be performed.

However, the trend is not physically unreasonable as it is expected for the flow to accelerate more with increasing blade collective plus the effect caused of increasing the advance ratio. The fin thrust increases with the same rate as in the previous collective and a slight increase of its magnitude at the maximum examined advance ratio. This is probably a result of an aerodynamic interaction, caused by the increased acceleration of the flow over the shroud, between the fin and the shroud. It can also be seen that the fin produces the same thrust as the shroud at low advance ratios which indicates that the fin would be more effective (in terms of rotor off-loading) at higer advance ratios and lower blade collectives.

The power polars for this blade collective and in comparison with the previous case indicate the profound effect of the blade collective on the power consumption. The power coefficient vary almost cubically with the advance ratio[1] and the rate of increase is higher than the $\theta_{0.75R} = 0°$ case. This power polar curve clearly resembles the trend of the power polar curve in hover.

[1]The increase in total rotor thrust for the power polars corresponds to the increase of the advance ratio.

By inspecting Fig 5.7, which shows the performance polar curves for $\theta_{0.75R} = 10^\circ - 15^\circ$ the same conclusions can be drawn with regards to the effect of the advance ratio and the blade collective. At $\theta_{0.75R} = 10^\circ$ the same trends appear for both the rotor and the shroud and clearly the shroud produces more thrust than the rotor. However, this result further requires validation with experimental data in order to make a decisive claim of this observation. Nonetheless, the resulting trends are as expected for both the shroud and the rotor. With regards to fin thrust it can be seen that fin's contribution to the total thrust increases and the rotor is off-loaded both by the shroud and the fin. The data presented in Fig 2.14 [7] however show that the operating blade collective of 10° will typically correspond to low advance ratios. The power polar curve for this angle bears no difference with the previous case of $\theta_{0.75R} = 5^\circ$ and the power coefficient appears to vary cubically with the advance ratio.

At $\theta_{0.75R} = 15^\circ$ the performance trends change and it can be seen that for the low advance ratios the rotor thrust is greater than the shroud and fin thrust (except at 80 knots). The polar curve for this case cannot be compared directly with the previous three blade collectives due to the fact that the range of examined advance ratios here is smaller (see Table 5.1). It can be seen that for this angle and at low advance ratios the rotor thrust is greater than the individual shroud and fin thrust. By inspecting the power polar curve (Fig 5.7d) it can be seen that the power consumption increases with increasing advance ratio as expected. It must be noted however that due to the different range of advance ratios that were considered for this blade collective, a conclusion whether the variation of the power is cubic or not can not be done.

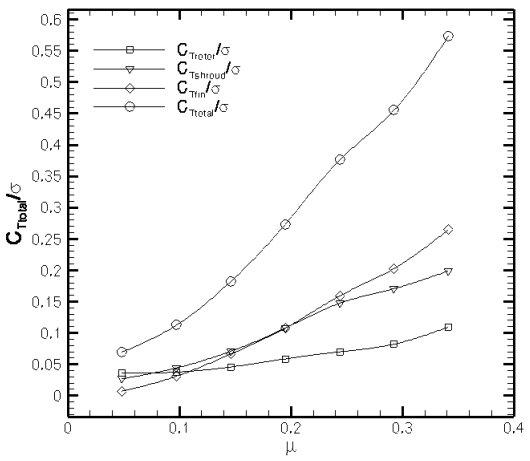

(a) Total thrust coefficient versus advance ratio, $\theta_{0.75R} = 10°$

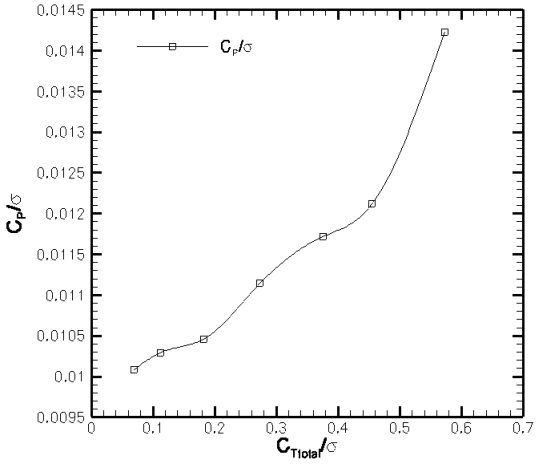

(b) Power coefficient versus total thrust coefficient, $\theta_{0.75R} = 10°$

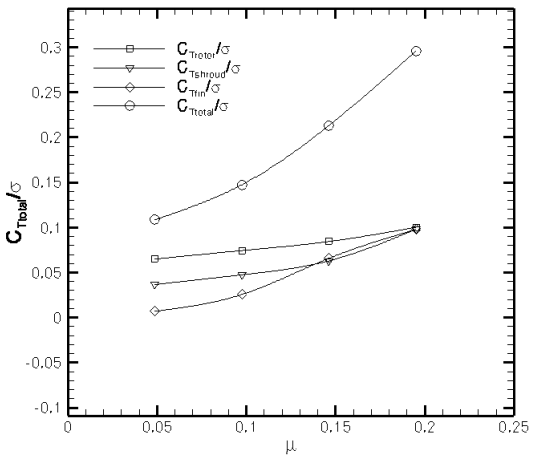

(c) Total thrust coefficient versus advance ratio, $\theta_{0.75R} = 15°$

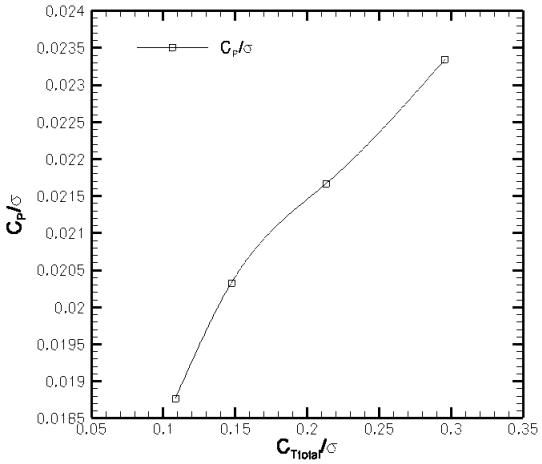

(d) Power coefficient versus total thrust coefficient, $\theta_{0.75R} = 15°$

Figure 5.7: Polar curves for $\theta_{0.75R} = 10°$, $15°$

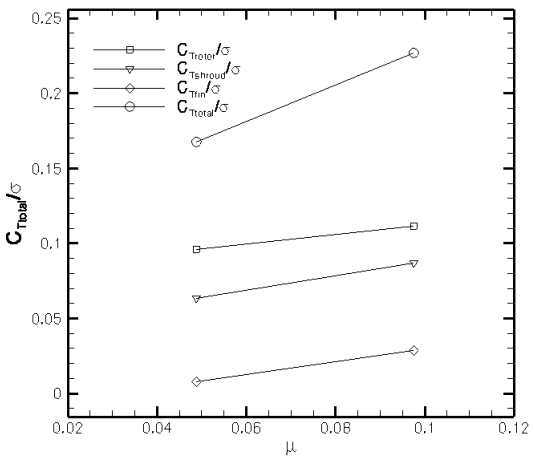

(a) Total thrust coefficient versus advance ratio, $\theta_{0.75R} = 20°$

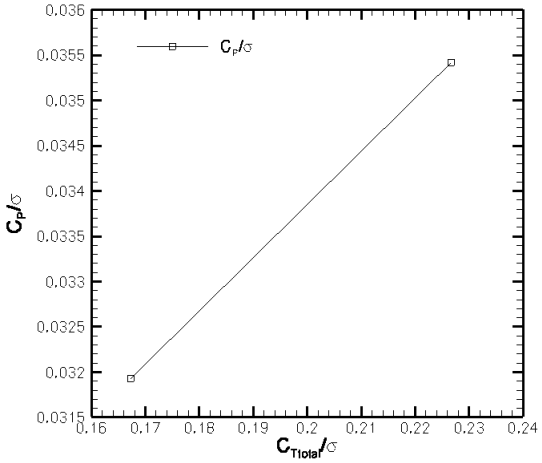

(b) Power coefficient versus total thrust coefficient, $\theta_{0.75R} = 20°$

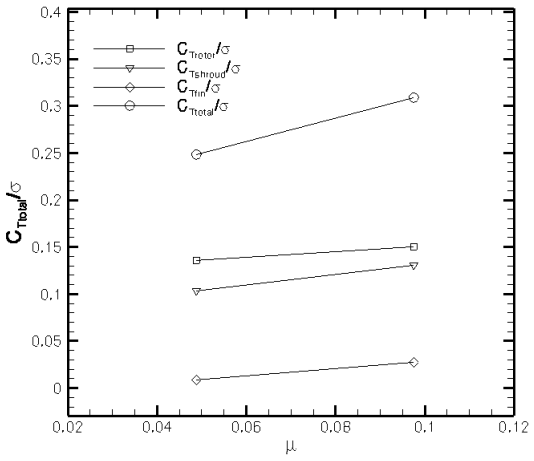

(c) Total thrust coefficient versus advance ratio, $\theta_{0.75R} = 25°$

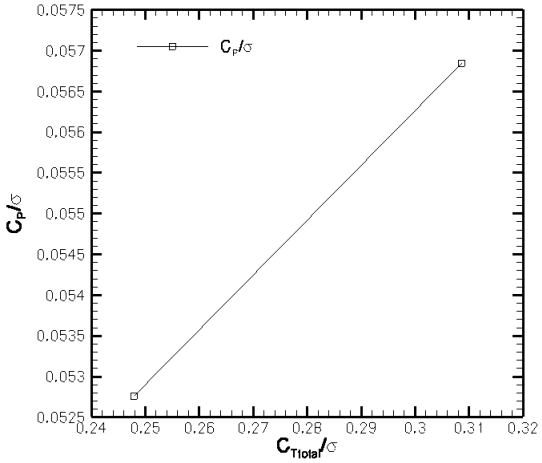

(d) Power coefficient versus total thrust coefficient, $\theta_{0.75R} = 0°$

Figure 5.8: Polar curves for $\theta_{0.75R} = 20°$, 25°

The performance polar curves for $\theta_{0.75R} = 20° - 25°$ are shown in Fig 5.8 and clearly the range of these collectives corresponds to very low advance ratios as also indicated by Wright[7]. The fin thrust is very low at these conditions as expected due to the low advance ratio. The variations for all the individual components for this very small range of advance ratios of 0.048 to 0.097 (20

and 40 knots respectively) are linear as expected (only two simulation points).

5.3 C_p Contours

The present section provides an overview of the pressure coefficient contours over the geometry of the configuration. The pressure coefficient contour plots are presented over the starboard surface of the configuration and a view of the complete geometry including the fin is given as well. In order to illustrate the effect of the advance ratio on the pressure distribution a single angle can be used and for this section the $\theta_{0.75R} = 5°$ is considered. The pressure coefficient distributions for the rest simulation points are shown in Appendix B.

By inspecting Figures 5.9-5.11 the profound effect of forward flight speed can be seen over the geometry. As it was explained before, a ducted tail rotor subjected to an edgewise flow will demonstrate assymetric pressure distributions over the windward and leeward side. This pressure asymmetry is present for each and every advance ratio and is due to the fact that the flow encounters firstly the windward side and then the leeward side. This can be seen from the highest pressure suction forces which are developed over the windward side of the side.

The effect of the advance ratio is to magnify this pressure assymetry e.g the assymetric pressure distribution is more apparent in the 140 knots case. It is noted though that with increasing advance ratio there is a small thrust gained at the edges of the shroud and this due to the flow acceleration (developed when the flow turns over the edges). As far as the fin is concerned, it acts as a fixed wing and it can be seen that suction forces are increasing over the leading edge with increasing advance ratio.

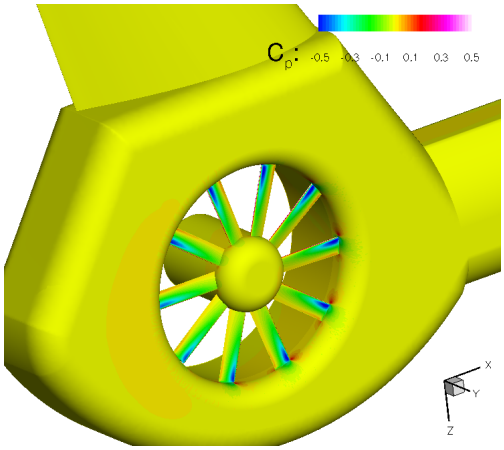

(a) Starboard view $\theta_{0.75R} = 5°$ at 20 knots

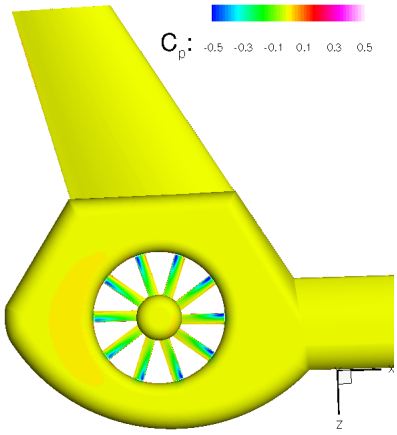

(b) Starboard view including fin $\theta_{0.75R} = 5°$ at 20 knots

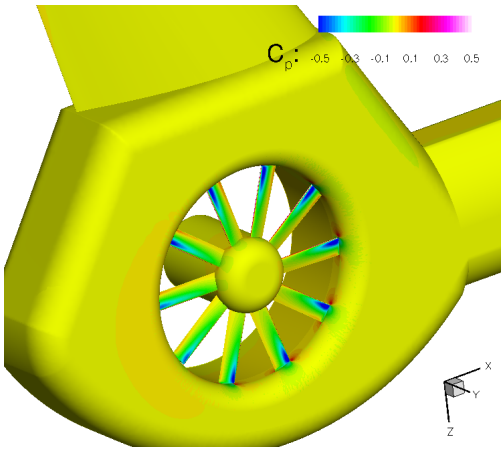

(c) Starboard view $\theta_{0.75R} = 5°$ at 40 knots

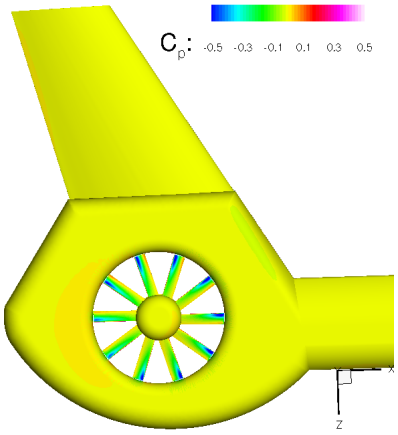

(d) Starboard view including fin $\theta_{0.75R} = 5°$ at 40 knots

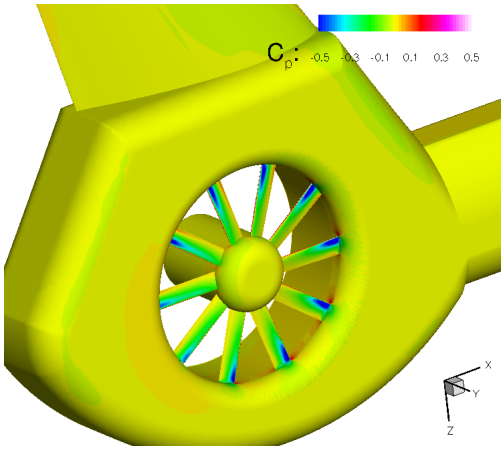

(e) Starboard view $\theta_{0.75R} = 5°$ at 60 knots

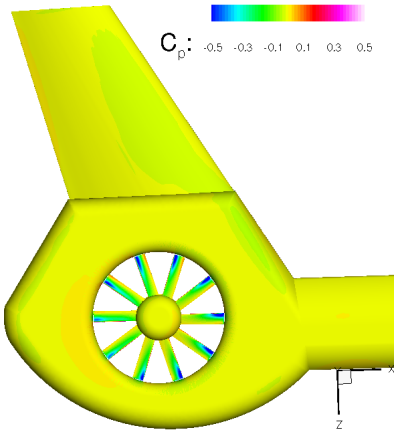

(f) Starboard view including fin $\theta_{0.75R} = 5°$ at 60 knots

Figure 5.9: Starboard C_p contours for blade collective angles 5°, at 20, 40 and 60 knots

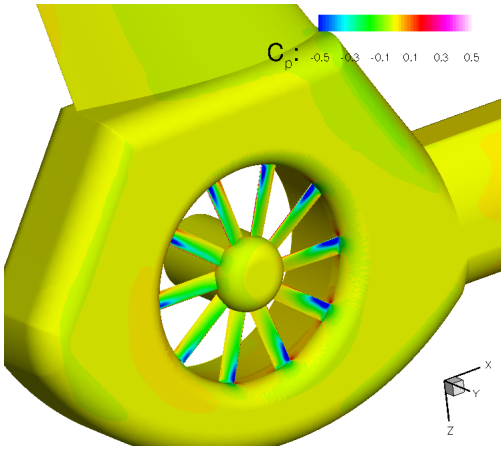

(a) Starboard view $\theta_{0.75R} = 5°$ at 80 knots

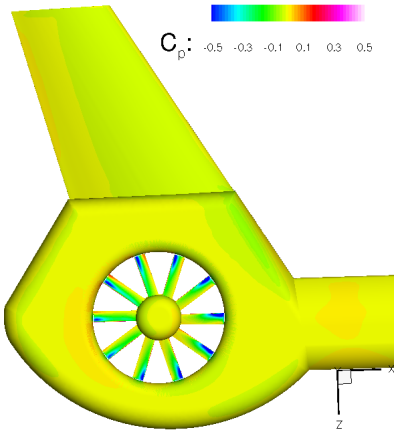

(b) Starboard view including fin $\theta_{0.75R} = 5°$ at 80 knots

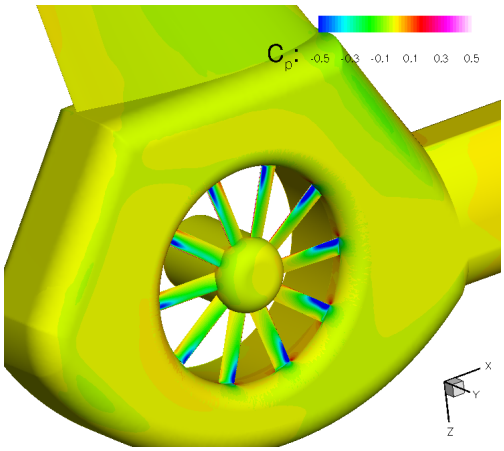

(c) Starboard view $\theta_{0.75R} = 5°$ at 100 knots

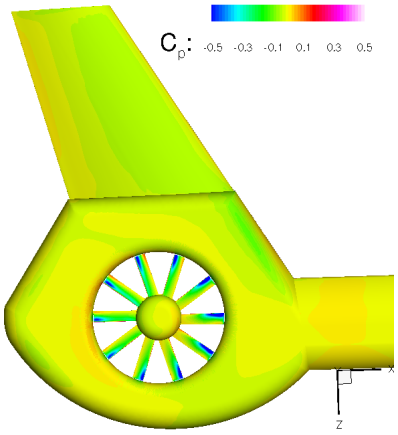

(d) Starboard view including fin $\theta_{0.75R} = 5°$ at 100 knots

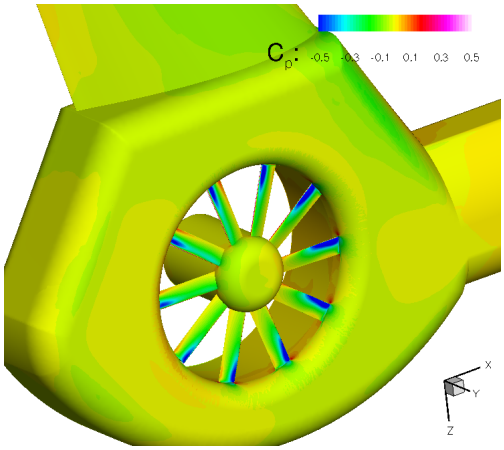

(e) Starboard view $\theta_{0.75R} = 5°$ at 120 knots

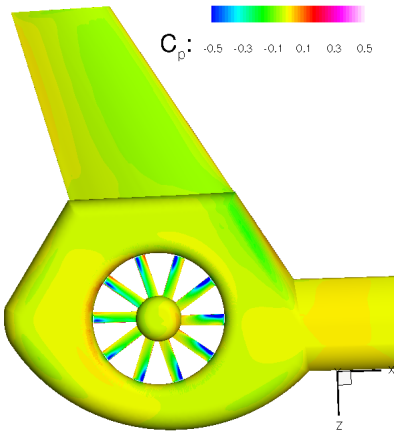

(f) Starboard view including fin $\theta_{0.75R} = 5°$ at 120 knots

Figure 5.10: Starboard C_p contours for blade collective angles 5°, at 80, 100 and 120 knots

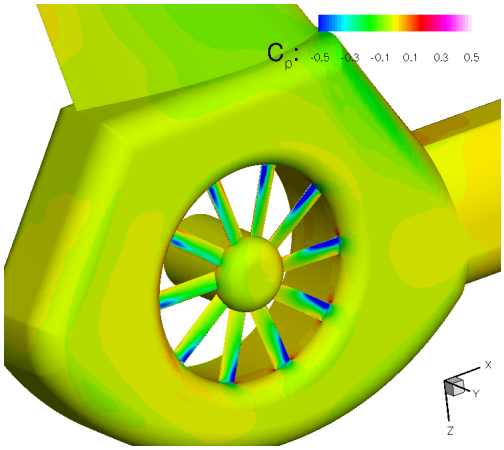

(a) Starboard view $\theta_{0.75R} = 5°$ at 140 knots

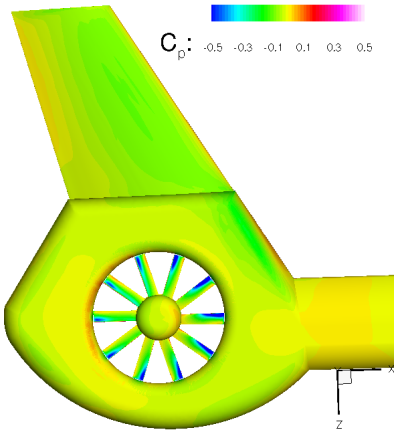

(b) Starboard view including fin $\theta_{0.75R} = 5°$ at 140 knots

Figure 5.11: Starboard C_p contours for blade collective angles 5°, at 140 knots

5.4 Flow-Field Visualisation

As it was done for the hover case, the complex flow regime at forward flight will be discussed in the following section. This will be done by illustrating the velocity vectors for two blade collective angles and at different forward flight speeds. In addition, the total pressure and axial velocity (induced velocity) distributions at the inlet, rotor (upstream and downstream) and diffuser plane will be discussed.

5.4.1 Velocity Vector Plots

The velocity vector plots for the forward flight case, as depicted in Figures 5.12-5.15, were drawn at the mid-azimuth plane for $\theta_{0.75R} = 0°$ and $\theta_{0.75R} = 5°$ at 4 distinct forward flight speeds (20-140 knots with an increment of 40 knots). This range of blade collective angles and flight speeds was chosen as an example in order to illustrate the effect of increasing blade collective angle and increasing forward flight speed. The illustrated plots show the overall flow distribution as well as the local distribution at the blade tip gap of the windward side. By inspecting the plots it can be seen that the blade collective angle has a global effect of promoting higher induced velocities within the duct. However, the increase in the local velocity magnitude (for the blade collective angles shown here) is still small. Increased velocities within the duct will only be present at higher blade collectives as it was shown in the hover flow case. For both angles, it can be acknowledged that by increasing forward flight speed, the local velocity magnitude above and below the duct increases as expected. The flow distribution between the windward and leeward sides is not uniform, which is expected for forward flight, and this behavior is more clear for $\theta_{0.75R} = 5°$.

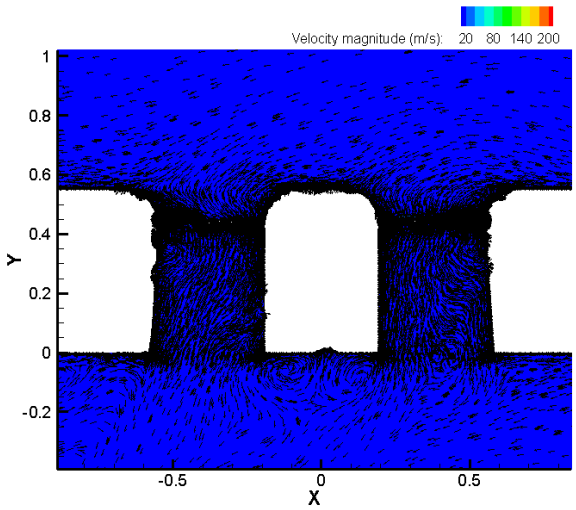

(a) Velocity vectors at mid-azimuth, $\theta_{0.75R} = 0°$ at 20 knots

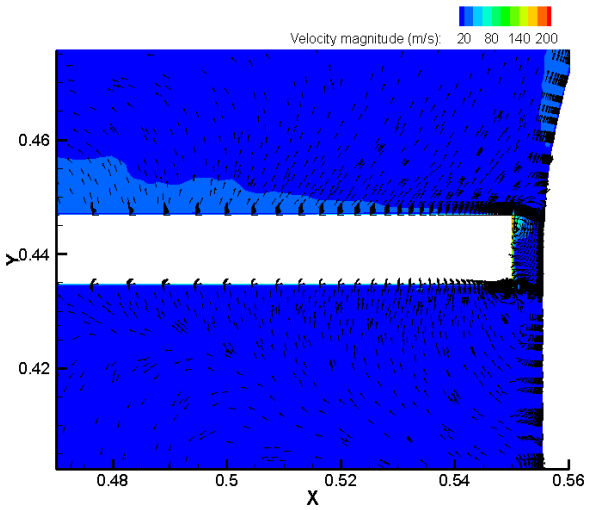

(b) Velocity vectors at blade tip region, $\theta_{0.75R} = 0°$ at 20 knots

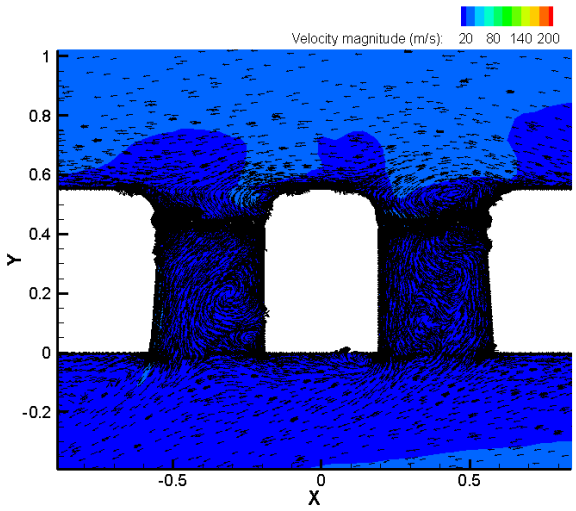

(c) Velocity vectors at mid-azimuth, $\theta_{0.75R} = 0°$ at 60 knots

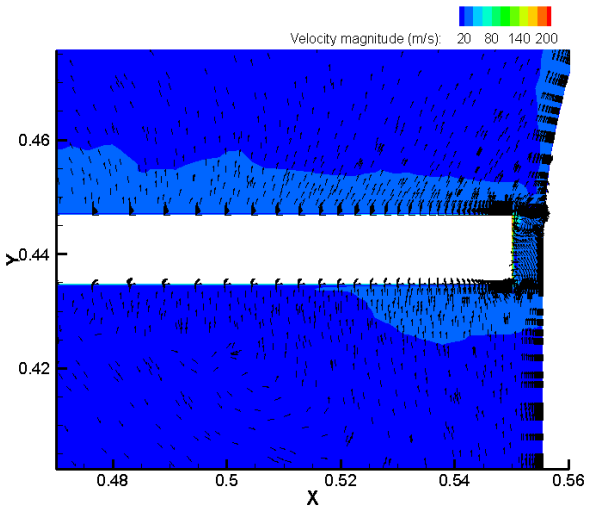

(d) Velocity vectors at blade tip region, $\theta_{0.75R} = 0°$ at 60 knots

Figure 5.12: Vector plots for $\theta_{0.75R} = 0°$ at 20 & 60 knots

It must be mentioned here, that these plots only depict a snapshot of the flow at the particular plane. The overall effect of the flow over the surface of the shroud and the blades i.e. the generated thrust force (pressure distribution) can be better comprehended by inspecting the C_p contours.

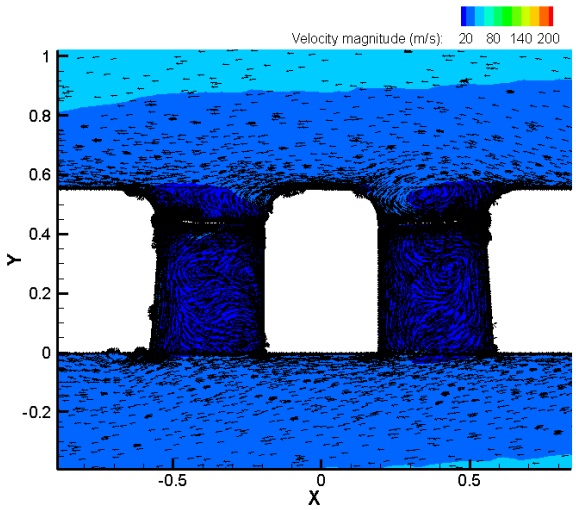

(a) Velocity vectors at mid-azimuth, $\theta_{0.75R} = 0°$ at 100 knots

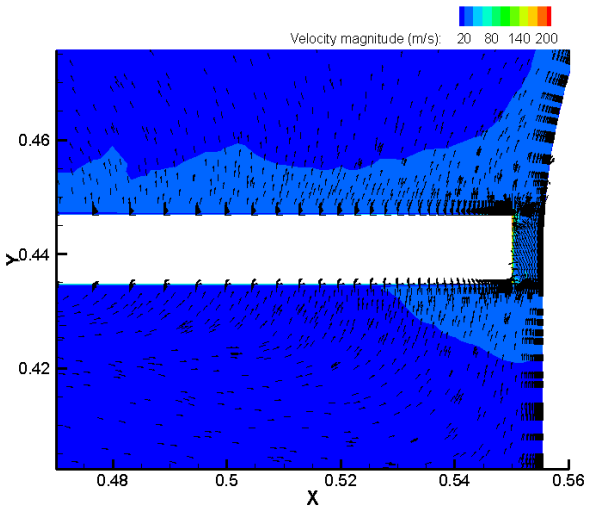

(b) Velocity vectors at blade tip region, $\theta_{0.75R} = 0°$ at 100 knots

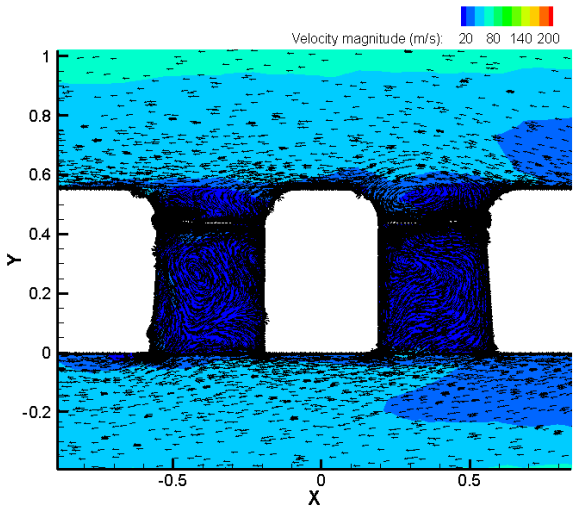

(c) Velocity vectors at mid-azimuth, $\theta_{0.75R} = 0°$ at 140 knots

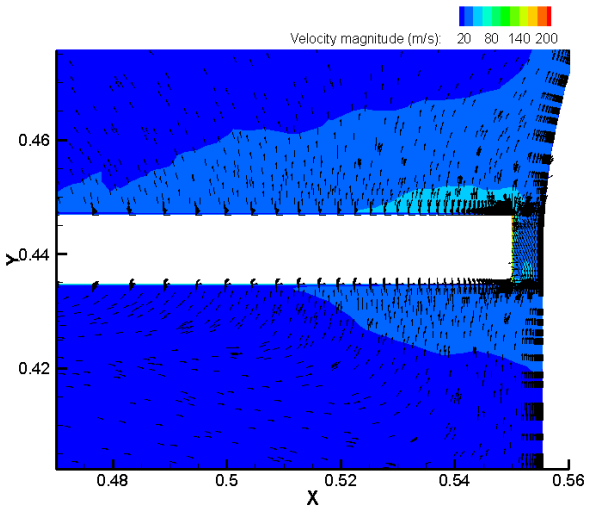

(d) Velocity vectors at blade tip region, $\theta_{0.75R} = 0°$ at 140 knots

Figure 5.13: Vector plots for $\theta_{0.75R} = 0°$ at 100 & 140 knots

This approach, in terms of presenting the overall flow behavior, is followed by leading researchers in the field of ducted tail rotors [8, 43, 39]. The velocity vector plots indicate that by increasing the forward flight speed, there is a flow separation at the inlet lip of the windward side. This flow separation

will be associated with the higher velocities encountered at the windward side of the disc (as it will be shown later) and the increased total pressure losses (compared to the leeward side) at this region. The flow separation occurs due to the geometry of the inlet lip, where the flow will turn. It is clear that as the flow momentum increases i.e. higher forward flight speeds, a portion of the flow will inevitably separate. Within the duct it can be seen that the flow for $\theta_{0.75R} = 0°$ does show some recirculation regions at higher velocities. This is due to the flow reversal that occurs at the blade tip and it is associated with the negative blade angle as it was explained in the subsection 4.4.

On the contrary, for $\theta_{0.75R} = 5°$ regions of recirculating flow are not present except towards the plane of the diffuser, where the flow will turn as it meets the mainstream flow below the duct. This behavior is more apparent at higher forward flight speeds. Finally, it can be said that the velocity vector plots can indicate the complex flow structure encountered at a ducted tail rotor in forward flight. However, these plots should be examined in conjuction the the C_p contours and the total pressure distributions in order to discuss the overall flow behavior. The main flow pattern, which can be deduced from the presented plots is the flow separation at the windward side.

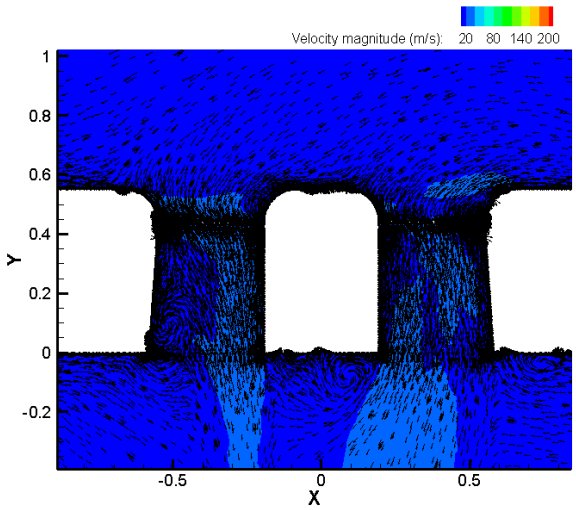

(a) Velocity vectors at mid-azimuth, $\theta_{0.75R} = 5°$ at 20 knots

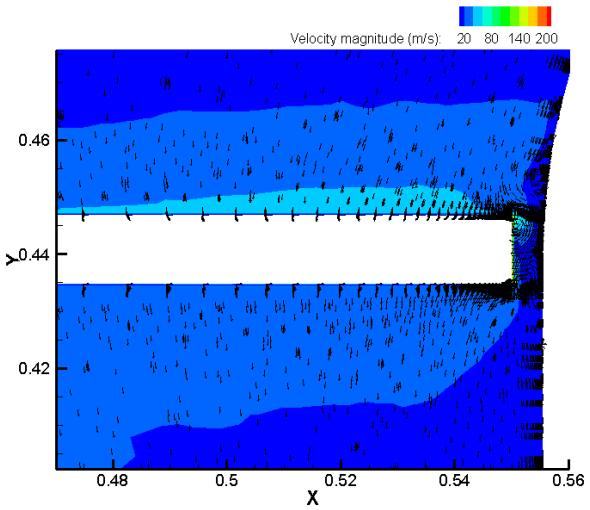

(b) Velocity vectors at blade tip region, $\theta_{0.75R} = 5°$ at knots

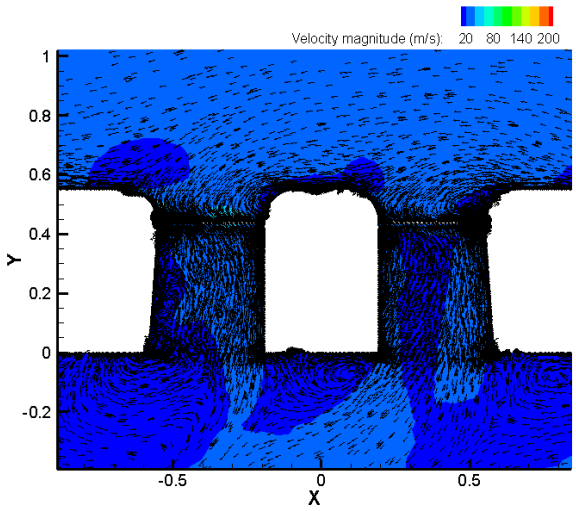

(c) Velocity vectors at mid-azimuth, $\theta_{0.75R} = 5°$ at 60 knots

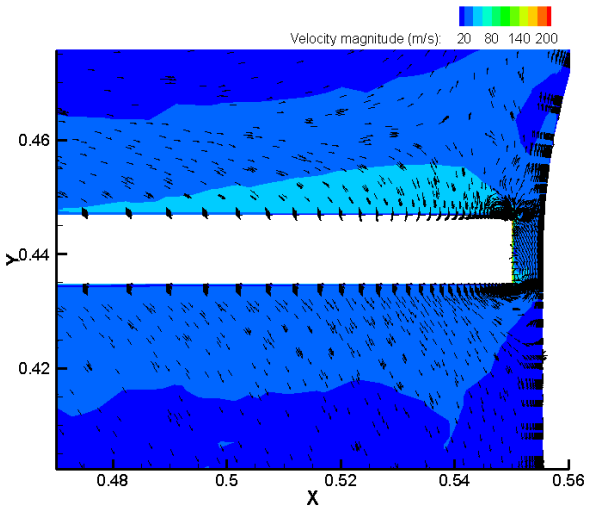

(d) Velocity vectors at blade tip region, $\theta_{0.75R} = 5°$ at 60 knots

Figure 5.14: Vector plots for $\theta_{0.75R} = 5°$ at 20 & 60 knots

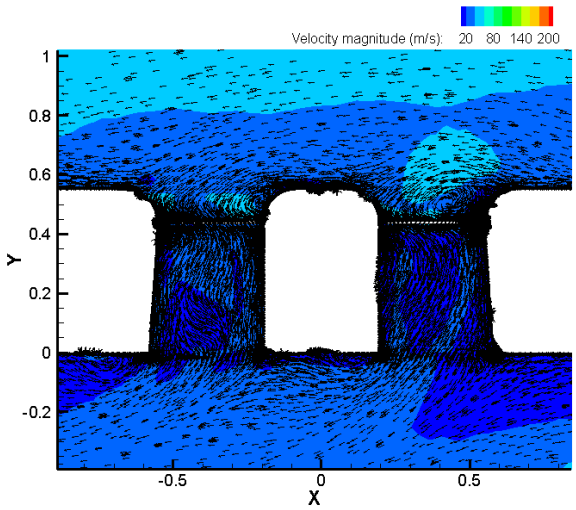

(a) Velocity vectors at mid-azimuth, $\theta_{0.75R} = 5°$ at 100 knots

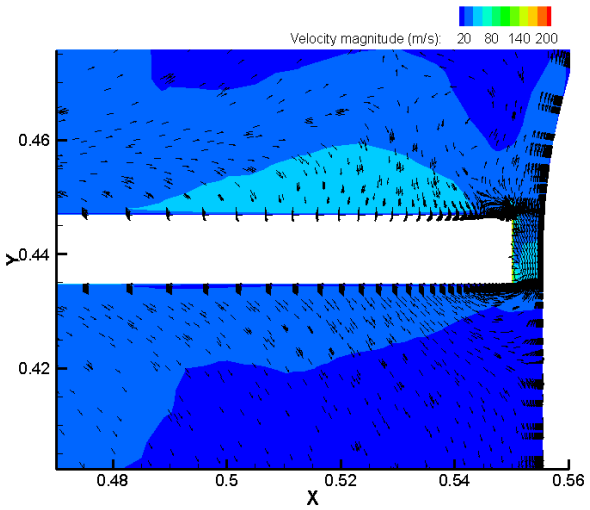

(b) Velocity vectors at blade tip region, $\theta_{0.75R} = 5°$ at 100 knots

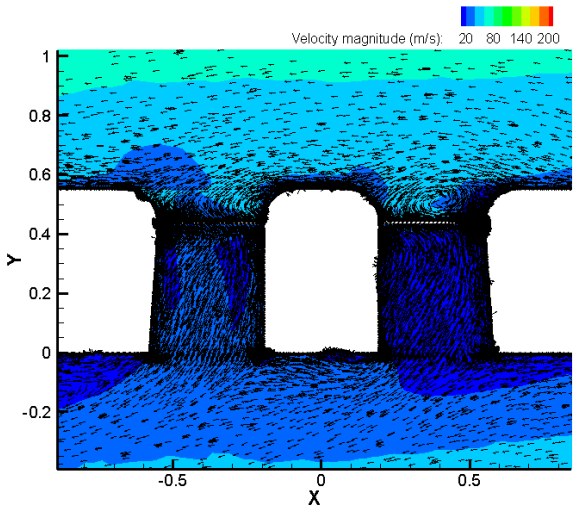

(c) Velocity vectors at mid-azimuth, $\theta_{0.75R} = 5°$ at 140 knots

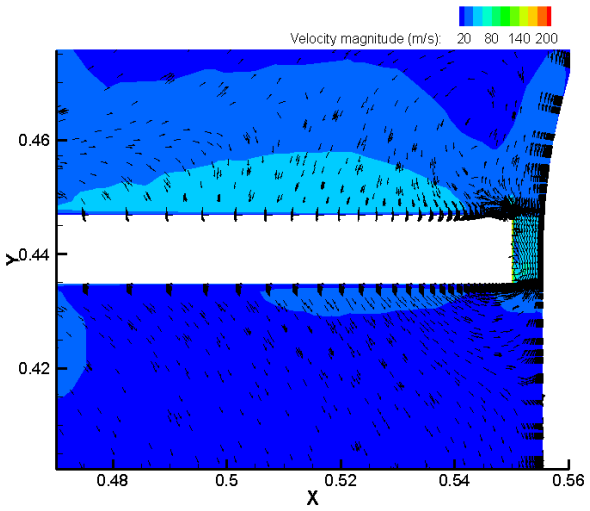

(d) Velocity vectors at blade tip region, $\theta_{0.75R} = 5°$ at 140 knots

Figure 5.15: Vector plots for $\theta_{0.75R} = 5°$ at 100 & 140 knots

5.4.2 Total Pressure Planes

In the current sub-section the total pressure distributions are shown in order to further describe the flow at forward flight. Figures 5.16-5.23 show the total pressure distributions for $\theta_{0.75R} = 0°$ and $\theta_{0.75R} = 5°$, at the same forward flight speeds as in the velocity vector plots. The main flow pattern that can be deduced by inspecting the total pressure distribution plots is the non-uniform flow. This non-uniformity grows stronger as the forward flight speed increases and it is more apparent at the highest blade collective angle shown. By inspecting the total pressure distribution plots at the inlet plane, it can be seen that at higher velocities the total pressure decreases at the windward side (positive r(m) values) whereas it increases at the leeward side (negative r(m) values). This happens due to the increased flow turning at the windward side which is also manifested at the C_p contours. The decreases total pressure is associated with the higher velocities at this region and the high total pressure at the leeward side corresponds to the high overpressure (decreased velocity) at this region. This phenomenon is solely caused by the increase of the velocity magnitude of the mainstream flow. As the flow travels from the tailboom towards the inlet lip it meets firstly the windward side, which justifies the increased velocity hence the high suction forces (lower values of static pressure). This behavior is better shown at the highest blade collective angle shown, due to the highest values induced velocity caused by increasing the blade collective angle (as discussed in the hover case). Therefore, it is acknowledged that the flow at high forward flight speeds is highly distorted. The longitudinal variations across the disc at the mid-azimuth plane will be illustrated better at the two-dimensional plots which will be shown later.

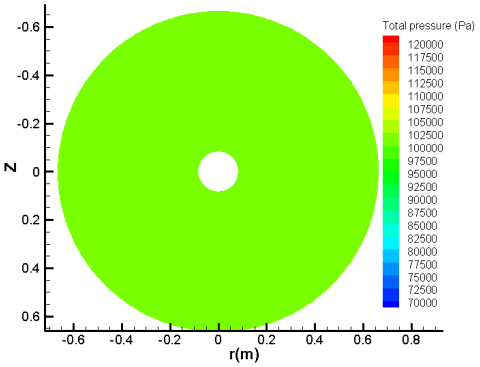

(a) Total pressure distribution over the inlet plane, $\theta_{0.75R} = 0°$ at 20 knots

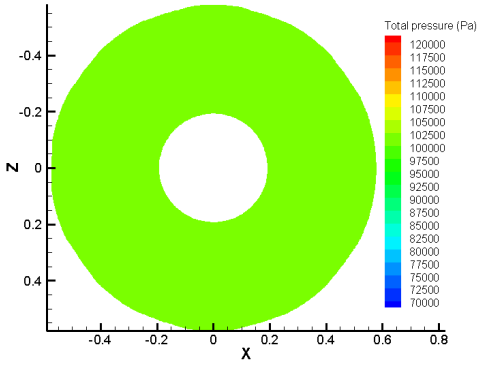

(b) Total pressure distribution over the diffuser plane, $\theta_{0.75R} = 0°$ at 20 knots

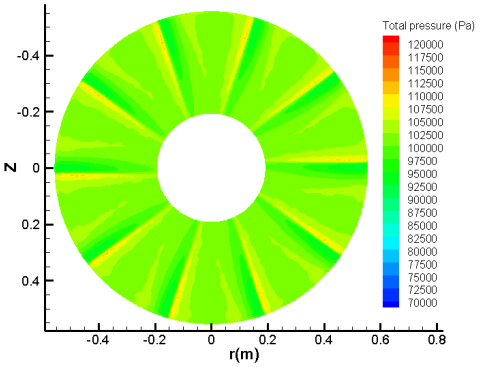

(c) Total pressure distribution over the upstream rotor plane,$\theta_{0.75R} = 0°$ at 20 knots

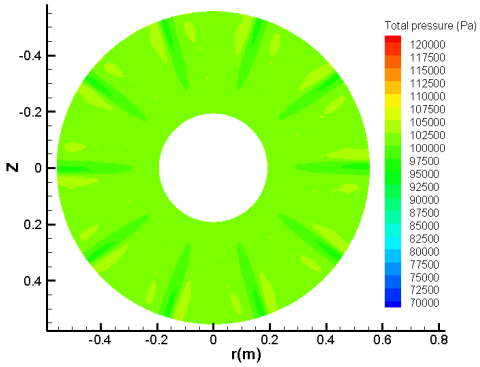

(d) Total pressure distribution over the downstream rotor plane, $\theta_{0.75R} = 0°$ at 20 knots

Figure 5.16: Total pressure distribution, $\theta_{0.75R} = 0°$ at 20 knots

However, it must be stressed once again that the two-dimensional plots represent a snapshot of the flow, at the particular plane where the plots are being derived from. Figures 5.19a and 5.23a clearly show the non-uniform distribution which is present at a large portion of the disc. Therefore, the total pressure distribution plots over the different planes of the disc, along with the two-dimensional plots along a polyline drawn at the mid-azimuth plane, shall be examined together.

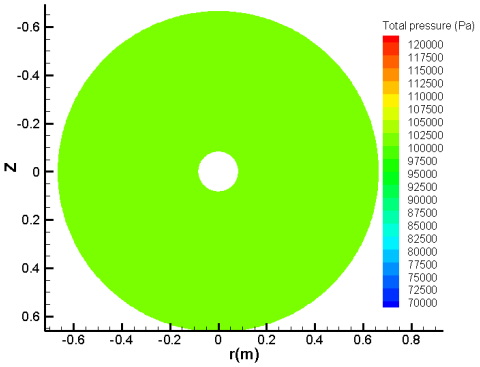

(a) Total pressure distribution over the inlet plane, $\theta_{0.75R} = 0°$ at 60 knots

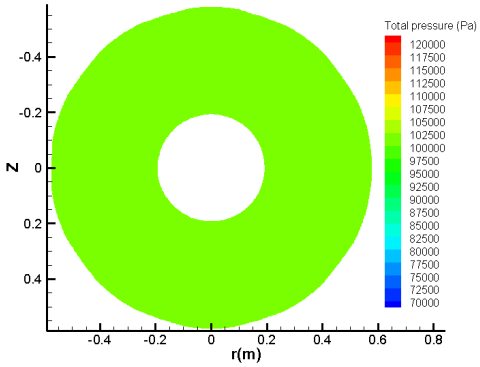

(b) Total pressure distribution over the diffuser plane, $\theta_{0.75R} = 0°$ at 60 knots

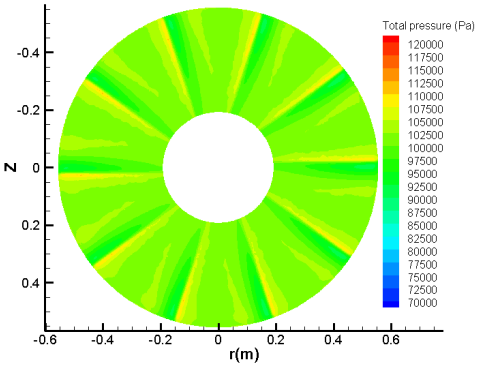

(c) Total pressure distribution over the upstream rotor plane, $\theta_{0.75R} = 0°$ at 60 knots

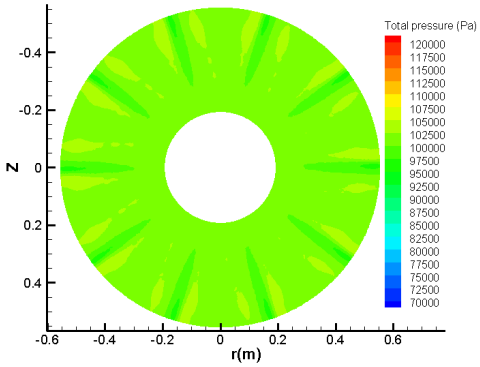

(d) Total pressure distribution over the downstream rotor plane, $\theta_{0.75R} = 0°$ at 60 knots

Figure 5.17: Total pressure distribution, $\theta_{0.75R} = 0°$ at 60 knots

The total pressure distributions over the rotor planes (upstream and downstream) show similar trends, at low speed forward flight speeds, as in the hover case. Total pressure increases as it passes through the rotor and the flow distribution is almost uniform. However, as the forward flight speed increases a non-uniform distribution develops and this behavior is better illustrated in the highest blade collective angle shown (see Figures 5.23c and 5.23d).

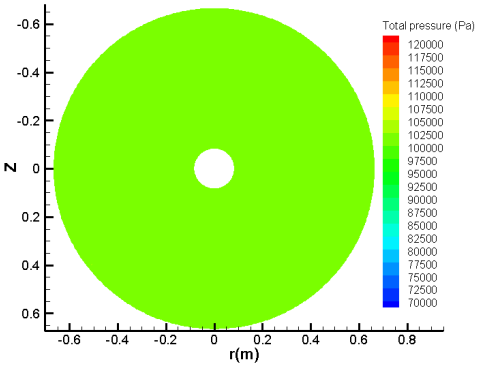

(a) Total pressure distribution over the inlet plane, $\theta_{0.75R} = 0°$ at 100 knots

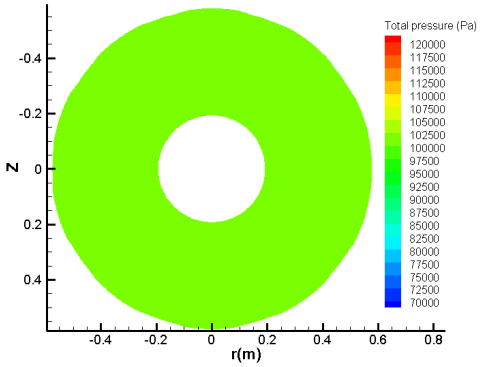

(b) Total pressure distribution over the diffuser plane, $\theta_{0.75R} = 0°$ at 100 knots

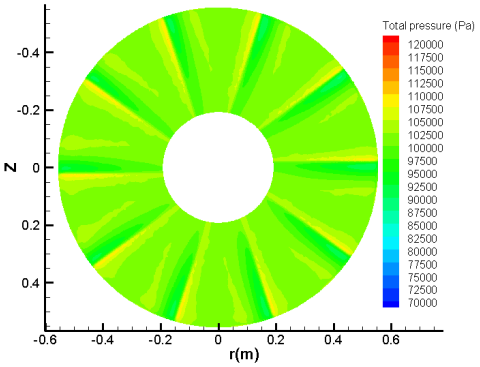

(c) Total pressure distribution over the upstream rotor plane, $\theta_{0.75R} = 0°$ at 100 knots

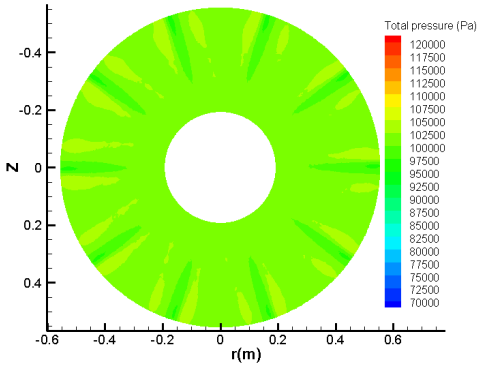

(d) Total pressure distribution over the downstream rotor plane, $\theta_{0.75R} = 0°$ at 100 knots

Figure 5.18: Total pressure distribution, $\theta_{0.75R} = 0°$ at 100 knots

This flow behavior shows both the effect of increasing the blade collective angle and the forward flight speed. At the diffuser planes and for all the plots shown the trends are comparable with the hover case. To be more precise, the total pressure distribution does not seem to be affected by the forward flight speed variations. However, the two-dimensional do show a slight variation. It must be mentioned though that the trends of the total pressure distribution at the diffuser plane are in accordance with the trends shown in hover.

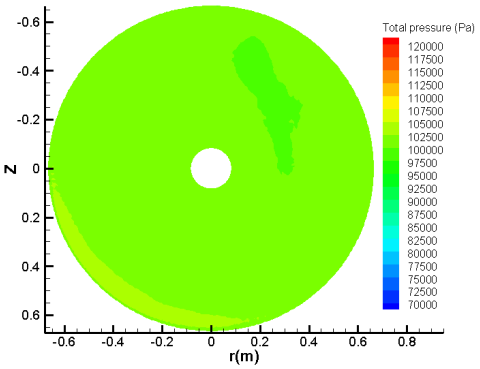

(a) Total pressure distribution over the inlet plane, $\theta_{0.75R} = 0°$ at 140 knots

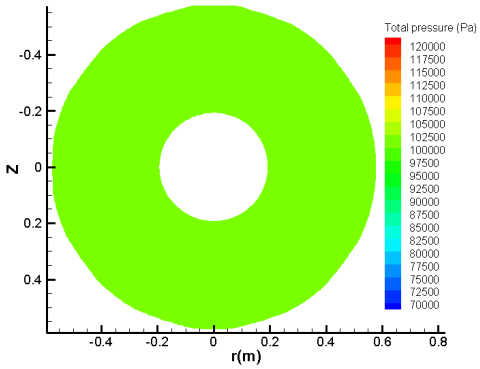

(b) Total pressure distribution over the diffuser plane, $\theta_{0.75R} = 0°$ at 140 knots

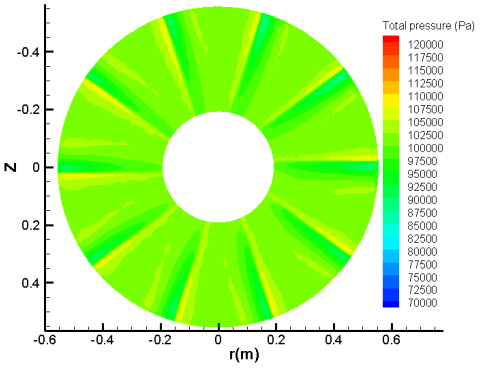

(c) Total pressure distribution over the upstream rotor plane, $\theta_{0.75R} = 0°$ at 140 knots

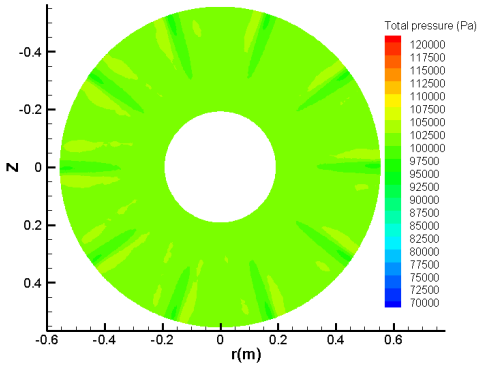

(d) Total pressure distribution over the downstream rotor plane, $\theta_{0.75R} = 0°$ at 140 knots

Figure 5.19: Total pressure distribution, blade collective $\theta_{0.75R} = 0°$ at 140 knots

This behavior shows that the forward flight speed does not have a strong effect on the contraction or the expansion of the wake. If there was either a contraction or expansion of the wake there would be a corresponding longitudinal variation of the wake at the exit of the diffuser. Therefore, it can be acknowledged that the blade collective angle plays the key role in the effective contraction or expansion of the wake (see Table 4.2).

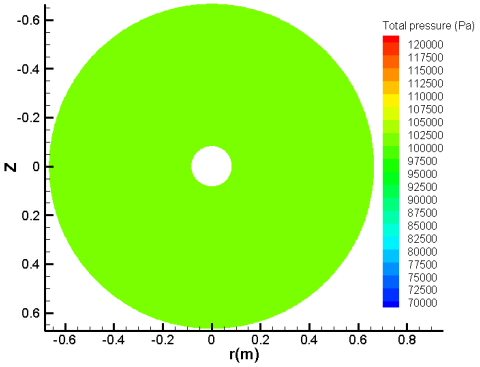

(a) Total pressure distribution over the inlet plane, $\theta_{0.75R} = 5°$ at 20 knots

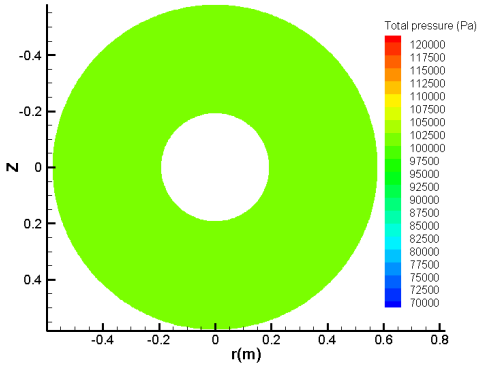

(b) Total pressure distribution over the diffuser plane, $\theta_{0.75R} = 5°$ at 20 knots

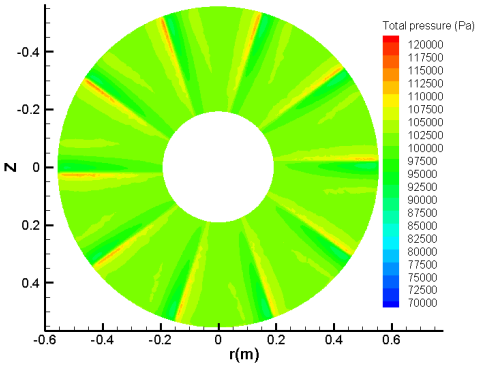

(c) Total pressure distribution over the upstream rotor plane, $\theta_{0.75R} = 5°$ at 20 knots

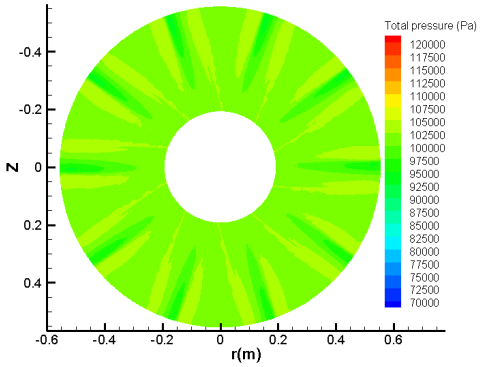

(d) Total pressure distribution over the downstream rotor plane, $\theta_{0.75R} = 5°$ at 20 knots

Figure 5.20: Total pressure distribution, $\theta_{0.75R} = 5°$ at 20 knots

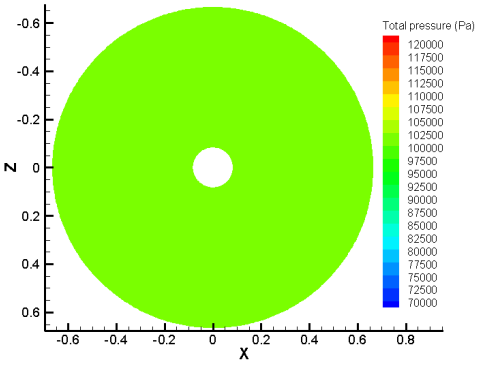

(a) Total pressure distribution over the inlet plane, $\theta_{0.75R} = 5°$ at 60 knots

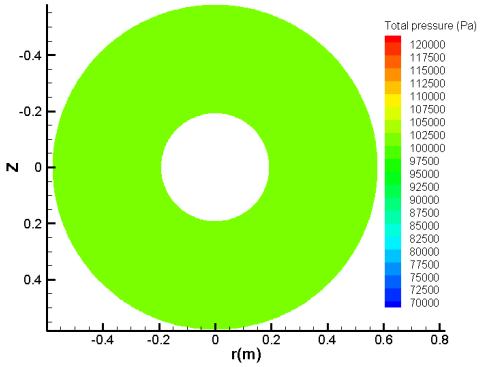

(b) Total pressure distribution over the diffuser plane, $\theta_{0.75R} = 5°$ at 60 knots

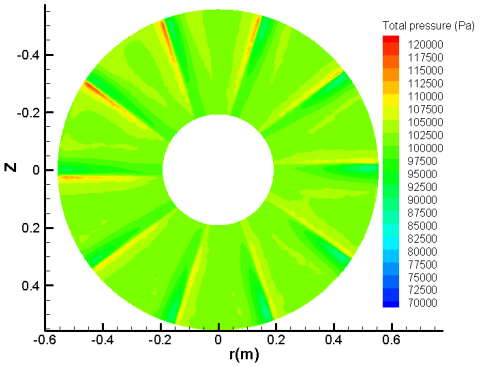

(c) Total pressure distribution over the upstream rotor plane, $\theta_{0.75R} = 5°$ at 60 knots

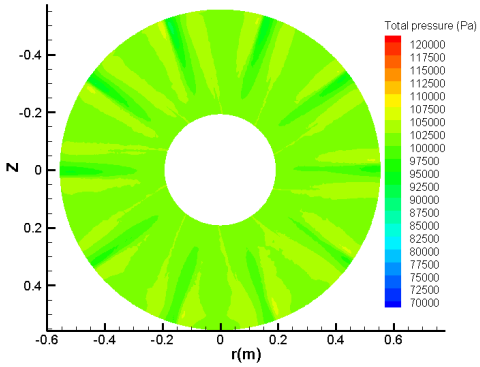

(d) Total pressure distribution over the downstream rotor plane, $\theta_{0.75R}5°$ at 60 knots

Figure 5.21: Total pressure distribution, $\theta_{0.75R} = 5°$ at 60 knots

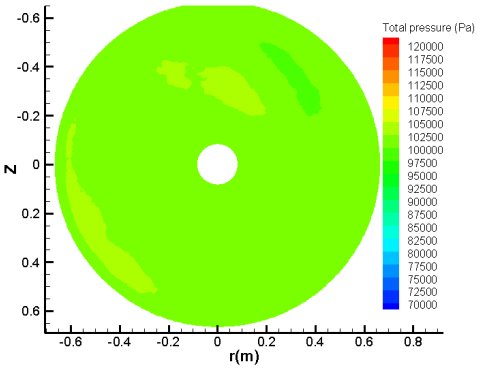

(a) Total pressure distribution over the inlet plane,$\theta_{0.75R} = 5°$ at 100 knots

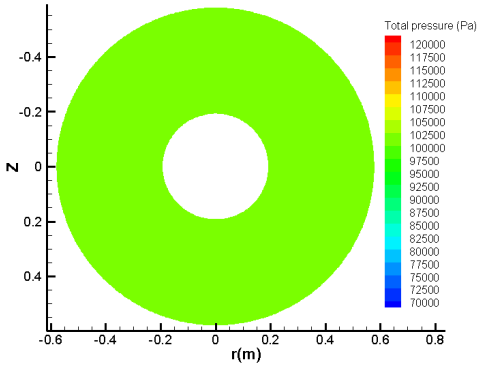

(b) Total pressure distribution over the diffuser plane, $\theta_{0.75R} = 5°$ at 100 knots

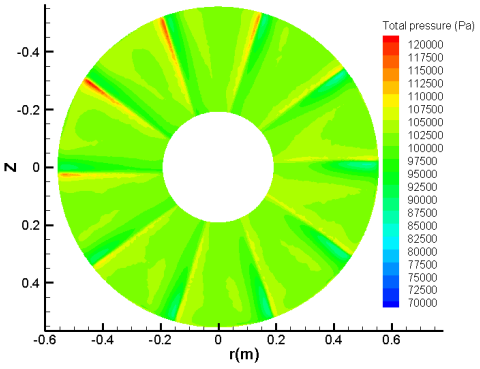

(c) Total pressure distribution over the upstream rotor plane, $\theta_{0.75R} = 5°$ at 100 knots

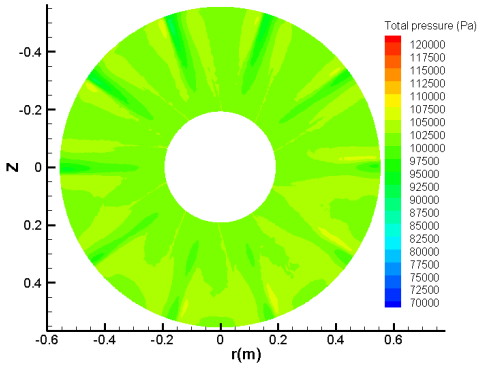

(d) Total pressure distribution over the downstream rotor plane, $\theta_{0.75R} = 5°$ at 100 knots

Figure 5.22: Total pressure distribution, $\theta_{0.75R} = 5°$ at 100 knots

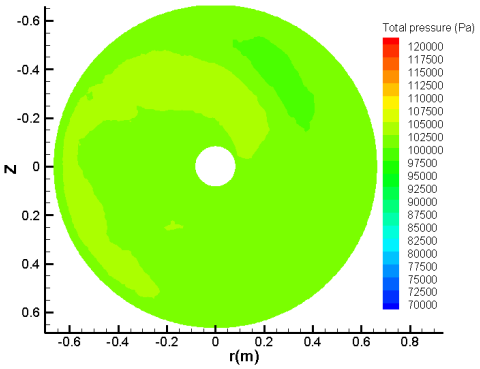

(a) Total pressure distribution over the inlet plane, $\theta_{0.75R} = 5°$ at 140 knots

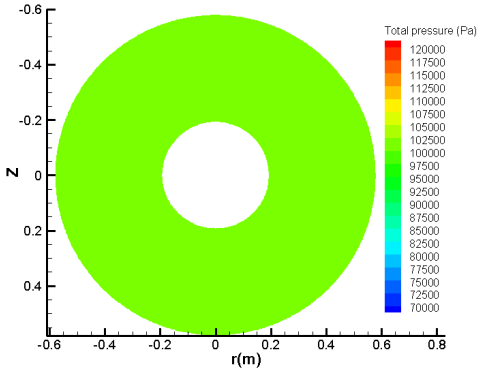

(b) Total pressure distribution over the diffuser plane, $\theta_{0.75R} = 5°$ at 140 knots

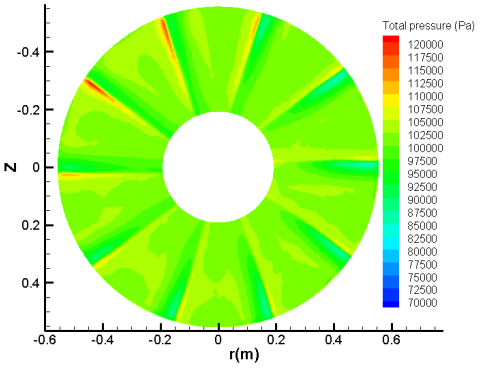

(c) Total pressure distribution over the upstream rotor plane, $\theta_{0.75R} = 5°$ at 140 knots

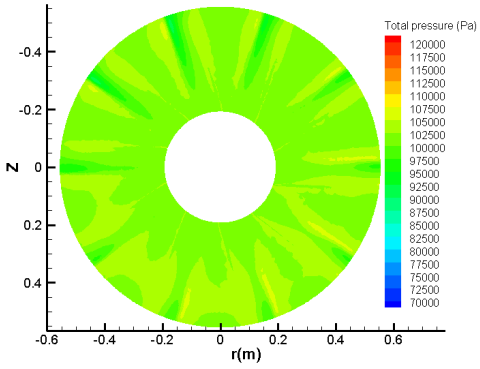

(d) Total pressure distribution over the downstream rotor plane, $\theta_{0.75R} = 5°$ at 140 knots

Figure 5.23: Total pressure distribution, $\theta_{0.75R} = 5°$ at 140 knots

5.4.3 Total Pressure & Axial Velocity Distributions

The total pressure and axial velocity distributions along a polyline drawn at the mid-azimuth plane are shown here. Figure 5.24 shows the total pressure distribution for $\theta_{0.75R} = 0°$ at the examined forward flight speeds. It can be said that at very low speeds (20 and 40 knots), the trends are almost identical to the hover case. Nevertheless, at the windward side, the total pressure is slightly decreased compared to the leeward side. This non-uniformity is more apparent as the forward flight speed increases. By looking at the inlet plane distribution, the total pressure at windward side has lower values. This corresponds to the increased flow velocity and means that there will be higher suction forces at this region. The non-uniformity of the flow-field is also depicted in the rotor planes and shows the importance of representing the distributions on a two-dimensional plot.

It can be seen that at the windward side, the total pressure peak (local minimum) has lower values, compared to the leeward side. This is associated to the highest suction forces which are present upstream of the rotor. The same trend applies for the distribution downstream of the rotor plane. The total pressure distributions show also the direct effect of forward flight speed. As the forward flight speed increases the peaks at the rotor planes distributions decrease which mean that the thrust will be greater. This conclusion was also verified at the polar curves which were presented before. At the diffuser plane, it can be seen that the distributions are comparable, in terms that there is no remarkable difference between the leeward and windward sides as well as in terms of longitudinal variation. This behavior verifies the fact that the contraction or expansion of the wake is solely dictated by the value of blade collective angle .

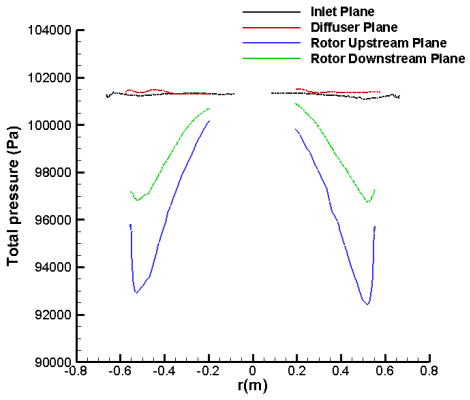

(a) Total pressure distributions over the inlet, rotor and diffuser planes at $\theta_{0.75R} = 0°$, 20 knots

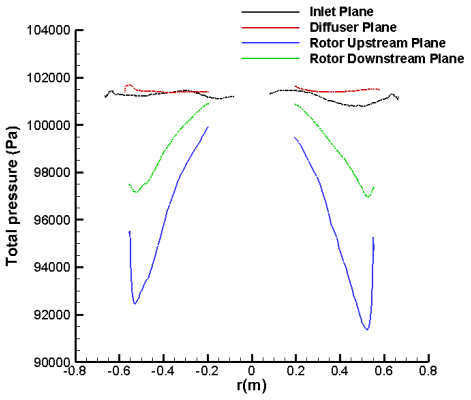

(b) Total pressure distributions over the inlet, rotor and diffuser planes at $\theta_{0.75R} = 0°$, 60 knots

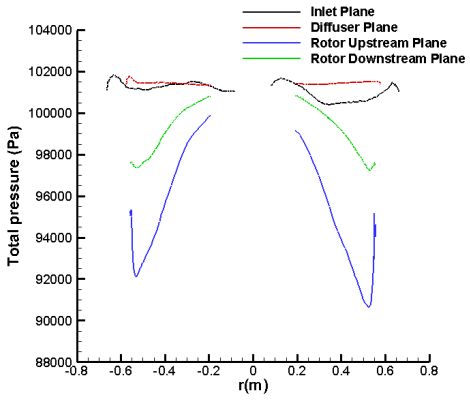

(c) Total pressure distributions over the inlet, rotor and diffuser planes at $\theta_{0.75R} = 0°$, 100 knots

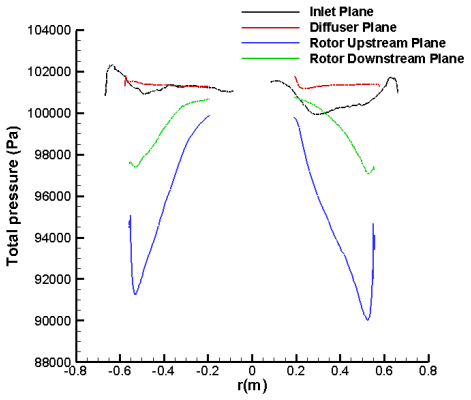

(d) Total pressure distributions over the inlet, rotor and diffuser planes at $\theta_{0.75R} = 0°$, 140 knots

Figure 5.24: Total pressure distributions over the inlet, rotor and diffuser planes at $\theta_{0.75R} = 0°$

Figure 5.25 shows the total pressure distributions for $\theta_{0.75R} = 5°$. By comparing the distributions between the two blade collective angles it can be seen that the total pressure, at the rotor planes, is decreased for the highest angle.This corresponds to the highest suction forces i.e. highest thrust which is expected. By inspecting the distributions at the inlet plane, it can be seen at low speeds (20 and 40 knots) the trends are comparable. However, when the forward flight speed increases, the non-uniformity between the windward

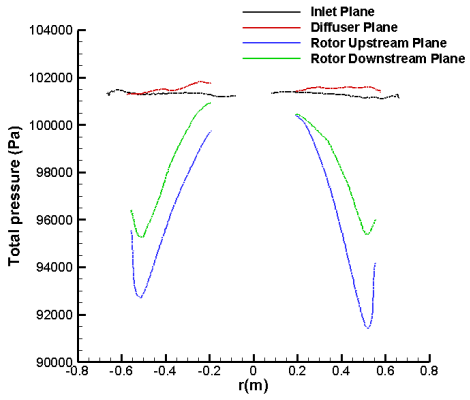

(a) Total pressure distributions over the inlet, rotor and diffuser planes at $\theta_{0.75R} = 5°$, 20 knots

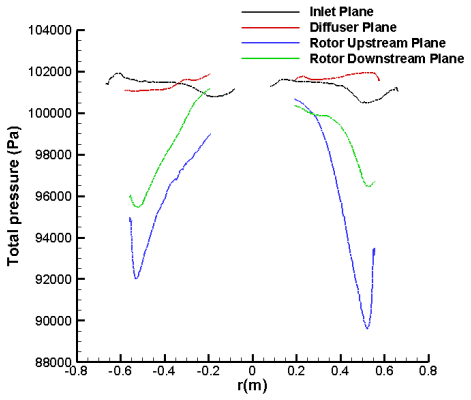

(b) Total pressure distributions over the inlet, rotor and diffuser planes at $\theta_{0.75R} = 5°$, 60 knots

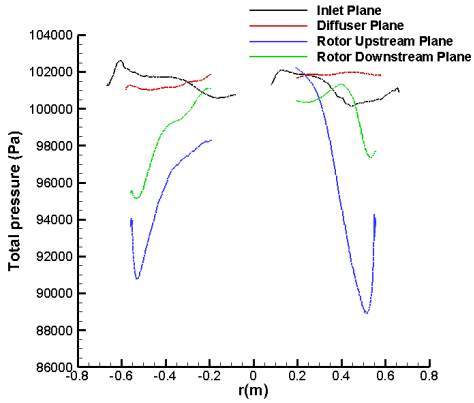

(c) Total pressure distributions over the inlet, rotor and diffuser planes at $\theta_{0.75R} = 5°$, 100 knots

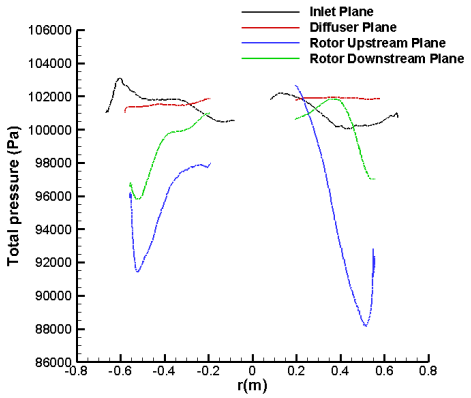

(d) Total pressure distributions over the inlet, rotor and diffuser planes at $\theta_{0.75R} = 5°$, 140 knots

Figure 5.25: Total pressure distributions over the inlet, rotor and diffuser planes at $\theta_{0.75R} = 5°$

and leeward sides increases as well. The peaks of total pressure at the leeward side near to the hub, which are more apparent at higher forward flight speeds, correspond to flow separation at the hub. This behavior has also been observed in the available literature [43]. Upstream of the rotor the trends are comparable to the $\theta_{0.75R} = 0°$ distributions. However, downstream of the rotor the total pressure is increased at the windward side which corresponds to the higher thrust values at this region.

This behavior comes in agreement with the C_p contours which show that at the windward side the pressure coefficient has lower values which correspond to higher suction forces hence increased thrust. It must also be noted that for all forward flight speeds, the total pressure values are similar at the diffuser plane. This is due to the fact that the effective contraction or expansion of the wake is dictated by the blade collective angle. It was shown before that expansion occurs at high blade collective angles (see Table 4.2).

Figures 5.26 and 5.27 show the axial velocity distributions for $\theta_{0.75R} = 0°$ and $\theta_{0.75R} = 5°$ respectively. For $\theta_{0.75R} = 0°$ the axial velocity at 20 knots bears similarities to the distribution of the hover case. The trends are simiilar between the hover and forward flight cases, in terms of flow reversal due to the negative angle at the blade tip region. At the inlet plane, it can be seen that the induced velocity increases as the forward flight speed increases. The increase in induced velocity is more apparent at the windward side as the forward flight speed increases. As it was discussed before, this directly corresponds to the higher velocities which exist at this region. In addition, it can be seen that the flow is not uniform, which implies that the presented distributions should be read in conjunction with the C_p contours.

The global effect of changing the forward flight speed is depicted in the rotor polar curves. At the rotor planes, the flow reversal as towards the blade tip region is present, as in the hover case. The effect of forward flight speed is to increase the value of the induced velocity which is expected. Between the windward and leeward sides, there are differences in the maximum induced value, which corresponds to the higher values of thrust at the windward region. To be more precise, the flow reversal is "stronger" at the windward side. The flow at the diffuser plane is not-uniform, which is caused by the forward flight speed increase and the differences in flow distribution between

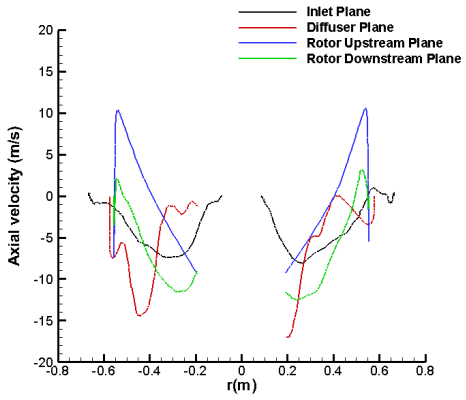

(a) Axial velocity distributions over the inlet, rotor and diffuser planes at $\theta_{0.75R} = 0°$, 20 knots

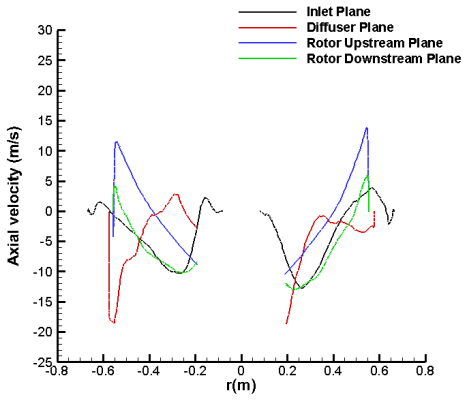

(b) Axial velocity distributions over the inlet, rotor and diffuser planes at $\theta_{0.75R} = 0°$, 60 knots

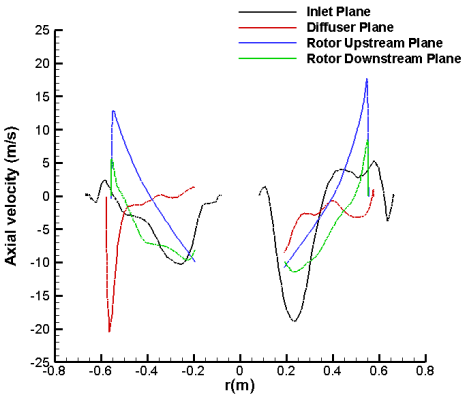

(c) Axial velocity distributions over the inlet, rotor and diffuser planes at $\theta_{0.75R} = 0°$, 100 knots

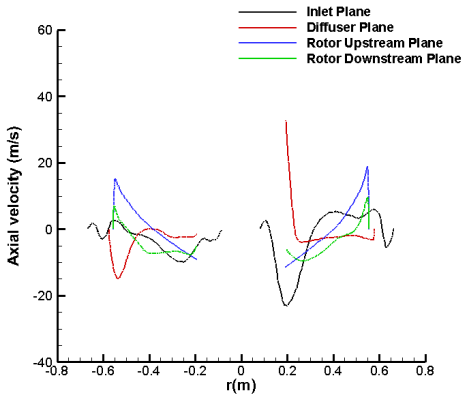

(d) Axial velocity distributions over the inlet, rotor and diffuser planes at $\theta_{0.75R} = 0°$, 140 knots

Figure 5.26: Axial velocity distributions over the inlet, rotor and diffuser planes at $\theta_{0.75R} = 0°$

the windward and leeward sides. At the windward side, the flow starts to reverse at the hub region where the maximum flow reversal occurs at 140 knots. The induced velocity approaches zero values close to the wall due to the blockage effect of the shroud. At the leeward side, the induced velocity has low values, due to the decreased velocity magnitude at this region. Near the hub the flow reverses with increasing forward flight speed. Finally, it can be seen that at the leeward side the induced velocity has higher values. This

is due to the fact that flow reversal is stronger at the windward side. For $\theta_{0.75R} = 5°$ the axial velocity distributions show that the flow still reverses at the blade tip region. This is due to the low angle at the blade tip (which will be 2.5° directly at the blade tip). At the inlet plane, it is shown that the axial velocity peak at the windward is shifted towards the hub as the forward flight speed increases. This is clearly due to the inlet lip separation and this flow behavior has also been reported in the available literature [58]. At the leeward side, the axial velocity distribution does not significantly change as the flow does not separate in such a high degree as in the windward side and it is less affected.

At the rotor planes, it can be seen that the induced velocity is generally higher at the windward side as expected and the value of the induced velocity increases with increasing forward flight speed. It must be mentioned herem that the induced velocity spikes to the highest value. Thich corresponds to the blade tip region's reversal and immediately reaches zero at the shroud due to its blockage effect. This behavior is present for both blade collective angles. At the diffuser plane, the flow distribution is not uniform between the windward and leeward sides as expected. However, for $\theta_{0.75R} = 5°$ it can be aknowledged that the flow is not reversed at this region. This is a direct effect onf increasing the blade collective angle which alleviates the negative thrust behavior at $\theta_{0.75R} = 0°$ which was discussed before for the hover flow regime.

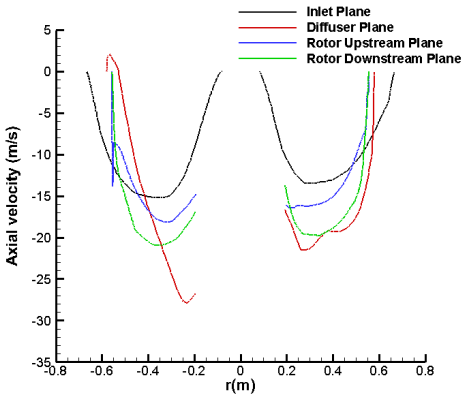

(a) Axial velocity distributions over the inlet, ro-tor and diffuser planes at $\theta_{0.75R} = 5°$, 20 knots

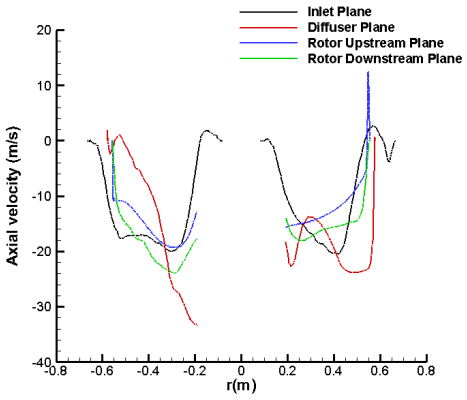

(b) Axial velocity distributions over the inlet, ro-tor and diffuser planes at $\theta_{0.75R} = 5°$, 60 knots

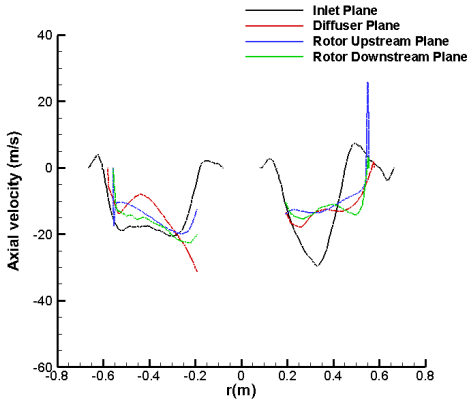

(c) Axial velocity distributions over the inlet, ro-tor and diffuser planes at $\theta_{0.75R} = 5°$, 100 knots

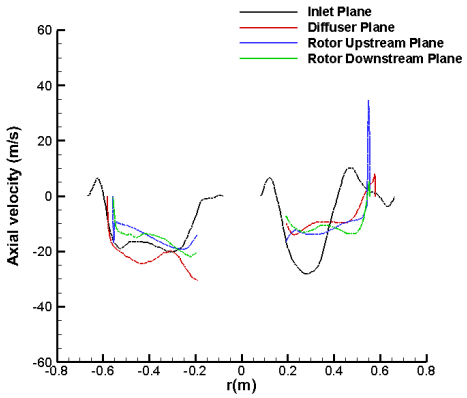

(d) Axial velocity distributions over the inlet, ro-tor and diffuser planes at $\theta_{0.75R} = 5°$, 140 knots

Figure 5.27: Axial velocity distributions over the inlet, rotor and diffuser planes at $\theta_{0.75R} = 5°$

5.5 Implementation of Performance Subroutine

In order to check the validity of the derived performance maps, a comparison was made with power consumption data derived by an in-house rotorcraft comprehensive code called HEliCopTer Omni-disciplinary Research platform (HECTOR). HECTOR utilizes a lifting line approach in order to estimate the performance of a specified helicopter configuration. A detailed presentation of HECTOR will not be provided here and more information can be find here [59].

In pursuit of comparing the performance of a conventional tail rotor as predicted by HECTOR and the generic ducted tail rotor, a medium size helicopter configuration was used. The available medium size helicopter configuration that currently is available in HECTOR is based on the SA 330 PUMA. HECTOR can provide the power consumption of a specified helicopter configuration with respect to increasing advance ratio. A reference simulation has been done using a combination of available rotor parameters [3] in terms of rotor's characteristics. However, it must be stressed that a different combination of parameters can also be used.

Ω_{main}	N_b main and tail rotor	R_M	R_T	Tail rotor gear ratio	x_T
27 rad/s	4	7.5 m	1.56 m	4.82	9 m

Table 5.2: Deployed conventional helicopter parameters for reference simulation [3]

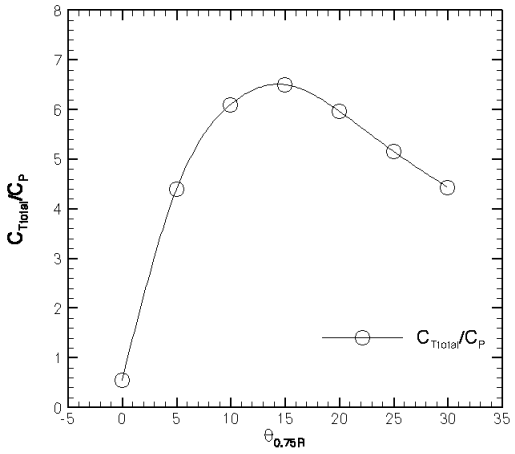

Figure 5.28: C_T/C_P variation with $\theta_{0.75R}$

Fig 5.28 illustrates the power loading (in non-dimensional form) of the generic ducted tail rotor in hover. The C_T/C_P has a maximum value of about 6.5 This value is considerably low and values of C_T/C_P for conventional helicopter configurations are around twice this value [60].

Figure 5.29 illustrates the results for the conventional tail rotor and the generic ducted tail rotor. In addition, as a means of validating the results the power consumption of the SA 341 Gazelle Fenestron is also given. By inspecting Figure 5.29a and 5.29b it can be seen that at least qualitatively (the geometries are different) the two plots bear strong similarities. First of all, a noticeable trend of these curves is the behavior of the ducted tail rotor configuration in hover. The CFD results confirm with the fact that a ducted tail rotor configuration requires more power in hover than in forward flight. According to Mouille [4] this is due to "the small size of the rotor, dictated by the necessity to integrate it into a reasonable-sized vertical fin, results in reduced propulsion efficiency". This propulsion efficiency quoted by Mouille is of course, the static thrust efficiency since hover is concerned.

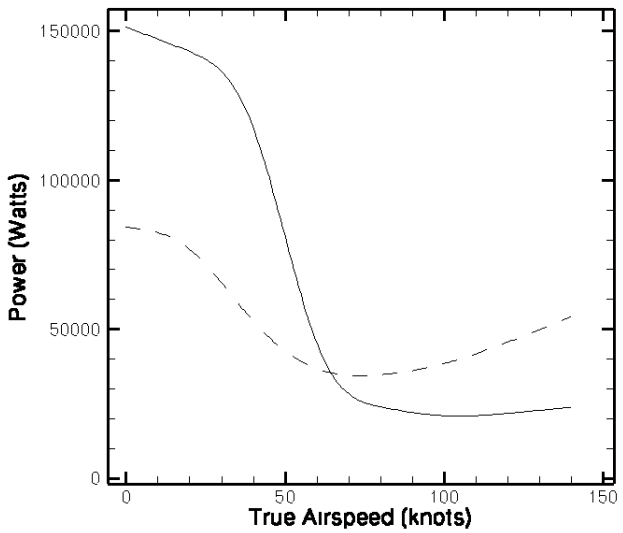

(a) Power consumption comparison between conventional tail rotor (HECTOR results) and generic ducted tail rotor (CFD results)

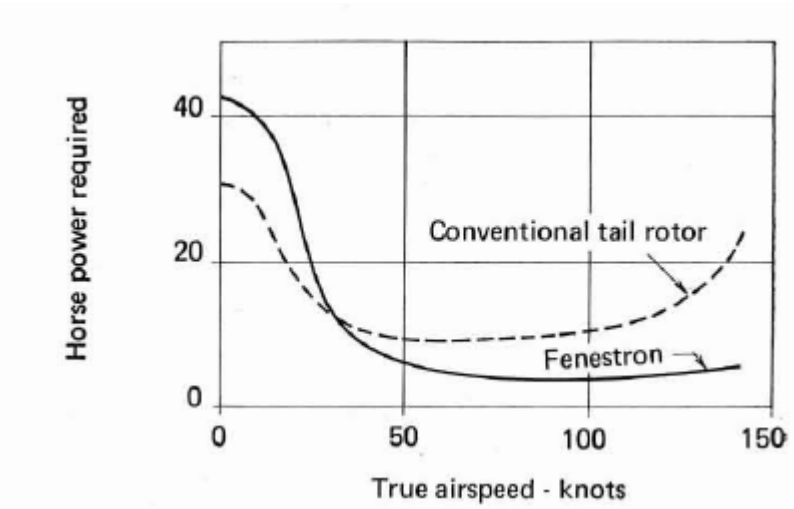

(b) Power consumption comparison between conventional tail rotor and ducted tail rotor [4]

Figure 5.29: Power required versus forward flight speed, qualitative comparison between generic ducted tail rotor and conventional tail rotor

\	Power in hover (Watts)	Power in forward flight (Watts)
Conventional rotor	84289.5	54117.0
Ducted rotor	151,222.9	23828.4
Percentage difference %	79	-56

Table 5.3: Absolute values and percentage differences in absorbed power for the conventional and ducted tail rotor

Mouille mentions that for the SA 341 Gazelle the power absorbed in hover from the ducted tail rotor was 38% higher than the conventional tail rotor and the power absorbed in forward flight was 70% less at 136 knots in forward flight. It was also reported that the economy in the absorbed power from the tail rotor in forward flight "is not integrally gained for the whole aircraft as the antitorque thrust provided by the fin adds additional drag". Table 5.3 shows the absolute values of absorbed power in hover and high speed forward flight for both the conventional and ducted tail rotor. The results suggest a 79% higher power consumption for the ducted tail rotor in hover and around 56% less power consumption in forward flight at 140 knots. In addition, by inspecting Figure 5.29a it can be seen that the power consumption of the ducted tail rotor, at high speed forward flight (140 knots), is around 20,000 Watts. The power consumption at 140 knots, for a blade collective range $\theta_{0.75R} = 0° - 5°$, is 13,905 and 26,103 Watts respectively. This means that the operating blade collective angle at 140 knots lies within the aforementioned range. This conclusion is similar to the data presented by Wright [7] (see Fig 2.14) for the H-76 FANTAIL which is a helicopter of similar class (medium). Therefore, this conclusion further supports the argument that the presented methodology can provide similar results which are published in the available literature.

5.6 Chapter Summary

The forward flight performance maps as well as the implementation of the performance subroutine has been presented and discussed. Firstly, the deployed grid topology and computational domain was explained. The grid topology has been performed by using the same methodology as in the validation case. Thus, the resulting grid had similar grid distribution as in the validation case. The computational domain consists of a rectangular parallelepiped, which deploys pressure inlet and pressure outlet boundary conditions, for the entrance and exit of the domain respectively. Symmetry boundary conditions were applied in the forward flight case in order to represent zero-shear viscous walls.

In the hover simulations, all the boundaries were assigned pressure inlet conditions and pressure outlet at the bottom of the domain. Furthermore, on the grounds of saving computational time, and the fact that for the derivation of the performance maps, macroscopic values are needed, steady-state simulations were performed. In addition, the results of the grid independence study have been presented, which qualitatively showed that the results between the employed medium and refined grids were comparable.

Secondly, the performance polar curves have been presented. The performance polar curves at forward flight indicate, as compared to the hover case, additionally the effect of increasing forward flight speed and blade collective angle. The ducted tail rotor configuration has the distinct feature, of the off-loading of the rotor by the fin's thrust with increasing forward flight speed. Thus, the simulations were done with a specific increment of 20 knots and for decreasing blade collective angle (see Table 5.1). The performance polar curves showed that the shroud, rotor and fin thrust increase with increasing advance ratio as expected.

By increasing the forward flight speed, the mass flow through the rotor increases as well which corresponds to the increase in thrust. However, a similar comparison with momentum theory could not be made, due to the fact that it is applied only in hover flight. Ideal thrust augmentation factors in forward flight could be derived by the synergy of experiments and flight test campaigns. However, it was shown that the overall behavior of the generic ducted tail rotor is well captured. More precisely, the off-loading of the rotor from the fin is clearly illustrated in Fig 5.29. Finally, the power consumption comparison between the conventional tail rotor, as estimated by HECTOR, and the CFD results compared well with available public domain data [4] (see Fig 5.29). In addition, the operational range of blade collective angles at high forward flight speed is comparable with available public domain data [7] (see Fig 2.14)

Chapter 6

Conclusions and Future Work

6.1 Summary and Conclusions

The ducted tail rotor helicopter configuration or Fenestron as it is worldwide known can be considered as an aerospace system which can offer significant performance benefits. More specifically, it can contribute to the reduction of pollutants such as CO_2 and NO_x in the global helicopter traffic, due to its unparalleled performance (at least for single and medium sized helicopters) in forward flight. In addition, it can offer reduced noise emissions due to the shrouding of the rotor and the enhanced safety features that it can offer. Although this technology has been around for many years, there exists limited CFD related work with regards to its performance prediction especially in forward flight, as compared to available work in open rotors.

On the grounds of filling the gap in the literature in terms of detailed CFD simulations with discrete blades which cover the full flight envelope in hover and forward flight (low to high speed flight), a systematic and thorough numerical investigation has been performed. The presented work concludes with the following achievements. Firstly, a complete body of CFD simulations has

been generated by using a generic geometry which was as realistic as possible in terms of its geometric parameters and aerodynamic design. Secondly, the implementation of a methodology based on CFD in order to derive performance maps which can give the power distribution of the ducted tail rotor with respect to its forward flight speed. This methodology can be integrated under certain assumptions with a rotorcraft comprehensive code in order to be used in helicopter mission analysis studies.

In the first phase of the present research work an introduction was given to the ducted tail rotor configuration as applied to helicopter configurations. Also, a detailed literature review was provided which sed light into the complex shroud-rotor system as well as portraying its aerodynamic characteristics and its dependency on a certain subset of geometric parameters. In addition, reference was given to the previous work done, on ducted tail rotor configurations, as well as the analytical and state of the art CFD methods which have been used for performance prediction purposes. The second phase of this research work accounted for the description of the proposed methodology.

Firstly, the assumptions (Mach and Reynolds number effects on the thrust and power coefficients) regarding the construction of the performance maps were given which was followed by the specifics of the implemented performance subroutine. Consequently, the generic ducted tail rotor geometry was described as well as a validation case, of a ducted tail rotor in hover with similar geometry. The third and final phase consisted of the discussion of the generated performance maps in hover and forward flight as well as a qualitative comparison of the results provided by the performance subroutine with a real helicopter ducted tail rotor configuration.

The derived results have shown the strong capability of CFD in simulating such a complex geometry which is characterized by heterogeneous components and high turbulent flow. Despite the lack of experimental data and the steady flow assumptions (in forward flight) the results suggest that the incorporated CFD model can provide reliable overall performance characteristics. Especially, the results of the performance subroutine have shown that the CFD results can provide realistic correlations about the global behavior, such as the low efficiency of the ducted tail rotor in hover, compared to the conventional tail rotor, as well as the performance benefits in forward flight.

6.2 Future Work

With regards to future work, there are numerous ways for additional research which could build upon this work and extend it. The most apparent additional work is to perform a parametric study of different shroud inlet lip radius, diffuser length and angle as well as different blade tip clearance. The results of such a study could be provided to the performance subroutine which can provide the overall performance benefits of every different case. In addition, unsteady CFD simulations with a sliding mesh approach can be performend in order to show the effect of unsteady flow on the gross performance parameters. With regards to the CFD methodology a Chimera grid could also be applied which can further simplify the time consuming grid generation process.

Another avenue which can be followed in order to expand the current work is its integration with a rotorcraft comprehensive code. Such an integration can be used in order to perform helicopter mission analysis studies. Another research work which can strongly stress the applicability of the proposed methodology

in the design of novel configurations is the aerodynamic analysis of a ducted tail rotor incorporated with an electric motor as well. Every current helicopter configuration incorporates a mechanically driven motor which is always coupled and dependent on the main rotor.

An electric motor could perhaps offer benefits in hover and in forward flight by switching off completely the ducted tail rotor at high forward flight speed. Such a flow regime is a perfect candidate for rigorous CFD analysis in order to investigate the flow over the stopped rotor as well as the contribution of the shroud to the total thrust on this occasion. Finally, additional work could lie in the integration of the performance maps with a rotorcraft comprehensive code. The integration could be necessary in order to provide results in real time for helicopter mission analysis studies. In order to make this methodology more generic more simulation points are needed in order to make sure that the process works for a wide range of different helicopters (with different masses). However, due to the time limitations that such computations possess, an integration could not be performed for numerous conditions such as a wide envelope of sideslip angles and fuselage angles of attack. As a first attempt this could be done in hover and forward flight assuming steady level flight (zero fuselage angle of attack and sideslip angle).

Bibliography

[1] C Yihua, L Dong, Q Zhang, and B Hang. Recent Development of Rotorcraft Configuration. *Recent Patents on Engineering*, pages 49–70, 2007.

[2] J.G Leishman. *Principles of Helicopter Aerodynamics*. Cambridge University Press, 2006.

[3] Gareth D. Padfield. *Helicopter Flight Dynamics*. Blackwell Science, 1996.

[4] R. Mouille. The Fenestron, Shrouded Tail Rotor of the SA.341 Gazelle. *Journal of American Helicopter Society*, pages 31–37, 1970.

[5] A. Vuillet and F. Morelli. New Aerodynamic Design of the Fenestron for Improved Performance. *12th European Rotorcraft Forum*, 1986.

[6] E Alpman, L.N Long, and B.D Kothmann. Toward a Better Understanding of Ducted Rotor Antitorque and Directional Control in Forward Flight. *American Helicopter Society 59th Annual Forum Proceedings, Phoenix, AZ*, May 6-8,2003.

[7] G.P Wright, J.T Driscoll, and Jr J.D Nickerson. Handling Qualities of the H-76 FANTAIL TM Demonstrator. *American Helicopter Society 47th Annual Forum Proceedings*, pages 123–135, 1991.

[8] A. D'Alascio, L.F Chuiton, E. Mouterde, L. Sudre, S. Kirstein, and H. P Kau. Aerodynamic Study of the EC135 Fenestron In Hovering Flight

Conditions by means of CFD. *American Helicopter Society 64th Annual FForum*, 2008.

[9] J L.Pereira. *Hover and Wind Tunnel Testing of Shrouded Rotors for Improved Micro Air Vehicle Design*. PhD thesis, Univerisy of Maryland, 2008.

[10] V.K Lakshminarayan. *Computational Investigation of Micro-Scale Coaxial Rotor Aerodynamics in Hover*. PhD thesis, University of Maryland, 2009.

[11] G. C. Ruzicka and R. C. Strawn. Discrete Blade CFD Analysis of a Ducted Tail Fan Flow. *42th AIAA Aerospace Sciences Meeting and Exhibit*, 2004.

[12] A.H Sacks and J.A Burnell. Ducted Propellers , A Critical Review of the State of the Art. *In Progress in Aeronautical Sciences*, 3:85–135, 1962.

[13] L Kort. Combined Device of a Ship Propeller Enclosed by a Nozzle. *US Patent No. 2-030-375*, (2-030-375), February 11, 1936.

[14] L Stipa. Experiments with Intubed Propellers. *NACA TM 655*, Jan 30, 1932.

[15] L Stipa. Stipa Monoplane with Venturi Fuselage. *NACA TM 753*, Sep 1934.

[16] W Kruger. On Wind Tunnel Tests and Computations Concerning the Problem of Shrouded Propellers. *NACA TM 1202*, Feb 1949 Translation of ZWB Forschungsbericht Nr. 1949, Aerodynamischen Versuchsanstalt (AVA), Gottingen, Germany, Jan 21, 1944, Feb 1949.

[17] J.L Beveridge. Design and Performance of Bow Thrusters. *Naval Ship Research and Development Center Bethesda, Md.*, 2003.

[18] Jr R.J Platt. Static Tests of a Shrouded and an Unshrouded Propeller. *NACA RM L7H25, Langley Memorial Aeronautical Laboratory*, Feb 9, 1948.

[19] John D.Anderson Jr. *Fundamentals of Aerodynamics*. McGraw-Hill, 2007.

[20] V Hrishikeshavan. *Experimental Investigation of a Shrouded Rotor Micro Air Vehicle in Hover and Edgewise Gusts*. PhD thesis, University of Maryland, 2011.

[21] H.H Hubbard. Sound Measurements for Five Shrouded Propellers at Static Conditions. *NACA TN 2024, Langley Memorial Aeronautical Laboratory,*, Apr 1950.

[22] D R. Clark. Aerodynamic Design Rationale for the Fan-in-Fin on the S-67 Helicopter. *American Helicopter Society 31st Annual National Forum*, 1975.

[23] C Keys, M Sheffler, S Weiner, and R Heminway. LH Wind Tunnel Testing: Key to Advanced Aerodynamic Design. *American Helicopter Society 47th Annual Forum Proceedings Phoenix AZ*, pages 77–87, May 6-8 1991.

[24] J.E Fairchild, N.N Batra, and R.L Stewart. Influence of Design Parameters on Fan-in-Fin Static Performance. *American Helicopter Society 29th National Forum*, 1973.

[25] B. N. Bourtsev and S.V. Selemenev. Fan-in-Fin Performance at Hover Computational Method. *26th European Rotorcraft Forum*, 2000.

[26] J Philippe. 30 Years of Rotorcraft Aerodynamics Research at ONERA. *Heli Japan*, TP 2007-33, 2006.

[27] D Kuchemann and J Weber. Concerning the Flow About Ring-Shaped Cowlings Part VI: Further Measurements on Inlet Devices. *NACA TM 1327*, Dec 1951.

[28] A.R Krieber and M.R Mendehall. Predicted and Measured Performance of Two Full-Scale Ducted Propellers,. *Proceedings of the CAL/USAAVLABS Symposium on Aerodynamic Problems Associated with V/STOL Aircraft*, 2, Jun 1966.

[29] M.R Mendehall and S.B Spangler. Theoretical Study of Ducted Fan Performance. *NASA CR 1494*, Jan 1, 1970.

[30] Jr B. W McCormick. *Aerodynamics of V/STOL Flight Aerodynamic*. Press, 1976.

[31] I.S Gibson. Theoretical Studies of Tip Clearance and Radial Variation of Blade Loading on the Operation of Ducted Fans and Propellers. *Journal of Mechanical Engineering Science*, 16:367–376, 1974.

[32] B.D Kothmann and S.J Ingle. RAH-66 Comanche Linear Aeroservoelastic Stability Analysis: Model Improvements and Flight Test Correlation. *American Helicopter Society International 54th Annual Forum Proceedings*, pages 620–643, May 20-22, 1998.

[33] W.J McCroskey. Some Rototcraft Applications of Computational Fluid Dynamics. *NASA TM 100066*, March 1988.

[34] A.T Conlisk. Modern Helicopter Aerodynamics. *Annu. Rev. Fluid. Mech*, 29:515–567, 1997.

[35] F.X Caradonna and C Tung. Experimental and Analytical Studies of a Model Helicopter Rotor in Hover. *NASA TM 81232*, September 1981.

[36] G. R. Srinivasan, V. Raghavan, and E.P.N. Duque. Flowfield Analysis of Modern Helicopter Rotors in Hover by Navier-Stokes Method. *International Technical Specialists Meeting: Rotorcaft Acoustics and Rotor Fluid Dynamics*, 1991.

[37] R.G. Rajagopalan and C.N. Keys. Detailed Aerodynamic Analysis of the RAH-66 FANTAIL. *Journal of American Helicopter Society*, pages 310–320, 1997.

[38] H.D Lee and O. J Kwon. Detailed Aerodynamic Analysis of a Shrouded Tail Rotor using an Unstructured Mesh Flow Solver. *Transactions Japan Aerospace Society*, 47:23–29, 2004.

[39] E. Mouterde, L. Sudre, A.M. Dequin, A. D'Alascio, and P. Haldenwang. Aerodynamic Computations of Isolated Fenestron in Hover Conditions. *33th European Rotorcraft Forum*, 2007.

[40] T.A Nygaard, A.C Dimanlig, and E.T Meadowcroft. Application of a Momentum Source Model to the RAH-66 Comanche FANTAIL. *American Helicopter Society 4th Decennial Specialists*, Jan 21-23, 2004.

[41] T Schwarz. The Overlapping Grid technique for the Time Accurate Simulation of Rotorcraft. *31st European Rotorcraft Forum*, 2005.

[42] M Gazaix, A Jolles, and M Lazareff. The elsA object-oriented computational tool for industrial application. *23rd ICAS Conference*, September 2002.

[43] P Gardarein, S Canard, and J Prieur. Unsteady Aerodynamics and Aeroacoustic Simulations of a Fenestron Tail Rotor. *American Helicopter Society 62nd Annual Forum, PhoeniX, AZ*, May 9-11, 2006.

[44] EUROCOPTER. Technical data for as365 n3. Technical report.

[45] A Filippone. *Flight Performance of Fixed and Rotary Wing Aircraft.* Elsevier Aerospace Engineering Series, 2006.

[46] M Tarascio, M Gervais, T Gowen, J Ma, and Y Zhao. Raven SAR Rotorcraft Advanced Rotor Control Concept. *Alfrew Gessow Research Center, University of Maryland*, 2001.

[47] W Johnson. *Rotorcraft Aeromechanics.* Cambridge University Press, 2013.

[48] J Young. Helicopter Vertical Stabilizer Design Considerations. Master's thesis, NAVAL Postgraduate School, 1983.

[49] D Raymer. *Aircraft Design: A Conceptual Approach.* AIAA Education Series, 1992.

[50] P.J Roache. Perspective: A Method for Uniform Reporting of Grid Refinement Studies. *Journal of Fluids Engineering*, 116/405, 1994.

[51] *ANSYS FLUENT Users guide.*

[52] V. Patankar. *Numerical Heat Transfer and Fluid Flow.* Mc Graw-Hill, 1980.

[53] F.R Menter. Two Equation Eddy-Viscosity Turbulence Models for Engineering Applications. *AIAA Journal*, 32:1598–1605, 1994.

[54] John W. Slater. Examining Spatial (Grid) Convergence, July 2008.

[55] Rumsey C.L. CFL3d Test Validation Cases - NASA Langley Geometry Laboratory, August 2012.

[56] R. E Peacock. A review of turbomachinery tip gap effects part 1:Cascades. *International Journal of Hear and Fluid Flow*, 1982.

[57] R. E Peacock. A review of turbomachinery tip gap effects part 1:Rotating Machinery. *International Journal of Hear and Fluid Flow.*

[58] A. Akturk. *Ducted Fan Inlet/Exit and Rotor Tip Flow Improvements for Vertical Lift Systems.* PhD thesis, Pennsylvania State University, 2010.

[59] I. Goulos, P. Giannakakis, V. Pachidis, and P Pilidis. Mission Performance Simulation of Integrated Helicopter Engine Systems using an Aeroelastic Rotor Model. *Proceedings of ASME Turbo Expo 2013, San Antonio, Texas,*, 34(4), 2013.

[60] R. W. Prouty. Helicopter Performance, Stability and Control. *Krieger Publishing Company, Malabar FL*, 1995.

[61] A. I. Abrego and R. W Bulaga. Performance Study of a Ducted Fan System. *American Helicopter Society Aerodynamics, Acoustics, and Test and Evaluation Technical Specialists Meeting*, Jan 23-25 2002.

[62] Preston B.M and J.G Leishman. Trailing Vortex Measurements in the Wake of a Hovering Rotor Blade with Various Tip Shapes. *American Helicopter Society Annual Forum*, June 11-13, 2002.

[63] J Chow, G Zilliac, and P Bradshaw. Turbulence Measurementsin the Near Field of a Wingtip Vortex. *NASA Technical Memorandum 110418*, 1997.

[64] W.J Rife Devenport, M.C Liapis, and S.I Follin. The Structure and Development of a Wingtip Vortex. *Journal of Fluid Mechanics*, 312, 1996.

[65] Karthikeyan Duraisamy. *Studies in Tip Vortex Formation, Evolution and Control.* PhD thesis, University of Maryland, 2005.

[66] K.G. Dyer. Aerodynamic Study of a Small, Ducted VTOL Aerial Vehicle, MSc Thesis. Master's thesis, Massachusetts Institute of Technology, 2002.

[67] B Edwards and C Cox. Revolutionary Concepts for Helicopter Noise Reduction - S.I.L.E.N.T Program. *NASA/CR 211650*, 2002.

[68] Grasmeyer J.M and Keennon M. T. Development of the black widow Micro Air Vehicle. In *39th AIAA Aerospace Sciences Meeting and Exhibit*, 2001.

[69] You J.Y, Kwon O.J, and Y. O. Han. Viscous Flow Simulation of Rotor Blades with Tip Slots in Hover. *Journal of the American Helicopter Society*, 54-012006, 2009.

[70] J.G Leishman. Rotorcraft Aeromechanics : Getting through the Dip. *American Helicopter Society*, 55, 2010.

[71] Romuald Morvant. *The Investigation of Blade-Vortex Interaction Noise Using Computational Fluid Dynamics*. PhD thesis, University of Glasgow, 2004.

[72] R. Mouille and F. d, Ambra. "The Fenestron" A Shrouded Tail Rotor Concept for Helicopters. *American Helicopter Society 42nd Annual Forum Proceeedings*, pages 597–606, 1986.

[73] O. Ohanian. *Ducted Fan Aerodynamics and Modeling, with Applications of Steady and Synthetic Jet Flow Control*. PhD thesis, Virginia Polytechnic Institute and State University, 2011.

[74] Roe P.L. Approximate Riemann Solvers, Parameter Vectors and Difference Schemes. *Journal of Computational Physics*, 43:357–372, 1981.

[75] Kundu K. Pijush and M.Cohen Ira. *Fluid Mechanics*. Academic Press, 2002.

[76] Stephen Pope. *Turbulent Flows*. Cambridge University Press, 2000.

[77] M Ramasamy. *Contributions to the Measurement and Analysis of Helicopter Blade Tip Vortices*. PhD thesis, University of Maryland, 2004.

[78] P.R Spalart. Airplane Trailing Vortices. *Annual Review of Fluid Mechanics*, 30, 1998.

[79] P.R Spalart and Allmaras S.R. A One Equation Model for Aerodynamic Flows. *AIAA Paper 92-0439*, 1992.

[80] Roxana Vasilescu. *Helicopter Blade Tip Vortex Modification in Hover Using Piezoelectrically Modulated Blowing*. PhD thesis, Georgia Institute of Technology, 2004.

[81] University of Wisconsin. Me 563 intermediate fluid mechanics lecture notes. Lecture Notes.

Appendix A

A.1 momentum theory Equations

This appendix provides a brief overview of the momentum theory as applied in the open and ducted rotor in order to show the derivation of the mathematical equations that have been used to estimate the different thrust component augmentation factors. The derivation of these equations has been taken from Leishman [2].

A.1.1 Open Rotor in hover

momentum theory plays an important role in helicopter aerodynamics due to the fact that it can provide a first estimate about the performance of the rotor, in a very simple and straightforward manner. momentum theory is basen on the conservation laws of fluid mechanics and assumes an inviscid, incompressible fluid. The flow is characterized as steady in time and quasi-one dimensional with no swirl in the wake of the rotor where only axial momentum is imparted. momentum theory also assumes that the flow expands back to ambient atmospheric pressure at the far wake of the open rotor or at the diffuser exit plane for the case of the ducted rotor.

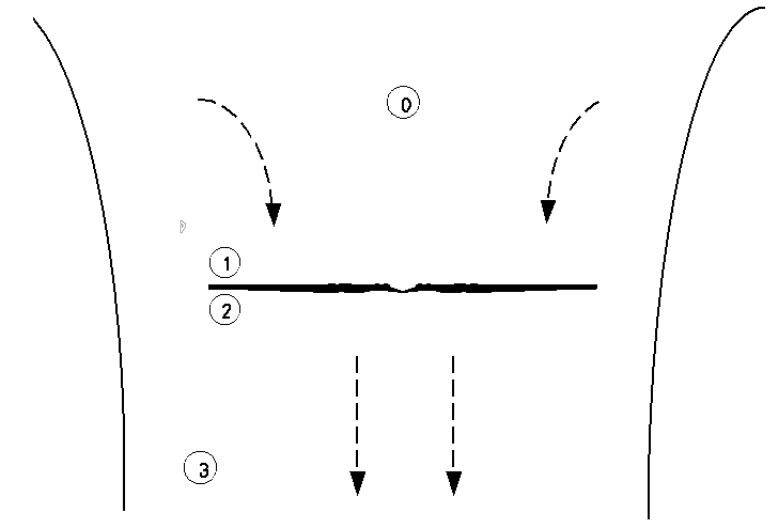

(a) Open Rotor

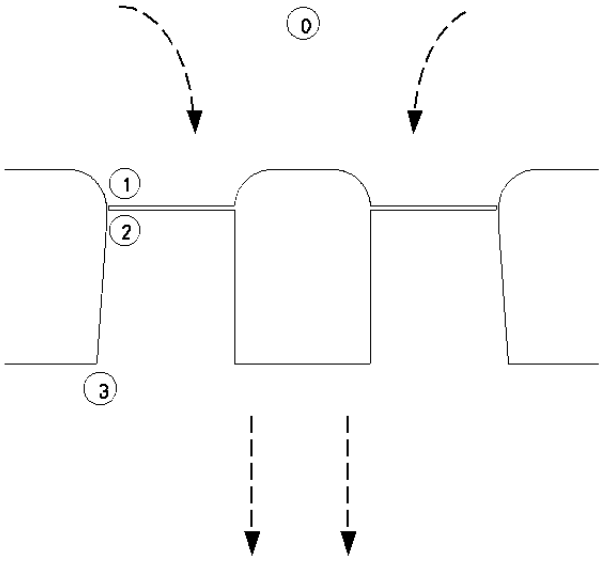

(b) Ducted rotor

Figure A.1: Control volumes of the open and ducted rotor

The control volume of the open rotor is shown in Fig A.1. In this analysis normally the freestream values upstream of the rotor (station 0) are represented by ∞. The next two stations lie immediately above and below the rotor respectively (stations 1 and 2 respectively). Station 3 represents the far wake of the rotor. By applying the conservation laws the thrust and power relationships are the following:

- Conservation of Mass: $\dot{m} = \rho A v_i$ (A.1)
- Conservation of Momentum: $T_{rotor} = \dot{m} w$ (A.2)
- Conservation of Energy: $P_i = \frac{1}{2}\dot{m} w^2$ (A.3)

The thrust of the rotor can be expressed as a pressure jump when the rotor is approximated as an infinitely thin disk (actuator disk theory). Therefore the thrust between the suction and the pressure side of the rotor is given by:

$$T_{rotor} = \Delta p A \tag{A.4}$$

where $\Delta p = p_2 - p_1$ is the pressure jump caused by the rotor

By applying Bernoulli equation between stations 0 and 1 and stations 2 and 3 and considering that

$$v_0 = 0,\ v_1 = v_2 = v_i,\ v_3 = w$$

$$A_1 = A_2 = A_3$$

$$p_0 = p_3 = p_{atm}$$

the pressure jump of the rotor can be written as:

$$p_0 + \frac{1}{2}\rho v_0^2 = p_1 + \frac{1}{2}\rho v_1^2$$

$$p_2 + \frac{1}{2}\rho v_2^2 = p_3 + \frac{1}{2}\rho v_3^2$$

$$\Delta p = \frac{1}{2}\rho w^2 \tag{A.5}$$

Combining equations A.5 and A.4 the thrust of the rotor can be written as:

$$T_{rotor} = \frac{1}{2}\rho A w^2 \tag{A.6}$$

Then by combining equations A.6, A.1 and A.3 the induced power of the rotor can be written as:

$$P_i = T_{rotor} v_i \tag{A.7}$$

Rearranging equations A.7, A.2 and A.3 the expression between the far wake velocity and the induced velocity can be written as:

$$w = 2v_i \tag{A.8}$$

Combining equations A.6 and A.8 the induced velocity can be written as:

$$v_i = \sqrt{\frac{T_{rotor}}{2\rho A}} \tag{A.9}$$

Finally by combining equations A.9 and A.7 the induced power can be written as:

$$P_i = \frac{T_{rotor}^{3/2}}{\sqrt{2\rho A}} \tag{A.9}$$

A.1.2 Ducted Rotor in hover

The ducted rotor has the benefit of restricting the wake contraction while maintaining a fixed rotor disk area. Thus the area at the exit of diffuser is: $A_e = \sigma_d A$ where A is the rotor disk area. Conservation of mass gives $\dot{m} = \rho A v_i = \rho A_e w = \sigma_d \rho A w$ and provides the far wake velocity for the ducter rotor:

$$w = \frac{v_i}{\sigma_d} \tag{A.10}$$

Equation A.10 shows that the expansion ratio of the shroud controls the far wake velocity and a value of $\sigma_d = 0.5$ corresponds to an open rotor. Conservation of momentum will give:

$$T_{total} = T_{rotor} + T_{shroud} = \dot{m}w = \rho A \frac{\upsilon_i^2}{\sigma_d} \tag{A.11}$$

Equation A.11 provides the relationship for the induced velocity:

$$\upsilon_i = \sqrt{\frac{\sigma_d T_{total}}{\rho A}} \tag{A.12}$$

The rotor thrust component augmentation factor can be given by combining A.6 and A.11:

$$\frac{T_{rotor}}{T_{total}} = \frac{\frac{1}{2}\rho A w^2}{\rho A \upsilon_i w} = \frac{w}{2\upsilon_i} = \frac{1}{2\sigma_d} \tag{A.13}$$

Thus by taking into account the conservation of energy, the induced power of the rotor becomes:

$$P_i = T_{rotor}\upsilon_i = \left(\frac{T_{total}}{2\sigma_d}\right)\sqrt{\frac{\sigma_d T_{total}}{\rho A}}$$

$$= \frac{T_{total}^{3/2}}{\sqrt{4\sigma_d \rho A}} \tag{A.14}$$

Finally, the contribution of the shroud thrust can be provided by combining A.11 and A.13:

$$\frac{T_{shroud}}{T_{total}} = 1 - \frac{1}{2\sigma_d} \tag{A.15}$$

Appendix B

B.1 C_p Distributions Forward Flight

The pressure coefficient distributions are provided in this appendix. The main conclusion that can be derived from all the simulatio points is that by increasing blade collective angle the same behavior exists in terms of the asymmetric pressure distribution. However, by increasing the collective the magnitude of the suction and over-pressure forces increases which results in increased rotor, shroud and fin thrust. This is due to the increased mass flow which consists the effect of increasing the blade collective. Therefore, in the same way as in hover, the configuration draws more air thereby increasing the induced velocity.

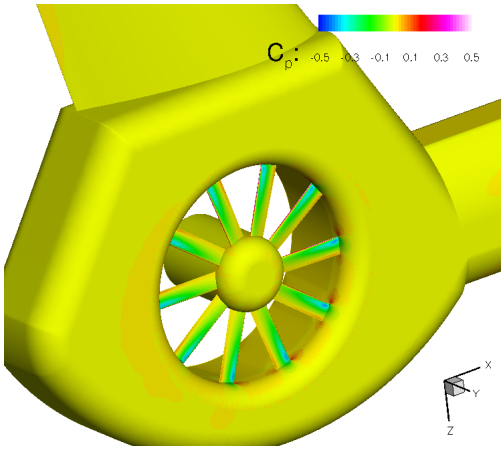

(a) Starboard view $\theta_{0.75R} = 0°$ at 20 knots

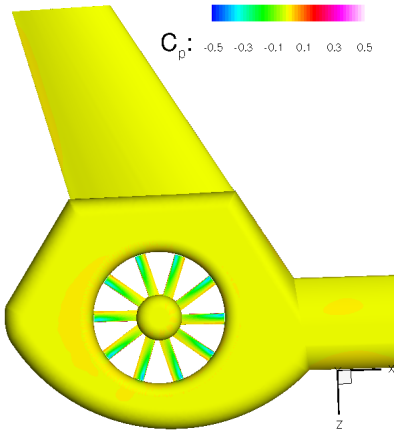

(b) Starboard view including fin $\theta_{0.75R} = 0°$ at 20 knots

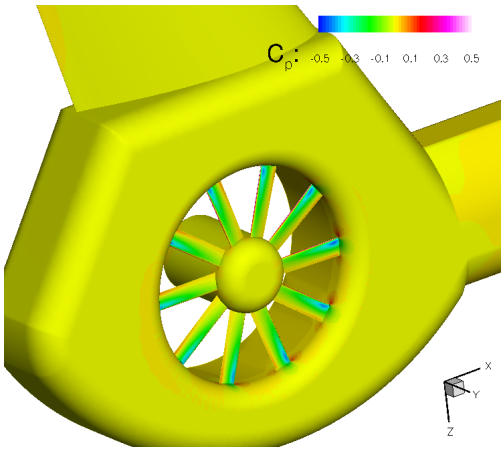

(c) Starboard view $\theta_{0.75R} = 0°$ at 40 knots

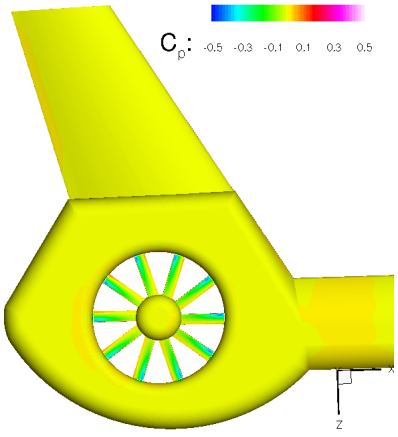

(d) Starboard view including fin $\theta_{0.75R} = 0°$ at 40 knots

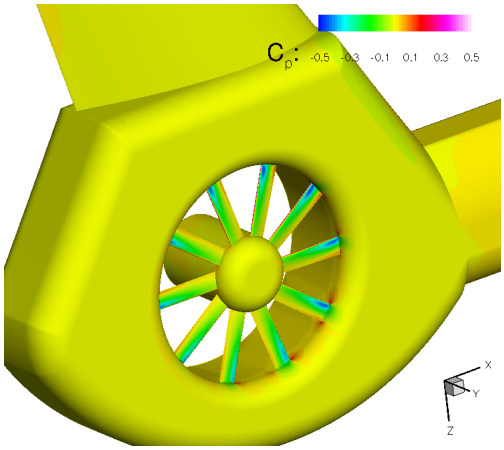

(e) Starboard view $\theta_{0.75R} = 0°$ at 60 knots

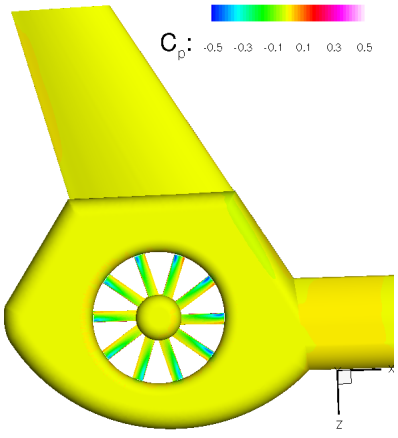

(f) Starboard view including fin $\theta_{0.75R} = 0°$ at 60 knots

Figure B.1: Starboard C_p contours for blade collective angle 0°, at 20, 40 and 60 knots

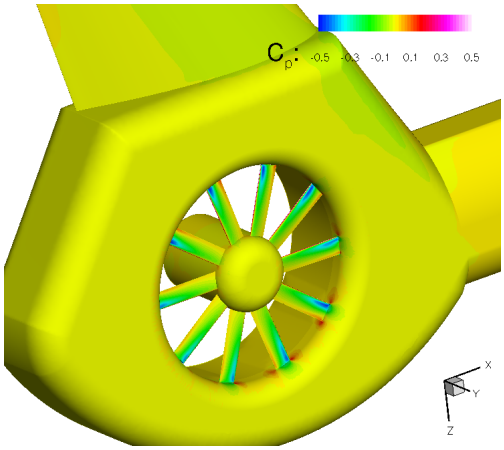

(a) Starboard view $\theta_{0.75R} = 0°$ at 80 knots

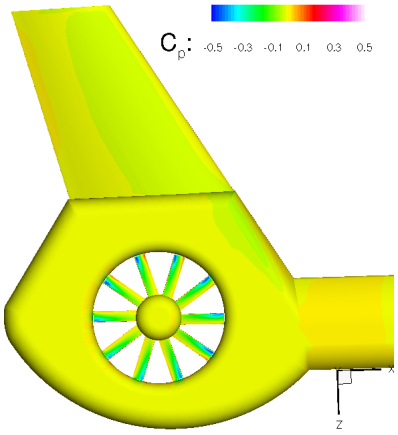

(b) Starboard view including fin $\theta_{0.75R} = 0°$ at 80 knots

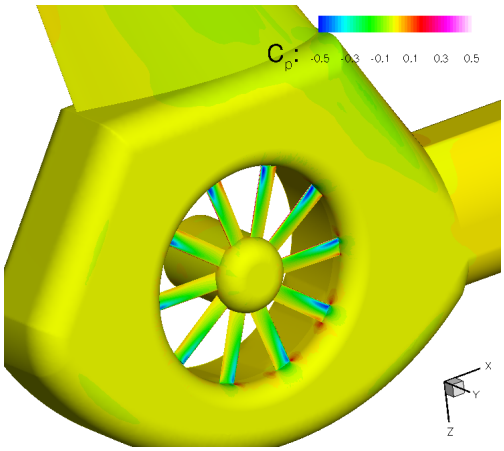

(c) Starboard view $\theta_{0.75R} = 0°$ at 100 knots

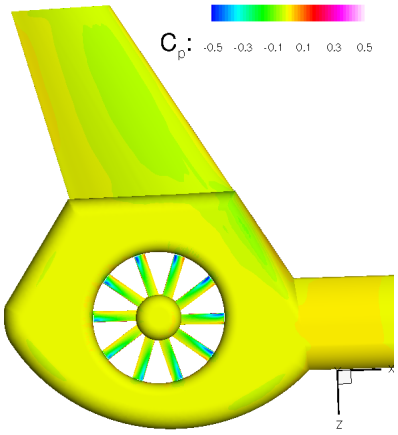

(d) Starboard view including fin $\theta_{0.75R} = 0°$ at 100 knots

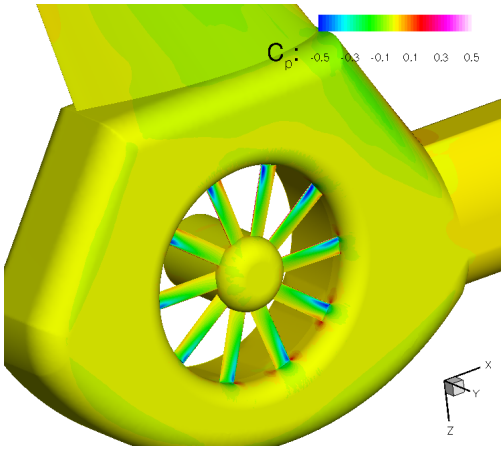

(e) Starboard view $\theta_{0.75R} = 0°$ at 120 knots

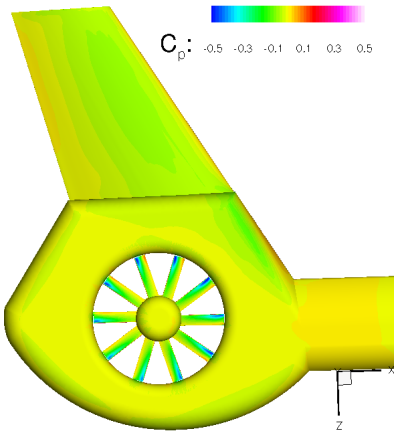

(f) Starboard view including fin $\theta_{0.75R} = 0°$ at 120 knots

Figure B.2: Starboard C_p contours for blade collective angle 0°, at 80, 100 and 120 knots

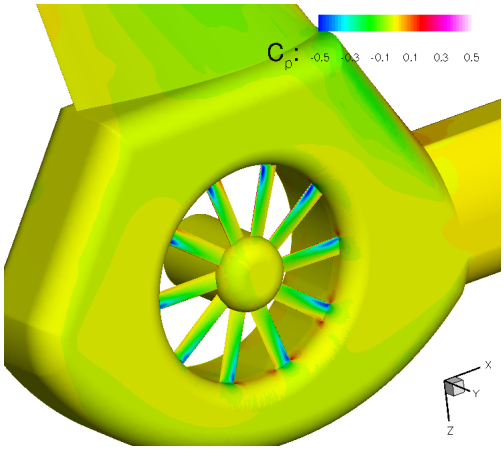

(a) Starboard view $\theta_{0.75R} = 0°$ at 140 knots

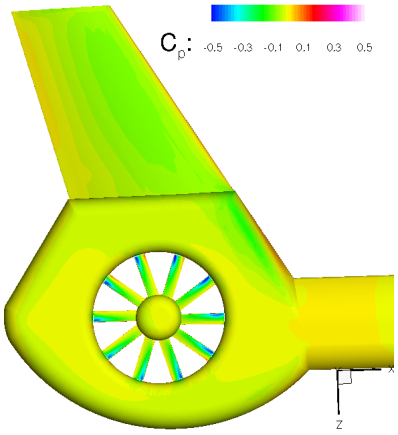

(b) Starboard view including fin $\theta_{0.75R} = 0°$ at 140 knots

Figure B.3: Starboard C_p contours for blade collective angle 0°, at 140 knots

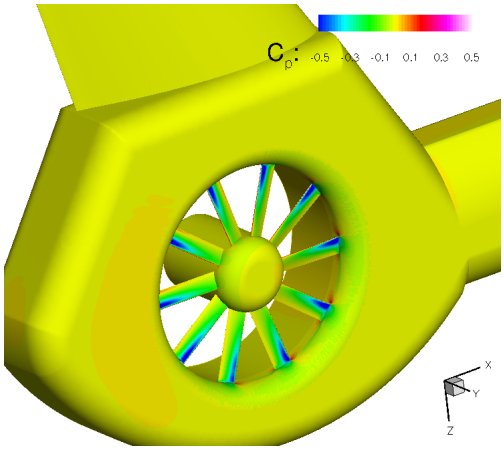

(a) Starboard view $\theta_{0.75R} = 10°$ at 20 knots

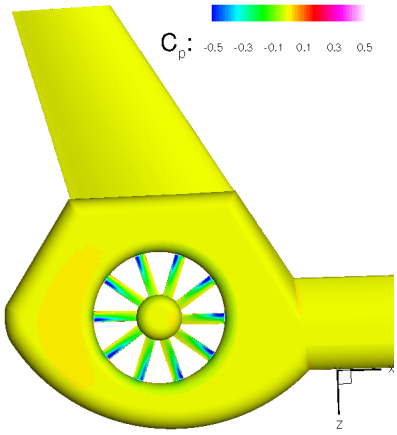

(b) Starboard view including fin $\theta_{0.75R} = 10°$ at 20 knots

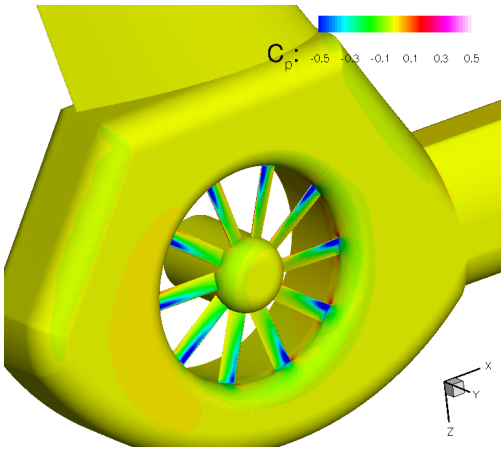

(c) Starboard view $\theta_{0.75R} = 10°$ at 40 knots

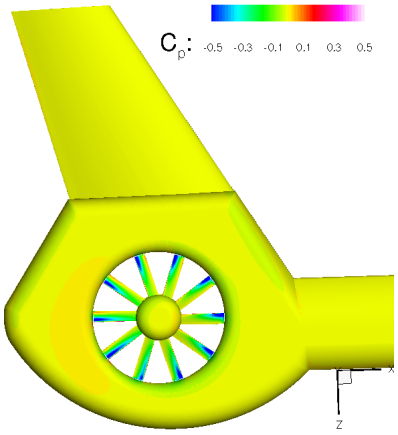

(d) Starboard view including fin $\theta_{0.75R} = 10°$ at 40 knots

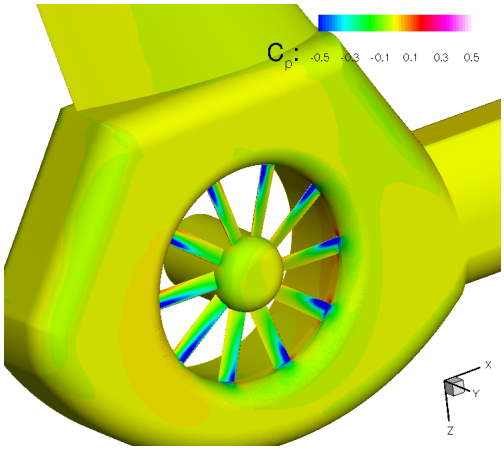

(e) Starboard view $\theta_{0.75R} = 10°$ at 60 knots

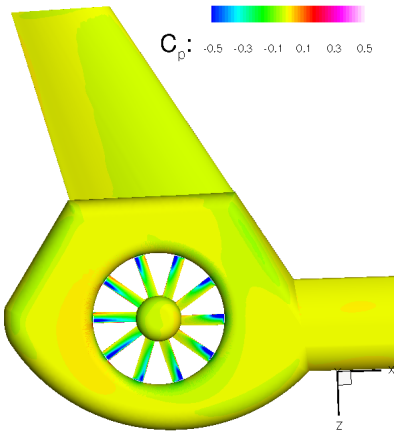

(f) Starboard view including fin $\theta_{0.75R} = 10°$ at 60 knots

Figure B.4: Starboard C_p contours for blade collective angle 10°, at 20, 40 and 60 knots

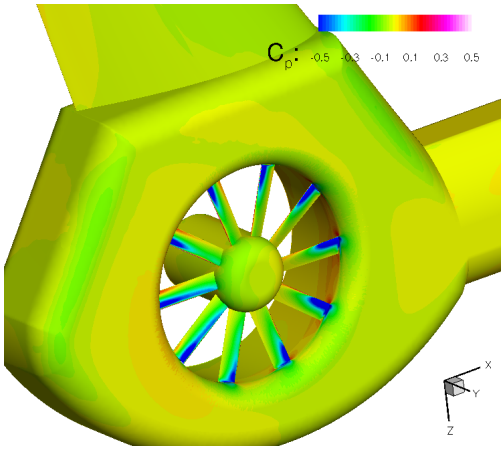

(a) Starboard view $\theta_{0.75R} = 10°$ at 80 knots

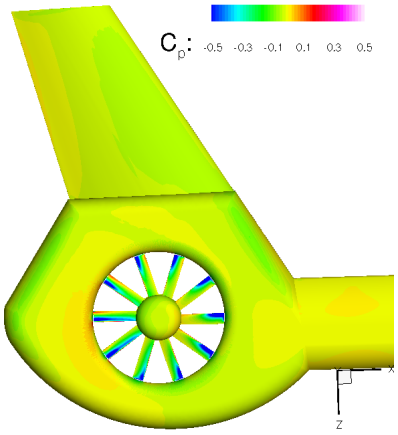

(b) Starboard view including fin $\theta_{0.75R} = 10°$ at 80 knots

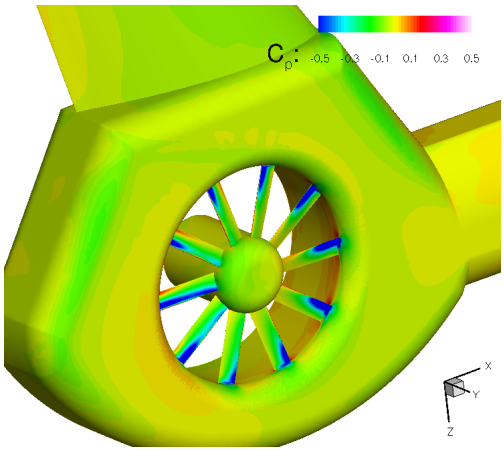

(c) Starboard view $\theta_{0.75R} = 10°$ at 100 knots

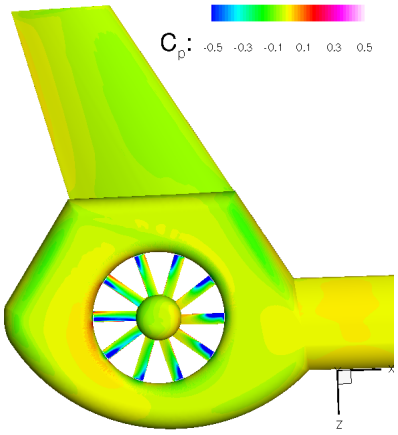

(d) Starboard view including fin $\theta_{0.75R} = 10°$ at 100 knots

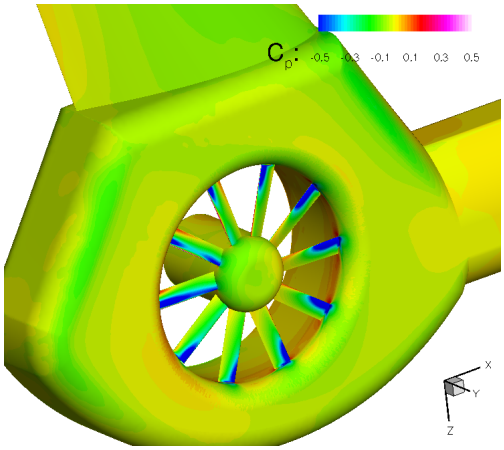

(e) Starboard view $\theta_{0.75R} = 10°$ at 120 knots

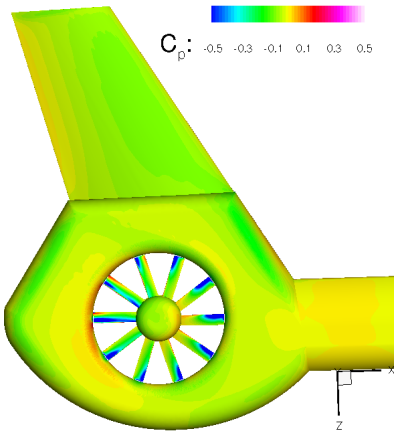

(f) Starboard view including fin $\theta_{0.75R} = 10°$ at 120 knots

Figure B.5: Starboard C_p contours for blade collective angle 10°, at 80, 100 and 120 knots

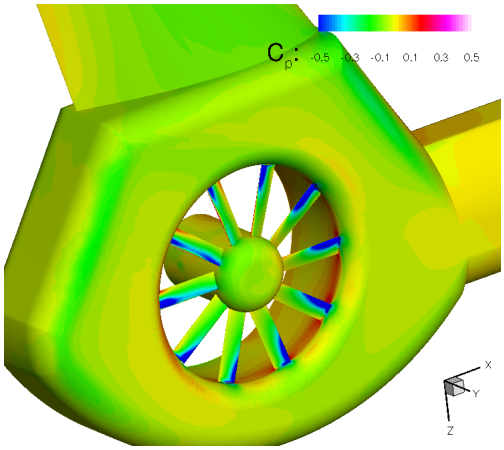

(a) Starboard view $\theta_{0.75R} = 10°$ at 140 knots

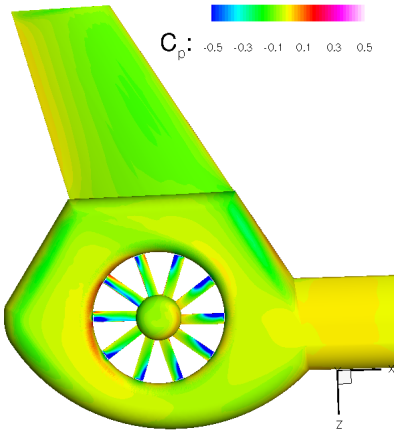

(b) Starboard view including fin $\theta_{0.75R} = 10°$ at 140 knots

Figure B.6: Starboard C_p contours for blade collective angle 10°, at 140 knots

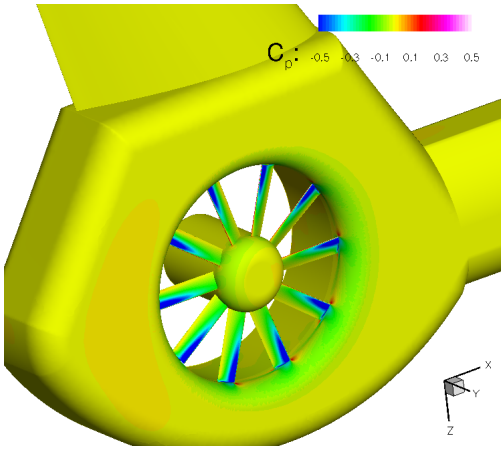

(a) Starboard view $\theta_{0.75R} = 15°$ at 20 knots

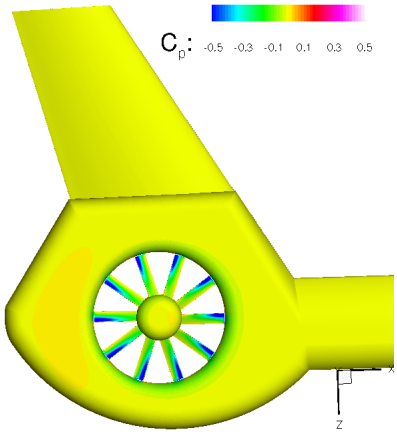

(b) Starboard view including fin $\theta_{0.75R} = 15°$ at 20 knots

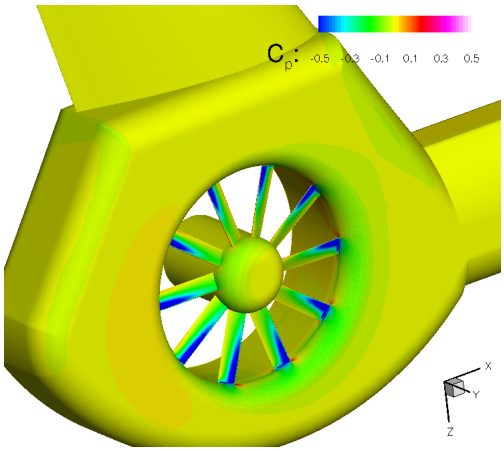

(c) Starboard view $\theta_{0.75R} = 15°$ at 40 knots

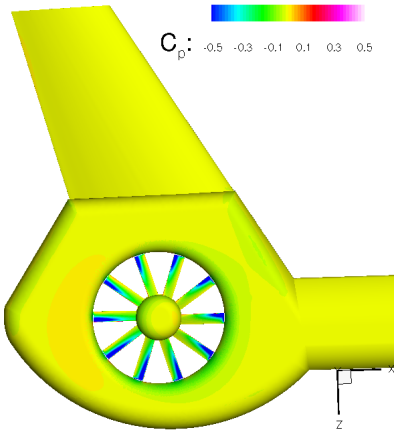

(d) Starboard view including fin $\theta_{0.75R} = 15°$ at 40 knots

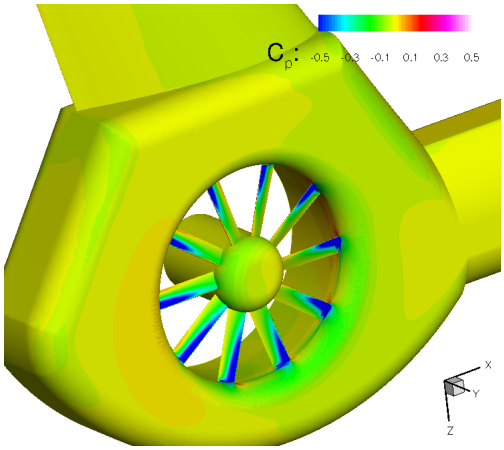

(e) Starboard view $\theta_{0.75R} = 15°$ at 60 knots

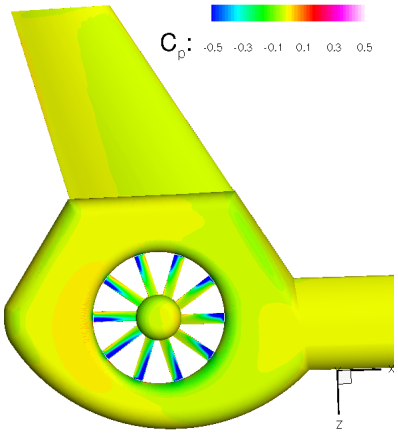

(f) Starboard view including fin $\theta_{0.75R} = 15°$ at 60 knots

Figure B.7: Starboard C_p contours for blade collective angle 15°, at 20, 40 and 60 knots

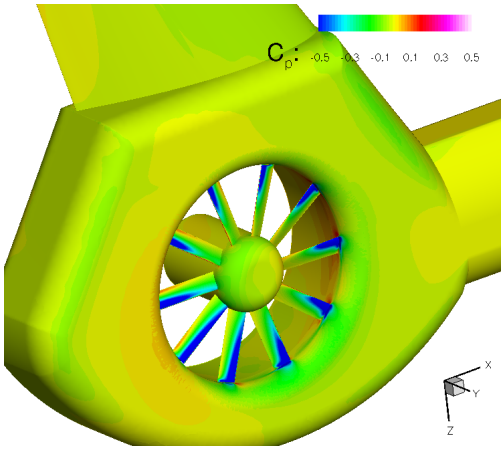

(a) Starboard view $\theta_{0.75R} = 15°$ at 80 knots

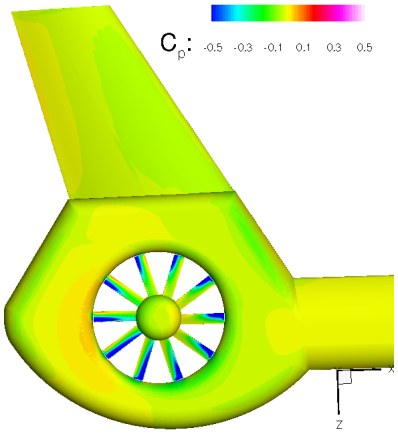

(b) Starboard view including fin $\theta_{0.75R} = 15°$ at 80 knots

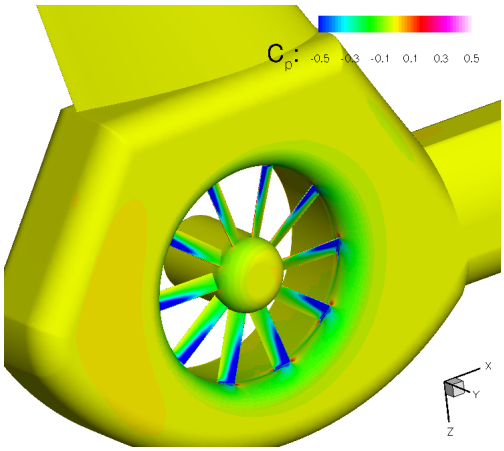

(c) Starboard view $\theta_{0.75R} = 20°$ at 20 knots

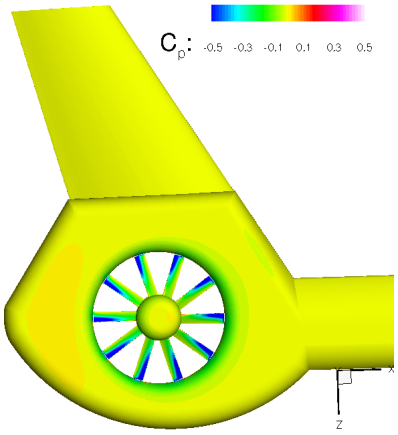

(d) Starboard view including fin $\theta_{0.75R} = 20°$ at 20 knots

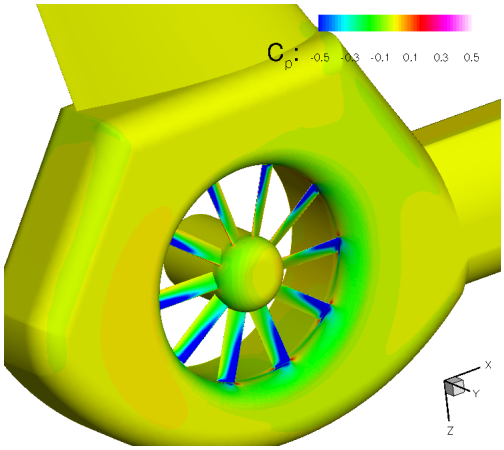

(e) Starboard view $\theta_{0.75R} = 20°$ at 40 knots

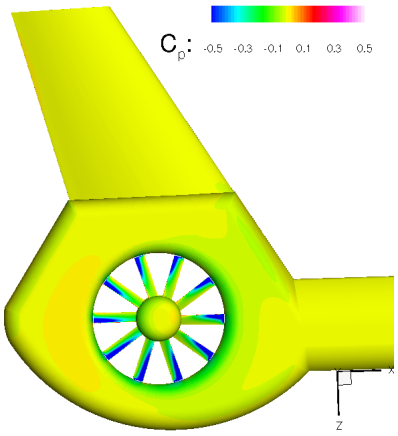

(f) Starboard view including fin $\theta_{0.75R} = 20°$ at 40 knots

Figure B.8: Starboard C_p contours for blade collective angle 15°, at 80 knots and 20^0 at 20 and 40 knots

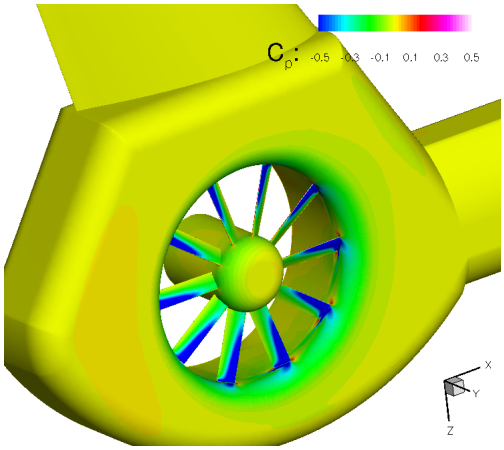

(a) Starboard view $\theta_{0.75R} = 25°$ at 20 knots

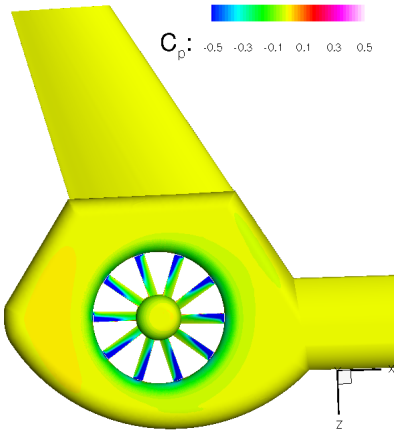

(b) Starboard view including fin $\theta_{0.75R} = 25°$ at 20 knots

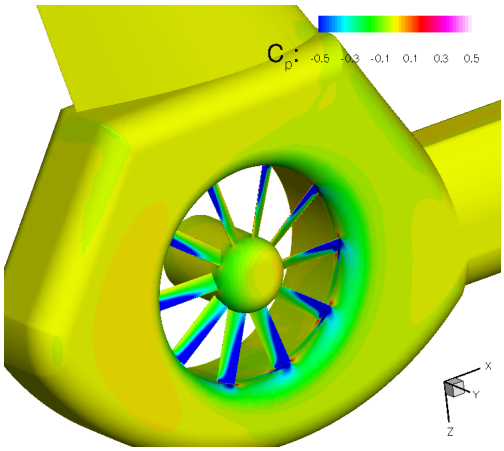

(c) Starboard view $\theta_{0.75R} = 25°$ at 40 knots

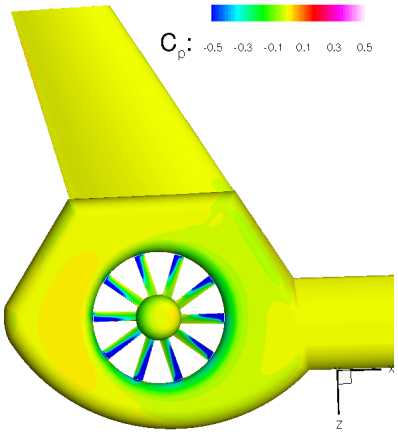

(d) Starboard view including fin $\theta_{0.75R} = 25°$ at 40 knots

Figure B.9: Starboard C_p contours for blade collective angle 25°, at 20 and 40 knots